

UC Davis

UC Davis Electronic Theses and Dissertations

Title

Discrete Element Modeling and Experimental Investigation on the Effects of Soil Fabric and Gradation on the Behavior of Granular Soils

Permalink

<https://escholarship.org/uc/item/1776q6j2>

Author

Basson, Mandeep Singh

Publication Date

2023

Peer reviewed|Thesis/dissertation

Discrete Element Modeling and Experimental Investigation on the
Effects of Soil Fabric and Gradation on the Behavior of Granular Soils

By

MANDEEP SINGH BASSON
DISSERTATION

Submitted in partial satisfaction of the requirements for the degree of

DOCTOR OF PHILOSOPHY

in

Civil and Environmental Engineering

in the

OFFICE OF GRADUATE STUDIES

of the

UNIVERSITY OF CALIFORNIA

DAVIS

Approved:

Alejandro Martinez, Chair

Jason T. DeJong

Katerina Ziotopoulou

Committee in Charge

2023

To my family, mentors, and friends who inspire me everyday

Discrete Element Modeling and Experimental Investigation on the Effects of Soil Fabric and Gradation on the Behavior of Granular Soils

Abstract

The inherent particulate nature of granular soils, such as sands and gravels, plays an important role in their engineering behavior. This dissertation aims to advance the fundamental understanding of the effect of fabric- and stress-induced anisotropy, and gradation on the micro- and macro-scale behavior of coarse-grained granular soils.

The first portion of this dissertation addresses the direction-dependent characteristics exhibited by soils reflected in the anisotropy of their responses. Studies have shown that both the depositional processes and particle arrangements (i.e., fabric-induced anisotropy), and the stress state and history (i.e., stress-induced anisotropy) impact the anisotropic behaviors observed at the macroscopic level. Quantifying these anisotropies has been challenging, necessitating specialized geotechnical testing and imaging equipment. To overcome these challenges, a novel experimental testing setup is introduced, designed to measure shear wave velocities (V_s) along different orientations and polarization planes using piezoelectric bender elements (BEs) to obtain angular distributions of V_s . Subsequently, two investigations on shear wave propagation are presented, using the developed setup and Discrete Element Method (DEM) simulations, to explore the effects of fabric- and stress-induced anisotropy on the V_s anisotropy. The experimental tests were

performed on glass beads and angular natural sands, while the DEM simulations used spherical and rod-like clumped particles. These specimens were subjected to isotropic and one-dimensional (1D) compression. The results reveal that the angular distributions of V_s and measurements obtained along different polarization planes (i.e. $V_{s,HH}$, $V_{s,HV}$, and $V_{s,VH}$) can discern the effects of fabric and stress anisotropy. The observed trends indicate a relationship between the angular distributions of V_s and of the alignment of particles and interparticle contact forces. A framework is presented based on the V_s measurements along various orientations and polarization planes which is validated using the presented results. When presented in terms of the ratio of V_s measurements along different orientations and polarization planes, namely the $V_{s,HV}/V_{s,VH}$ and $V_{s,HV}/V_{s,HH}$ ratios, and of the newly introduced Anisotropy parameter (A_e), this framework facilitates the evaluation of the stress- and fabric-induced anisotropy in soil specimens. The results also highlight the challenges in discerning the effects of stress and fabric anisotropy when both simultaneously influence the soil response.

Geosystems built on coarse-grained soils with broader gradations are typically designed and analyzed using methodologies developed for poorly-graded soils without explicit consideration of the effects of gradation, potentially leading to uncertainty in performance predictions. In the second portion of this dissertation, the effects of changes in the gradation on various aspects of monotonic and cyclic response of coarse-grained soil behavior are investigated using DEM simulations. The simulations include monotonic isotropically-consolidated drained and undrained triaxial tests, and cyclic undrained direct simple shear tests conducted on specimens with coefficients of uniformity (C_u) between 1.9 and 6.4 composed of non-spherical particles. The triaxial simulation results indicate that an increase

in C_U leads to increases in peak shear strength, dilative volume change, rate of dilation, negative pore pressure generation, and rate of pore pressure generation. These findings are compared with established frameworks to highlight the differences in response resulting from variations in C_U .

Particle-level measurements from the monotonic simulations highlight the influence of gradation on both the packing characteristics and the transmission of contact forces within the soil assembly. In particular, for the broadly graded specimens, the coarsest particles exhibit a disproportionately higher number of connections and carry significantly greater contact forces compared to the coarsest particles in poorly graded soils. The coarsest particles for the broadly graded specimen are connected to a disproportionately higher number of particles and carry disproportionately higher contact forces as compared to coarsest particles in poorly graded soils. The enhanced interlocking of the coarser particles results in greater dilation during shearing, leads to higher peak shear strengths for the more broadly graded specimens. Additionally, the particles smaller than D_{10} are inactive in contact force transmission, while the percentage of particles active in contact force transmission increases with an increasing C_U .

During cyclic shearing, specimens with broader gradations yield lower liquefaction-triggering resistance than poorly graded specimens at similar relative densities. Conversely, the opposite trends emerge when compared at similar initial state parameters. Post-liquefaction, specimens with broader gradation accumulate shear strains at a smaller rate. A comparison is presented, examining the interpretation of grading-dependent behavior by choosing relative density or initial state parameters as the state definition for both

monotonic and cyclic response, highlighting the efficacy of initial state parameter in capturing the systematic differences in the response because of changes in gradation. The improved interlocking in more broadly graded specimens results in a lower percentage of sliding contacts for both strong and weak force-carrying contacts at the initiation of liquefaction and in subsequent cycles, which is linked to the slower rate of post-liquefaction strain accumulation in well-graded specimens.

The combination of macro and micro observations, from the research efforts presented in this dissertation, highlight the influence of fabric- and stress-induced anisotropy and gradation on soil behavior through a combination of novel experimental testing and DEM simulations, and contribute to the advancements in the geotechnical site characterization, design methodologies, numerical simulation techniques, and constitutive modeling of granular soils.

Acknowledgments

I am deeply grateful to the numerous extraordinary individuals, organizations, and resources who have contributed to the completion of this dissertation. Without their unwavering support, this journey would not have been possible.

First, and foremost, I would like to thank my advisor and mentor, Prof. Alejandro Martinez, for a wonderful opportunity to be a part of this project and his group. Throughout the years, he has shown immense patience, guiding me through the challenges and uncertainties of this journey. His unwavering kindness, encouragement, and support have been a constant source of strength, inspiring me to venture beyond my comfort zone of numerical simulations. Particularly, one of the biggest highlights of our collaboration was publishing my first paper as an experimental testing paper with ASTM GTJ, which I will cherish for a long time. I am thankful for him recognizing and nurturing my passion for teaching and mentorship, which has become a profound source of joy and fulfillment. Thank you for encouraging me to explore this path, which has become a passion project. Outside of research, I have immensely enjoyed our random talks about food, cultures, bands, traveling, academia, and general life during our weekly meetings, which I will miss the most.

I am grateful to my thesis committee members Prof. Jason T. DeJong and Prof. Katerina Ziotopoulou. Jason has been a beacon of wisdom throughout this journey, and his ability to connect my micro-scale analysis with a bigger picture of practical geotechnical engineering has been immensely helpful. I am grateful for his expertise and constructive feedback that has been indispensable to this work and for the moments we have shared outside research,

ranging from help with the students in my class to general life philosophy. Katerina's passion for teaching and all things computer has been my biggest source of inspiration. I have been mesmerized and learned a lot about her way of teaching students, dealing with accommodations, and being professional in my communications. I enjoyed our talks about Python, computers, coding, and being bold in life (which I am slowly practicing).

I would also like to thank Prof. Ross Boulanger for inspiring me to get out of my computer world and develop the art of engineering judgment in all my analyses. I greatly appreciate all his insights into my research and the world of academia. Discussions with Prof. Yannis Dafalias and Prof. Mark Rashid have been immensely helpful regarding the exciting world of computational mechanics and the mathematics behind numerical modeling. I am thankful to Prof. Matt Evans for his crucial contribution to my qualifying exam committee and all the discussions about DEM simulations. Prof. I. M. Idriss for his handshake and words of wisdom during the GGSS round table. Prof. Colleen Bronner has been immensely helpful in providing me with resources to be successful as a teacher and helping me explore engineering education.

This research would naturally not have been possible without funding sources and support from the staff and students. I want to thank the National Science Foundation (NSF) for funding this research under the grant CMMI #1916152. I am also grateful to the UC Davis College of Engineering for the fellowship funding, generous travel awards, and the EPRIME scholarship. I am thankful to Andrew Cobb, Daret Kahlet, and Victor Jones for helping me with the experimental setup, and Jasmine Miller for collaborating on creating the experimental testing setup and soldering lots of bender elements. I want to thank Dr. Robert

Jaeger and George Hu from Division of Safety of Dams for their collaboration and industry perspective on the EPRIME levees project.

I feel very fortunate for all the interactions and friendships I have created at UC Davis. I am thankful for all the collaborations and conversations with the Granular Materials group, including Lin Huang, Dr. Yuyan Chen, Dr. Sharif Ahmed, Olivia Hunt, Sam Follett, Damon Nguyen, and Dr. Srikanth Madabushi. I want to thank the old Geotechnical Graduate Student Society (GGSS) group with Alexandra San Pablo, Dr. Sumeet Sinha, Matthew Burrall, Dr. Patrick Bassal, Dr. Renmin Pretell, Dr. Francisco Humire, Dr. Han Yang, Dr. Kevin Kuei, Dr. Alena Raymond, Casey Phradichith, and Hussain Alshawaf for all the interactions which made me comfortable during my first few years at Davis. The new GGSS group with Riya Anilkumar, Mitch DeJager, Katherine Cheng, Irene Liou, Dora de Melo, Laura Luna, Maziar Mivechi, and Kat Spence have been a breath of fresh air and their interactions have filled my life with optimism (and a lot of fresh memes). Overall, GGSS has enriched the experience at Davis, and I hope the camaraderie stays for years to come. Outside GGSS, I want to thank everyone from the Indian and Sikh communities who supported me throughout my time at Davis.

I want to thank the unwavering love and support from my family. Thank you, Mom, for all your effort and sacrifices for my education and your constant encouragement in reaching my goals. I hope I can be a great teacher like you. Thank you, Dad, for all the opportunities and engineering discussions, and for being a role model for hard work. A big thank you to my extended family for checking in on me when I would randomly go AWOL. I appreciate all the support and encouragement.

Finally, I want to thank my wife, Simrit, for the love, encouragement, support, and being by my side throughout this journey. Your constant support has been my anchor, and your belief in me has been my guiding light. Your patience during long hours of work, understanding during moments of stress, and celebrating every small victory (enjoyed all the enchilada and ice cream runs) have made this journey memorable. Your presence has been my greatest gift, and I am beyond grateful for the love that has carried me through this milestone. I hope I can support you with equal passion in the future and beyond, and I am excited to see what the future holds for us.....

Contents

Abstract.....	iii
Acknowledgements.....	vii
Contents.....	xi
List of Tables.....	xvi
List of Figures.....	xviii
1 Introduction.....	1
1.1 Background.....	1
1.2 Scope and organization.....	5
1.3 References.....	7
2 A multi-orientation system for determining the angular distributions of shear wave velocity in soil specimens.....	10
2.1 Abstract.....	10
2.2 Introduction.....	11
2.3 Bender element tests.....	15
2.3.1 Notations for shear wave velocities.....	15
2.3.2 Multi-orientation bender element system.....	16
2.3.3 Instrumentation systems and signal interpretations.....	18
2.3.4 Materials, sample preparation, and stress conditions.....	21
2.4 Results.....	23

2.4.1	Influence of mean effective confining stress on V_S	24
2.4.2	Angular variation of shear wave velocity.....	27
2.4.3	Discussion and comparison with other studies.....	31
2.5	Conclusions	33
2.6	Acknowledgements.....	36
2.7	References	36
2.8	Tables and figures.....	48
3	Numerical and experimental estimation of anisotropy in granular soils using multi-orientation shear wave velocity measurements	63
3.1	Abstract.....	63
3.2	Introduction	64
3.3	DEM model and laboratory bender element (BE) setup	67
3.3.1	Notation.....	67
3.3.2	DEM model.....	68
3.3.3	Experimental testing setup.....	72
3.4	Results	75
3.4.1	DEM simulations: angular distributions of shear V_S and fabric metrics....	75
3.4.2	Experimental bender element testing: angular distributions of shear wave velocities	82
3.5	Interpretation framework.....	84
3.5.1	$V_{S,HV}/V_{S,HH}$ and $V_{S,HV}/V_{S,VH}$ ratios	84
3.5.2	Shear wave anisotropy parameter, A_e	87
3.6	Conclusions	90

3.7 Acknowledgements.....	92
3.8 References	92
3.9 Tables and figures.....	101
4 Effect of particle size distribution and contact parameters on the particle connectivity and contact force transmission of granular assemblies	121
4.1 Abstract.....	121
4.2 Introduction.....	122
4.3 DEM simulation details.....	125
4.4 Results and discussion.....	127
4.4.1 Effect of particle size distribution.....	128
4.4.2 Effect of simulation parameters	132
4.4.2.1 Effect of particle friction coefficient (μ).....	132
4.4.2.2 Effect of particle stiffness (k/D).....	133
4.4.2.3 Effect of global viscous damping (ξ).....	134
4.5 Conclusions	135
4.6 Acknowledgements.....	136
4.7 References	136
4.8 Tables and figures.....	142
5 DEM investigation of the effect of gradation on the strength, dilatancy, and fabric evolution of coarse-grained soils	153
5.1 Abstract.....	153
5.2 Introduction.....	154
5.3 Simulation methodology.....	157

5.3.1	Simulated granular materials	157
5.3.2	Simulation methodology.....	160
5.4	Triaxial compression simulations	162
5.4.1	Critical state lines	163
5.4.2	Drained triaxial response.....	165
5.4.3	Stress-dilatancy behavior.....	167
5.5	Fabric evolution during drained triaxial simulations.....	169
5.5.1	Particle connectivity.....	169
5.5.2	Contact force transmission.....	171
5.5.3	Anisotropy in contact force distribution.....	173
5.6	Undrained triaxial response and fabric evolution	174
5.7	Gradation effects on stress-dilatancy and pore pressure generation	176
5.8	Conclusions	178
5.9	Data availability statement	179
5.10	Acknowledgements	180
5.11	References.....	180
5.12	Tables and figures.....	191
6	DEM simulations of the liquefaction triggering resistance and post-triggering strain accumulation of coarse-grained soils with varying gradations.....	217
6.1	Abstract.....	217
6.2	Introduction.....	218
6.3	Simulation methodology.....	222
6.3.1	Simulated granular materials.....	222

6.3.2	Simulation procedure	224
6.4	Cyclic direct simple shear simulations	228
6.4.1	Cyclic direct simple shear response	229
6.4.2	Liquefaction triggering resistance	231
6.4.3	Post-liquefaction shear strain accumulation	233
6.5	Fabric evolution during cyclic shearing	235
6.5.1	Particle connectivity	235
6.5.2	Contact sliding	238
6.5.3	Contact force fabric anisotropy	240
6.6	Conclusions	242
6.7	Acknowledgements	244
6.8	References	244
6.9	Tables and figures	257
7	Conclusions	282
7.1	Estimation of soil fabric	284
7.2	Effect of gradation on the mechanical behavior of soils	286
7.3	Recommendations for future work	289

List of Tables

Table 2.1: Testing conditions and average parameters of angular V_s ($V_{s,vh}$ to $V_{s,hv}$) distributions.....	48
Table 3.1: DEM simulations parameters	101
Table 3.2: Average V_s ratios and V_s anisotropy parameters from DEM simulations and BE experiments	102
Table 4.1: Average properties of the simulated gradations.....	142
Table 4.2: DEM simulations parameters. Parameters in bold font indicate the control parameters for parametric study	142
Table 4.3: Summary of tests conducted with the obtained void ratios, mechanical coordination numbers, and % of inactive particles at 100 kPa. Bold parameters indicate the parameters changed for parametric study.	143
Table 5.1: Gradation characteristics of the simulated materials	191
Table 5.2: DEM simulations parameters	191
Table 5.3: Parameters of drained triaxial simulations.....	192
Table 5.4: Parameters of undrained triaxial simulations	193
Table 5.5: Anisotropy of contact normal force angular for drained simulations	194
Table 6.1: Gradation and packing characteristics of the simulated materials.....	257

Table 6.2: Parameters of specimens tested in constant volume cyclic DSS. Each specimen was tested at three CSRs at p' of 100 kPa	258
Table 6.3: DEM simulations parameters	259
Table 6.4: a and b parameters from the liquefaction triggering curves at p' of 100 kPa ..	260
Table 6.5: Parameters at the triggering of liquefaction for 100A, 33ABC, and 25ABCD specimens at p' of 100 kPa	261
Table 6.6: Anisotropy of contact normal force angular distributions.....	262

List of Figures

Figure 2.1: Notation for different shear waves propagating through a soil specimen.....	49
Figure 2.2: (a) Photograph and (b,c) cross-sectional drawing of the bottom end cap with five BEs. The top end cap has the same configuration as the bottom end cap.	50
Figure 2.3: Schematics of devices for (a) isotropic and (b) 1D compression tests. The major differences in the setups are italicized.	51
Figure 2.4: Schematic of the peripheral electronics for the multi-bender element system.	52
Figure 2.5: Typical transmitted and received signal pair, with the arrival time obtained between the start time and the end time.....	53
Figure 2.6: Photographs of (a) glass beads, (b) 100C sand, and (c) grain size distributions for both materials.	54
Figure 2.7: Received BE signals for glass beads sand under isotropic compression.	55
Figure 2.8: Received BE signals for 100C under isotropic compression.	56
Figure 2.9: Increase in V_s with increase in mean effective stress for glass beads and 100C sand under isotropic and 1D compression.	57
Figure 2.10: β exponent V_s . α coefficient for glass beads and 100C sand for different BE orientations. The small crosses represent the datapoints presented in Cha et al. (2014).	58
Figure 2.11: Polar plots of V_s for glass beads and 100C sand subjected to varying levels of confining stress.....	59

Figure 2.12: Evolution of the a_n parameter with mean effective stress for the angular distribution of V_S ($V_{S,VH}$ to $V_{S,HV}$)..... 60

Figure 2.13: Comparison of $V_{S,VH}$, $V_{S,HV}$, and $V_{S,HH}$ measurements with values from various experimental studies: (a) $V_{S,HH}$ versus $V_{S,HV}$, (b) $V_{S,HV}$ versus $V_{S,VH}$, and (c) $V_{S,HH}$ versus $V_{S,VH}$ 61

Figure 2.14: Comparison of $V_{S,VH}$, $V_{S,HV}$, and $V_{S,HH}$ measurements with values from field tests reported by Ku and Mayne (2013): (a) $V_{S,HH}$ versus $V_{S,HV}$, (b) $V_{S,HV}$ versus $V_{S,VH}$, and (c) $V_{S,HH}$ versus $V_{S,VH}$ 62

Figure 3.1: Notation for the various shear waves propagating through the soil specimen.103

Figure 3.2: Images of (a) spheres, (b) elongated clump used in DEM simulations, (c) glass beads, (d) 100C sand used in experiments, and (e) grain size distributions for the materials. 104

Figure 3.3: (a) Image of DEM specimen with clumps, and (b,c,d,e) map of particle velocities at different times during the simulation showing the propagation of the shear wave. 105

Figure 3.4: Numerical wave transmission setup for $V_{S,VH}$, $V_{S,40^\circ VHtoHV}$, and $V_{S,HV}$ waves showing the transmitter and receiver bins..... 106

Figure 3.5: (a) Influence of input frequency on the received signals in the DEM simulations and (b) waterfall plot from the received signals from each of the receiver bins for a specimen made of spheres and isotropically compressed at a p' of 20 kPa..... 107

Figure 3.6: Transmitted and received BE signals during (a) a simulation of an isotropically-compressed spheres specimen and (b) an experiment an isotropically-compressed glass beads specimen..... 108

Figure 3.7: Photograph of (a) horizontal BEs, (b) top and bottom end caps, (c,d) cross-sectional drawing of the bottom end cap with five Bs, and schematics of the equipment used for (e) 1D and (f) isotropic compression tests, where the major differences in the setups are highlighted in italic font. The top end cap has the same configuration as the bottom end cap. 109

Figure 3.8: Angular distributions of (a,c) contact normals and (b,d) contact normal forces for the spheres specimens subjected to isotropic and 1D compression of 40 kPa; dashed lines show the best fit lines using Eqs. 1 and 2. 110

Figure 3.9: Angular distributions of (a,d) contact normals, (b,e) contact normal forces, and (c,f) particle long axes for the clumps specimens subjected to isotropic and 1D compression of 40 kPa; dashed lines show the best fit lines using Eqs. 1, 2, and 3..... 111

Figure 3.10: DEM angular distributions of V_s for (a,b) sphere and (c,d) clump specimens subjected to varying p' magnitudes; dashed lines show the best fit lines for the VH to HV and VH to HV sweeps using Eq. 4. 112

Figure 3.11: Comparison of α coefficients and β exponents for the VH to HV from experiments and DEM and VH to HH sweep from DEM. The solid line shows the best fit and the dashed lines shows the one standard deviation bounds of data presented in Cha et al. 2014. Different colors denote the angular orientation of BEs with shades of green for experimental results and shades of blue for DEM results..... 113

Figure 3.12: Experimental angular distributions of V_s for (a,b) glass bead and (c,d) 100C sand specimens subjected to varying stress magnitudes; dashed lines show the best fit lines for the VH to HV and VH to HV sweeps using Eq. 4. Note: (a) and (b) are plotted for respective p' values and (c) and (d) are plotted for respective σ'_v values..... 114

Figure 3.13: Illustration of (a) fabric and (b) stress state for normally consolidated soil under 1D compression, and (c) stress conditions for VH, HV, and HH waves. 115

Figure 3.14: Shear wave velocity ratios for the different fabric and stress states at an effective stress of 40 kPa along with data from the literature. 116

Figure 3.15: Comparison between the net anisotropy, A_e , and (a) $V_{s,HV}/V_{s,VH}$ and (b) $V_{s,HV}/V_{s,HH}$ ratio for numerical and experimental specimens and literature data..... 117

Figure 3.16: Increase in V_s with increase in σ'_m for spheres and clumps under isotropic (Iso) and 1D compression for VH to HV sweep..... 118

Figure 3.17: Increase in V_s with increase in σ'_m for spheres and clumps under isotropic (Iso) and 1D compression for VH to HH sweep. 119

Figure 3.18: Increase in V_s with increase in σ'_m for glass beads and 100C sand under isotropic (Iso) and 1D compression. 120

Figure 4.1: (a) Particle size distribution, and images of the specimen for (b) mono-sized, (c) 100A, (d) 25ABCD, (e) curved and (f) bimodal gradations. 144

Figure 4.2: Cumulative distribution of particle connectivity for (a) number of particles and (b) volume of particles, and (c) variation of PC with particle sizes in specimens made of

mono-sized, 100A, 25ABCD, bimodal, and curved gradations. The vertical lines denote the D_{10} of the gradation. 145

Figure 4.3: (a) Particle size distribution, and force chain maps of the specimen for (b) mono-sized, (c) 100A, (d) 25ABCD, (e) curved and (f) bimodal gradations. 146

Figure 4.4: Distribution of F_n/\bar{F}_n with particle sizes (as percent passing) for specimens with (a) 100A, (b) curved, (c) 25ABCD, and (d) bimodal gradations. 147

Figure 4.5: Variation of cumulative distribution of particle connectivity for (a) number of particles and (b) volume of particles, and (c) variation of PC with particle sizes in specimen of 25ABCD gradation with change in μ values of 0.01, 0.1, 0.2, and 0.4. 148

Figure 4.6: Comparison of percentage of inactive particles by number with (a) void ratio, and (b) mechanical coordination number for the various parametric cases. 149

Figure 4.7: Variation of cumulative distribution of particle connectivity for (a) number of particles and (b) volume of particles, and (c) variation of PC with particle sizes in 25ABCD gradation specimen with change in the k/D values of $1e9 \text{ N/m}^3$, $1e8 \text{ N/m}^3$, and $1e7 \text{ N/m}^3$ 150

Figure 4.8: Schematic showing the contacts between coarser particles (yellow) and finer particle (green) for (a) lower k/D , (b) intermediate k/D , and (c) high k/D values without gravity. 151

Figure 4.9: Variation of cumulative distribution of particle connectivity for (a) number of particles and (b) volume of particles, and (c) variation of PC with particle sizes in 25ABCD gradation specimen with change in the ξ of 0.05, 0.25, 0.50. 152

Figure 5.1: (a) Particle size distribution of the simulated materials and (b) templates for clumped particles.....	195
Figure 5.2: Comparison of (a) particle shape parameters between real (box and whiskers) and simulated particles, (b) e_{max} and e_{min} for different clump mixes, and (c) bounds for e_{max} and e_{min} from experiments and DEM simulations for different gradations. Note: $Re.$ = regularity and S = sphericity.	196
Figure 5.3: Images of 100A, 33ABC, 25ABCD, and 25ABCD (1.5x) specimens. The particle color is normalized between the maximum (red) and minimum (blue) diameter in the specimen.....	197
Figure 5.4: Comparison of the (a) q , (b) ε_v , (c) stress path in q - p' space, and (d) stress path in e - $\log(p')$ space between drained triaxial simulations and experiments.	198
Figure 5.5: Stress paths and critical state lines with respective fittings in the e - $\log(p')$ and q - p' spaces for (a) 100A, (b) 33ABC, and (c) 25ABCD.	199
Figure 5.6: Drained triaxial results at $p' = 100$ kPa for (a) 100A, (b) 33ABC, and (c) 25ABCD.	200
Figure 5.7: Drained triaxial results at $p' = 800$ kPa for (a) 100A, (b) 33ABC, and (c) 25ABCD.	201
Figure 5.8: Comparison of (a) q/p' and (b) ε_v for 100A, 33ABC, and 25ABCD specimens with $\xi_0 = -0.1$ and $p' = 100$ kPa subjected to drained shearing.....	202
Figure 5.9: (a) $\phi'_p - \phi'_{cs}$ versus ψ_{max} , and (b) $\phi'_p - \phi'_{cs}$ versus p' for monotonic drained triaxial tests. The black lines in (b) represent the bounds from Bolton (1986).	203

Figure 5.10: (a) Cumulative distribution of PC, (b) variation of PC with the particle size, (c,d,e) distribution of contact normal forces with particle sizes (as percent passing), and (f,g,h) angular distributions of contact forces for the peak strength states for 100A, 33ABC and 25ABCD specimens subjected drained triaxial compression at $p' = 100$ kPa and $\xi_0 = -0.1$.
 204

Figure 5.11: (a) Cumulative distribution of PC, (b) variation of PC with the particle size, (c,d,e) distribution of contact normal forces with particle sizes (as percent passing), and (f,g,h) angular distributions of contact forces for the critical states for 100A, 33ABC and 25ABCD specimens subjected drained triaxial compression at $p' = 100$ kPa and $\xi_0 = -0.1$. 205

Figure 5.12: Undrained triaxial results at $p' = 100$ kPa for (a) 100A, (b) 33ABC, and (c) 25ABCD. 206

Figure 5.13: Undrained triaxial results at $p' = 800$ kPa for (a) 100A, (b) 33ABC, and (c) 25ABCD. 207

Figure 5.14: Comparison of (a) q and (b) ε_v for 100A, 33ABC, and 25ABCD specimens with $\xi_0 = -0.1$ and $p' = 100$ kPa subjected to undrained shearing. 208

Figure 5.15: Variation of (a) ϕ'_p , (b) $\phi'_p - \phi'_{cs}$, (c) ψ_{max} , (d) u_{min} , and (e) $(\delta u / \delta \varepsilon_a)_{min}$ with ξ_0 for drained and undrained tests..... 209

Figure 5.16: Variation of (a) $\phi'_p - \phi'_{cs}$ and (b) ϕ'_p with D_R for drained tests. 210

Figure S5.1: Comparison of the (a) q , (b) ε_v , (c) stress path in q - p' space, and (d) stress path in e - $\log(p')$, space between 25ABCD and 25ABCD (2.1x) specimen for drained triaxial simulations at $p' = 100$ kPa. 211

Figure S5.2: (a) Cumulative distribution of PC, (b) variation of PC with the particle size, (c,d,e) distribution of contact normal forces with particle sizes (as percent passing), and (f,g,h) angular distributions of contact forces for the initial states for 100A, 33ABC and 25ABCD specimens subjected to drained triaxial compression at $p' = 100$ kPa and $\xi_0 = -0.1$.
 212

Figure S5.3: Comparison of obtained data and fitted lines using equation 7 at (a) initial (Fig. S3(h)), (b) peak (Fig. 10(h)) and (c) critical (Fig. 11(h)) state for strong forces for 25ABCD specimen subjected to drained triaxial compression at $p' = 100$ kPa and $\xi_0 = -0.1$ 213

Figure S5.4: (a) Cumulative distribution of PC, (b) variation of PC with the particle size, (c,d,e) distribution of contact normal forces with particle sizes (as percent passing), and (f,g,h) angular distributions of contact forces for the initial states for 100A, 33ABC and 25ABCD specimens subjected to undrained triaxial compression at $p' = 100$ kPa and $\xi_0 = -0.06$.
 214

Figure S5.5: (a) Cumulative distribution of PC, (b) variation of PC with the particle size, (c,d,e) distribution of contact normal forces with particle sizes (as percent passing), and (f,g,h) angular distributions of contact forces for the peak states for 100A, 33ABC and 25ABCD specimens subjected to undrained triaxial compression at $p' = 100$ kPa and $\xi_0 = -0.06$.
 215

Figure S5.6: (a) Cumulative distribution of PC, (b) variation of PC with the particle size, (c,d,e) distribution of contact normal forces with particle sizes (as percent passing), and (f,g,h) angular distributions of contact forces for the critical states for 100A, 33ABC and

25ABCD specimens subjected to undrained triaxial compression at $p' = 100$ kPa and $\xi_0 = -0.06$ 216

Figure 6.1: (a) Particle size distribution, (b) templates for clumped particles, (c) particle shape parameter distributions between real (box and whiskers) and clumped particles, and (d) e_{max} and e_{min} of the simulated materials. Note: Re . represents regularity and S represents sphericity..... 263

Figure 6.2: 100A, 33ABC, 25ABCD, and 25ABCD (2.1x) specimens. The colors represent the particle diameters and are normalized between the maximum (red) and minimum (blue) diameter across the specimen. 264

Figure 6.3: Critical state lines in the $e-\log(p')$ space based on the best fits presented in Basson et al. 2023(b). The dashed lines represent the respective e_{max} values, and dotted lines represent the respective e_{min} values. 265

Figure 6.4: The variation of γ_{xz} and τ_{xz} with iteration number during the DSS simulation for a 100A specimen at a CSR of 0.2..... 266

Figure 6.5: Comparison of the DSS results as (a,d) τ_{xz} versus p' , (b,e) τ_{xz} versus γ_{xz} , and (c,d) CSR versus N curve between DEM simulations and experiments for specimens prepared at a $D_R \sim 43\%$ and $\xi_0 \sim -0.11$, respectively. (a,b,d,e) present the response for specimen at CSR of 0.10. The dashed-dotted lines represent the failure slope (M_f) approximating the dilation phase of the butterfly-shaped response..... 267

Figure 6.6: Comparison of DEM simulations results in terms of the (a) τ_{xz} versus p' , (b) τ_{xz} versus γ_{xz} , (c) r_U versus N , and (d) γ_{xz} versus N between 25ABCD and 25ABCD (2.1x) specimens.....	268
Figure 6.7: Comparison of DSS DEM simulation results for (a) 100A, (b) 33ABC, and (c) 25ABCD at p' of 100kPa and D_R between 39-43%.....	269
Figure 6.8: Comparison of DSS DEM simulation results for (a) 100A, (b) 33ABC, and (c) 25ABCD at p' of 100kPa and D_R between 58-61%.....	270
Figure 6.9: Comparison of DSS DEM simulation results as (a) τ_{xz} versus p' , (b) τ_{xz} versus γ_{xz} , and (c) r_U versus N for 100A, 33ABC, and 25ABCD at $\xi_0 \sim -0.06$	271
Figure 6.10: Liquefaction triggering curves in terms of CSR versus N for specimens with (a) similar D_R and (b) similar ξ_0 for 100A, 33ABC, and 25ABCD specimens at p' of 100kPa....	272
Figure 6.11: Comparison of cyclic strengths at N_L of 10 with (a) D_R and (b) ξ_0 for 100A, 33ABC, and 25ABCD specimens.....	273
Figure 6.12: Comparison of (a) γ_{sa} and (b) γ_{da} with N , and (c) γ_{sa} and (d) γ_{da} with $N_{posttrig}$ for 100A, 33ABC, and 25ABCD specimens. Black dots represent the point of triggering.	274
Figure 6.13: Comparison of MCN with N for (a,b) 100A, (c,d) 33ABC, and (e) 25ABCD specimens. Black dots represent the point of triggering liquefaction.....	275
Figure 6.14: Schematic of point picked for fabric analysis at (1) start of shearing, (2) , (3) contraction phase immediately after triggering, and (4) end of first dilation phase post	

triggering on (a) τ_{xz} versus p' , (b) τ_{xz} versus γ_{xz} , (c) r_U versus N , and (d) γ_{xz} versus N for 25ABCD specimen at a ξ_o of -0.06 tested for a CSR of 0.10. 276

Figure 6.15: Cumulative distribution of PC for (a) initial state, (b) dilation before liquefaction, (c) contraction phase immediately after triggering, and (d) dilation phase post triggering for 100A, 33ABC, and 25ABCD specimens. 277

Figure 6.16: Variation of PC with the particle size for (a) initial state, (b) dilation before liquefaction, (c) contraction phase immediately after triggering, and (d) dilation phase post IL for 100A, 33ABC, and 25ABCD specimens. 278

Figure 6.17: Percentage of sliding contacts carrying (a) strong forces and (b) weak forces with N for 100A, 33ABC, and 25ABCD specimens. Black dots represent the point of triggering. 279

Figure 6.18: Angular distributions of normalized contact forces for (a) initial state, (b) dilation before liquefaction, (c) contraction phase immediately after triggering, and (d) dilation phase post triggering for strong forces for 100A, 33ABC, and 25ABCD specimens. 280

Figure 6.19: Angular distributions of normalized contact forces for (a) initial state, (b) dilation before liquefaction, (c) contraction phase immediately after triggering, and (d) dilation phase post triggering for weak forces for 100A, 33ABC, and 25ABCD specimens. 281

Chapter 1

Introduction

1.1 Background

At the micro-scale, coarse-grained soils are composed of discrete particles that interact at the points of contact. The mechanical behavior of these granular soils is influenced by various inherent properties, including (i) soil fabric, which is defined by the geometric arrangement of the particles, contact normals, and contact forces, (ii) stress state, determined by the applied boundary stresses and the loading sequence, and (iii) gradation representing the width of particle sizes within a specimen. Accurately quantifying and characterizing these inherent properties, and their concomitant effects, has proven challenging due to the complex interactions among particles, limitation induced by laboratory testing equipment and specimen size, and the effect of boundary conditions. This dissertation presents the research effort of two projects aimed at the measurement of fabric- and stress-induced anisotropy using DEM simulations and a modified experimental testing setup and the effect of gradation on the mechanical behavior of coarse-grained granular soils using DEM simulations.

The particulate nature of granular soils can lead to anisotropy in strength and stiffness due to the (i) anisotropy in inherent soil fabric, which consists of the arrangement of

particles, contacts, and voids and is a result of deposition and post-deposition processes, as well as to the soil gradation and particle shape, and (ii) anisotropy in the stress state resulting from the imposed loading conditions and history which affects the distribution of forces transmitted at interparticle contacts (Oda et al. 1972a, 1972b; Oda et al. 1982; Yamashita et al. 2005). The first portion of this dissertation aims to identify the presence of stress- and fabric-induced anisotropies in coarse-grained soils. This can help further the fundamental understanding of the origin of anisotropy in soils and its evolution during loading. Understanding the interplay between micro-scale fabric- and stress-induced anisotropies and macro-scale behavior of soils, such as strength, stiffness, dilatancy, and permeability, is critical for geotechnical analysis and design. However, quantifying stress-induced and fabric-induced anisotropy *in-situ* or in a specimen in the laboratory has remained a challenge due to the need for specialized equipment, constraints related to smaller specimen sizes, and the limited number anisotropy measurements throughout loading cycle.

The effect of stress-induced anisotropy on the macro-scale response of soil specimens has received significant attention, typically assessed through anisotropically-consolidated triaxial compression, hollow cylinder, or oedometer tests (Roesler 1979; Oda et al. 1985; Zdravković and Jardine 2001). Several direct and indirect measurement techniques have been proposed to estimate the evolution of fabric anisotropy for different loading conditions. Specifically, indirect measurement of anisotropy using non-destructive testing has been accomplished by measuring soil responses in various orientations through soil specimens. The use of measurements of soil response to deduce anisotropy in a soil specimen constitutes an inverse problem (Santamarina and Fratta 2005). These techniques employ

measurements of anisotropy in the thermal conductivity (Choo et al. 2013), electrical conductivity (Anandarajah and Kuganenthira 1995), or seismic wave velocity (Chaney et al. 2001; Mitaritonna et al. 2010; Mital et al. 2020; Dutta et al. 2020; Otsubo et al. 2020). Particularly, shear wave velocity (V_s) or shear modulus (G_{max}) measurements are advantageous because they can be obtained with low-strain perturbations that do not modify the fabric or produce permanent deformations (Cascente and Santamarina 1996). Consequently, measuring the stiffness anisotropy through V_s measurements offers a non-destructive method of characterizing the fabric- and stress-induced anisotropies in soil specimens. Additionally, V_s is routinely measured in the field, laboratory, and numerical simulations, making it a strong candidate for linking the macro-, meso-, and micro-scale behavior of granular soils.

The second portion of this dissertation is part of a broader endeavor to investigate the effects of gradation on the monotonic and cyclic response of coarse-grained soils. Soils commonly found in natural deposits, such as alluvial gravelly soils, contain a wide range of particle sizes. Naturally deposited by braided rivers and glaciers, these deposits contain coarser particles significantly larger than clean sands, leading to coefficient of uniformity (C_u) values of 40 or higher (DeJong et al. 2016). The particle size distribution (PSD) of these soils plays a governing role in their behavior (Cubrinovski and Ishihara 2002). Understanding the strength, stress-dilatancy, critical state, and pre-and post-liquefaction response of these soils is crucial due to their frequent presence within or beneath critical geosystems such as dams, levees, tunnels, bridges, foundations, and pavements.

In practice, the design and analysis of geosystems built on coarse-grained soils with broader gradations are typically based on the methodologies developed for clean sands without explicit consideration of the effects of gradation, potentially leading to uncertainty in performance predictions. For instance, the stress-dilatancy response of well-graded gravelly soils is typically assessed using relationships developed by Bolton (1986). These widely adopted relationships are based on experimental data acquired from testing on poorly graded clean sands. Over the years, these relationships have been revisited, and additional ones have been proposed to capture the effects of particle shape, gradation, mineralogy, stress history, relative density and state, and fabric (e.g., Vaid and Sasitharan 1992, Simoni and Houlsby 2006, Muir Wood and Maeda 2008, Chakraborty and Salgado 2010). Given the numerous case studies documenting liquefaction in coarse-grained broadly graded soils in the field (e.g., Kokusho et al. 1995; Towhata et al. 2014; Zhou et al. 2020), it is also vital to isolate the effect of gradation on the liquefaction resistance and post-liquefaction strain accumulation to design resilient infrastructure. Despite recent advances, there are still gaps in the understanding of the specific mechanisms responsible for the effects of gradation on the mechanical behavior of soils, such as which state variable better captures the effects of density and effective stress, what is the role of the finer and coarser fractions of the soil in the mobilization of strength and dilatancy, and what corrections, if any, are needed to predict the strength, stress-dilatancy, liquefaction triggering response and post-liquefaction strain accumulation of well-graded soils with established frameworks.

1.2 Scope and organization

This dissertation is organized into seven chapters constituting two sub-parts based on the underlying topics. The first part of the dissertation (Chapters 2-3) focuses on the investigation of the effect of stress- and fabric-induced anisotropy on the mechanical behavior of soils. The effects of stress- and fabric-induced anisotropy on the shear wave velocity are investigated through experiments and discrete element method (DEM) simulations. A novel system using piezoelectric bender elements (BEs) was developed and used to measure V_s anisotropy, enabling non-destructive indirect assessment of anisotropy in soil specimens. A framework is proposed that helps distinguish between the effects of stress- and fabric-induced anisotropy on the stiffness of soil specimen. The second part of the dissertation (Chapters 4-6) focuses on the effect of gradation on the isotropic compression, monotonic shear strength, stress-dilatancy, liquefaction potential, and post-liquefaction shear strain accumulation of coarse-grained soils. Additionally, the influence of gradation on the particle packing, including the particle connectivity and proportion of inactive particles, as well as on the contact force transmission characteristics in a specimen, are presented to highlight the disparities in microscale response between different gradations.

Chapter 2 introduces a novel experimental setup that utilizes piezoelectric BEs to measure V_s along different orientations and polarization planes. The experimental results demonstrate the capability of the multi-BE system to identify fabric and stress anisotropy. This non-destructive assessment method complements other advanced techniques like X-ray computed tomography and particle-based numerical simulations.

Chapter 3 investigates the influence of stress- and fabric-induced anisotropies on V_s anisotropy. The effects of the stress state, particle alignment, and interparticle contact forces on the angular distributions of shear wave velocity are examined. A framework that combines the results of experimental BE tests and DEM simulations is proposed, consisting of ratios of V_s measurements along different orientations and polarization planes and of the newly introduced Anisotropy parameter (A_e). This framework enables the evaluation of stress- and fabric-induced anisotropies.

Chapter 4 examines the influence of the PSD and the contact law parameters, including the particle stiffness, interparticle friction, and damping, on the proportion of inactive particles and contact force transmission within granular assemblies. Mono-sized, poorly-graded, broadly graded, bimodal, and curved gradations are considered in this chapter.

Chapter 5 focuses on the effects of changes in gradation on the monotonic behavior of coarse-grained soils. Three-dimensional DEM simulations of isotropically-consolidated drained and undrained triaxial tests are performed to highlight the gradation effects on the drained and undrained triaxial response, critical state lines, and parameters such as peak friction angle (ϕ'_p), difference of the peak and critical state friction angles ($\phi'_p - \phi'_{cs}$) and maximum dilation angle (ψ_{max}), excess pore pressure (u_{min}), and excess pore pressure generation rate ($(\delta u / \delta \epsilon_a)_{min}$). This research compares the results with established frameworks to highlight the differences resulting from variations in gradation, along with a comparison of results on the basis of relative density and initial state parameter, to identify a measure of state that captures systematic differences in the response of broadening of gradation. Particle-level measurements provide insights into the packing characteristics,

contact force transmission, and interlocking of particles, contributing to a better understanding of stress mobilization in soils of varying gradation.

Chapter 6 investigates the influence of gradation on the pre- and post-liquefaction behavior of granular soils. The research employs DEM simulations of cyclic direct simple shear tests on isotropically consolidated cubical specimens with varying gradations. Macro-scale analysis focuses on liquefaction triggering resistance and shear strain accumulation, while micro-scale measurements examine the evolution of fabric and contact forces within the specimen. Additionally, the results are compared at similar relative densities and initial state parameters to emphasize the significance of selecting the appropriate measure of state to capture the effects of gradation. The findings provide valuable insights into pre- and post-liquefaction behavior and the implications of the micromechanical processes driving the observed global behavior.

Chapter 7 summarizes the main conclusions of this dissertation and presents recommendations for future research.

1.3 References

- Anandarajah, A., and N. Kuganenthira. 1995. "Some aspects of fabric anisotropy of soil." *Géotechnique*, 45 (1): 69–81.
- Chakraborty, T., and R. Salgado. 2010. "Dilatancy and shear strength of sand at low confining pressures." *Journal of Geotechnical and Geoenvironmental Engineering*, 136 (3): 527–532.
- Chaney, R., K. Demars, V. Fioravante, and R. Capoferri. 2001. "On the use of multi-directional piezoelectric transducers in triaxial testing." *Geotechnical Testing Journal*, 24 (3): 243.

- Choo, J., Y. J. Kim, J. H. Lee, T. S. Yun, J. Lee, and Y. S. Kim. 2013. "Stress-induced evolution of anisotropic thermal conductivity of dry granular materials." *Acta Geotechnica*, 8 (1): 91–106.
- DeJong, J. T., A. P. Sturm, and M. Ghafghazi. 2016. "Characterization of gravelly alluvium." *Soil Dynamics and Earthquake Engineering*, 91: 104–115.
- Dutta, T. T., M. Otsubo, R. Kuwano, and T. Sato. 2020. "Estimating multidirectional stiffness of soils using planar piezoelectric transducers in a large triaxial apparatus." *Soils and Foundations*, 60 (5): 1269–1286.
- Kokusho, T., Y. Tanaka, T. Kawai, K. Kudo, K. Suzuki, S. Tohda, and S. Abe. 1995. "Case study of rock debris avalanche gravel liquefied during 1993 hokkaido-nansei-oki earthquake." *Soils and Foundations*, 35 (3): 83–95.
- Mital, U., R. Kawamoto, and J. E. Andrade. 2020. "Effect of fabric on shear wave velocity in granular soils." *Acta Geotechnica*, 15 (5): 1189–1203.
- Mitaritonna, G., A. Amorosi, and F. Cotecchia. 2010. "Multidirectional bender element measurements in the triaxial cell: equipment set-up and signal interpretation." *Rivista Italiana Geotecnica*, (1): 50–70.
- Muir Wood, D., and K. Maeda. 2008. "Changing grading of soil: effect on critical states." *Acta Geotechnica*, 3 (1): 3–14.
- Otsubo, M., J. Liu, Y. Kawaguchi, T. T. Dutta, and R. Kuwano. 2020. "Anisotropy of elastic wave velocity influenced by particle shape and fabric anisotropy under k condition." *Computers and Geotechnics*, 128: 103775.
- Simoni, A., and G. T. Houlsby. 2006. "The direct shear strength and dilatancy of sand–gravel mixtures." *Geotechnical and Geological Engineering*, 24 (3): 523–549.

- Towhata, I., S. Maruyama, K. Kasuda, J. Koseki, K. Wakamatsu, H. Kiku, T. Kiyota, S. Yasuda, Y. Taguchi, S. Aoyama, and T. Hayashida. 2014. "Liquefaction in the kanto region during the 2011 off the pacific coast of tohoku earthquake." *Soils and Foundations*, 54 (4): 859-873.
- Vaid, Y. P., and S. Sasitharan. 1992. "The strength and dilatancy of sand." *Canadian Geotechnical Journal*, 29 (3): 522-526.
- Zhou, Y.-G., P. Xia, D.-S. Ling, and Y.-M. Chen. 2020. "Liquefaction case studies of gravelly soils during the 2008 wenchuan earthquake." *Engineering Geology*, 274: 105691.

Chapter 2

A multi-orientation system for determining the angular distributions of shear wave velocity in soil specimens

Author's note: This paper was published in the ASTM Geotechnical Testing Journal under the following citation and is presented herein with minor edits.

Basson, M. S., and A. Martinez. 2023. "A Multi-orientation System for Determining Angular Distributions of Shear Wave Velocity in Soil Specimens." Geotech. Test. J., 46 (2): 20210277. <https://doi.org/10.1520/GTJ20210277>.

2.1 Abstract

Soils typically have anisotropic mechanical and hydraulic properties due to the micro-scale interactions between particles, which are influenced by the particle morphology and depositional processes that can lead to particular particle arrangements (i.e., fabric anisotropy) and by the imposed loading conditions and history (i.e., stress anisotropy). The experimental assessment of the soil specimen anisotropy is a challenging feat, typically accomplished using specialized geotechnical testing and imaging equipment. The anisotropy of a soil specimen can also be assessed based on measured responses, such as the velocity of

propagating shear waves, which constitutes an inverse problem. This paper presents the development of a system that enables measurement of shear wave velocity (V_s) along different orientations and polarization planes using seven pairs of piezoelectric bender elements (BEs) to obtain angular distributions of V_s . Specimens of glass beads and angular natural sands were tested in isotropic and one dimensional (1D) compression to demonstrate the results obtained with the multi-BE system. The experimental results indicate that the effects of fabric and stress anisotropy can be identified by the angular distributions in V_s as well as measurements obtained along different polarization planes (i.e., $V_{s,HH}$, $V_{s,HV}$, and $V_{s,VH}$). The level of anisotropy in soil specimens can be quantified either in terms of ratios of shear wave velocities or of parameters used to fit the angular V_s distribution. The results also show that the parameters describing the relationship between V_s and mean effective stress are dependent on the orientation of the propagating wave. The proposed system may enable non-destructive assessment of soil specimen anisotropy using conventional laboratory equipment, which would complement other more sophisticated experimental methods such as X-ray Computed Tomography (CT) and particle-based numerical simulations.

2.2 Introduction

Coarse-grained soils can exhibit anisotropy in their engineering (i.e., macro-scale) behavior that originates from anisotropy in how particles are geometrically arranged and how they interact with one another (i.e., micro-scale) (Oda et al. 1972a, 1972b; Oda et al. 1982; Yamashita et al. 2005). Anisotropy in the macro-scale behavior can affect the mechanical (i.e., stiffness, strength, dilatancy) and hydraulic (i.e., permeability) response of soils. In

particular, the anisotropy in the small-strain shear stiffness, the latter quantified via the small-strain or elastic shear modulus G_{max} , and V_s has been of crucial concern in geotechnical engineering for a few decades, where G_{max} and V_s are related to one another by the following equation:

$$G_{max} = \rho V_s^2 \quad (2.1)$$

where ρ is the total mass density of the soil.

The small-strain shear stiffness is an engineering soil property that plays a significant role in the fundamental understanding of soil behavior and in analyzing the response of geosystems, such as settlements of foundations, soil-structure interaction, liquefaction of soils, and seismic ground response (e.g., Seed et al. 1986; Stokoe et al. 1994, 1999; Stokoe and Santamarina 2000). Numerous experimental, field, and numerical studies have investigated the causes leading to stiffness anisotropy (e.g., Kuwano et al. 1999; Otsubo et al. 2020; Mital et al. 2019; Wang and Mok 2008). At the micro-scale, this stiffness anisotropy is primarily produced by the state of stresses, referred to as the stress-induced anisotropy, and by the arrangement and interactions between particles, referred to as the fabric-induced anisotropy. The latter anisotropy is a result of particle shape, soil gradation, and depositional and post-depositional processes, all of which affect the arrangement of particles, particle contacts, and void spaces in a soil (Oda 1972a, 1972b; Yang et al. 2008).

The effect of stress-induced anisotropy on the macro-scale response of soil specimens has received significant attention, typically assessed through anisotropically-consolidated triaxial compression, hollow cylinder, or oedometer tests (Roesler 1979; Oda et al. 1985; Zdravković and Jardine 2001). In contrast, the quantification of the fabric anisotropy of a

soil specimen and its effect on soil behavior represents an experimental challenge. Several direct and indirect measurement techniques have been proposed to estimate the evolution of fabric anisotropy for varied loading conditions. One of the earliest examples of the direct measurement of fabric anisotropy is the work by Oda (1972b), who saturated sand specimens with an epoxy resin and then dissected them in thin slices to obtain distributions of contact normal and particle long-axis orientations. These measurements were used to quantify the inherent fabric anisotropy at different stages of triaxial compression tests. Yang et al. (2008) and Kodicherla et al. (2018) present more recent investigations using this methodology. The advances in X-ray CT techniques and post-processing methods have enabled researchers to make non-destructive estimations of inherent fabric and its anisotropy (Farber et al. 2003; Cnudde and Boone 2013; Viggiani et al. 2015; Wiebicke et al. 2020). While X-ray CT allows estimation of the evolution of fabric anisotropy during deformation of soil specimens, its requirement of specialized equipment and complex analysis restricts its use to a small number of laboratories worldwide.

Using measurements of soil response to deduce anisotropy in a soil specimen constitutes an inverse problem (Santamarina and Fratta 2005). Particularly, V_S or G_{max} measurements are advantageous because they can be obtained with low-strain perturbations that do not modify the fabric or produce permanent deformations (Cascante and Santamarina 1996). Piezoelectric transducers, such as bender elements (BEs), are routinely used as actuators and receivers to send and record V_S measurements in experimental testing (e.g., Viggiani and Atkinson 1995; Fiovarante and Capoferri 2001; Alvarado and Coop 2012).

Experimental investigations have employed BEs in the vertical or horizontal direction in triaxial and oedometer cells to explore the evolution of fabric during deformation and its effect on the stiffness of soil specimens. This has been done by comparing vertical and horizontal V_S measurements during sample preparation, consolidation, and shearing (Kuwano et al. 1999; Zeng and Ni 1998; Roesler 1979; Kaviani-Hamedani et al. 2021; Mitaritonna et al. 2014). Such experiments produce bidirectional shear wave propagation measurements, providing information regarding the relationship between stress and fabric anisotropy and the anisotropy in V_S and G_{max} . However, obtaining an angular distribution of V_S and G_{max} throughout the specimen, which could be used to provide more complete information of a specimen's anisotropy, remains a unique challenge. This has been attempted in previous investigations such as Fioravante (2000) who assessed the anisotropy in small-strain shear and constrained moduli in specimens of silica and carbonic sand. More recently, Chamorro-Zurita and Ovando-Shelley (2020) included horizontal and vertical BEs in a large oedometer device to measure shear wave velocity along different orientations in specimens of lacustrine clay.

This paper presents the development of a new multi-orientation testing setup that has seven BE pairs to enable the measurement of V_S along different orientations between 0° (horizontal) to 90° (vertical) and polarization planes (vertically to horizontally polarized shear waves) in specimens subjected to isotropic or one-dimensional, oedometric compression. Experimental results from specimens of glass beads and a sub-angular quartz sand are used to obtain angular distribution of V_S . These results highlight the effect of particle shape, which affects fabric, and stress anisotropy on the stiffness anisotropy of the specimens. The results are used to explore the dependency with orientation of the

parameters describing the relationship between V_S and mean effective stress and quantify the anisotropy of angular distributions of V_S . The results obtained from the new multi-orientation BE setup are compared to those from published laboratory and field investigations and suggest that the proposed testing setup can provide an accurate, indirect identification of fabric and stress anisotropy using standard laboratory equipment.

2.3 Bender element tests

This section provides an overview of the notations used to define the V_S measurements, details of the multi-orientation BE testing setup, instrumentation system and signal interpretation procedure, and a description of the materials and sample preparation methodology used in this investigation.

2.3.1 Notations for shear wave velocities

The stiffness anisotropy is typically evaluated using three independent shear wave velocity measurements $V_{S,VH}$, $V_{S,HV}$, and $V_{S,HH}$ in experimental (e.g., Fioravante 2000; Dutta et al. 2020; Gu et al. 2021), numerical (e.g., O'Donovan et al. 2015; Otsubo et al. 2020), and field (e.g., Stokoe and Santamarina 2000; Ku and Mayne 2013) studies. In typical literature notation, the first subscript denotes the direction of shear wave propagation, and the second subscript signifies the direction of particle motion. This is shown schematically in Fig. 2.1, where $V_{S,HV}$ indicates the velocity of a shear wave that propagates horizontally and causes particle motion in the vertical direction (green arrows in Fig. 2.1), $V_{S,HH}$ is the shear wave that propagates horizontally and causes particle motion in the horizontal direction (blue arrows in Fig. 2.1), and $V_{S,VH}$ is a wave that propagates vertically and causes particle motion in the

horizontal direction (red arrows in Fig. 2.1). This notation does not consider potential differences among different vertical planes, thus assuming that cross-anisotropy is valid.

2.3.2 Multi-orientation bender element system

The multi-orientation bender element (BE) system consists of seven BE pairs: three pairs capturing the $V_{S,VH}$, $V_{S,HV}$, and $V_{S,HH}$ measurements, and four additional BE pairs inclined at orientations of 75°, 65°, 55°, and 50°. Combined, these BE pairs can be used to obtain a sweep from $V_{S,VH}$ (i.e. 90°) to $V_{S,HV}$ (i.e., 0°). This system was designed to be mounted on a specimen with a diameter of 71 mm and height of 40 mm. This specimen height was used to increase the range of attainable angles (i.e., shorter specimens enable a wider range of angles) while maintaining a sufficiently large specimen size to facilitate preparation of the specimens with conventional techniques such as pluviation. The five BE pairs that measured $V_{S,VH}$ and along the 75°, 65°, 55°, and 50° orientations were mounted on custom-designed end caps fabricated from polycarbonate, as shown in Figs. 2.2(a,b,c). This material was selected due to its grounding properties. The top and bottom caps included vertical and inclined slots for the BEs as well as through holes for routing the cables. The two additional BE pairs were aligned in the horizontal configuration to provide the $V_{S,HV}$ and $V_{S,HH}$ measurements and mounted on a solid mold (Fig. 2.2(d)) and a flexible membrane.

Interferences such as p-wave interference, electromagnetic crosstalk, BE pair directivity, and near field effects commonly affect the interpretation of measurements obtained from piezoelectric BEs. The BEs used in this study were part number T220 procured from Mide Technology (Woburn, MA). Properly grounded parallel type connection was made on the outer electrode wafers to remove any crosstalk in the system (Brignoli et

al. 1996). Furthermore, shielded twisted cables were used to connect the BE pairs to the instrumentation setup to remove noise and phase effects in the signals (Montoya et al. 2012). All the BE pairs were mounted such that the receiver and the transmitter shared a collinear axis. The collinear in-plane directivity between the receiver and the transmitter reduces the overall influence of the compression wave on the received signal (Lee and Santamarina 2005). The current testing setup can be modified to achieve shallower BE angles and accommodate taller specimen for typical triaxial testing (i.e., with an aspect ratio of 2:1). In such cases, the inclined BEs can be mounted on the membrane instead of on the end caps.

Operation of BEs under various loading and specimen conditions requires appropriate consideration during the fabrication and installation. Each BE was coated with two coats of flexible industrial-grade solid epoxy adhesive (Loctite EA E-90FL). The protective coating acts as water insulator and enhances the durability of BE during the loading. BEs coated with this epoxy have been routinely used in centrifuge testing and testing in aggressive environments (Montoya et al. 2012). The coated BEs pairs that measured $V_{S,VH}$ and along the 75° , 65° , 55° , and 50° were bonded inside the slots made in the polycarbonate endcaps at the proper orientation using flexible silicone sealant. After 48 hours of curing, any excess sealant was removed using fine sandpaper. Long slits were machined on the faces of the top and bottom caps and then covered with a steel mesh to ensure a uniform distribution of suction during isotropic compression.

Researchers have noted that the installation of horizontal BEs is a challenging task that requires special care (Fioravante and Capoferri 2001; Dutta et al. 2020; Wang and Mok 2008; Kaviani-Hamedani et al. 2021). Based on procedures provided in past research (Gomez et al.

2018; Martinez et al. 2019), horizontal BE probes were created by gluing epoxy-coated BEs into a reducing hex nipple using flexible silicone sealant. The flexible silicone sealant isolates the BEs from the mold and end caps, minimizing the effect of external vibration on the shear wave signal. One of the major considerations with horizontal BE installation is the coupling of BEs with adjacent soil particles. To address this issue, the BE probes were glued in the four slits cut through the latex membrane for specimen under isotropic compression (Fig. 2.3(a)) and glued into the four holes drilled on the rigid mold for specimens under 1D compression (Fig. 2.3(b)). The rigid mold for 1D compression was 2.5 mm in thickness and fabricated out of polycarbonate. The BE probes protruded 3 mm into the specimen and made direct contact with the soil, eliminating any damping effects from the membrane or mold and resulting in a clearer signal to be transmitted and received through the specimen (e.g., Jamiolkowski et al. 1995; Pennington et al. 1997; Fioravante and Capoferri. 2001; Pennington et al. 2001; Kaviani-Hamedani et al. 2021)

2.3.3 Instrumentation systems and signal interpretations

The instrumentation setup used to transmit and receive BE signals is shown in Fig. 2.4, consisting of a function generator, an oscilloscope, a filter box, and a computer. A single sinusoidal pulse of specific amplitude and frequency was produced using the function generator based on the recommendations from previous shear wave studies (Lee and Santamarina 2005; Leong et al. 2005; Alvarado and Coop 2012; Ogino et al. 2015). The amplitude and frequency of the input signal are typically chosen such that the received signal is free from the near-field compression effects and excessive attenuation caused by inherent material damping; the choice of amplitude and frequency is dependent on the specimen size, distance between BEs, and attenuation of the signal as it passes through the specimen

(Arulnathan et al. 1996; Fioravante and Capoferri 2001). Lee and Santamarina (2005) recommend keeping the input signal frequency close to the resonant frequency of the specimen to obtain a strong output signal. In this study, a parametric calibration was done where the frequency of the input signal was varied between 5, 10, and 15 kHz, for the $V_{S,VH}$, $V_{S,HV}$, and $V_{S,HH}$ waves. The signals were then assessed to verify that the output signal was free of near-field and/or damping attenuation. A high-quality signal with the largest amplitude was achieved for the input frequency of 5 kHz and input amplitude of 4.5 V. These values were used for all the V_S measurements presented in this paper, which are in the range presented in the literature (Brignoli et al. 1996; Yamashita et al. 2009). The R_d values, which is the ratio of distance between the BEs and the wavelength of the shear wave computed using the frequency of the input signal, from all the signals obtained from the different BE pairs and the various stresses were greater than 2, indicating a high wave quality, which is in line with the observations reported in the literature (Sanchez-Salerino et al. 1986; Jovičić et al. 1996; Arulnathan et al. 1998; Arroyo 2003).

The input signals from the function generator were sent to the transmitting BEs and received by the receiving BEs. Typically, the received signals had a low amplitude, thus they were sent through a Butterworth filter box which amplified them with a gain value of 20 and filtered them using a band pass filter to eliminate low frequencies below 60 Hz and high frequencies above 10 kHz. The distinctive characteristics of the received signal that are crucial for determining wave arrival were unaffected by the signal filtration, and for consistency, the same signal filtration method was applied to all specimens. Both the transmitted and received filtered signals were fed into a *PicoScope* oscilloscope box which was programmed with an automatic trigger to start recording the received signal when the

transmitted signal was detected. All the signals were merged and saved on a computer system for post-processing and interpretation.

There are different interpretation methods to determine the travel time (t_{BE}) of shear waves. Numerous approaches, such as direct measurement in the time domain, cross-correlation, and frequency-domain methods, have been proposed to provide a systematic way of estimating travel times (e.g., Arulnathan et al. 1998; Blewett et al. 1999; Yamashita et al. 2009; Ogino et al. 2015). The direct measurement of the first arrival is arguably the most widely used method. The first dip, the first zero following the crossing, and the first peak are frequently used distinctive points of arrival. This study uses the first zero after the crossing, and examples of validation of this method can be found with analytical results (Lee and Santamarina 2005; Zhou and Chen 2007), with cross-correlation and frequency domain methods (Ogino et al. 2015), and with resonant column experiments (Payan et al. 2016). Figure 2.5 shows one such transmitted wave, and one pair of unfiltered and filtered received waves. The arrival time (t_t) is measured as the time difference between the black arrow (i.e. start of the transmitted signal) and the red arrow (i.e. first zero after crossing for the received signal). Additional testing was carried out to determine the signal time delay caused by the protective coating applied to the BEs (Δt). This was done by measuring the travel times when the two BEs were in direct contact, as done by Brignoli et al. (1996) and Pennington et al. (2001). An average Δt in the range of 30 μs was measured for each BE pair in the multi-orientation BE system. After determination of the travel time, the V_s magnitudes were calculated as follows:

$$V_s = \frac{L_{BE}}{t_t - \Delta t} \quad (2.2)$$

where the wave travel distance, L_{BE} , was calculated using the specimen height and the protrusion of the BE outside the end caps.

2.3.4 Materials, sample preparation, and stress conditions

The range of possible fabric anisotropy in soils increases with particle shape irregularity (Oda 1972a; Yamashita et al. 2005; Tong et al. 2014; Dutta et al. 2020; Otsubo et al. 2020). To highlight the effects of particle shape, rounded glass beads and a natural, quartz sand with sub-angular particles, were chosen for this investigation. The rounded, mono-sized glass beads are likely to lead to specimens with a near-isotropic fabric, whereas the angular sand can produce the expected effect of fabric-induced anisotropy. Additionally, the effects of stress-induced anisotropy are also explored by subjecting specimens of both materials to isotropic or one-dimensional compression, where the latter imposes anisotropic loading (i.e., at rest or K_0) conditions.

The mono-sized glass beads were made of Borosilicate glass with an average diameter of 0.5 mm (+/- 0.02 mm). The e_{max} value of 0.78 was obtained by slow deposition of the spheres into a cylinder, and this value is close to the typical very loose random packing of spheres. The e_{min} value was used as 0.44 based on the typical values of close random packing of spheres (Bernal and Mason 1960). The natural sand, termed sand 100C, was sourced from the Cape May Formation near Mauricetown, New Jersey. The sand is composed of sub-angular particles and has a mean particle diameter (D_{50}) of 1.31 mm, a coefficient of uniformity (C_u) of 1.54, and a coefficient of curvature (C_c) of 1.03, with an e_{max} value of 0.84 and an e_{min} value of 0.56. This sand has been well characterized and tested in triaxial

compression, direct simple shear, and centrifuge cone penetration tests (Sturm 2019; Sawyer 2020; Reardon et al. 2022). Figures 2.6(a,b) show photographs of the glass beads and 100C sand and Fig. 2.6(c) shows the corresponding grain size distributions.

The shape of particles can be quantified using parameters such as the Roundness (R), Sphericity (S), and Aspect Ratio (AR). Roundness is defined as the ratio of the radius of curvature of the asperities to the radius of the largest inscribed circle, and quantifies the relative size of the particles' surface asperities; sphericity is defined as the ratio of the largest inscribed circle to the smallest circumscribed circle and quantifies how close a particle is to a circle; and aspect ratio is defined as the ratio of the longest to shortest particle axes and quantification a particle's elongation (e.g., Cho et al. 2005; Altuhafi et al. 2016). By definition, the R , S , and AR parameters all have a value of 1.0 for circular or spherical particles. In this study, particle shape parameters were quantified based on the two-dimensional projection of microscopic images of 120 randomly selected particles of 100C sand particles and glass beads using the methodology presented in Zheng and Hryciw (2015). In the case of 100C sand particles, the average R , S , and AR were measured as 0.60, 0.77, and 1.86, respectively, which corresponds to sub-angular with medium sphericity as per Krumbein and Sloss (1963). For the glass beads, the average R , S , and AR were measured as 0.89, 0.99, and 1.00.

The method used to prepare specimens has been shown to impact the resulting fabric, with gravity deposition methods such as air pluviation typically leading to an anisotropic fabric in specimens composed of angular and elongated particles (Oda 1972(a); Yamashita et al. 2005; Wang and Mok 2008; Otsubo et al. 2020). Dry pluviation was used in this investigation to prepare glass beads and 100C sand specimens which would highlight the

effects of particle shape. This process consisted of raining particles from a constant height into the mold or membrane until the specimen reached a height of 40 mm. The surface of the soil was vacuumed to level the surface before inserting the top cap. The average void ratio (e) for the glass beads specimen was 0.54 and for the 100C specimens was 0.68, corresponding to relative density values (D_R) of 71% and 64%, respectively.

The specimens used in the isotropic compression tests were prepared inside a 3D printed custom-made split mold. During testing, the specimens were isotropically compressed to a mean effective stress of 20, 40, and 60 kPa using suction pressure through a vacuum pump connected to the bottom cap and a vacuum gauge was connected to the top cap to measure the suction within the specimen (Fig. 2.3(a)). The specimens used in the 1D compression tests were pluviated inside a rigid mold, as shown in Fig. 2.3(b). A loading frame was used to apply a force on the specimen top cap to establish K_0 stress conditions. The specimens were compressed to a vertical stress of 20, 40, and 60 kPa. A slight gap was maintained between the mold and the top cap, which was lubricated with silicone oil, to avoid interlocking of particles between these two parts. V_s measurements for the different BE pairs were obtained at each stress increment during both isotropic and 1D compression.

2.4 Results

This section presents the results obtained from the BE tests conducted on glass beads and 100C sand specimens subjected to isotropic and 1D compression. First, the influence of mean effective confining stress on the V_s measured on different orientations is presented. Following that, angular variations of V_s are provided, and their implications on the stress- and fabric-induced anisotropies are discussed. Finally, the observed trends in the differences

in $V_{S,VH}$, $V_{S,HV}$, and $V_{S,HH}$ for glass beads and 100C sand specimens are compared to those presented in select published studies.

2.4.1 Influence of mean effective confining stress on V_s

The transmission or propagation of a shear wave through a soil specimen is a particle-scale phenomenon that captures the contact stiffness of the particles in the assembly, which is in turn affected by several parameters such as particle shape, particle arrangement, contact orientations, coordination number, confining stress, and void ratio (Cascante and Santamarina 1996; Fioravante 2000). Increases in confining stress lead to greater inter-particle contact forces and thus a greater contact stiffness (i.e., as described for two elastic spheres by Hertz theory) as well as to the creation of new contacts through a compression of the soil. The increase in contact stiffness causes a concomitant increase in V_s . Prior research has investigated the effect of the effective stresses on the wave propagation direction and the particle motion direction on the V_s magnitude and have proposed relationships to analyze the stress dependency of V_s (e.g., Hardin and Richart 1963; Roesler 1979; Cascante and Santamarina 1996; Cho et al. 2006; Cha et al. 2014; Otsubo et al. 2020). Most relationships take the form of a power-law described as:

$$V_s = \alpha \left(\frac{\sigma'_w + \sigma'_p}{2} \right)^\beta = \alpha (\sigma'_m)^\beta \quad (2.3)$$

where σ'_m is the mean effective stress in the polarization plane, which is the arithmetic mean of stresses between the wave propagation (σ'_w) and the particle motion (σ'_p) directions; the coefficient α is the V_s at an effective confining stress of 1 kPa which is dependent on various factors such as soil packing type, void ratio, over consolidation, and cementation; and the exponent β reflects the sensitivity of skeletal stiffness to σ'_m and is influenced by particle

compressibility (Cho et al. 2005). Previous studies have used different exponents to isolate the influence of σ'_w and σ'_p on the shear modulus of sands (e.g., Kuwano and Jardine 2002). In this study, a single exponent β is used to reflect the influence of σ'_m on V_s magnitudes based on the recommendations of Cascante and Santamarina (1996b).

The mean effective stresses for the polarization planes for $V_{S,VH}$, $V_{S,HV}$, and $V_{S,HH}$ can be defined as:

$$\sigma'_{m,VH} = \frac{\sigma'_V + \sigma'_H}{2} = \frac{\sigma'_V + K_0\sigma'_V}{2} = \frac{\sigma'_V (1 + K_0)}{2} \quad (2.4)$$

$$\sigma'_{m,HV} = \frac{\sigma'_H + \sigma'_V}{2} = \frac{K_0\sigma'_V + \sigma'_V}{2} = \frac{\sigma'_V (1 + K_0)}{2} \quad (2.5)$$

$$\sigma'_{m,HH} = \frac{\sigma'_H + \sigma'_H}{2} = \frac{K_0\sigma'_V + K_0\sigma'_V}{2} = K_0\sigma'_V \quad (2.6)$$

For a given soil specimen, the $\sigma'_{m,VH}$ and $\sigma'_{m,HV}$ stresses have the same magnitude, leading to an expected negligible effect of stress-induced anisotropy between $V_{S,VH}$ and $V_{S,HV}$ owing to the single β coefficient used in Eq. 2.3. The K_0 values for normally consolidated sands are typically less than one, therefore $\sigma'_{m,HH}$ is expected to be lower than the $\sigma'_{m,VH}$ and $\sigma'_{m,HV}$, leading to an expected lower $V_{S,HH}$ as compared to $V_{S,VH}$ and $V_{S,HV}$. It is also noted that the mean stress on any plane between $V_{S,VH}$ and $V_{S,HV}$ remains unchanged as demonstrated by the rotation of effective stresses equations.

Figure 2.7 shows shear wave signals, $V_{S,VH}$, V_s at 50° , $V_{S,HV}$, and $V_{S,HH}$ obtained in a specimen of glass beads subjected to isotropic compression stresses of 20, 40, and 60 kPa, while Fig. 2.8 shows corresponding results for a specimen of 100C sand. Similar results obtained for V_s at 55° , 65° , and 75° are not included here for the sake of brevity. As shown,

the arrival times decrease for all shear wave orientations as σ'_m is increased for both materials, as shown by the downward pointing arrows which indicate an increase in V_S per Eq. 2.2. The effect of increases in σ'_m is further shown in Fig. 2.9, which presents $V_{S,VH}$, V_S at 50° , $V_{S,HV}$, and $V_{S,HH}$ measurements from glass beads and 100C sand specimens subjected to isotropic and 1D compression. For the 1D compressed specimens, the mean effective stress was computed using Eq. 2.4-2.6, where the K_θ values for glass beads and 100C were computed using Jaky's equation, i.e., $K_\theta = 1 - \sin(\phi')$, where ϕ' is the effective friction angle. The value of ϕ' was chosen as 20° for the glass beads and 32° for the 100C sand, as measured by Ahmed et al. (2021).

The V_S measurements exhibit the typical power-law trend with mean effective stress for both isotropic and 1D compression results. As shown, the isotropically-compressed glass beads specimens have isotropic behavior with similar magnitudes of $V_{S,VH}$, V_S at 50° , $V_{S,HV}$, and $V_{S,HH}$. For example, at 40 kPa, the average $V_{S,VH}$, V_S at 50° , $V_{S,HV}$, and $V_{S,HH}$ values are 161 m/s, 158 m/s, 161 m/s and 163 m/s, respectively. In contrast, the effect of stress-induced anisotropy is seen for the 1D-compressed glass beads specimens, which have a lower $V_{S,HH}$ than $V_{S,VH}$ with respective values of 115 m/s and 173 m/s. The $V_{S,VH}$ value has a similar magnitude to $V_{S,HV}$, while V_S at 50° takes an intermediate value between $V_{S,HH}$ and $V_{S,VH}$. The isotropically-compressed 100C sand specimen has a greater V_S magnitudes at 50° , $V_{S,HV}$, and $V_{S,HH}$ compared to the $V_{S,VH}$ magnitudes. This difference in magnitudes is likely caused by the preferential horizontal alignment of the particle long axes caused by the air pluviation process. The 1D-compressed 100C sand specimen has similar $V_{S,VH}$, V_S at 50° , $V_{S,HV}$, and $V_{S,HH}$, which are influenced by the combined effects of stress- and fabric-induced anisotropies. These effects are further discussed in the proceeding section.

Figure 2.10 shows the values of α -coefficients and β -exponents obtained by fitting Eq. 2.3 to the V_S measurements shown in Fig. 2.9. The α -coefficients vary between 43.9 and 131.1. The β -exponents vary between 0.175 and 0.361. The α -coefficients and β -exponents values for all the specimens in this investigation are within the range reported in the literature (Cha et al. 2014; Dutta et al. 2020). The data shows no specific trends with respect to the orientation along which V_S is obtained, likely because only three data points were used to define the relationships shown in Fig. 2.9. However, all the β -exponents are higher than 0.167, which is the theoretical value for a pure Hertzian contact between spheres (Cascante and Santamarina 1996). This indicates that the particles experience particle rearrangement or contact asperity yielding in all the specimens, as is expected for glass beads and natural sands (Cho et al. 2006).

2.4.2 Angular variation of shear wave velocity

Fabric anisotropy can be quantified in terms of the spatial distributions of contact normal orientations as well as particle long-axis orientations (Oda 1972a, 1972b; Yang et al. 2008). Vector analysis of these orientations is often used to determine angular distributions to quantify the evolution of fabric anisotropy as a soil specimen is loaded or deformed. These distributions are frequently represented as polar plots (Rothenburg and Bathurst 1989; Otsubo et al. 2020; Basson and Martinez 2020). The polar histograms are typically fitted with analytical expressions with the following form:

$$E(\theta) = E_{avg} (1 + a \cos 2 (\theta - \theta_n)) \quad (2.7)$$

where E is the quantity of interest, a is the magnitude of anisotropy, θ is the angle measured from the horizontal, θ_n is the preferred orientation of the angular distribution, and E_{avg} is the

average quantity taken along all directions (Rothenburg and Bathurst 1989). An equation with the same form as Eq. 2.7 is proposed to fit the angular distribution in the $V_{S,VH}$ to $V_{S,HV}$ plane, as follows:

$$V_S = V_{S,avg} (1 + a_n \cos 2 (\theta - \theta_n)) \quad (2.8)$$

where a_n is anisotropy in the polar V_S distribution, θ is the orientation at which the V_S measurement is obtained (90° (vertical) 75° , 65° , 55° , 50° and 0° (horizontal)), and $V_{S,avg}$ is the average V_S for different BE orientations for a given mean stress. The parameters a_n and θ_n are obtained via least-squares fitting of the polar histograms of V_S (Basson et al. 2021). This equation is defined such that an isotropic distribution of V_S yields a circular polar plot with a_n value of zero, whereas an anisotropic distribution would yield an ellipse- or peanut-shaped plot with a higher a_n value. In the case of anisotropic distributions, θ_n provides the orientation of the plane with the greatest V_S magnitude, measured from the horizontal direction.

The angular distributions of V_S for the specimens reflect the stress- and fabric-induced anisotropies. The distributions for the glass beads and 100C sand specimens under isotropic and 1D compression are presented in Fig. 2.11, which include fitted distributions using Eq. 2.8. Because the experimental setup only allows for the V_S measurements at orientations from 0° to 90° , all the results are plotted in the first quadrant of the polar plots. The anisotropy values, a_n , of the fitted distributions are presented as a function of mean effective stress in Fig. 2.12, and Table 2.1 summarizes the average a_n and θ_n values obtained for all the specimens. The glass bead specimens under isotropic compression exhibit a near-circular distribution of V_S (Fig. 2.11(a)) due to the applied uniform state of stress and the negligible

fabric anisotropy. The a_n values of the fitted distributions have magnitudes smaller than 0.061, with an average value of 0.039 (Table 2.1, Fig. 2.12). The polar histograms of V_s for different σ'_m are concentric, representing an increase in V_s magnitude with increase in mean effective stress for the various orientations. Furthermore, the $V_{s,HH}$ values are similar to the $V_{s,VH}$ and $V_{s,HV}$ ones, confirming the overall near-isotropy in the specimen.

One-dimensional compression of the glass beads specimen leads to an anisotropic stress state, which can be explained by comparing σ'_m along the different planes according to Eqs. 2.5–2.7. For example, for an applied vertical effective stress of 60 kPa, the mean effective confining stresses $\sigma'_{m,VH}$, $\sigma'_{m,HV}$, and $\sigma'_{m,HH}$ are 48.9, 48.9, and 39.6 kPa, respectively, which are the effective stress magnitudes in the polarization planes of $V_{s,VH}$, $V_{s,HV}$, and $V_{s,HH}$. Because the $\sigma'_{m,VH}$ and $\sigma'_{m,HV}$ magnitudes are the same, the magnitudes of $V_{s,VH}$ and $V_{s,HV}$ should be similar, as corroborated by the circular V_s polar plot and a low a_n values that yield an average of 0.022 (Table 2.1, Figs. 2.11b and 2.12). In this specimen, the $V_{s,HH}$ values are about 28% smaller than the $V_{s,VH}$ and $V_{s,HV}$ values due to the lower stress $\sigma'_{m,HH}$, demonstrating the effects of stress-induced anisotropy. These observations agree with those reported in the literature (Zeng and Ni 1998; Fioravante 2000; Wang and Mok 2008; Goudarzy et al. 2018; Gu et al. 2021; Otsubo et al. 2020; Dutta et al. 2020).

Fabric anisotropy is a key component in the angular distribution of V_s for the 100C sand specimens. For this material, the $V_{s,HH}$ and $V_{s,HV}$ magnitudes are greater than $V_{s,VH}$ for the specimens compressed isotropically (Fig. 2.11(c)). This difference is attributed to a combination of particle shape effects and pluviation used in the preparation of specimens. Pluviation under gravity produces the tendency for particles to align with their long axis in

the horizontal plane. This observation has been confirmed by examining the fabric of specimens prepared by pluviation using X-ray tomography (Sun et al. 2019; Shi et al. 2021), image processing of specimen slices (Yang et al. 2008; Ibrahim and Kagawa 1991), and discrete element modeling of non-circular particles (Otsubo et al. 2020). Sun et al. (2019) and Shi et al. (2021) plotted the directional variation of long axis orientation of a specimen prepared by pluviation of sub-angular particles revealing a predominant anisotropy with particle long axes oriented horizontally. Otsubo et al. (2020) generated angular variations of fabric from discrete element simulations of elongated particles, demonstrating that the long axis of pluviated particles aligns with the horizontal direction and resulting in a $V_{S,HH}/V_{S,HV}$ and $V_{S,HH}/V_{S,VH}$ ratios greater than one. The likely horizontally-aligned particle long axes produce the ellipse-shaped V_S distribution with an average a_n value of 0.156 and a preferred orientation of 5.4° from the horizontal, as shown in Table 2.1, Fig. 2.11(c), and Fig. 2.12. For context, an a_n of 0.156 corresponds a ratio of the maximum to minimum V_S in the polar distribution of 1.36. The greater magnitude of $V_{S,HH}$ and $V_{S,HV}$ compared to $V_{S,VH}$ suggests that fabric anisotropy influences the magnitude of V_S for waves traveling in the horizontal direction (HV and HH waves) regardless of particle motion direction and are in agreement with previously published results from experimental and DEM studies (Fioravante 2000; Otsubo et al. 2020).

The V_S magnitudes for 100C sand specimens under 1D compression show the combined effects of fabric- and stress-induced anisotropy. It appears that the effects of a horizontally aligned fabric and greater vertical effective stress offset each other, resulting in an angular V_S distribution that resembles a circle, with an average a_n value of 0.056 (Table 2.1, Figs.

2.11(d) and 2.12). For this specimen, the $V_{S,HH}$ values are close in magnitude to the $V_{S,HV}$ values, further showing a small anisotropy in the angular distribution.

Overall, the a_n values do not appear to be sensitive to changes in the mean effective stress, particularly for the isotropically- and 1D-compressed glass beads and the 1D-compressed 100C sand (Fig. 2.12). This is likely due to the fact that the stress anisotropy is controlled by the ratio of the vertical to horizontal effective stresses, which likely remains constant as the mean effective stress increases. The decrease in a_n with mean effective stress for the isotropically-compressed 100C sand may be an indication of a slight reduction in the fabric anisotropy caused by the imposed isotropic stresses, as described by Barreto et al. (2009).

2.4.3 Discussion and comparison with other studies

The three V_s measurements for specimens with negligible fabric- and stress-induced anisotropy, such as the glass beads specimen under isotropic compression, are similar in magnitude and lie close to the 1:1 line when plotted in terms of $V_{S,HH}$ versus $V_{S,HV}$, $V_{S,HV}$ versus $V_{S,VH}$, and $V_{S,HH}$ versus $V_{S,VH}$ (red circles in Figs. 2.13(a,b,c)). The effect of stress-induced anisotropy is demonstrated by the glass beads specimen under 1D compression, where $V_{S,VH}$ is greater than $V_{S,HH}$ (green Xs in Figs. 2.13(a,c)) because the effective stress in the polarization plane of the former is greater than in the plane of the latter as indicated by Eqs. 2.5–2.7. It is noted that a K_0 value greater than one would lead to greater effective stresses in the horizontal plane (i.e., $\sigma'_{m,HH}$), resulting in an expected $V_{S,HH}$ value greater than $V_{S,VH}$. The effect of fabric anisotropy is exhibited by the isotropically-compressed 100C sand for the $V_{S,HV}$ versus $V_{S,VH}$ and $V_{S,HH}$ versus $V_{S,VH}$ plots (blue diamonds in Figs. 2.13(b,c)), where the

preferential horizontal alignment of the particles results in a greater $V_{S,HV}$ and $V_{S,HH}$ magnitudes which propagate on the horizontal plane, as compared to the $V_{S,VH}$ magnitudes. Finally, the competing mechanism between the fabric- and stress-induced anisotropy for the 1D-compressed 100C sand decreases the overall anisotropy in V_S , resulting in the data points being located close to the 1:1 line in all three plots (orange crosses).

Figures 2.13(a,b,c) also include data from a number of experimental studies on isotropically and 1D-compressed Toyoura, Ottawa, Kenya, Ticino, Han, Rhein, and rounded sands as well as crushed glass. The data pertain to specimens with confining stresses under 200 kPa for Gu et al. (2021). Comparisons can be made to highlight similarities between the published data with the data presented in this study, which are especially evident in the $V_{S,HH}$ versus $V_{S,VH}$ plot (Fig. 2.13(c)). Particularly, the isotropically compressed Toyoura, Ticino, and Kenya sand have greater $V_{S,HH}$ values than the $V_{S,VH}$ values, likely showing the effect of fabric anisotropy. Also, the 1D-compressed Toyoura, Ottawa, Han, Rhein, and rounded sands and the crushed glass all have $V_{S,HH}$ values that are smaller than the $V_{S,VH}$ values, exhibiting the effects of stress anisotropy.

The results obtained from the glass beads and 100C specimens can complement the interpretation of results obtained from in-situ tests. Figures 2.14(a,b,c) show a comparison of the laboratory data with in-situ measurements obtained by Ku and Mayne (2013). In in-situ testing, $V_{S,VH}$ is typically measured through downhole testing, and $V_{S,HV}$ and $V_{S,HH}$ are measured through crosshole testing. Those authors performed downhole and crosshole tests in deposits of normally-consolidated sand (Po river, Treasure Island, and Higashi NC sands with OCR values ranging from 1 to 1.3) and over-consolidated clay (London, Pisa, Oxford and

Amherst OC clays with OCR values ranging from 2 to greater than 25). As shown, the V_s measurements for NC sands are similar to the those obtained for the 100C sand and glass beads under 1D compression. This likely reflects a slight stress anisotropy, due to a K_0 value smaller than one which is characteristic of normally-consolidated sands, and a small degree of fabric anisotropy, with a preferential orientation of the particle long axes in the horizontal direction due to the depositional process. The slight stress anisotropy likely causes the in-situ results to plot slightly below the 1:1 line in $V_{s,HH}$ versus $V_{s,HV}$ and $V_{s,HH}$ versus $V_{s,VH}$ spaces (Figs. 2.14(a,c)). The V_s measurements reported by Ku and Mayne (2013) for OC clay plot in a similar location in Figs. 2.14(a,b,c) as the results for the isotropically-compressed 100C specimen, with $V_{s,HH} > V_{s,HV} > V_{s,VH}$. This similarity may be an indication of fabric-induced anisotropy. As previously described, the particles in the 100C specimens likely have a preferential horizontal alignment due to the pluviation process used in the specimen preparation. Analogously, the overconsolidation process results in a horizontal preferential alignment of the clay particles which typically leads to anisotropy in the strength and stiffness in fine-grained soils (Mitchell and Soga 2005; Pennington et al. 1997; Pennington et al. 2001). However, it is noted that the OC clay deposit may also have stress-induced anisotropy, which would influence the V_s measurements. Overall, these comparisons suggest that systematic testing of soils in the laboratory could help separate the stress- and fabric-induced anisotropies deduced from field V_s measurements.

2.5 Conclusions

This paper describes a newly developed testing setup that consists of seven bender element pairs that allow measuring shear wave velocity in different angular orientations and

polarization planes. This system provides $V_{S,VH}$, $V_{S,HV}$, and $V_{S,HH}$ measurements, as well as V_S measurements at 75° , 65° , 55° , and 50° (from the horizontal) to provide a sweep between $V_{S,VH}$ and $V_{S,HV}$. Experiments with the multi-orientation BE system were performed on specimens of glass beads and angular sand subjected to either isotropic or 1D compression. These experiments were performed to assess the effects of stress- and fabric-induced anisotropy on the differences in V_S obtained along different orientations and polarization planes. The main findings from the experimental results are summarized as follows:

- The V_S magnitudes are strongly influenced by the magnitude of effective stress in specimens, irrespective of the material and loading conditions. This dependency was observed in measurements obtained in all orientations and polarization planes, and the α -coefficient and β -exponent values obtained in fits to Eq. 2.3 are in agreement with values published in the literature. The results show that the α -coefficient and β -exponent values are not constant for a given specimen, but they depend on the orientation of the wave and the polarization plane.
- The $V_{S,VH}$ and $V_{S,HV}$ measurements along with the V_S at 75° , 65° , 55° , and 50° allow creating polar histograms that provide a visual representation of the anisotropy in shear wave velocity. An equation to describe the experimentally determined angular distribution of V_S was proposed, which has the same form as established relationships used to describe the distribution of particle orientation and contact normal vectors. The coefficient a_n appears to appropriately quantify the anisotropy in the angular V_S distribution.
- Specimens of isotropically compressed glass beads produce near-isotropic V_S angular distributions due to their negligible fabric and stress anisotropy. Under 1D compression,

the glass beads specimens emphasize the effects of stress-induced anisotropy due to the greater vertical effective stress leading to a smaller $V_{S,HH}$ than $V_{S,VH}$ and $V_{S,HV}$.

- Specimens of angular sand compressed isotropically highlight the effects of fabric-induced anisotropy, producing angular V_S distributions that were elongated horizontally. This is attributed to the preferential horizontal alignment of the particles produced by the pluviation process used to prepare the samples. The sand specimens subjected to 1D compression produced apparent isotropic V_S distributions; it is possible that the effects of stress- and fabric-induced anisotropy offset each other to produce such a distribution.

The testing setup described in this paper, along with the presented results, emphasize the utility of using V_S measurements along different orientations and polarization planes to assess the anisotropy of soil specimens. While sophisticated methods such as X-ray CT can provide a direct measurement of anisotropy, V_S measurements can provide an indirect assessment of soil anisotropy that employs conventional laboratory equipment. The results provide evidence suggesting that the presence of stress- and fabric-induced anisotropy can be identified by means of the parameters describing the angular distribution of V_S (a_n and θ_n in Eq. 2.8) as well as by comparing $V_{S,HV}$ to $V_{S,HH}$ and $V_{S,VH}$ to $V_{S,HH}$, respectively. Additionally, comparison of the obtained data to the field studies indicates that the presence of stress- and fabric-induced anisotropy can be obtained indirectly through V_S measurements using existing methodologies such as SCPT, cross hole and down hole testing. This information could be crucial for the design and analysis of geosystems affected by soil fabric, such as seepage beneath a dam. However, these observations should be verified with direct measurements of fabric anisotropy. Future developments to the proposed method could focus on considering the contribution of the different stresses (i.e., σ_p , σ_w , and stress along

the out-of-plane direction σ_o) to the magnitude of V_S , since previous work such as Kuwano and Jardine (2002) has shown small but measurable different influences from σ_p and σ_w as well as a small influence of the out of plane stress (σ_o). Nonetheless, measurements on specimens with systematic differences in stress- and fabric-induced anisotropies as presented herein can help further the fundamental understanding of the origin of anisotropy in soils and its evolution during loading.

2.6 Acknowledgements

The support of the University of California, Davis, College of Engineering is acknowledged. The authors would also like to acknowledge the support of Jasmine Miller in the initial developments of the multi-orientation BE system.

2.7 References

- Ahmed, S. S., A. Martinez, and J. T. DeJong 2021. "Effect of gradation on the drained and undrained triaxial compression behavior of coarse-grained soils." *Journal of Geotechnical and Geoenvironmental Engineering* 149(5):04023019.
- Altuhafi, F. N., M. R. Coop, and V. N. Georgiannou. 2016. "Effect of particle shape on the mechanical behavior of natural sands." *Journal of Geotechnical and Geoenvironmental Engineering* 142, no. 12: 04016071.
- Alvarado, G. and M. R. Coop. 2012. "On the performance of bender elements in triaxial tests." *Géotechnique* 62, no. 1: 1-17.
- Arroyo, M., D. Muir Wood, and P. D. Greening. 2003. "Source near-field effects and pulse tests in soil samples." *Géotechnique* 53, no. 3: 337-45.

- Arroyo, M., D. Muir Wood, P. D. Greening, L. Medina, and J. Rio. 2006. "Effects of sample size on bender-based axial G_0 measurements." *Géotechnique* 56, no. 1: 39–52.
- Arulnathan, R., R. W. Boulanger, and M. F. Riemer. 1998. "Analysis of bender element tests." *Geotechnical Testing Journal* 21, no. 2 (June): 120–131.
- Barreto, D., C., O'Sullivan, and L. Zdravkovic. 2009. "Quantifying the evolution of soil fabric under different stress paths." In: Nakagawa, M and Luding, S. (eds). *Proceedings of the 6th International Conference on Micromechanics of Granular Media*, Golden, Colorado, USA. AIP Conference Proceedings.
- Basson, M. S., J. Miller, and A. Martinez. 2021. "Experimental estimation of fabric in granular materials using shear wave velocity measurements." In: Sitharam T.G., Dinesh S.V., Jakka R. (eds) *Soil Dynamics. Lecture Notes in Civil Engineering*, vol 119. Springer, Singapore.
- Basson, M. S. and A. Martinez. 2020. "A DEM study of the evolution of fabric of coarse-grained materials during oedometric and isotropic compression." In *Proceedings Geo-Congress 2020*, Minneapolis, Minnesota, USA.
- Bernal, J.D. and J. Mason. 1960. "Co-ordination of randomly packed spheres." *Nature* 188: 910–911.
- Blewett, J., I. J. Blewett, and P. K. Woodward. 1999. "Measurement of shear-wave velocity using phase-sensitive detection techniques." *Canadian Geotechnical Journal* 36, 6.
- Blewett, J., I. J. Blewett, and P. K. Woodward. 2000. "Phase and amplitude responses associated with the measurement of shear-wave velocity in sand by bender elements." *Canadian Geotechnical Journal* 37, 10.

- Brignoli, E. G. M., M. Gotti, and K. H. Il Stokoe. 1996. "Measurement of shear waves in laboratory specimens by means of piezoelectric transducers." *Geotechnical Testing Journal* 19, no. 4: 384–397.
- Brocanelli, D. and V. Rinaldi. 1998. "Measurement of low-strain material damping and wave velocity with bender elements in the frequency domain." *Canadian Geotechnical Journal* 35: 1032–1040.
- Cascante, G. and J. C. Santamarina. 1996a. "Interparticle contact behavior and wave propagation." *Journal of Geotechnical Engineering* 122, no. 10: 831–839.
- Cascante, G. and J. C. Santamarina. 1996b. "Stress anisotropy and wave propagation: a micromechanical view." *Canadian Geotechnical Journal* 33: 770–782.
- Cha, M., J. C. Santamarina, H.-S. Kim, and G.-C. Cho. 2014. "Small-strain stiffness, shear-wave velocity, and soil compressibility." *Journal of Geotechnical and Geoenvironmental Engineering* 140, no. 10: 06014011.
- Chamorro-Zurita, C. and E. Ovando-Shelley. 2020. "Anisotropy of lacustrine soils in a large oedometer equipped with bender elements." *Soils and Foundations* 60, no. 2: 372–383.
- Cho, G.-C., J. Dodds, and J. C. Santamarina. 2006. "Particle shape effects on packing density, stiffness, and strength: natural and crushed sands." *Journal of Geotechnical and Geoenvironmental Engineering* 132, no. 5: 591–602.
- Cnudde, V. and M. N. Boone. 2013. "High-resolution X-ray computed tomography in geosciences: A review of the current technology and applications." *Earth-Science Reviews* 123: 1–17.

- Dutta, T. T., M. Otsubo, R. Kuwano, and T. Sato. 2020. "Estimating multidirectional stiffness of soils using planar piezoelectric transducers in a large triaxial apparatus." *Soils and Foundations* 60, no. 5: 1269–1286.
- Farber, L., G. Tardos, and J. N. Michaels. 2003. "Use of X-ray tomography to study the porosity and morphology of granules." *Powder Technology* 132, no. 1: 57–63.
- Fioravante, V. 2000. "Anisotropy of small strain stiffness of Ticino and Kenya sands from seismic wave propagation measured in triaxial testing." *Soils and Foundations* 40, no. 4: 129–142.
- Fioravante, V. and R. Capoferri. 2001. "On the use of multi-directional piezoelectric transducers in triaxial testing." *Geotechnical Testing Journal* 24, no. 3: 243.
- Fonseca, A.V., C. Ferreira, and M. Fahey. 2009. "A framework interpreting bender element tests, combining time-domain and frequency-domain methods." *ASTM Geotechnical Testing Journal* 32, no. 2: 1–17.
- Fu, P. and Y. F. Dafalias. 2015. "Relationship between void- and contact normal-based fabric tensors for 2D idealized granular materials." *International Journal of Solids and Structures* 63: 68–81.
- Goudarzy, M., D. König, J. C. Santamarina, and T. Schanz. 2018. "The influence of the anisotropic stress state on the intermediate strain properties of granular material." *Géotechnique* 68, no. 3: 221–232.
- Gomez, M. G., C. M. R. Graddy., J. T. DeJong, D. C. Nelson, M. Tsesarsky. 2018. "Stimulation of native microorganisms for biocementation in samples recovered from field-scale treatment depths." *Journal of Geotechnical and Geoenvironmental Engineering* 144, Issue 1.

- Gu, Q., D. Sarkar, M. Goudarzy, and T. Wichtmann. 2021. "Combined effect of grain shape and grading on the small-strain stiffness of granular soils at different densities and stress states." In *Proceedings Conference: 3. Bodenmechanik Tagung*
- Gu, X., X. Liang, Y. Shan, X. Huang, and A. Tessari. 2020. "Discrete element modeling of shear wave propagation using bender elements in confined granular materials of different grain sizes." *Computers and Geotechnics* 125: 103672.
- Hardin, B. and F. Richart. 1963. "Elastic wave velocities in granular soils." *Journal of the Soil Mechanics and Foundations Division* 89, no. 1.
- Ibrahim, A., and T. Kagawa. 1991. "Microscopic Measurement of Sand Fabric from Cyclic Tests Causing Liquefaction." *Geotech. Test. J.*, 14 (4): 371.
- Jamiolkowski, M., R. Lancellotta, and D. C. F. Lo Presti. 1995. "Remarks on the stiffness at small strain of six Italian clays." In *Proceedings of I International Symposium On Prefailure Deformation Characteristics of Geomaterials*, IS, Sapporo, Shibuya, Mitachi and Miura, Eds. Balkema, 2: 817–836.
- Jovičić, V., M. R. Coop, and M. Simić. 1996. "Objective criteria for determining G_{max} from bender element tests." *Géotechnique* 46, no. 2: 357–362.
- Kaviani-Hamedani, F., K. Fakharian, and A. Lashkari. 2021. "Bidirectional shear wave velocity measurements to track fabric anisotropy evolution of a crushed silica sand during shearing." *Journal of Geotechnical and Geoenvironmental Engineering* 147, no. 10: 04021104.
- Kodicherla, S. P. K., G. Gong, L. Fan, C. K. S. Moy, and J. He. 2018. "Effects of preparation methods on inherent fabric anisotropy and packing density of reconstituted sand." *Cogent Engineering* (V. Felipe, ed.) 5, no. 1.

- Krumbein, W. C., and Sloss, L. L. 1963. "Stratigraphy and sedimentation", 2nd Ed., Freeman and Company, San Francisco.
- Ku, T. and P. W. Mayne. 2013. "Evaluating the in situ lateral stress coefficient (K_0) of soils via paired shear wave velocity modes." *Journal of Geotechnical and Geoenvironmental Engineering* 139, no. 5: 775–787.
- Kuwano, R., T. M. Connolly, and J. Kuwano. 1999. "Shear stiffness anisotropy measured by multidirectional bender element transducers." In *Proceedings of II International Symposium On Prefailure Deformation Characteristics of Geomaterials*, Torino, Jamiolkowsky, Lancellotta, and Lo Presti, Eds., Balkema, 1: 205–212.
- Kuwano, R. and R. J. Jardine. 2002. "On the applicability of cross-anisotropic elasticity to granular materials at very small strains." *Géotechnique* 52, no. 10: 727–749.
- Lee, C.-J. and H. Y. Huang. 2007. "Wave velocities and their relation to fabric evolution during the shearing of sands." *Soil Dynamics and Earthquake Engineering* 27, no. 1: 1–13.
- Lee, J.-S. and J. C. Santamarina. 2005. "Bender elements: performance and signal interpretation." *Journal of Geotechnical and Geoenvironmental Engineering* 131, no. 9: 1063–1070.
- Leong, E. C., S. H. Yeo, and H. Rahardjo. 2005. "Measuring shear wave velocity using bender elements." *Geotechnical Testing Journal* Vol. 28, Issue 5, p. 12196
- Liu, X. and J. Yang. 2018. "Shear wave velocity in sand: effect of grain shape." *Géotechnique* 68, no. 8: 742–748.
- Martinez, A., L. Huang and M. G. Gomez. 2016. "Thermal conductivity of MICP-treated sands at varying degrees of saturation" *Géotechnique Letters* 9(1): 15-21.

- Mitaritonna, G., A. Amorosi, and F. Cotecchia. 2014. "Experimental investigation of the evolution of elastic stiffness anisotropy in a clayey soil." *Géotechnique*, 64(6), 463–475.
- Mital, U., R., Kawamoto, and J. E., Andrade. 2020. "Effect of fabric on shear wave velocity in granular soils." *Acta Geotechnica*, 15(5), 1189–1203.
- Mitchell, J.K. and K. Soga. 2005 "Fundamentals of soil behavior", *John Wiley & Sons, Hoboken*.
- Montoya, B. M., R. Gerhard, J. T. DeJong, D. W. Wilson, M. H. Weil, B. C. Martinez, and L. Pederson. 2012. "Fabrication, operation, and health monitoring of bender elements for aggressive environments." *Geotechnical Testing Journal*, 35 (5): 103300.
- Ning, Z., A. Khoubani, and T. M. Evans. 2015. "Shear wave propagation in granular assemblies." *Computers and Geotechnics* 69: 615–626.
- O'Donovan, J., E. Ibraim, C. O'Sullivan, S. Hamlin, D. Muir Wood, and G. Marketos. 2016. "Micromechanics of seismic wave propagation in granular materials." *Granular Matter* 18, no. 3.
- O'Donovan, J., C. O'Sullivan, G. Marketos, and D. Muir Wood. 2015. "Analysis of bender element test interpretation using the discrete element method." *Granular Matter* 17, no. 2: 197–216.
- Oda, M., S. Konishi, and S. Nemat-Nasser. 1982. "Experimental micromechanical evaluation of strength of granular materials: Effects of particle rolling." *Mechanics of Materials* Vol 1: 269–283.
- Oda, M. 1972a. "Initial fabric and their relations to mechanical properties of granular materials." *Soils and Foundations* 12, no. 1: 17-36.

- Oda, M. 1972b. "The mechanism of fabric changes during compressional deformation of sands, soils and foundations." *Soils and Foundations* 12, no. 2: 1–18.
- Ogino, T., T. Kawaguchi, S. Yamashita, and S. Kawajiri. 2015. "Measurement deviations for shear wave velocity of bender element test using time domain, cross-correlation, and frequency domain approaches." *Soils and Foundations* 55, no. 2: 329–342.
- Otsubo, M. and C. O'Sullivan. 2018. "Experimental and DEM assessment of the stress-dependency of surface roughness effects on shear modulus." *Soils and Foundations* 58, no. 3: 602–614.
- Otsubo, M., J. Liu, Y. Kawaguchi, T. T. Dutta, and R. Kuwano. 2020. "Anisotropy of elastic wave velocity influenced by particle shape and fabric anisotropy under K condition." *Computers and Geotechnics* 128: 103775.
- Payan, M., A. Khoshghalb, K. Senetakis, and N. Khalili. 2016. "Small-strain stiffness of sand subjected to stress anisotropy." *Soil Dynamics and Earthquake Engineering* 88: 143–151.
- Pennington, D. S., D. F. T. Nash, and M. L. Lings. 1997. "Anisotropy of G_0 shear stiffness in Gault Clay." *Géotechnique* 47, no. 3: 391–398.
- Pennington, D., M. Lings, and D. F. T. Nash. 2001. "Horizontally mounted bender elements for measuring anisotropic shear moduli in triaxial clay specimens." *Geotechnical Testing Journal* 24, no. 2: 133.
- Reardon, R., F. Humire, S. S. Ahmed, K. Ziotopoulou, A. Martinez, J. T. Dejong. 2022. "Effect of gradation on the strength and stress-dilatancy of coarse-grained Soils: a comparison of monotonic direct simple shear and triaxial tests" In *Proceeding of GeoCongress 2022*, Charlotte, North Carolina.

- Roesler, S.K. 1979. "Anisotropic shear modulus due to stress anisotropy." *Journal of the Geotechnical Engineering Division ASCE*. [https://doi.org/10.1016/0148-9062\(79\)90065-2](https://doi.org/10.1016/0148-9062(79)90065-2)
- Rojek, J., N. Madan, and S. Nosewicz. 2019. "Micro–macro relationships in the simulation of wave propagation phenomenon using the discrete element method." *Materials* 12, no. 24: 4241.
- Rothenburg, L. and R. J. Bathurst. 1989. "Analytical study of induced anisotropy in idealized granular materials." *Géotechnique* 39, no. 4: 601–614.
- Sanchez-Salerino, I., J. M. Roesset, and K. H. II Stokoe. 1986. "Analytical studies of wave propagation and attenuation." In *Geotechnical Engineering Report No GR86-15* Civil Engineering Department, University of Texas, Austin.
- Santamarina, J. C., and D. Fratta. 2005. "Discrete signals and inverse problems: an introduction for engineers and scientists." *John Wiley & Sons, Hoboken*.
- Sawyer, B.D. 2020. "Cone penetration testing of coarse-grained soils in the centrifuge to examine the effects of soil gradation and centrifuge scaling." *University of California, Davis, ProQuest Dissertations Publishing, 28255722*.
- Seed, H. B., R. T. Wong, I. M. Idriss, and K. Tokimatsu. 1986. "Moduli and damping factors for dynamic analyses of cohesionless soils." *Journal of Geotechnical Engineering* 112, no. 11: 1016–1032.
- Shi, J., W. Haegeman, A. Mascini, and V. Cnudde. 2021. "X-ray analysis on the effect of sample preparation on the microstructure of calcareous sands." *Marine Georesources & Geotechnology*, 39 (3): 302–311.

- Stokoe, K.H., M. B. Darendeli, R. D. Andrus, and L. T. Brown. 1999. "Dynamic soil properties: laboratory, field and correlation studies." In *Proceeding of the 2nd international conference on earthquake geotechnical engineering*, Lisbon, Portugal. 811–45.
- Stokoe, K. H. II and J. C. Santamarina. 2000. "Seismic wave based testing in geotechnical engineering." In *International Conference on Geotechnical and Geological Engineering* 1490–1536.
- Stokoe, K. H., S. G. Wright, J. A. Bay, and J. M. Roesset. 1994. "Characterization of geotechnical sites by SASW method." In *Geophysical characterization of sites*, ISSMFE Technical Committee #10, edited by R. D. Woods, Oxford Publishers, New Delhi..
- Sturm, A.P. 2019. "On the liquefaction potential of gravelly soils: characterization, triggering and performance." *University of California, Davis. ProQuest Dissertations Publishing*, 27663210.
- Sun, Q., J. Zheng, H. He, and Z. Li. 2019. "Characterizing Fabric Anisotropy of Air-Pluviated Sands." *E3S Web Conf.*, (A. Tarantino and E. Ibraim, eds.), 92: 01003.
- Tong, Z., P. Fu, S. Zhou, and Y. F. Dafalias. 2014. "Experimental investigation of shear strength of sands with inherent fabric anisotropy." *Acta Geotechnica* 9, no. 2: 257–275.
- Fioravante, V. and R. Capoferri. 2001. "On the use of multi-directional piezoelectric transducers in triaxial testing." *Geotechnical Testing Journal* 24, no. 3: 243–255.
- Viggiani, G., E. Andò, D. Takano, and J. C. Santamarina. 2014. "Laboratory X-ray tomography: a valuable experimental tool for revealing processes in soils." *Geotechnical Testing Journal* 38, no. 1: 20140060.
- Viggiani, G., and J. H. Atkinson. 1995. "Interpretation of bender element tests." *Géotechnique* 45, no. 1: 149–154.

- Wang, Y. H. and C. M. Mok. 2008. "Mechanisms of small-strain shear-modulus anisotropy in soils." *Journal of Geotechnical and Geoenvironmental Engineering* 134, no. 10: 1516–1530.
- Wiebicke, M., E. Andò, G. Viggiani, and I. Herle. 2020. "Measuring the evolution of contact fabric in shear bands with X-ray tomography." *Acta Geotechnica* 15, no. 1: 79–93.
- Yamashita, S., T. Hori, and T. Suzuki. 2005. "Effects of initial and induced anisotropy on initial stiffness of sand by triaxial and bender elements tests." In *Geomechanics: Testing, modeling, and simulation*, 350–369.
- Yamashita, S., T. Kawaguchi, Y. Nakata, T. Mikami, T. Fujiwara, and S. Shibuya. 2009. "Interpretation of international parallel test on the measurement of G_{max} using bender elements." *Soils and Foundations* 49, no. 4: 631–650.
- Yang, J. and X. Q. Gu. 2013. "Shear stiffness of granular material at small strains: does it depend on grain size?" *Géotechnique* 63, no. 2: 165–179.
- Yang, Z. X., X. S. Li, and J. Yang. 2008. "Quantifying and modelling fabric anisotropy of granular soils." *Géotechnique* 58, no. 4: 237–248.
- Zdravković, L., and R. J., Jardine 2001. "The effect on anisotropy of rotating the principal stress axes during consolidation." *Géotechnique* 51(No 1), 69–83.
- Zeng, X., and B., Ni. 1998. "Application of bender elements in measuring g_{max} of sand under k_0 condition." *Geotechnical Testing Journal*, 21(3), 251.
- Zheng, J. and R. D. Hryciw. 2015. "Traditional soil particle sphericity, roundness and surface roughness by computational geometry." *Géotechnique* 65: 494–506.

Zhou, Y.-G. and Y.-M. Chen. 2007. "Laboratory investigation on assessing liquefaction resistance of sandy soils by shear wave velocity." *Journal of Geotechnical and Geoenvironmental Engineering* 133, no. 8: 959–972.

2.8 Tables and figures

Table 2.1: Testing conditions and average parameters of angular V_s ($V_{s,VH}$ to $V_{s,HV}$) distributions.

<i>Material</i>	<i>Testing condition</i>	a_n	θ (°)
Glass beads	Isotropic	0.039 (0.029)	2.3 (0.7)
Glass beads	1D	0.022 (0.025)	87.2 (2.8)
100C	Isotropic	0.156 (0.067)	5.4 (0.9)
100C	1D	0.059 (0.013)	1.6 (1.5)

Note: The average and standard deviation values provided were obtained from specimens subjected to stresses of 20, 40, and 60 kPa.

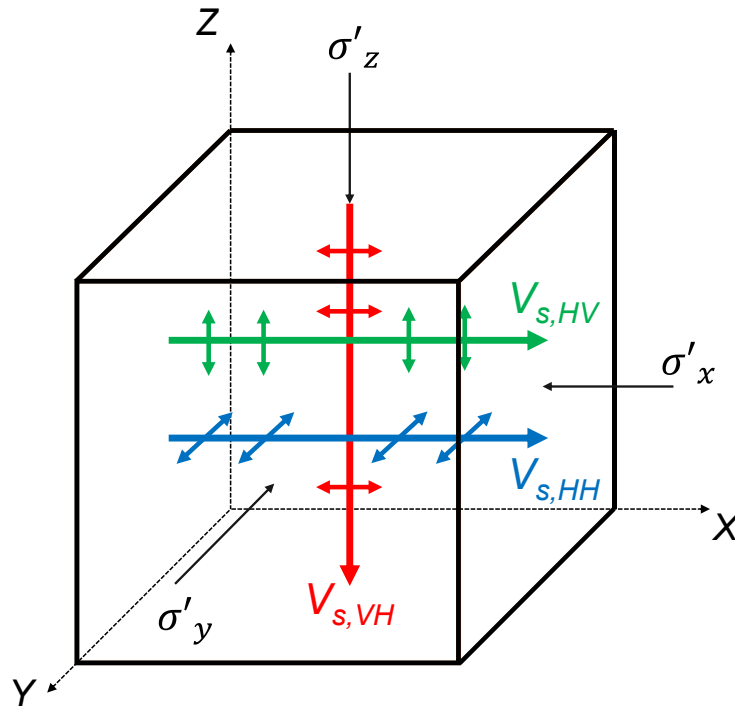


Figure 2.1: Notation for different shear waves propagating through a soil element..

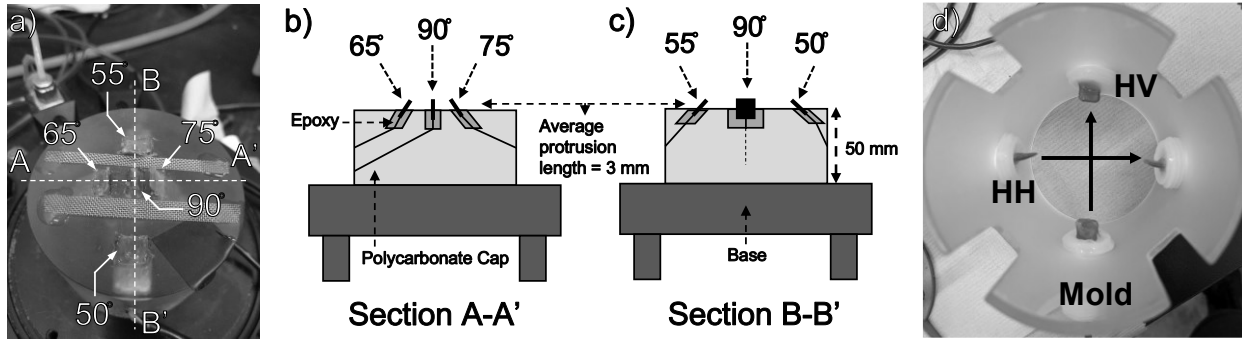


Figure 2.2: (a) Photograph and (b,c) cross-sectional drawing of the bottom end cap with five BEs (note: the top end cap has the same configuration as the bottom end cap). (d) Photograph of the horizontally mounted BEs in the 1D compression mold.

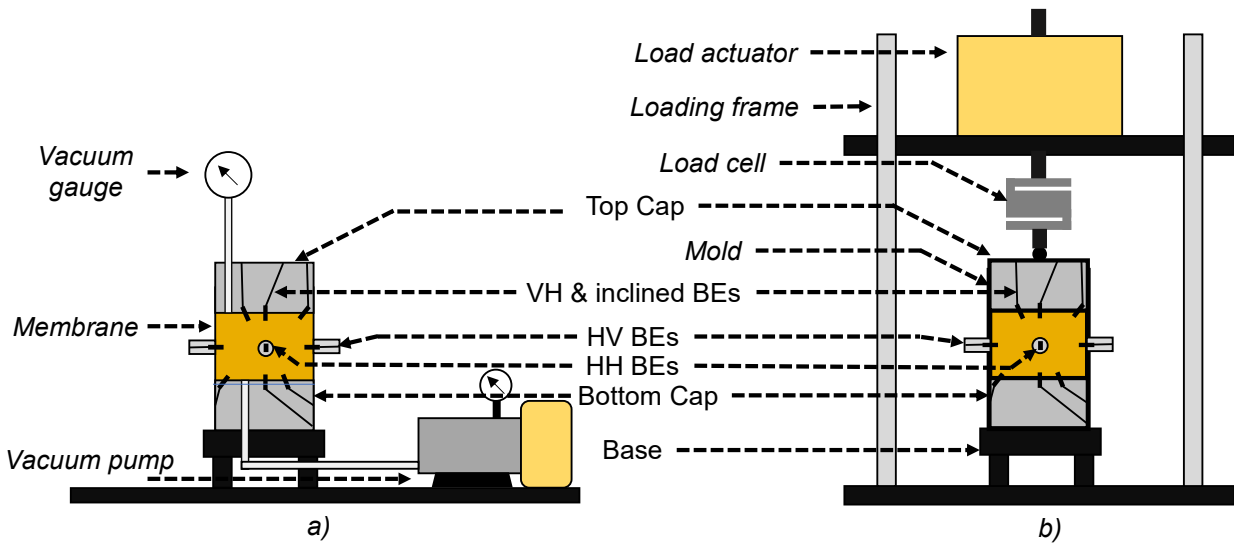


Figure 2.3: Schematics of devices for (a) isotropic and (b) 1D compression tests. The major differences in the setups are italicized.

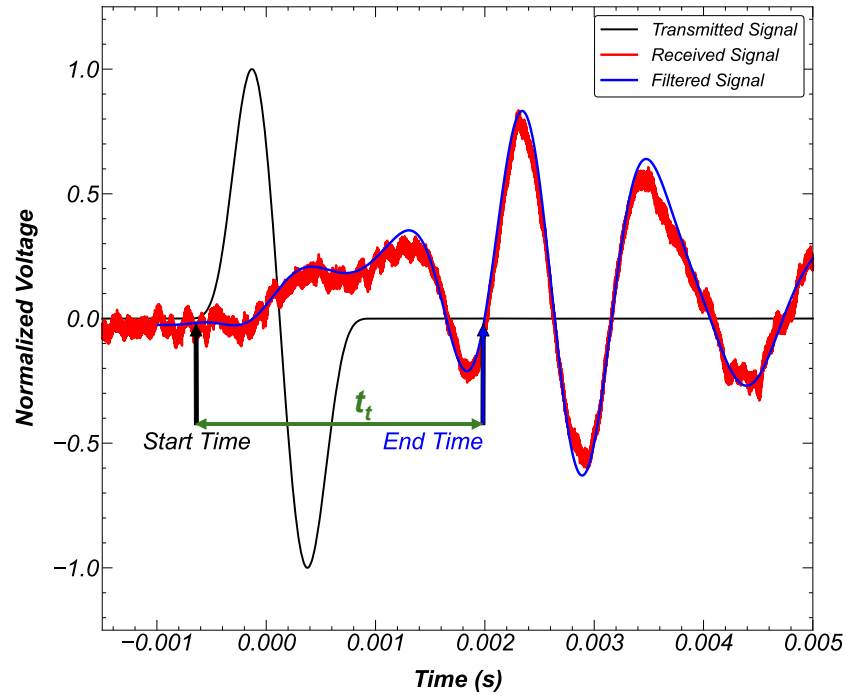


Figure 2.5: Typical transmitted, unfiltered received and filtered received signal, with the arrival time obtained between the start time and the end time.

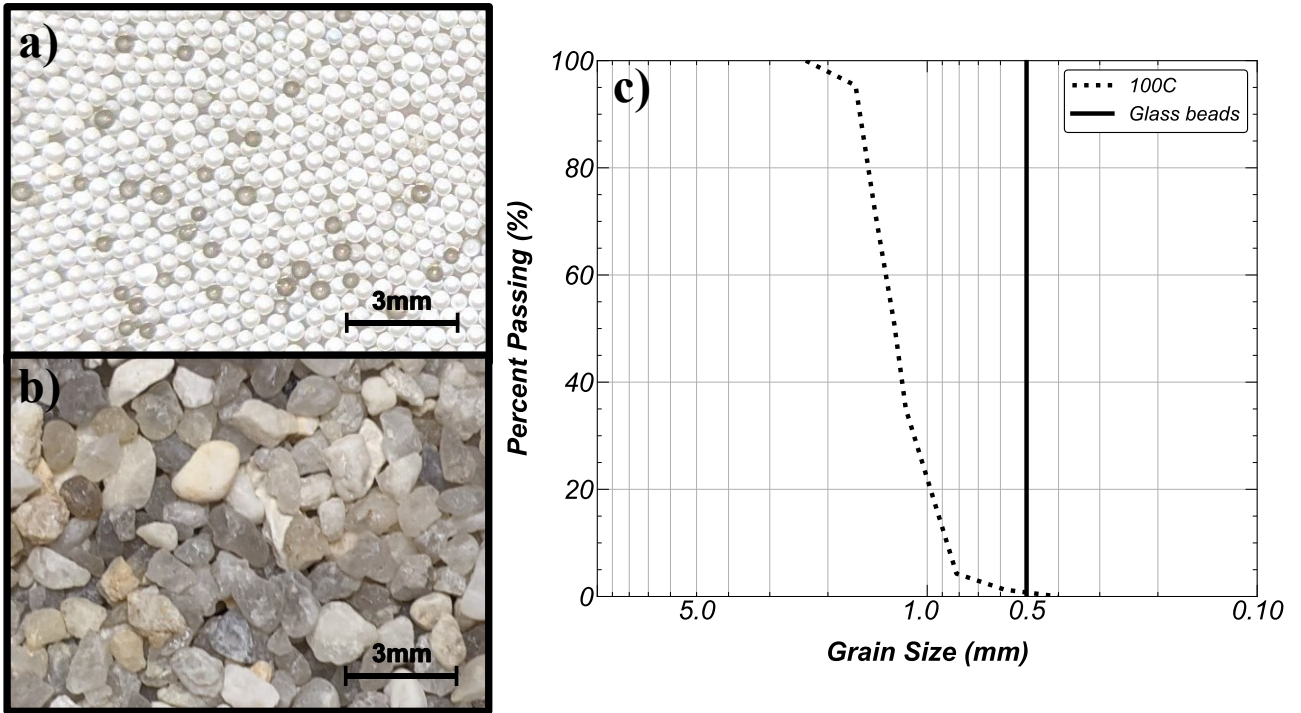


Figure 2.6: Photographs of (a) glass beads, (b) 100C sand, and (c) grain size distributions for both materials.

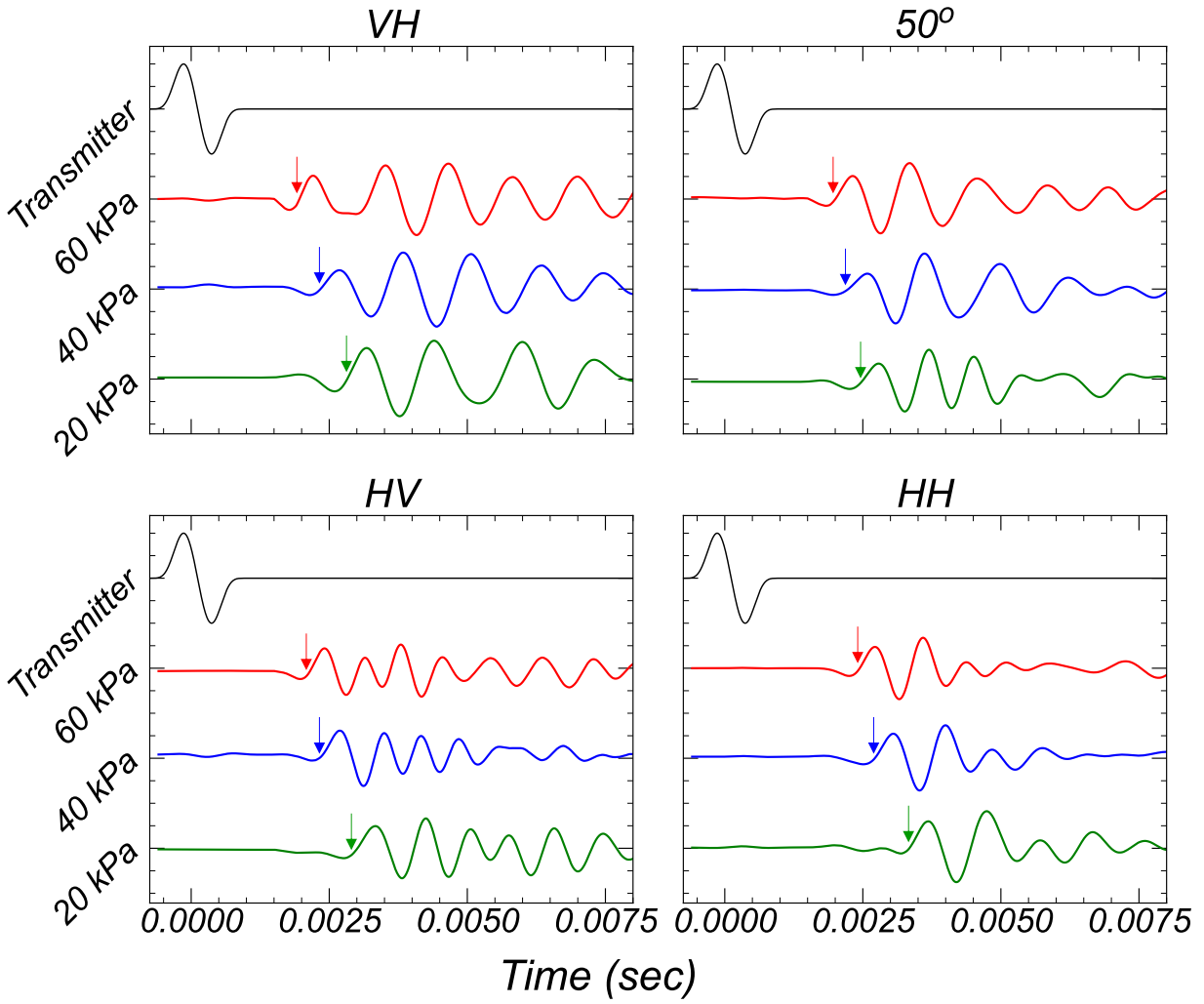


Figure 2.7: Received BE signals for glass beads under isotropic compression at three different vertical stresses. The arrows indicate the first arrival of the received signal.

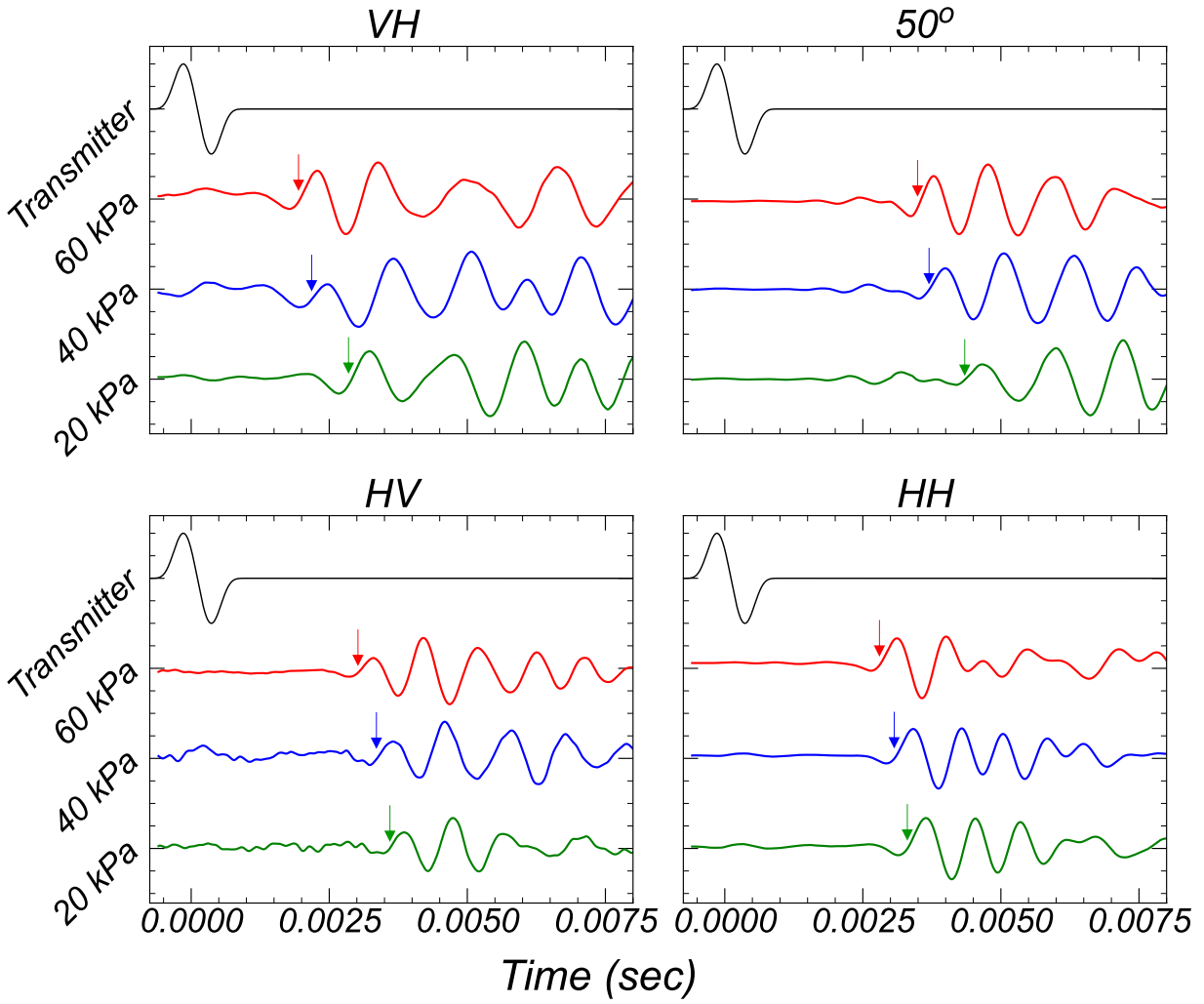


Figure 2.8: Received BE signals for 100C under isotropic compression at three different vertical stresses. The arrows indicate the first arrival of the received signal.

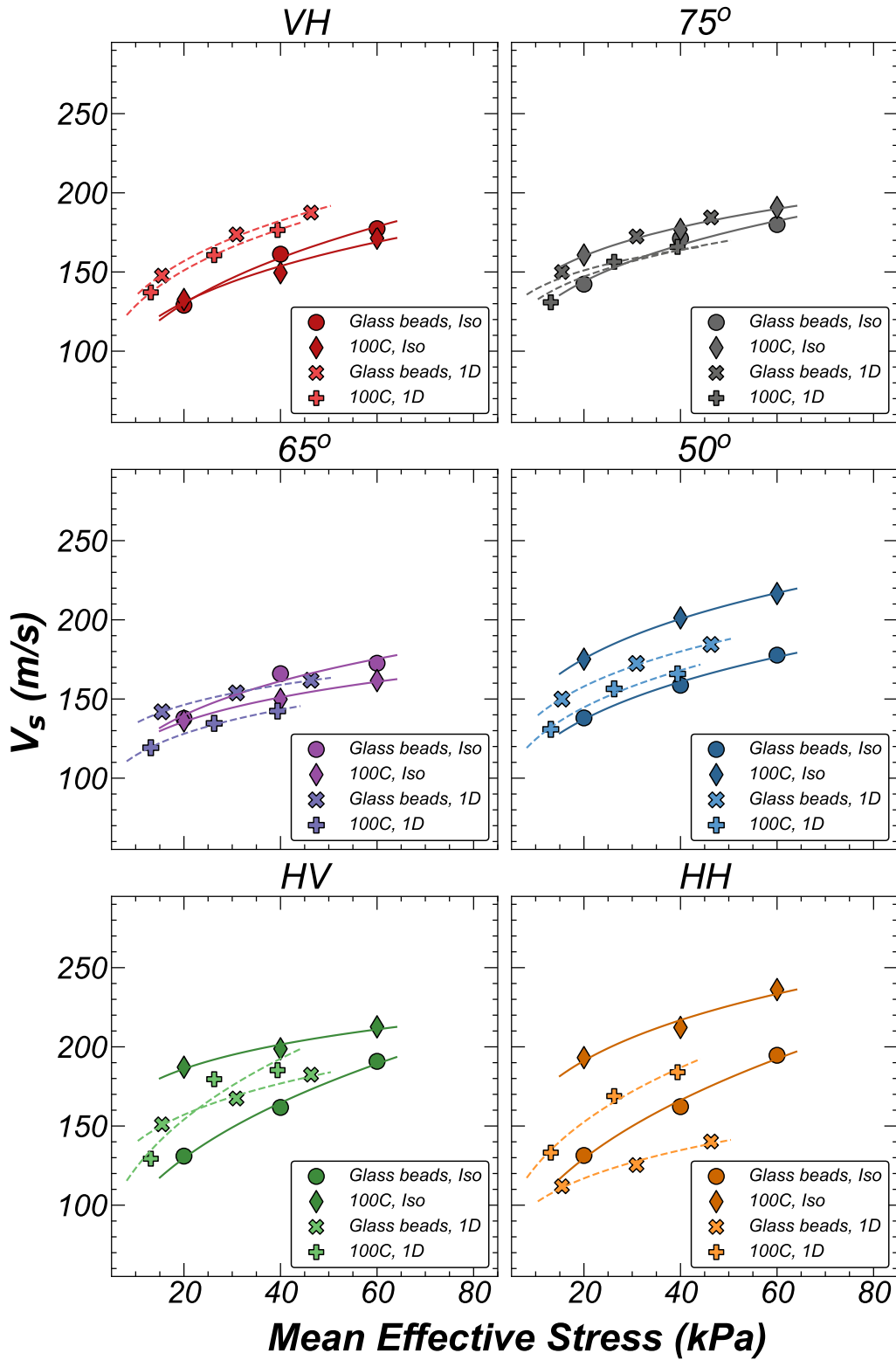


Figure 2.9: Increase in V_s with increase in mean effective stress for glass beads and 100C sand under isotropic and 1D compression.

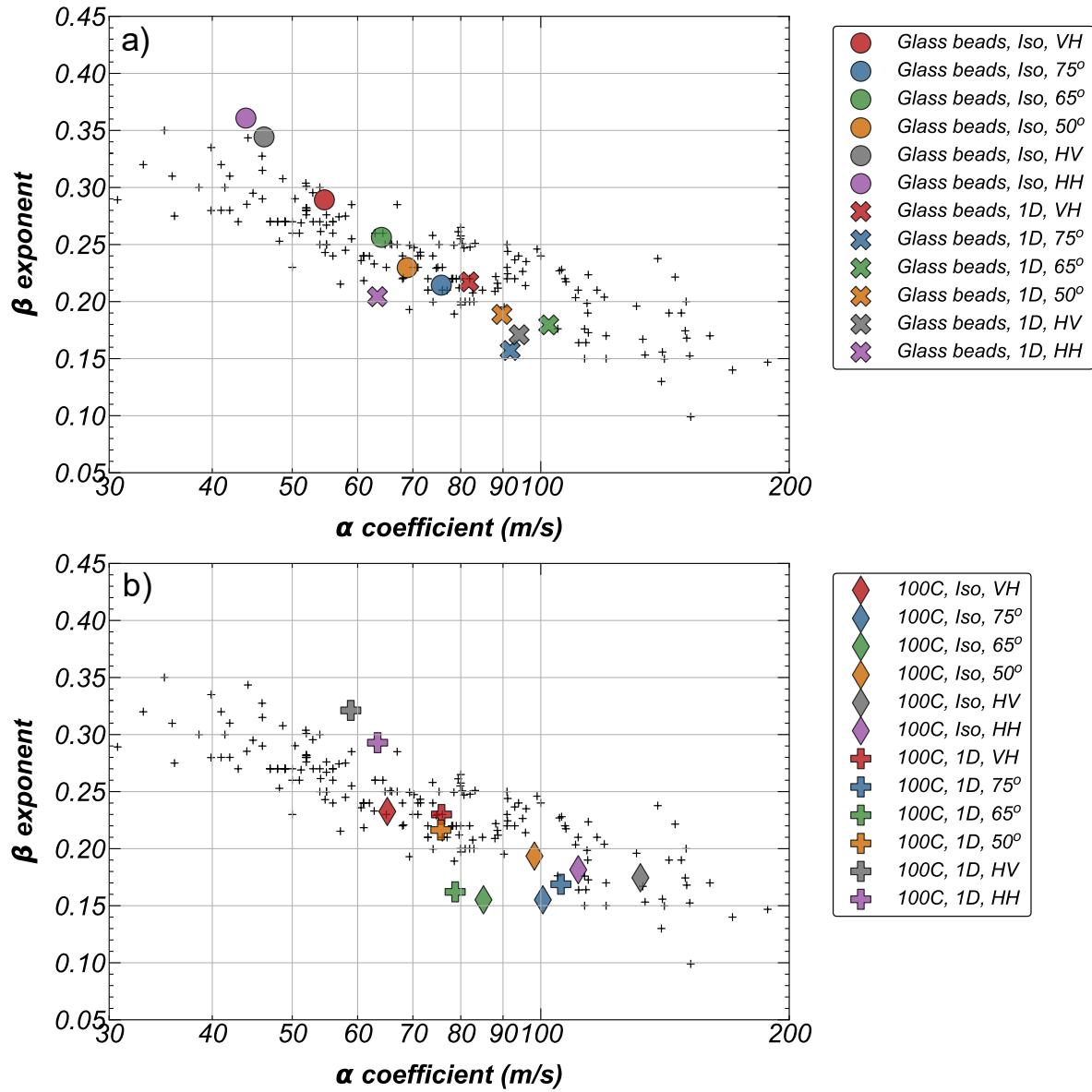


Figure 2.10: β exponent versus α coefficient for (a) glass beads and (b) 100C sand for different BE orientations. The small crosses represent the datapoints presented in Cha et al. (2014).

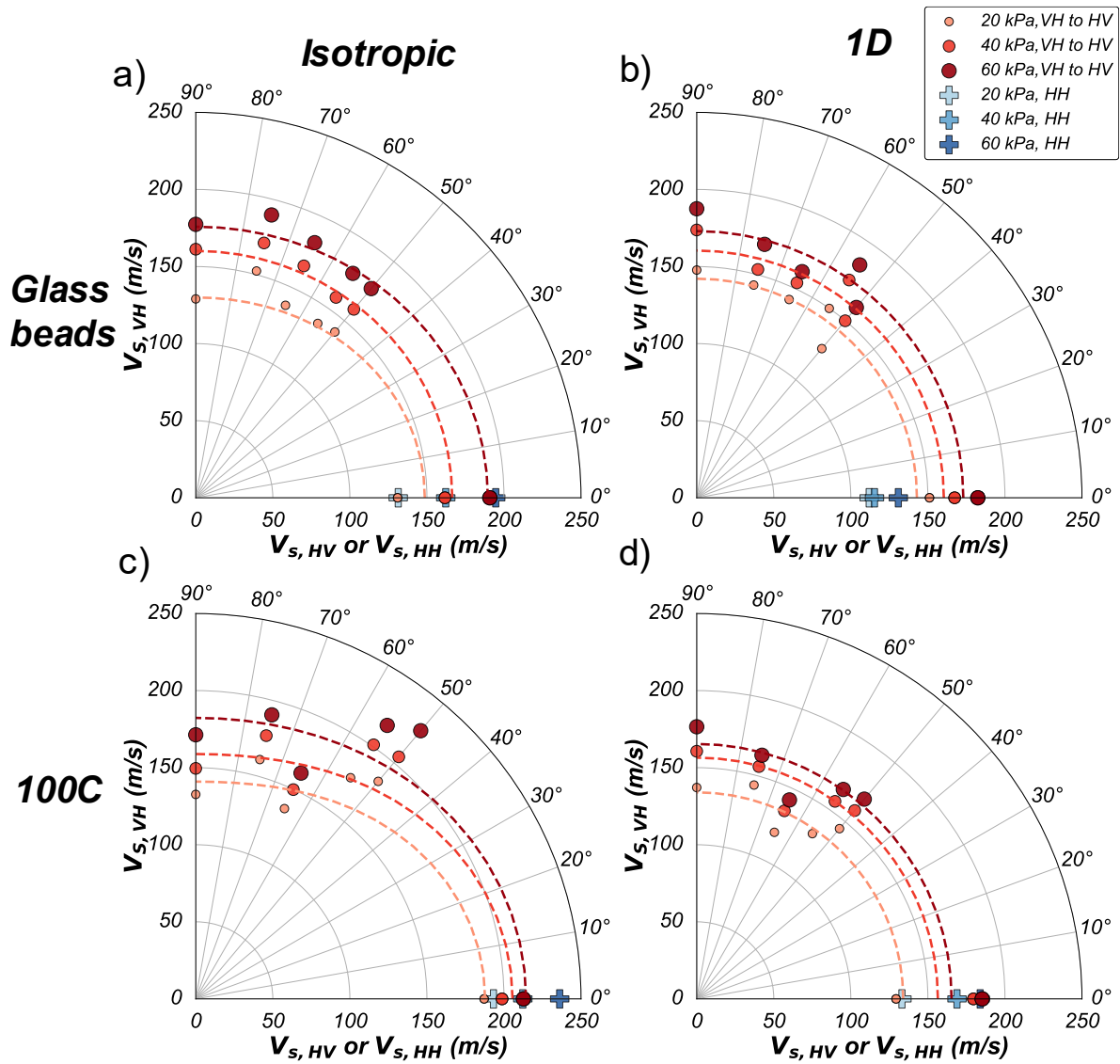


Figure 2.11: Polar plots of V_s for glass beads and 100C sand subjected to varying levels of confining stress.

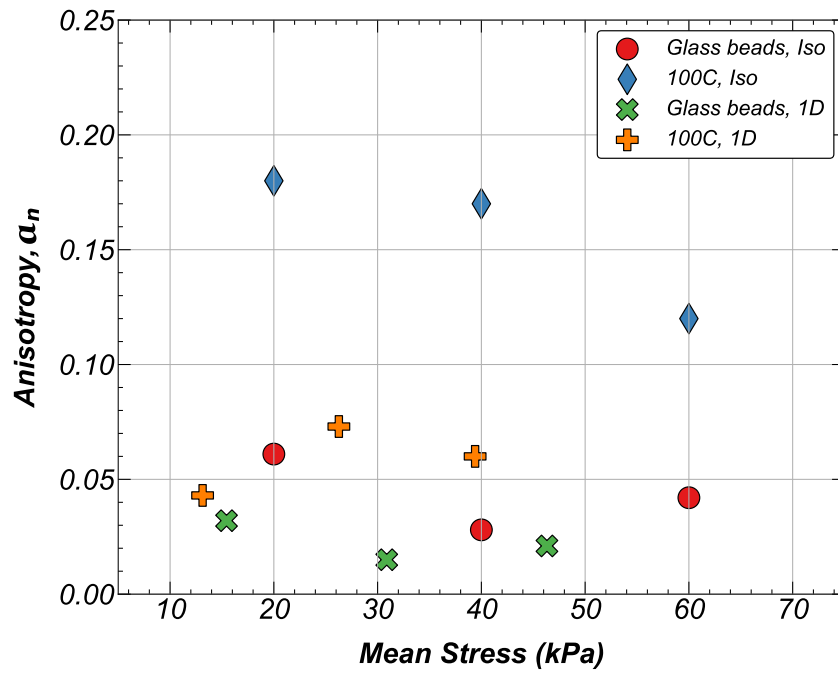


Figure 2.12: Evolution of the a_n parameter with mean effective stress for the angular distribution of V_S ($V_{S,vH}$ to $V_{S,hV}$).

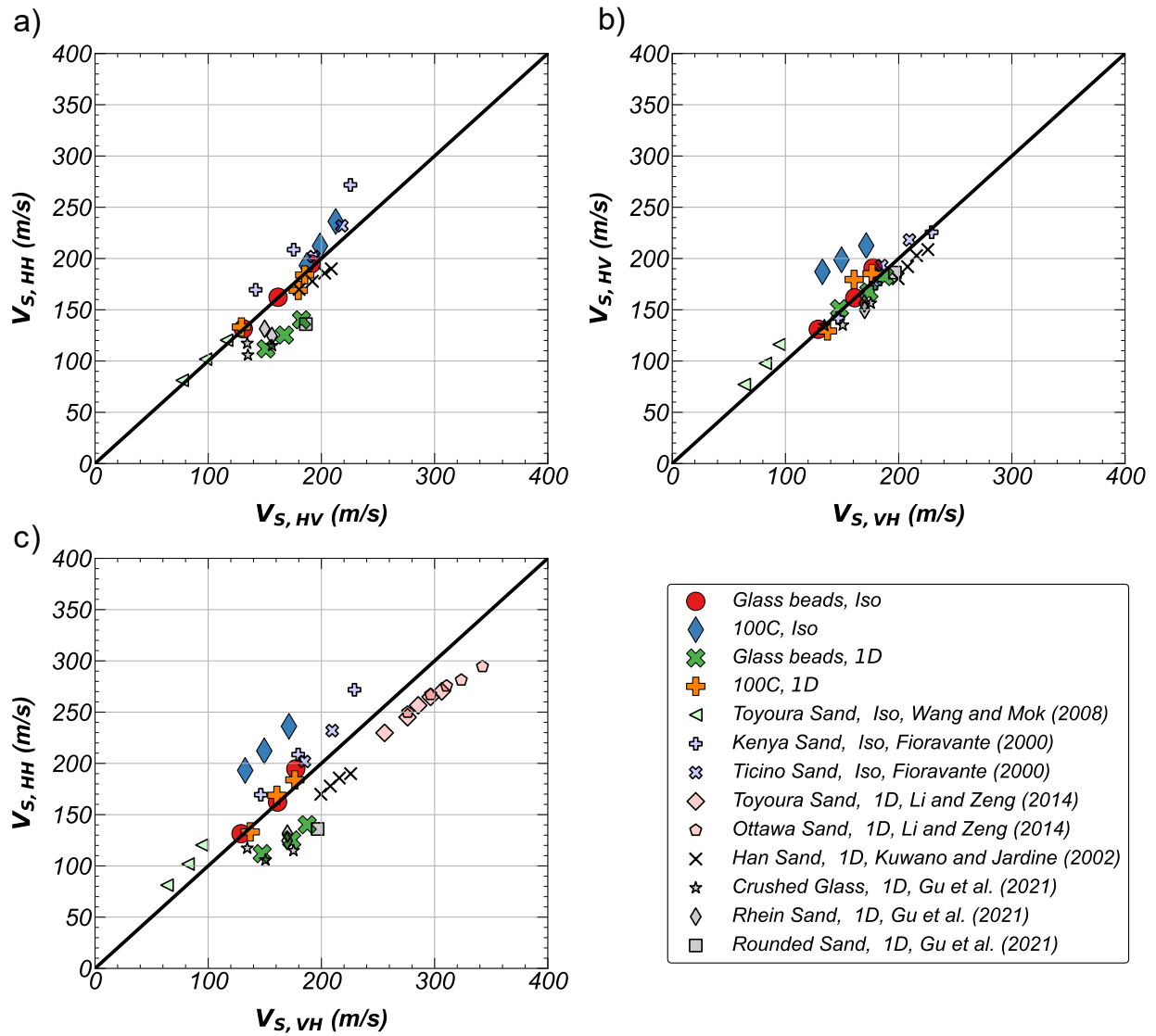


Figure 2.13: Comparison of $V_{S,VH}$, $V_{S,HV}$, and $V_{S,HH}$ measurements with values from various experimental studies: (a) $V_{S,HH}$ versus $V_{S,HV}$, (b) $V_{S,HV}$ versus $V_{S,VH}$, and (c) $V_{S,HH}$ versus $V_{S,VH}$.

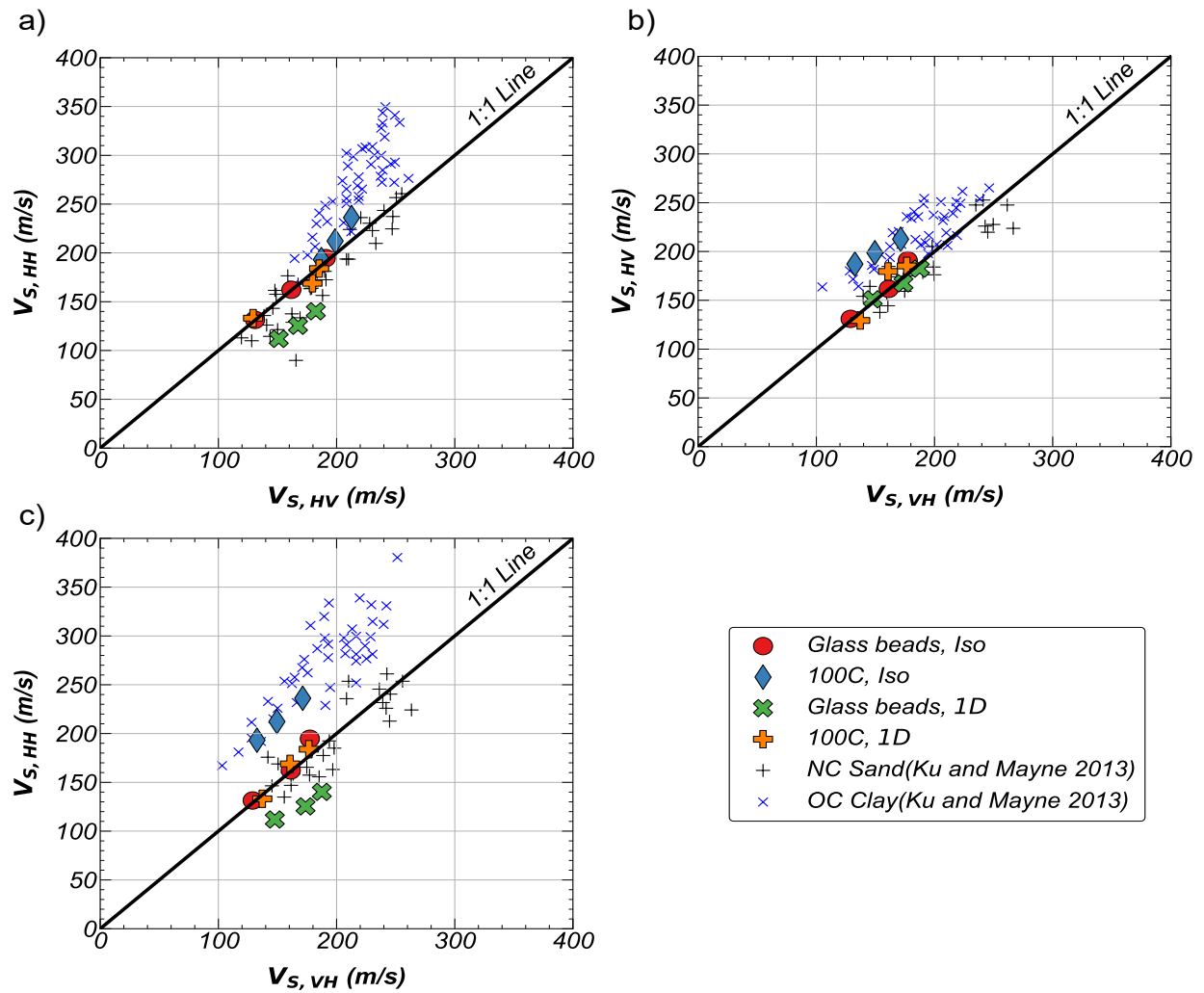


Figure 2.14: Comparison of $V_{S,VH}$, $V_{S,HV}$, and $V_{S,HH}$ measurements with values from field tests reported by Ku and Mayne (2013): (a) $V_{S,HH}$ versus $V_{S,HV}$, (b) $V_{S,HV}$ versus $V_{S,VH}$, and (c) $V_{S,HH}$ versus $V_{S,VH}$.

Chapter 3

Numerical and experimental estimation of anisotropy in granular soils using multi-orientation shear wave velocity measurements

Author's note: This paper was published in Springer Granular Matter under the following citation and is presented herein with minor edits.

Basson, M.S., and A. Martinez. 2023. "Numerical and experimental estimation of anisotropy in granular soils using multi-orientation shear wave velocity measurements." Granular Matter 25, 55. <https://doi.org/10.1007/s10035-023-01345-8>

3.1 Abstract

Soils can have direction-dependent characteristics reflected by the anisotropy of their responses. Studies have demonstrated the impact of the stress state and history (i.e., stress-induced anisotropy), and the depositional processes and associated particle arrangements (i.e., fabric-induced anisotropy) on the anisotropy of macroscopic behaviors. However, quantifying the stress- and fabric-induced anisotropy remains a challenge. This study presents two investigations on the effects of stress- and fabric-induced anisotropy on the anisotropy of shear wave velocity (V_s). A framework based on the V_s measurements along various orientations and polarization planes obtained from discrete element method (DEM) simulations and experimental bender element (BE) tests is presented; this framework is

tested using the results from specimens of spherical and non-spherical particles under isotropic and 1D compression. The observed trends indicate that the angular distributions of V_s are related to the angular distributions of particle alignment and interparticle contact forces. This framework, when presented in terms of the ratio of V_s measurements along different orientations and polarization planes and of the newly introduced Anisotropy parameter (A_e), can assist in evaluating the stress- and fabric-induced anisotropy of soil specimens. The results also highlight the challenges in discerning the effects of stress and fabric anisotropy when both influence the soil response.

3.2 Introduction

The mechanical properties of coarse-grained granular soils are dependent on a wide range of parameters, including but not limited to particle shape, particle size distribution, mineralogy, fabric, stress state, and stress history (e.g., Arthur and Menzies 1972; Yamamuro and Wood 2004; Yang et al. 2008). These factors produce an anisotropy that is generally categorized as stress- or fabric-induced anisotropy. The stress-induced anisotropy is primarily produced by the state of stress and stress history (Roesler 1979; Oda et al. 1985; Kuhn et al. 2015), while the fabric-induced anisotropy results from the spatial arrangement of the particles, particle contacts, and pore spaces (e.g., Oda 1972a; Bathurst and Rothenburg 1990; Yimsiri and Soga 2010). Understanding the interplay between micro-scale stress- and fabric-induced anisotropies and macro-scale behavior of soils, such as strength, stiffness, dilatancy, and permeability, is critical for geotechnical analysis and design. Nonetheless, quantifying stress- and fabric-induced anisotropy *in-situ* or in a specimen in the laboratory has remained a challenge.

Several studies have quantified the effect of stress-induced anisotropy on the macro-scale behaviors using laboratory tests through anisotropically-consolidated triaxial compression, hollow cylinder, and oedometer tests (e.g., Hardin and Drnevich 1972; Roesler 1979; Pennington et al. 1997; Goudarzy et al. 2018) and numerical methods using discrete element method (e.g., Otsubo et al. 2017; Otsubo and O’Sullivan 2018; Mital et al. 2020). In contrast, quantifying fabric-induced anisotropy and its impact on the macro-scale soil behavior continues to be an experimental challenge. Past research has developed destructive and non-destructive procedures to quantify fabric-induced anisotropy in different loading conditions. For the destructive procedures, the specimen is cut into thin sections to obtain images at discrete locations; this method has enabled quantification of the distributions of contact normal and particle long-axis orientation (e.g., Oda 1972a; Yang et al. 2008; Kodicherla et al. 2018). One challenge is that the images can only be obtained at the end of the experiment, resulting in limited information regarding the evolution of fabric during shearing. Recent advancements in image processing and X-ray CT techniques have enabled researchers to non-destructively quantify fabric anisotropy using high-quality 3D full-field scans of the specimen (e.g., Viggiani et al. 2014; Wiebicke et al. 2017, 2020). These procedures can reliably measure the kinematics at the grain scale, such as particle displacements, strains, and rotations, throughout the loading. However, X-ray CT tomography requires specialized equipment and is typically limited to small specimens.

Non-destructive testing can also be accomplished by measuring soil responses in various orientations to indirectly measure the stress- and fabric-induced anisotropy. These techniques employ measurements of anisotropy in the thermal conductivity (Choo et al. 2013), electrical conductivity (Anandarajah and Kuganenthira 1995) or shear wave velocity

(V_s) (e.g., Chaney et al. 2001a; Mitaritonna et al. 2010; Mital et al. 2020; Dutta et al. 2020; Otsubo et al. 2020) in specific orientations throughout the specimen. Shear wave propagation is a small-strain phenomenon that is considered to not cause plastic deformations, thus preserving the inherent soil fabric (Santamarina and Cascante 1996). Consequently, measuring the stiffness anisotropy through V_s measurements offers a non-destructive method of characterizing anisotropy in a soil specimen. Additionally, V_s is routinely measured in the field, laboratory, and numerical simulations, making it a strong candidate for linking the macro-, meso-, and micro-scale behavior of granular soils.

Several experimental studies have explored the applicability of using bidirectional V_s measurements, typically in the vertical and horizontal directions, to obtain information regarding stress- and fabric-induced anisotropies (e.g., Chaney et al. 2001b; Mitaritonna et al. 2010; Asadzadeh and Soroush 2018; Dutta et al. 2020; Kaviani-Hamedani et al. 2021). Experimental results show that the stress- and fabric-induced anisotropies influence the evolution and anisotropy of V_s during sample preparation, loading, and unloading. However, quantifying the magnitude of the anisotropy and characterizing its source (i.e., stress- versus fabric-induced anisotropy) remains a unique challenge. Recently, numerical DEM simulations have been used to fill knowledge gaps and supplement the experimental testing results (e.g., Wang and Mok 2008; O'Donovan et al. 2016; Gu and Yang 2018; Mital et al. 2020; Gu et al. 2020; Otsubo et al. 2020). In DEM simulations, the stress and fabric states of the specimen can be controlled and monitored and their effect on the V_s anisotropy can be studied along any arbitrary orientation.

This study presents the results of experimental and DEM investigations on the effects of stress- and fabric-induced anisotropy on the anisotropy of V_s . These results are used to develop a framework based on the ratio of V_s along different planes. Stress anisotropy is induced by subjecting specimens to isotropic and oedometric (1D) compression, while fabric anisotropy is induced by testing specimens of spherical or elongated particles. Isotropic and 1D compression conditions were selected in this study to represent two well-represented initial states of stresses that are common for in situ and in laboratory experiments (i.e., isotropically and anisotropically consolidated triaxial compression tests). The obtained V_s angular distributions are compared to the contact normal and long-axis orientations obtained from the DEM simulations to highlight the effect of soil fabric anisotropy. The numerical and experimental results are used to develop an initial framework that helps distinguish between the effects of stress- and fabric-induced anisotropy on the stiffness of the soil specimen.

3.3 DEM model and laboratory bender element (BE) setup

This section describes the notations used to define the different V_s waves, DEM simulation, experimental bender element testing setup, and the materials and sample preparation methodologies used in this study.

3.3.1 Notation

Directional variation in V_s and soil stiffness is typically obtained by transmitting waves in specific orientations of wave propagation and particle motion directions. Three independent V_s measurements, namely $V_{s,VH}$, $V_{s,HV}$, and $V_{s,HH}$, have been routinely used in experimental, numerical, and field studies (e.g., Fioravante et al. 1998; Ku and Mayne 2013; Dutta et al.

2020; Otsubo et al. 2020). In this notation, the first subscript refers to the direction of the wave propagation and the second subscript indicates the direction of particle motion within the specimen. Figure 3.1 illustrates this notation, where $V_{S,VH}$ is a vertically propagating wave with horizontal particle motion, $V_{S,HV}$ is a horizontally propagating wave with vertical particle motion, and $V_{S,HH}$ is a horizontally propagating wave with horizontal particle motion. Additional V_S measurements were taken at various orientations between the $V_{S,VH}$ to $V_{S,HV}$ and $V_{S,HV}$ to $V_{S,HH}$ to obtain angular distributions, as described below.

3.3.2 DEM model

Particle shape irregularities can impact the fabric anisotropy of a specimen: a specimen with spherical particles produces a nearly isotropic fabric, whereas elongated or angular particles can produce specimens with considerable fabric anisotropy. Shear wave propagation along different planes and orientations was simulated using the open-source 3D DEM code YADE (Šmilauer et al. 2010). Mono-sized spherical particles and rod-like clumped particles made of the three mono-sized spherical particles with a diameter of 3.15mm (Fig. 3.2 (a,b,e)) were used to create specimens with a contrast in the fabric anisotropy, where spherical particles produce specimens with negligible fabric anisotropy and rod-like clumps produce specimen with considerable fabric anisotropy. The shape characteristics of the particles were quantified using the Sphericity (S) and Aspect Ratio (AR) parameters, which quantify the closeness of the particle shape to a circle and the particle elongation, respectively. The two-dimensional projections of spherical and rod-like clump particles were used to characterize the particle shape based on the procedure described in (Zheng and Hryciw 2015). The spherical particles have an S and AR value both equal to 1.0, whereas the rod-like clumps have an S of 0.68 and an AR of 2.0. Cubical specimens of size 30 cm by 30 cm by 30 cm were

created using periodic boundary condition. The total number of simulated particles was 124,000 for mono-sized spherical particles and 52,000 for clumps. Periodic boundaries were adopted to prepare homogenous specimens and eliminate boundary effects during shear wave transmission. Absorbing boundary conditions were implemented on all the specimen sides to absorb the shear waves to avoid reflections that would cause interference with the V_S measurements. Figure 3.3(a) shows one such specimen made of clumped particles.

The complete simulation process consisted of three phases: (i) specimen generation with the desired fabric orientation, (ii) compression to the target state of stresses, and (iii) propagation of shear waves through the specimen. For specimens with negligible fabric anisotropy, non-contacting particles were generated during the first phase using a randomization algorithm and then compressed to the desired stress state. To produce specimens with fabric-induced anisotropy, an attempt was made to recreate the pluviation process, as it promotes the orientation of particle long axes in the horizontal direction (Yamamuro and Wood 2004; Suits et al. 2008). The pluviated specimens were generated by settling under gravity a layer of particles with a thickness of about three particle diameters from a height of two particle diameters. After equilibrium was attained, the particle positions were copied, rotated 45° clockwise, and duplicated a distance of two diameters above the settled particle layer before being settled under gravity. This process was repeated until the specimen was filled with pluviated particles.

The effect of stress-induced anisotropy is explored by regulating the state of stresses during the compression phase. Specimens under isotropic compression exhibit no stress anisotropy, while specimens under 1D compression show significant stress-induced

anisotropy due to differences in the effective stresses in the vertical and horizontal directions. The specimens were compressed to mean confining effective stresses (p') of 20, 40, and 60 kPa for both isotropic and 1D compression. During compression, gravity was switched off to eliminate the stress gradient along the vertical direction. For spheres and clumps, an average void ratio of 0.66 and 0.53 was achieved for the various p' values. Average K values of 0.56 and 0.31 were measured during 1D compression of spheres and clumps, respectively.

The particle contact interactions were modeled using the Hertz-Mindlin contact model, with a Young's modulus of 70 GPa, Poisson's ratio of 0.3, and particle density of 2,650 kg/m³ (Table 3.1). An interparticle friction coefficient of 0.1 and global viscous damping of 0.1 was used during the compression phase to produce dense specimens. The inertial number and unbalanced force ratio were kept below 10^{-4} and 10^{-3} , respectively, to achieve a quasi-steady state rate of deformation (Lopera Perez et al. 2016). The friction coefficient was increased to 0.5 during the shear wave propagation phase to ensure minimal tangential sliding at the contacts, as recommended by (Otsubo et al. 2017, 2020). After reaching the desired stress state in the compression phase, the specimens were cycled for 50,000 steps with a global viscous damping of 0.5 to dampen the particle motions (Ning et al. 2015; Gu et al. 2020). The global viscous damping was then reduced to 0.05 during the shear wave propagation phase to eliminate the effect of excessive contact damping.

Typically in DEM simulations, clumps of simulated particles are used to transmit and receive shear waves through a specimen (Ning et al. 2015; O'Donovan et al. 2016; Gu and Yang 2018; Gu et al. 2020). A sinusoidal excitation in the form of particle displacements was

applied to the transmitter clumps and tracked using the receiver clumps at multiple locations throughout the specimen. In this study, shear waves were generated by exciting a thin clump of particles at one end of the specimen. The width and thickness of the transmitter clump were eight times and two times the mean particle diameter, respectively. Due to the wider aspect ratio, the transmitter clump produces a wide spherical wavefront, reducing the P-wave interference observed in laboratory testing using sources such as bender elements (Arroyo et al. 2006). One such snapshot of the shear wave propagation at various times through a specimen of spherical particles is shown in Figs. 3.3(b,c,d,e) using particle velocities. The transmitted shear wave was received through ten cubical receiver clumps that were four times the mean particle diameter in size and evenly spaced at distances equivalent to seven times the mean particle diameter. The transmitter and receiver clumps were rotated along the y-axis to create pairs at inclined orientation for angular V_s measurements at angles of 90° , 65° , 40° , 15° , 0° , -15° , -40° , -65° , and -90° from the horizontal direction. Figure 3.4 presents the simulation setup with the transmitting and receiving clumps providing measurements for $V_{s,VH}$, $V_{s,40^\circ}$, and $V_{s,HV}$ waves.

The amplitude and frequency of the input shear wave signal affect the characteristics of the received signal. Sinusoidal waves of various amplitudes and frequencies were used to probe the specimens to obtain a set of parameters that produce a resonant response (Lee and Santamarina 2005; Gu et al. 2020). Figure 3.5(a) shows an example: a specimen made of spheres compressed to a mean confining stress of 20 kPa was probed with input shear waves of 1 kHz, 5 kHz, 10 kHz, and 20 kHz frequencies. A frequency of 5 kHz was selected for all the specimen as it produced a pronounced and clear received signal. The amplitude of the shear wave was 10^{-7} m for clumps to 10^{-5} m for spheres which produced shear wave with distinct

characteristics, limited contact sliding, and negligible stress fluctuations with an unbalanced force ratio smaller than 10^{-3} . These parameters are within the range reported in the literature (Ning et al. 2015; O'Donovan et al. 2016; Gu and Yang 2018).

The waterfall plot of received shear waves at receiver bins presented in Figure 3.5b demonstrates that the signals received at the bins located closer to the transmitter clump are clear, have minor P-wave interference, and did not require additional noise filtering. The received waves exhibit an initial downwards dip, followed by a consistent climb to the signal's peak value. The first reversal point, where the climbing signal first crosses the x-axis, was taken as the arrival time of the received shear waves (Lee and Santamarina 2005; Payan et al. 2016). The arrows in Figure 3.6(a) provide an example of the arrival times for sphere specimens under isotropic effective stresses of different p' magnitudes. The V_s was computed as a ratio of the closest edge-to-edge distance between the transmitting and receiver bins and the measured travel time. Further details about the arrival time and travel distance selection are presented by (2023).

3.3.3 Experimental testing setup

Multi-orientation shear wave velocity measurements were acquired experimentally using seven piezoelectric BE pairs in isotropically- and 1D- compressed specimens using the setup described by (Basson and Martinez 2023). Three of the BE pairs captured the $V_{S,VH}$, $V_{S,HV}$, and $V_{S,HH}$ measurements, and four additional BE pairs were inclined at orientations of 75° , 65° , 55° , and 50° to obtain a sweep from $V_{S,VH}$ (vertical at 90°) to $V_{S,HV}$ (horizontal at 0°). $V_{S,VH}$ and the 75° , 65° , 55° , and 50° BE pairs were mounted inside custom fabricated end caps fitted on a conventional triaxial testing setup with a diameter of 71 mm. The top and bottom end caps

were constructed of polycarbonate and slotted holes for the BEs and internal cables (Figs. 3.7(a,b,c,d)). A height of 40 mm was chosen to achieve a broader range of angles while remaining large enough for the specimens to be prepared by air pluviation. The horizontal BE pairs measuring the $V_{S,HV}$ and $V_{S,HH}$ were installed based on recommendations from past research (e.g., Fioravante et al. 1998; Chaney et al. 2001b; Pennington et al. 2001). They were glued into a reducing hex nipple using flexible silicone sealant. For isotropic compression, the nipple-glued BEs were sealed into a slit cut into the membrane, while for 1D compression the BEs were sealed into drilled holes in a rigid polycarbonate mold. The current testing setup can be modified to accommodate specimens for triaxial testing. In such case, proper waterproofing of BEs should be ensured with additional coats of epoxy resin for proper waterproofing (Montoya et al. 2012), and additional wiring harness and outlets would be required (Fioravante et al. 1998; Chaney et al. 2001a).

Glass beads and natural quartz sand were used to prepare specimens that highlight the effects of fabric anisotropy. Like in the numerical simulations, glass beads with a spherical particle shape were used to produce specimens with negligible fabric anisotropy, whereas a natural sand called 100C sand with an elongated particle shape was chosen to produce specimens with considerable fabric anisotropy. Microscopic images of the glass beads and 100C particles were used to obtain the particle shape characteristics. The glass beads had average roundness (R) of 0.99, S of 0.99, and AR of 1.00, and the 100C sand particles had an average R of 0.60, S of 0.77, and AR of 1.86. Figures 3.2(c,d) shows photographs of the glass beads and 100C sand, while Fig. 3.2(e) shows the corresponding grain size distributions. The mono-sized glass beads are made of borosilicate glass with an average diameter of 0.5 mm (\pm 0.02 mm), while the 100C sand was obtained from the Cape May Formation near

Mauricetown, New Jersey, is composed of sub-angular particles and has a mean particle diameter (D_{50}) of 1.31 mm, a coefficient of uniformity (C_u) of 1.54, and a coefficient of curvature (C_c) of 1.03, with maximum and minimum void ratios of 0.84 and 0.56 respectively (Sturm 2019).

The glass beads and 100C specimens were prepared by pluviating particles from a constant height until the specimen reached a height of 40 mm. The specimens used for isotropic compression tests were prepared using a custom 3D printed split mold, which held the membrane and BEs in place during pluviation. After preparation, a vacuum was used to isotropically compress the specimens to mean effective confining stresses of 20, 40, and 60 kPa. For 1D compression, a loading frame with a load cell was used to compress the specimens inside a rigid polycarbonate mold to effective vertical stresses (σ'_v) of 20, 40, and 60 kPa. The average void ratio achieved during pluviation was 0.54 for glass beads and 0.68 for 100C, corresponding to relative density (D_r) values of 71% and 64%, respectively. Schematics of the isotropic and 1D compression tests are presented in Figs. 3.7(e,f). The arrows in Fig. 3.6(b) provide an example of the arrival times from glass beads specimens under isotropic effective stresses of 20, 40, and 60 kPa. It is noted that the effect of the gravitational gradient is ignored in the interpretation of the laboratory results as is customary in soil mechanics testing practice. This assumption can translate to an error in the estimated effective stresses of 2.50%, 1.25%, and 0.83% for the specimens subjected to 20, 40, and 60 kPa, respectively.

3.4 Results

This section presents the results of two investigations: the first consists of DEM simulations on spheres and clumped particles and the second involves experiments on glass beads and natural sand. The results of both investigations are used to develop angular distributions of V_s and to determine ratios of V_s along different orientations and polarization planes for specimens with different stress and fabric anisotropies. Based on the DEM results, the angular distributions of V_s are compared with the distributions of contact normals, contact normal forces, and particle long-axis orientations. Then, the numerical and experimental results along with results of additional DEM simulations are synthesized in a framework that relates the anisotropies of stress state, fabric, and V_s .

3.4.1 DEM simulations: angular distributions of shear V_s and fabric metrics

The spatial orientations of the particles and their interactions with other particles are commonly assessed to quantify the fabric and stress state of a specimen (Oda 1972a; b; Wang et al. 2004; Yang et al. 2008). This is typically done by means of angular distributions of fabric metrics and contact forces (Bathurst and Rothenburg 1990). In this study, the angular distributions are represented as polar plots of (i) particle long axes, (ii) contact normals, and (iii) contact normal forces.

Analytical functions are typically fitted to the angular distributions to obtain anisotropy parameters (Rothenburg and Bathurst 1989; Mital et al. 2020; Basson et al. 2021). The general analytical functions for the contact normal ($E(\theta)$), contact normal force ($F(\theta)$), and particle long axis ($LA(\theta)$) distributions are defined as:

$$E(\theta) = E_{avg} (1 + a_{CN} \cos 2 (\theta - \theta_{CN})) \quad (3.1)$$

$$F(\theta) = f_{avg} (1 + a_{CNF} \cos 2 (\theta - \theta_{CNF})) \quad (3.2)$$

$$LA(\theta) = E_{long} (1 + a_{LA} \cos 2 (\theta - \theta_{LA})) \quad (3.3)$$

where a_{CN} , a_{CNF} , and a_{LA} are the anisotropy parameters and θ_{CN} , θ_{CNF} , and θ_{LA} are the preferred orientations of the angular distributions, respectively, θ is the orientation from the horizontal direction at which the respective quantities are binned, E_{avg} and E_{long} are $1/2\pi$ for contact normal and long-axis distributions, and the f_{avg} is the average contact force for the contact normal force distribution. A similar equation was proposed by (Basson and Martinez 2023) to quantify the anisotropy in V_s angular distribution, as follows:

$$V_s = V_{s,avg} (1 + a_{VS} \cos 2 (\theta - \theta_{VS})) \quad (3.4)$$

where a_{VS} is the magnitude of V_s anisotropy, θ_{VS} is the preferential orientation, θ is the orientation from the horizontal direction, and $V_{s,avg}$ is the average V_s for a given mean stress. The anisotropy parameter, a_{VS} , is reported as $a_{VS,VHtoHV}$ for the $V_{s,VH}$ to $V_{s,HV}$ sweep and $a_{VS,VHtoHH}$ for the $V_{s,VH}$ to $V_{s,HH}$ sweep. The parameters were obtained via least-squares fitting of the polar plots. More details about V_s fittings are presented in Basson et al. (2021).

The fabric- and stress-induced anisotropies control the shape of the fabric angular distributions and the magnitudes of the anisotropy. The angular distributions for the spheres and clumps specimens under isotropic and 1D compression are presented in Fig. 3.8 and Fig. 3.9, respectively, constructed by binning the contact normals, contact normal forces, and long-axis orientations along the x-z plane. The angular distributions of the isotropically-compressed spheres specimen are generally circular with anisotropy parameters with

magnitudes close to zero (Figs. 3.8(a,b), Table 3.2). A peanut-shaped contact normal force distribution with greater anisotropy is obtained for the 1D-compressed spheres specimen due to the difference between the vertical and horizontal stresses, while the distribution of contact normals is near-isotropic (Figs. 3.8(c,d), Table 3.2).

The angular distributions for the clumps specimen show a certain degree of crystallinity evidenced by the greater contact normal numbers and contact normal forces in the vertical and horizontal directions (Figs. 3.9(a,b)). The analytical function for the isotropically-compressed specimen shows a small degree of anisotropy for the contact normals, while the function fitted to the contact normal forces shows negligible anisotropy. In contrast, the long axes distribution shows a high degree of anisotropy, with most of the particles having their long axes aligned horizontally or near-horizontally (Fig 3.9(c)). The angular distributions for contact normals and particle long axes are similar for the 1D-compressed clumps specimen, while the contact normal force distribution shows a high anisotropy due to the greater vertical stress (Figs. 3.9(e,f)).

The V_s angular distributions were generated using measurements obtained at orientations between 90° to -90° from the horizontal direction, as shown in Figure 3.10. The $V_{s,VH}$ to $V_{s,HV}$ sweeps are presented with blue diamonds and the $V_{s,VH}$ to $V_{s,HH}$ sweeps are presented with red circles for effective stresses of 20, 40, and 60 kPa. The dashed lines represent the fitted distributions using Eq. 3.4, and the fitted anisotropy parameters are summarized in Table 3.2.

The isotropically-compressed spheres specimen (Figure 3.10a) reveals V_s magnitudes that are largely independent of their orientation and polarization plane, resulting in near-circular

V_S distributions. For example, at the mean confining stress of 40 kPa, the $V_{S,VH}$, shear wave obtained at 40° ($V_{S,40^\circ,VHtoHH}$), $V_{S,HV}$, and $V_{S,HH}$ for spheres are 313.3, 315.2, 316.2, and 315.2 m/s respectively. The radius of the circles increases with mean confining stress, as expected. The uniform V_S distributions are due to the negligible fabric- and stress-induced anisotropies shown in Figures. 3.8(a,b) and Table 3.2, resulting from the specimen generation procedure and the applied isotropic stresses applied.

The effective stress on a soil specimen influences the magnitude of contact forces and contact stiffness. This increase in contact stiffness is reflected in a concomitant increase in the V_S . A variety of relationships have been presented in past research relating the stress dependency of V_S to the effective stress using a power-law relationships, such as:

$$V_S = \alpha \left(\frac{\sigma'_{WP} + \sigma'_{PM}}{2} \right)^\beta = \alpha (\sigma'_m)^\beta \quad (3.5)$$

where σ'_m is the mean effective stress in the polarization plane, which is the arithmetic mean of the stress in the wave propagation (σ'_{WP}) and particle motion (σ'_{PM}) directions (Cha et al. 2014). The coefficient α is the V_S at a σ'_m of 1 kPa, which is dependent on a factors such as void ratio, fabric, and cementation. The exponent β reflects the dependency to changes in effective stress (Cho et al. 2006). Previous studies have proposed relationships comparing V_S to the stresses in wave propagation, particle motion, and out-of-plane directions, which have yielded different relationships (Roesler 1979; Zeng and Ni 1998; Goudarzy et al. 2018; Kaviani-Hamedani et al. 2021). In this study, a singular exponent β is used for the three stress components to reflect the overall effect of σ'_m on V_S and the effect of the out-of-plane direction is ignored, based on recommendations from (Cascante and Santamarina 1996; Sadek et al. 2007). The influence of σ'_m on the V_S measurements at different angular

orientations for the VH to HV and VH to HH sweeps are presented in the Fig. 3.16 and Fig. 3.17 of the supplementary data, respectively. As shown, the obtained V_s measurements show the typical power law increase with σ'_m for both isotropic and 1D compression and for both VH to HV and VH to HH sweeps. Figure 3.11 presents the values of α -coefficient and β -exponent obtained by fitting Equation 3.5 to the V_s measurements plotted in Figure 3.16 and Figure 3.17. The α -coefficient varies between 150 m/s and 266 m/s and the β -exponent varies between 0.085 and 0.187. No apparent correlation is observed between the values of the α -coefficient and β -exponent with the V_s orientation. The low values of β -exponent could be due to the high interparticle stiffness and a tighter packing as evidenced by crystallinity in the contact normal and contact normal force distributions. Nonetheless, the obtained values of α -coefficient and β -exponent are in the range reported for natural sands in literature, which indicates that Eq. 3.5 can be used to interpret the V_s measurements obtained from DEM simulations (Cha et al. 2014).

The σ'_m for the polarization planes for $V_{S,VH}$, $V_{S,HV}$, and $V_{S,HH}$ can be defined as:

$$\sigma'_{m,VH} = \frac{\sigma'_V + \sigma'_H}{2} = \frac{\sigma'_V + K\sigma'_V}{2} = \frac{\sigma'_V (1 + K)}{2} \quad (3.6)$$

$$\sigma'_{m,HV} = \frac{\sigma'_H + \sigma'_V}{2} = \frac{K\sigma'_V + \sigma'_V}{2} = \frac{\sigma'_V (1 + K)}{2} \quad (3.7)$$

$$\sigma'_{m,HH} = \frac{\sigma'_H + \sigma'_H}{2} = \frac{K\sigma'_V + K\sigma'_V}{2} = K\sigma'_V \quad (3.8)$$

where K is the lateral earth pressure coefficient and is equal to the ratio of horizontal to vertical effective stresses. As noted by Eqs. 3.6 and 3.7, the σ'_m for the $V_{S,VH}$ and $V_{S,HV}$ waves have the same magnitude; therefore, the stress-induced anisotropy should have the same

effect on $V_{S,VH}$ and $V_{S,HV}$. This is observed in the near-isotropic shape of the $V_{S,VH}$ to $V_{S,HV}$ sweep (Figure 3.10b). The K value for a specimen determines whether $\sigma'_{m,HH}$ is equal, lesser, or greater than $\sigma'_{m,VH}$ and $\sigma'_{m,HV}$, and consequently, according to equation 3.5, determines how the $V_{S,HH}$ compares to $V_{S,VH}$ and $V_{S,HV}$. The K values for both spheres (0.56) and clumps (0.31) are less than one, resulting in lower $V_{S,HH}$ compared to $V_{S,VH}$ and $V_{S,HV}$. Namely, for the spheres specimen under p' of 40 kPa, the $\sigma'_{m,VH}$, $\sigma'_{m,HV}$, and $\sigma'_{m,HH}$ were measured as 44.2, 44.2, and 32.5 kPa, respectively, while for the clumps specimen under p' of 40 kPa, the $\sigma'_{m,VH}$, $\sigma'_{m,HV}$, and $\sigma'_{m,HH}$ were measured as 48.2, 48.2, and 22.9 kPa, respectively.

The variations in $\sigma'_{m,VH}$, $\sigma'_{m,HV}$, and $\sigma'_{m,HH}$ for the 1D compression of spherical particles produces considerable stress anisotropy in the specimen. The lower magnitude of $\sigma'_{m,HH}$ as compared to $\sigma'_{m,VH}$ and $\sigma'_{m,HV}$ results in a gradual decrease from $V_{S,VH}$ to $V_{S,HH}$. For example, at a p' of 40 kPa, $V_{S,HH}$ is 10.2% and 6.6% lower than $V_{S,VH}$ and $V_{S,HV}$, respectively. The $V_{S,40^\circ,VHtoHH}$ has a magnitude of 288.6 m/s which is between $V_{S,VH}$ and $V_{S,HH}$, magnitudes of 305.5, and 277.9 m/s, respectively. The resulting V_S distribution is represented by a vertically oriented ellipse with an $a_{VS,VHtoHH}$ of 0.043 (Fig. 3.10(b)). These observations are validated by the vertically-aligned, peanut-shaped contact normal force distribution with a high a_{CNF} of 0.38 (Fig. 3.8(d)). In contrast, the $V_{S,VH}$ to $V_{S,HV}$ sweep exhibits negligible anisotropy ($a_{VS,VHtoHV} = 0.01$) due to the similar magnitudes of $\sigma'_{m,VH}$ and $\sigma'_{m,HV}$ (Fig. 3.10(b)).

The elongated particle shape and the pluviation process result in clump specimens with particles that tend to align their long axis in the horizontal direction (Figs. 3.9(c,f)), resulting in specimens with higher $V_{S,HH}$ and $V_{S,HV}$ than $V_{S,VH}$ for any given mean stress (Fig. 3.10(c)). For example, at a p' of 40 kPa, the values for $V_{S,HH}$, $V_{S,HV}$, $V_{S,40^\circ,VHtoHH}$, and $V_{S,VH}$ are 354.9, 348.8,

325.7, 291.7 m/s, respectively. An increase in both $V_{S,HH}$ and $V_{S,HV}$ compared to $V_{S,VH}$ reveals that the fabric anisotropy affects the specimen stiffnesses in both horizontal HV ($a_{V_{S,VH}toHV} = 0.058$), and HH ($a_{V_{S,VH}toHH} = 0.071$) planes. This indicates a greater stiffness on the horizontal propagation plane which appears to be relatively unaffected by the particle motion direction (i.e., $V_{S,HV}$ and $V_{S,HH}$ have similar magnitudes). Horizontally aligned elongated particles tend to form lesser number of contacts along the long axis, i.e., in the horizontal direction, than perpendicular to the long axis, i.e., in the vertical direction. For example, in an ideal cubic packing, elongated particles could form two contacts along the long axis (one to the left and one to the right) and six contacts perpendicular to the long axis (three on the top and three on the bottom). Under isotropic confining stresses, the lower number of horizontal contacts transmit higher contact forces (F_N) than the vertical contacts. As the shear stiffness of a Hertz-Mindlin contact is proportional to $(F_N)^{1/3}$, the contacts in the horizontal direction are stiffer than the vertical direction which is captured by the higher $V_{S,HH}$ and $V_{S,HV}$ than $V_{S,VH}$. Similar observations for contact stiffnesses in the horizontal and vertical direction related to the propagation of primary waves by elongated particles are presented in (Otsubo et al. 2020). Additionally, the presented results are in agreement with experimental and numerical results presented by (Yimsiri and Soga 2010; Zhao and Guo 2015; Liu et al. 2022), indicating that V_s is typically greater along the direction of preferential particle long axes.

The results of the clumps specimen under 1D compression show the complexity in soil response when both stress- and fabric-induced anisotropies are present. The angular V_s distribution for the clumps specimen under 1D compression shows minimal anisotropy with similar $V_{S,VH}$, $V_{S,40^\circ,VHtoHH}$, $V_{S,HV}$, and $V_{S,HH}$ magnitudes, with values of 325.9, 327.5, 329.4, and 325.2 m/s, respectively, at p' of 40 kPa. This is attributed to the competing effects between

the vertical preferential direction of the contact normal forces (Fig. 3.9(e)) and the horizontal preferential direction of the particle long axis orientations (Fig. 3.9(f)). In combination, the competing effect between the fabric and stress anisotropies results in a near-isotropic specimen stiffness, characterized by near circular V_s distributions and low $a_{VS,VHtoHV}$ and $a_{VS,VHtoHH}$ values of 0.017 and 0.020, respectively.

3.4.2 Experimental bender element testing: angular distributions of shear wave velocities

The experimentally measured V_s distributions exhibit the same trends described for the DEM simulations. Figure 3.12 presents the experimentally measured $V_{S,VH}$ to $V_{S,HV}$ sweeps for the glass beads and 100C sand specimens. The experimental setup only provides an angular sweep between $V_{S,VH}$ and $V_{S,HV}$, while no measurements are provided at intermediate angles between $V_{S,VH}$ and $V_{S,HH}$. Additionally, the testing setup is not enabled to measure the horizontal stresses. The obtained V_s measurements, presented in Figure 3.18 of the supplementary data, follow the typical power law (Eq. 3.5) with an increase in σ'_m . The experimental data shows smaller α -coefficients but larger β -exponents than the DEM data, likely due to the higher interparticle stiffness and crystallinity in the contact normal and contact normal force distributions (Fig. 3.9) in the simulations. For the experiments, the α -coefficient varies between 37 m/s and 142 m/s and the β -exponent varies between 0.145 and 0.368 (Fig. 3.11). Similar to the DEM simulations, no specific trends are observed between V_s orientation and the α -coefficient and β -exponent. The results for isotropic stress state (Figs. 3.12(a,c)) are plotted for respective p' values and the results for 1D compression (Figs. 3.12(b,d)) are plotted for respective vertical effective stresses (σ'_v). The plots for the isotropically compressed glass beads specimens are near-circular for any p' magnitude (Fig.

3.12(a)), with similar $V_{S,HV}$ and $V_{S,HH}$ magnitudes. The 1D-compressed glass beads specimen also shows near-circular $V_{S,VH}$ and $V_{S,HV}$ distributions due to the constant σ'_m between the corresponding planes, as previously described for the DEM simulations (Fig. 3.12(b)). However, the results show smaller $V_{S,HH}$ magnitudes due to the smaller σ'_m on this plane. Namely, the $V_{S,VH}$ and $V_{S,HV}$ for the specimens under a σ'_v of 40 kPa are 173.7 m/s and 167.2 m/s, respectively, while $V_{S,HH}$ is 125.4 m/s. For the applied σ'_v of 40 kPa, $\sigma'_{m,VH}$, $\sigma'_{m,HV}$ and $\sigma'_{m,HH}$ are 33.2, 33.2 and 26.4 kPa, respectively, using Eqs. 3.5, 3.6, 3.7 and a K value of 0.66. The K value was computed using Jaky's equation, i.e, $K = 1 - \sin(\phi')$, where the effective friction angle (ϕ') was taken as 20° . The magnitude of $V_{S,VH}$ is similar to $V_{S,HV}$ due to similar $\sigma'_{m,VH}$ and $\sigma'_{m,HV}$ stresses, whereas the lower $\sigma'_{m,HH}$ stress produces lower $V_{S,HH}$ magnitudes demonstrating the effect of stress-induced anisotropy on V_S magnitude.

The $V_{S,VH}$ and $V_{S,HV}$ distribution of the isotropically compressed 100C sand specimen is horizontally aligned, with $V_{S,HH}$ of 212.22 m/s, followed by $V_{S,HV}$ of 198.76 m/s and $V_{S,VH}$ of 149.53 m/s (Fig. 3.12(c)) at p' of 40 kPa. The trend is comparable to that shown by the isotropically compressed clumps in DEM (i.e., Fig. 3.10I) and likely indicates a preferential horizontal orientation of the sand particle long axes. As noted earlier, preparing specimens through pluviation under gravity increases the tendency of particles to align their long axis in the horizontal direction. This observation is supported experimentally by analyzing fabric produced in a specimen prepared using pluviation of sub-angular particles using X-ray tomography (Sun et al. 2019; Shi et al. 2021). In such specimens, the stiffer horizontal contacts increase the magnitude of $V_{S,HH}$ and $V_{S,HV}$ as compared to $V_{S,VH}$. The distributions of the 1D-compressed 100C sand specimens are close to circular (Fig. 3.12(d)), also in agreement with the DEM results (i.e., Fig. 3.10(d)), likely indicating a preferential vertical

alignment of the contact normal forces and a preferential horizontal alignment of the particle long axes, which in combination result in a net decrease in the V_S anisotropy in the specimen.

3.5 Interpretation framework

3.5.1 $V_{S,HV}/V_{S,HH}$ and $V_{S,HV}/V_{S,VH}$ ratios

The numerical and experimental investigations presented in the preceding sections show how the V_S varies due to anisotropy in fabric and stress state. This section presents a framework that uses ratios of V_S magnitudes to elucidate the effects of fabric- and stress-induced anisotropies; namely, the $V_{S,HV}/V_{S,HH}$ and $V_{S,HV}/V_{S,VH}$ ratios are used here. Figure 3.13 illustrates the reasoning for selecting these ratios. The $V_{S,HV}/V_{S,VH}$ ratio is used to identify the presence of fabric anisotropy because it is unaffected by the stress anisotropy, as shown by Eqs. 3.6 and 3.7 and the results in Figs. 3.10(b) and 3.12(b). The V_S has been shown to be greater along the orientation of preferential particle long axes (Yimsiri and Soga 2010; Zhao and Guo 2015; Sun et al. 2019; Shi et al. 2021; Liu et al. 2022). Therefore, for specimens with long axes oriented horizontally, $V_{S,HV}/V_{S,VH}$ would be greater than one, as is expected for pluviated specimens. In contrast, $V_{S,HV}/V_{S,VH}$ would be smaller than one if the particles have their long axes oriented vertically.

The $V_{S,HV}/V_{S,HH}$ ratio is used to identify the presence of stress anisotropy because the σ'_m magnitude along these two planes differs for cases where K is different than one (Eqs. 3.7 and 3.8). For example, normally consolidated specimens that typically have K values smaller than one (Fig. 13(b)) are expected to have a $V_{S,HV}/V_{S,HH}$ ratio greater than one, while the opposite is true for specimens with a K greater than one.

Figure 3.14 presents the ratios obtained from the numerical and experimental investigations in red and blue, respectively. Only results for a p' (DEM and experiments with isotropic compression) or σ'_v (experiments with 1D compression) of 40 kPa are presented for brevity; it is noted that the results at other stress levels show consistent trends. The results are presented in a $V_{S,HV}/V_{S,HH}$ versus $V_{S,HV}/V_{S,VH}$ space, where the y-axis highlights the fabric anisotropy while the x-axis shows the stress anisotropy. The origin of the plot is at the $V_{S,HV}/V_{S,HH}$ and $V_{S,HV}/V_{S,VH}$ of (1,1) and if the $V_{S,HV}/V_{S,HH}$ and $V_{S,HV}/V_{S,VH}$ ratios are less than one, the reciprocal value is plotted on the opposite quadrant as indicated in the corresponding axes labels. For example, if the $V_{S,HV}/V_{S,HH}$ and $V_{S,HV}/V_{S,VH}$ for a specimen are 0.8 and 0.9, the reciprocal values of 1.25 and 1.11 are plotted as $V_{S,HH}/V_{S,HV}$ and $V_{S,VH}/V_{S,HV}$ in the fourth quadrant.

The V_S ratios from the numerical and experimental measurements show consistent trends. The isotropically compressed spheres and glass beads exhibit $V_{S,HV}/V_{S,HH}$ and $V_{S,HV}/V_{S,VH}$ ratios close to one due to the isotropy in stress and fabric located near the center of the plot (circles). In 1D compression, the $V_{S,HV}/V_{S,HH}$ values for the spheres and glass beads increase to 1.06 and 1.34, respectively, with the datapoints located close to the positive x-axis (pentagons). The isotropically compressed clumps and 100C sand specimens yield $V_{S,HV}/V_{S,VH}$ ratios of 1.21 and 1.32, respectively, with the datapoints located near the positive y-axis (horizontal diamonds). In 1D compression, the clumps and 100C sand specimens (crosses) plot near the center of the plot due to the competing effects between the fabric- and stress-anisotropies.

Additional DEM simulations were performed to test the applicability of the proposed framework under a variety of additional fabric and stress states. The results of these additional simulations are plotted as the green data points in Fig. 3.14. These simulations include (i) spheres under 1D compression with K of 1.42 (pentagon), (ii) horizontally-aligned clumps under 1D compression with K of 2.55 (horizontal diamond), (iii) clumps rotated 90 degrees to create a specimen with vertically aligned particles (referred to as vertical clumps) and compressed isotropically (vertical diamonds), (iv) vertical clumps under 1D compression with K of 0.42 (star), and (v) vertical clumps under 1D compression with K of 2.38 (cross).

The response of the sphere specimen with a K of 1.42 plots close to the negative x-axis, showing considerable stress-anisotropy. Namely, $\sigma'_{m,HH}$ is greater than $\sigma'_{m,HV}$ and $\sigma'_{m,VH}$ for the specimen with greater K , resulting in a $V_{S,HH}/V_{S,HV}$ of 1.07. The V_S ratios plot in a location opposite to that of the spheres specimen with a K value of 0.67. For the 1D-compressed clumps with a K of 2.55, the stress anisotropy results in $V_{S,HH} > V_{S,HV}$ while fabric anisotropy results in $V_{S,HV} > V_{S,VH}$, characterized by a $V_{S,HH}/V_{S,HV}$ of 1.09 and a $V_{S,HV}/V_{S,VH}$ of 1.07, plotting on the second quadrant. When compressed isotropically, the vertical clumps specimen exhibits a greater $V_{S,VH}$ than $V_{S,HV}$ due to the preferential vertical alignment of the particles, resulting in a $V_{S,VH}/V_{S,HV}$ of 1.12, plotting near the negative y-axis. The 1D-compressed vertical clumps with a K of 0.42 (star) exhibit stress and fabric anisotropies resulting in $V_{S,VH} > V_{S,HV} > V_{S,HH}$, plotting the fourth quadrant with $V_{S,HV}/V_{S,HH}$ of 1.11 and $V_{S,VH}/V_{S,HV}$ of 1.14. Finally, the 1D-compressed vertical clumps with a K of 2.38 result in similar $V_{S,VH}$, $V_{S,HV}$, and $V_{S,HH}$ values because of the combined effects of stress and fabric anisotropies.

The results from several experimental studies on isotropically compressed Toyoura (angular), Hostun (sub-angular), and Ticino (sub-angular) sand, and 1D-compressed Ham (sub-rounded), Rhein (sub-angular), Rounded sand (sub-rounded) and Crushed glass (angular) are plotted in Figure 3.14. The comparison highlights the similarities between the published data and the data presented in this study. Particularly, the Toyoura, Hostun and Ticino sands under isotropic compression plot close to the y-axis, likely showing the effect of fabric resulting from their angular or sub-angular particle shape and the depositional process used to prepare the specimens. On the other hand, the Ham, Rhein, Rounded sands and Crushed Glass under 1D compression plot closer to the x-axis, showing the effect of stress anisotropy.

3.5.2 Shear wave anisotropy parameter, A_e

The shear wave anisotropy parameter, A_e , is defined to capture the overall anisotropy and is inspired by the electrical sensitivity parameter proposed by (Jang and Carlos Santamarina 2016). Numerically, A_e is the distance from the origin of a given datapoint in $V_{S,HV}/V_{S,HH}$ versus $V_{S,HV}/V_{S,VH}$ space, visually represented by the blue arrow in Fig. 3.14. The -1 terms are introduced because the origin in this space is defined with coordinates (1,1). A_e is defined as:

$$A_e = \sqrt{\left(\frac{V_{HV}}{V_{VH}} - 1\right)^2 + \left(\frac{V_{HV}}{V_{HH}} - 1\right)^2} \quad (3.12)$$

It is noted that if $V_{S,HV}/V_{S,HH}$ or $V_{S,HV}/V_{S,VH}$ are smaller than one, the reciprocal values (i.e., $V_{S,HH}/V_{S,HV}$ or $V_{S,VH}/V_{S,HV}$, respectively) are used.

As previously described, the $V_{S,HV}/V_{S,VH}$ ratio captures the fabric-induced anisotropy while the $V_{S,HV}/V_{S,HH}$ ratio captures the stress-induced anisotropy; this can be explored by

plotting the A_e parameter against the V_S ratios, as shown in Figs. 3.15(a,b). The results for all the specimens lie between a line with a slope of unity and origin at (1,0) due to the mathematical definition of A_e . In terms of $V_{S,HV}/V_{S,VH}$, the results from specimens with negligible stress and fabric anisotropy have a low A_e value (e.g., glass beads and spheres under isotropic compression, circle symbols) and lie closer to the origin (Fig. 3.15(a)). In contrast, the specimens with considerable fabric anisotropy but negligible stress anisotropy lie close to the line with a slope of unity because the $V_{S,HV}/V_{S,VH}$ is controlled by fabric anisotropy. Namely, the isotropically compressed 100C sand specimen has high A_e and $V_{S,HV}/V_{S,VH}$ values of 0.34 and 1.32, respectively, and the isotropically compressed clumps specimen also has high A_e and $V_{S,HV}/V_{S,VH}$ values of 0.22 and 1.21, respectively (horizontal diamonds). The results for both specimens lie close to the line with a slope of unity. Also, the results from isotropically compressed Toyoura, Hostun, and Ticino sands lie close to the line with a slope of unity, confirming the influence of fabric anisotropy. In contrast, the specimens with negligible fabric anisotropy but considerable stress anisotropy, such as the 1D-compressed glass beads (blue pentagon), plot closer to the positive y-axis with a high A_e value of 0.34 and a low $V_{S,HV}/V_{S,VH}$ ratio of 1.04. Similarly, the results from rounded sand under 1D compression also lie closer to the positive y-axis. Interestingly, the spheres with K of 1.42 (green pentagon) also lie closer to positive y-axis confirming the effect of stress anisotropy independent of the anisotropy direction.

The A_e values can be plotted against the $V_{S,HV}/V_{S,HH}$ ratios to provide another assessment of the anisotropies, as shown in Fig. 3.15(b). In this space, the results for all the specimens also lie between the line with a slope of unity and the positive y-axis. The results from specimens with stress-induced anisotropy but negligible fabric anisotropy (e.g., specimens

under 1D compression, pentagon symbols) are located closer to the 1:1 line and have large A_e and $V_{S,HV}/V_{S,HH}$ magnitudes because this V_S ratio is mainly influenced by the state of stresses. For example, the 1D-compressed glass beads specimen has a high A_e magnitude of 0.34 with a high $V_{S,HV}/V_{S,HH}$ ratio of 1.34. The 1D-compressed spheres specimens with K of 0.67 and 1.42 also plot near the line with a slope of unity. Similarly, the results from 1D compressed Ham, Rhein, Rounded sands, and Crushed Glass lie close to the line with a slope of unity, confirming the influence of stress anisotropy. In contrast, the specimens with negligible stress but considerable fabric anisotropy plot closer to the y-axis, as is the case for the isotropically-compressed 100C sand, clumps, and vertical clumps specimens (diamonds). Similarly, the results from isotropically-compressed Toyoura and Hostun sand lie close to the positive y-axis because of the dominant fabric anisotropy.

The preferential orientations of the stress- and fabric-induced anisotropy determine the existence of either supporting or competing effects. The data points for the specimen with a supporting mechanism are located between the slope line with a slope of unity and the y-axis. For instance, the clumps specimen under 1D compression with a K of 2.55 (green horizontal diamond) has an A_e of 0.12 and $V_{S,HV}/V_{S,VH}$ and $V_{S,HV}/V_{S,HH}$ of 1.07 and 1.09, respectively. Similarly, the vertically aligned clumps specimen under 1D compression with a K of 0.42 (green star) has an A_e of 0.17 and $V_{S,HV}/V_{S,VH}$ and $V_{S,HV}/V_{S,HH}$ of 1.13 and 1.1, respectively. In contrast, the specimens with competing effects have small A_e and shear wave velocity ratios. For example, the 1D-compressed clumps specimen (red cross) shows competing effects with an A_e of 0.02 and $V_{S,HV}/V_{S,VH}$ and $V_{S,HV}/V_{S,HH}$ of 1.01 and 1.01, respectively. Similarly, the 1D-compressed 100C sand specimen (blue cross) shows

competing effects with a low A_e of 0.08 and $V_{S,HV}/V_{S,VH}$ and $V_{S,HV}/V_{S,HH}$ of 1.07 and 1.02, respectively.

Overall, the framework presented here aids in identifying whether the anisotropy in stiffness originates from stress- or fabric-induced anisotropy when one type of anisotropy is negligible or when both anisotropies have supporting effects. However, the results highlight the difficulties in discerning the stress- and fabric-induced anisotropies when they have opposite effects using measured soil responses alone. This suggests that a full characterization of the specimen anisotropy requires some quantification of the fabric anisotropy by other methods, such as advanced imaging.

3.6 Conclusion

This paper describes the results of experiments and DEM simulations aimed at quantifying the anisotropy of shear wave velocity along different orientations and polarization planes in granular soil specimens. The results presented here highlight the influence of particle shape, depositional processes, and stress state on the V_s anisotropy using numerical simulations and standard laboratory testing equipment. The measured V_s polar distributions and anisotropies are then related to the corresponding distributions and anisotropies of stress and fabric. The experimental setup and DEM simulations allow obtaining $V_{S,VH}$, $V_{S,HV}$, and $V_{S,HH}$ measurements, as well as measurements at intermediate orientations. Specimens with different stress anisotropy (isotropic versus 1D compression) and fabric anisotropy (spheres versus elongated clumps in DEM, glass beads versus natural elongated sand in experiments) were tested to highlight the effect on the polar distributions of V_s and to

develop a framework for assessing the anisotropy of specimens. The main findings are summarized as follows:

- Angular distributions of V_s illustrate the stiffness anisotropy visually and fitting them with analytical equations (i.e., Eq. 3.4) provides quantitative metrics. The V_s polar distributions were found to be closely related to the contact normal force and particle long-axis orientation polar distributions.
- Specimens with negligible stress- (i.e., isotropic compression) and fabric-induced (spheres and glass beads) anisotropies have near-circular V_s polar distributions. Under 1D compression, these exhibit vertically elongated V_s polar distributions due to the greater vertical stresses and concomitant contact normal forces. Specimens of elongated clumps and angular natural sand show considerable fabric-induced anisotropy. Under isotropic compression, the V_s distribution for these specimens is horizontally elongated, which is controlled by the distribution of particle long-axis orientations.
- The preferential direction of the stress- and fabric-induced anisotropies determines the existence of a competing or supportive mechanism between them. When the anisotropies are in opposite directions (e.g., horizontally aligned elongated particles under 1D compression with $K < 1$), the V_s distribution is near-isotropic because their effect cancels out. When the anisotropies are in the same direction (e.g., vertically aligned elongated particles under 1D compression with $K < 1$), the net anisotropy in the specimen increases.
- Systematic comparison of $V_{s,HV}/V_{s,VH}$ and $V_{s,HV}/V_{s,HH}$ and the proposed shear wave anisotropy parameter, A_e , can help discerning the effects of stress- and fabric-induced

anisotropy on soil specimens. The specimen anisotropy can be visualized in $V_{S,HV}/V_{S,VH}$ versus $V_{S,HV}/V_{S,HH}$ space, or in A_e versus $V_{S,HV}/V_{S,VH}$ and $V_{S,HV}/V_{S,HH}$, which can help determine the source of anisotropy. However, challenges remain to decouple the effects of stress and fabric anisotropy when both simultaneously affect the response of a specimen.

The presented results from the DEM simulations and experimental testing suggest that the stress- and fabric-induced anisotropy in a specimen can be identified using the angular distribution of V_s and the ratios of $V_{S,HV}/V_{S,VH}$ and $V_{S,HV}/V_{S,HH}$. Future studies should focus on verifying the observations using direct measurements of fabric anisotropy (i.e., with x-ray CT) and on modifying the proposed DEM simulations and experimental methodologies to conduct isotropic and anisotropic triaxial compression tests to provide fundamental insights into the evolution of stress- and fabric-induced anisotropy during shearing.

3.7 Acknowledgements

The support of the University of California, Davis, College of Engineering is acknowledged. The authors would also like to acknowledge the support of Jasmine Miller in the initial developments of the multi-orientation BE system.

3.8 References

- Altuhafi, F. N., M. R. Coop, and V. N. Georgiannou. 2016. "Effect of particle shape on the mechanical behavior of natural sands." *Journal of Geotechnical and Geoenvironmental Engineering*, 142 (12): 04016071.
- Anandarajah, A., and N. Kuganenthira. 1995. "Some aspects of fabric anisotropy of soil." *Géotechnique*, 45 (1): 69–81.

- Arroyo, M., D. Muir Wood, P. D. Greening, L. Medina, and J. Rio. 2006. "Effects of sample size on bender-based axial g_0 measurements." *Géotechnique*, 56 (1): 39–52.
- Arthur, J. R. F., and B. K. Menzies. 1972. "Inherent anisotropy in a sand." *Géotechnique*, 22 (1): 115–128.
- Asadzadeh, M., and A. Soroush. 2018. "Evaluation of stress and strain non-uniformity during cyclic simple shear test using dem: effect of the horizontal platen asperities." *Granular Matter*, 20 (3): 43.
- Basson, M. S., and A. Martinez. 2023. "A multi-orientation system for determining angular distributions of shear wave velocity in soil specimens." *Geotechnical Testing Journal*, 46 (2): 20210277.
- Basson, M. S., J. Miller, and A. Martinez. 2021. "Experimental estimation of fabric in granular materials using shear wave velocity measurements." *Soil Dynamics, Lecture Notes in Civil Engineering*, T. G. Sitharam, S. V. Dinesh, and R. Jakka, eds., 311–323. Singapore: Springer Singapore.
- Bathurst, R. J., and L. Rothenburg. 1990. "Observations on stress-force-fabric relationships in idealized granular materials." *Mechanics of Materials*, 9 (1): 65–80.
- Cascante, G., and J. C. Santamarina. 1996. "Interparticle contact behavior and wave propagation." *Journal of Geotechnical Engineering*, 122 (10): 831–839.
- Cha, M., J. C. Santamarina, H.-S. Kim, and G.-C. Cho. 2014. "Small-strain stiffness, shear-wave velocity, and soil compressibility." *Journal of Geotechnical and Geoenvironmental Engineering*, 140 (10): 06014011.
- Chaney, R., K. Demars, V. Fioravante, and R. Capoferri. 2001a. "On the use of multi-directional piezoelectric transducers in triaxial testing." *Geotechnical Testing Journal*, 24 (3): 243.

- Chaney, R., K. Demars, D. Pennington, D. Nash, and M. Lings. 2001b. "Horizontally mounted bender elements for measuring anisotropic shear moduli in triaxial clay specimens." *Geotechnical Testing Journal*, 24 (2): 133.
- Cho, G.-C., J. Dodds, and J. C. Santamarina. 2006. "Particle shape effects on packing density, stiffness, and strength: natural and crushed sands." *Journal of Geotechnical and Geoenvironmental Engineering*, 132 (5): 591–602.
- Choo, J., Y. J. Kim, J. H. Lee, T. S. Yun, J. Lee, and Y. S. Kim. 2013. "Stress-induced evolution of anisotropic thermal conductivity of dry granular materials." *Acta Geotechnica*, 8 (1): 91–106.
- Dutta, T. T., M. Otsubo, R. Kuwano, and T. Sato. 2020. "Estimating multidirectional stiffness of soils using planar piezoelectric transducers in a large triaxial apparatus." *Soils and Foundations*, 60 (5): 1269–1286.
- Escribano, D. E., and D. F. T. Nash. 2015. "Changing anisotropy of g_0 in hostun sand during drained monotonic and cyclic loading." *Soils and Foundations*, 55 (5): 974–984.
- Fioravante, V. 2000. "Anisotropy of small strain stiffness of ticino and kenya sands from seismic wave propagation measured in triaxial testing." *Soils and Foundations*, 40 (4): 129–142.
- Fioravante, V., M. Jamiolkowski, D. C. F. L. Presti, G. Manfredini, and S. Pedroni. 1998. "Assessment of the coefficient of the earth pressure at rest from shear wave velocity measurements." *Géotechnique*, 48 (5): 657–666.
- Goudarzy, M., D. König, J. C. Santamarina, and T. Schanz. 2018. "The influence of the anisotropic stress state on the intermediate strain properties of granular material." *Géotechnique*, 68 (3): 221–232.

- Gu, Q., D. Sarkar, M. Goudarzi, and T. Wichtmann. 2021. "Combined effect of grain shape and grading on the small-strain stiffness of granular soils at different densities and stress states." *3. Bodenmechanik Tagung*, 9.
- Gu, X., X. Liang, Y. Shan, X. Huang, and A. Tessari. 2020. "Discrete element modeling of shear wave propagation using bender elements in confined granular materials of different grain sizes." *Computers and Geotechnics*, 125: 103672.
- Gu, X., and S. Yang. 2018. "Numerical investigation on wave propagation in anisotropic granular soils by discrete element method." *Proceedings of GeoShanghai 2018 International Conference: Fundamentals of Soil Behaviours*, A. Zhou, J. Tao, X. Gu, and L. Hu, eds., 882–892. Singapore: Springer Singapore.
- Hardin, B. O., and V. P. Drnevich. 1972. "Shear modulus and damping in soils: design equations and curves." *Journal of the Soil Mechanics and Foundations Division*, 98 (7): 667–692.
- Jang, J., and J. Carlos Santamarina. 2016. "Fines classification based on sensitivity to pore-fluid chemistry." *Journal of Geotechnical and Geoenvironmental Engineering*, 142 (4): 06015018.
- Kaviani-Hamedani, F., K. Fakharian, and A. Lashkari. 2021. "Bidirectional shear wave velocity measurements to track fabric anisotropy evolution of a crushed silica sand during shearing." *Journal of Geotechnical and Geoenvironmental Engineering*, 147 (10): 04021104.
- Kodicherla, S. P. K., G. Gong, L. Fan, C. K. S. Moy, and J. He. 2018. "Effects of preparation methods on inherent fabric anisotropy and packing density of reconstituted sand." *Cogent Engineering*, (V. Felipe, ed.), 5 (1): 1533363.

- Ku, T., and P. W. Mayne. 2013. "Evaluating the in situ lateral stress coefficient (k_0) of soils via paired shear wave velocity modes." *Journal of Geotechnical and Geoenvironmental Engineering*, 139 (5): 775–787.
- Kuhn, M. R., W. Sun, and Q. Wang. 2015. "Stress-induced anisotropy in granular materials: fabric, stiffness, and permeability." *Acta Geotechnica*, 10 (4): 399–419.
- Kuwano, R., and R. J. Jardine. 2002. "On the applicability of cross-anisotropic elasticity to granular materials at very small strains." *Géotechnique*, 52 (10): 727–749.
- Lee, J.-S., and J. C. Santamarina. 2005. "Bender elements: performance and signal interpretation." *Journal of Geotechnical and Geoenvironmental Engineering*, 131 (9): 1063–1070.
- Liu, J., M. Otsubo, Y. Kawaguchi, and R. Kuwano. 2022. "Anisotropy in small-strain shear modulus of granular materials: effects of particle properties and experimental conditions." *Soils and Foundations*, 62 (1): 101105.
- Lopera Perez, J. C., C. Y. Kwok, C. O'Sullivan, X. Huang, and K. J. Hanley. 2016. "Assessing the quasi-static conditions for shearing in granular media within the critical state soil mechanics framework." *Soils and Foundations*, 56 (1): 152–159.
- Mital, U., R. Kawamoto, and J. E. Andrade. 2020. "Effect of fabric on shear wave velocity in granular soils." *Acta Geotechnica*, 15 (5): 1189–1203.
- Mitaritonna, G., A. Amorosi, and F. Cotecchia. 2010. "Multidirectional bender element measurements in the triaxial cell: equipment set-up and signal interpretation." *Rivista Italiana Geotecnica*, (1): 50–70.

- Montoya, B. M., R. Gerhard, J. T. DeJong, D. W. Wilson, M. H. Weil, B. C. Martinez, and L. Pederson. 2012. "Fabrication, operation, and health monitoring of bender elements for aggressive environments." *Geotechnical Testing Journal*, 35 (5): 103300.
- Ning, Z., A. Khoubani, and T. M. Evans. 2015. "Shear wave propagation in granular assemblies." *Computers and Geotechnics*, 69: 615–626.
- Oda, M. 1972a. "Initial fabrics and their relations to mechanical properties of granular material." *Soils and Foundations*, 12 (1): 17–36.
- Oda, M. 1972b. "The mechanism of fabric changes during compressional deformation of sand." *Soils and Foundations*, 12 (2): 1–18.
- Oda, M., S. Nemat-Nasser, and J. Konishi. 1985. "Stress-induced anisotropy in granular masses."
- O'Donovan, J., E. Ibraim, C. O'Sullivan, S. Hamlin, D. Muir Wood, and G. Marketos. 2016. "Micromechanics of seismic wave propagation in granular materials." *Granular Matter*, 18 (3).
- Otsubo, M., J. Liu, Y. Kawaguchi, T. T. Dutta, and R. Kuwano. 2020. "Anisotropy of elastic wave velocity influenced by particle shape and fabric anisotropy under k condition." *Computers and Geotechnics*, 128: 103775.
- Otsubo, M., and C. O'Sullivan. 2018. "Experimental and dem assessment of the stress-dependency of surface roughness effects on shear modulus." *Soils and Foundations*, 58 (3): 602–614.
- Otsubo, M., C. O'Sullivan, K. J. Hanley, and W. W. Sim. 2017. "Influence of packing density and stress on the dynamic response of granular materials." *Granular Matter*, 19 (3).

- Payan, M., A. Khoshghalb, K. Senetakis, and N. Khalili. 2016. "Small-strain stiffness of sand subjected to stress anisotropy." *Soil Dynamics and Earthquake Engineering*, 88: 143–151.
- Pennington, D., M. Lings, and D. F. T. Nash. 2001. "Horizontally mounted bender elements for measuring anisotropic shear moduli in triaxial clay specimens." *Geotechnical Testing Journal*, 24 (2): 133.
- Pennington, D. S., D. F. T. Nash, and M. L. Lings. 1997. "Anisotropy of G_0 shear stiffness in gault clay." *Géotechnique*, 47 (3): 391–398.
- Roesler, S. K. 1979. "Anisotropic shear modulus due to stress anisotropy." *Journal of the Geotechnical Engineering Division*, 105 (7): 871–880.
- Rothenburg, L., and R. J. Bathurst. 1989. "Analytical study of induced anisotropy in idealized granular materials." *Géotechnique*, 39 (4): 601–614.
- Sadek, T., M. Lings, L. Diloru, and D. M. Wood. 2007. "Wave transmission in hostun sand: multiaxial experiments." *Rivista Italiana Geotecnica*, 41 (2): 69–84.
- Santamarina, J. C., and G. Cascante. 1996. "Stress anisotropy and wave propagation: a micromechanical view." *Canadian Geotechnical Journal*, 33 (5): 770–782.
- Santamarina, J. C., and G. C. Cho. 2004. "Soil behaviour: the role of particle shape." *Advances in geotechnical engineering: The skempton conference*, 604–617. Thomas Telford, London.
- Shi, J., W. Haegeman, A. Mascini, and V. Cnudde. 2021. "X-ray analysis on the effect of sample preparation on the microstructure of calcareous sands." *Marine Georesources & Geotechnology*, 39 (3): 302–311.

- Šmilauer, V., E. Catalano, B. Chareyre, S. Dorofeenko, J. Duriez, A. Gladky, J. Kozicki, C. Modenese, L. Scholtès, and L. Sibille. 2010. "Yade reference documentation." *Yade Documentation*, 474: 1–531.
- Sturm, A. 2019. "On the liquefaction potential of gravelly soils: characterization, triggering and performance." PhD Thesis. University of California Davis.
- Suits, L. D., T. C. Sheahan, D. Wanatowski, and J. Chu. 2008. "Effect of specimen preparation method on the stress-strain behavior of sand in plane-strain compression tests." *Geotechnical Testing Journal*, 31 (4): 101307.
- Sun, Q., J. Zheng, H. He, and Z. Li. 2019. "Characterizing fabric anisotropy of air-pluviated sands." *E3S Web of Conferences*, (A. Tarantino and E. Ibraim, eds.), 92: 01003.
- Viggiani, G., E. Andò, D. Takano, and J. C. Santamarina. 2014. "Laboratory x-ray tomography: a valuable experimental tool for revealing processes in soils." *Geotechnical Testing Journal*, 38 (1): 20140060.
- Wang, L. B., J. D. Frost, and J. S. Lai. 2004. "Three-dimensional digital representation of granular material microstructure from x-ray tomography imaging." *Journal of Computing in Civil Engineering*, 18 (1): 28–35.
- Wang, Y. H., and C. M. Mok. 2008. "Mechanisms of small-strain shear-modulus anisotropy in soils." *Journal of Geotechnical and Geoenvironmental Engineering*, 134 (10): 1516–1530.
- Wiebicke, M., E. Andò, I. Herle, and G. Viggiani. 2017. "On the metrology of interparticle contacts in sand from x-ray tomography images." *Measurement Science and Technology*, 28 (12): 124007.

- Wiebicke, M., E. Andò, G. Viggiani, and I. Herle. 2020. "Measuring the evolution of contact fabric in shear bands with x-ray tomography." *Acta Geotechnica*, 15 (1): 79–93.
- Yamamuro, J. A., and F. M. Wood. 2004. "Effect of depositional method on the undrained behavior and microstructure of sand with silt." *Soil Dynamics and Earthquake Engineering*, 24 (9–10): 751–760.
- Yang, Z. X., X. S. Li, and J. Yang. 2008. "Quantifying and modelling fabric anisotropy of granular soils." *Géotechnique*, 58 (4): 237–248.
- Yimsiri, S., and K. Soga. 2010. "DEM analysis of soil fabric effects on behaviour of sand." *Géotechnique*, 60 (6): 483–495.
- Zeng, X., and B. Ni. 1998. "Application of bender elements in measuring g_{max} of sand under k_0 condition." *Geotechnical Testing Journal*, 21 (3): 251.
- Zhao, J., and N. Guo. 2015. "The interplay between anisotropy and strain localisation in granular soils: a multiscale insight." *Géotechnique*, 65 (8): 642–656.
- Zheng, J., and R. D. Hryciw. 2015. "Traditional soil particle sphericity, roundness and surface roughness by computational geometry." *Géotechnique*, 65 (6): 494–506.

3.9 Tables and figures

Table 3.1: DEM simulations parameters

<i>Parameter</i>	<i>Symbol</i>	<i>Value</i>
Young's Modulus	E	70 GPa
Poisson's ratio	ν	0.3
Particle density	ρ	2,650 kg/m ³
Friction coefficient during sample preparation	μ_{prep}	0.1
Friction coefficient during shear wave transmission	μ_{wave}	0.5
Global damping during sample preparation	ξ_{prep}	0.1
Global damping during wave propagation	ξ_{wave}	0.05

Table 3.2: Average V_S ratios and V_S anisotropy parameters from DEM simulations and BE experiments

<i>Material</i>	<i>Stress Condition</i>	V_{HV} / V_{VH}	V_{HV} / V_{HH}	$a_{VS,VHtoHV}$	$a_{VS,VHtoHH}$	a_{CN}	a_{CNF}	a_{LA}
Spheres	Iso	1.00	1.00	0.006	0.004	0.003	0.001	-
Spheres	K ₀	0.97	1.06	0.010	0.043	0.036	0.380	-
Clumps	Iso	1.21	1.01	0.058	0.071	0.084	0.007	1.758
Clumps	K ₀	1.01	1.01	0.017	0.020	0.047	0.570	1.761
Glass beads	Iso	1.00	0.99	0.010	-	-	-	-
Glass beads	K ₀	0.96	1.34	0.009	-	-	-	-
100C	Iso	1.32	0.94	0.094	-	-	-	-
100C	K ₀	1.07	1.02	0.017	-	-	-	-

Note: The values were obtained from specimens subjected to 40 kPa of mean effective stress for isotropic compression or vertical effective stress for 1D compression.

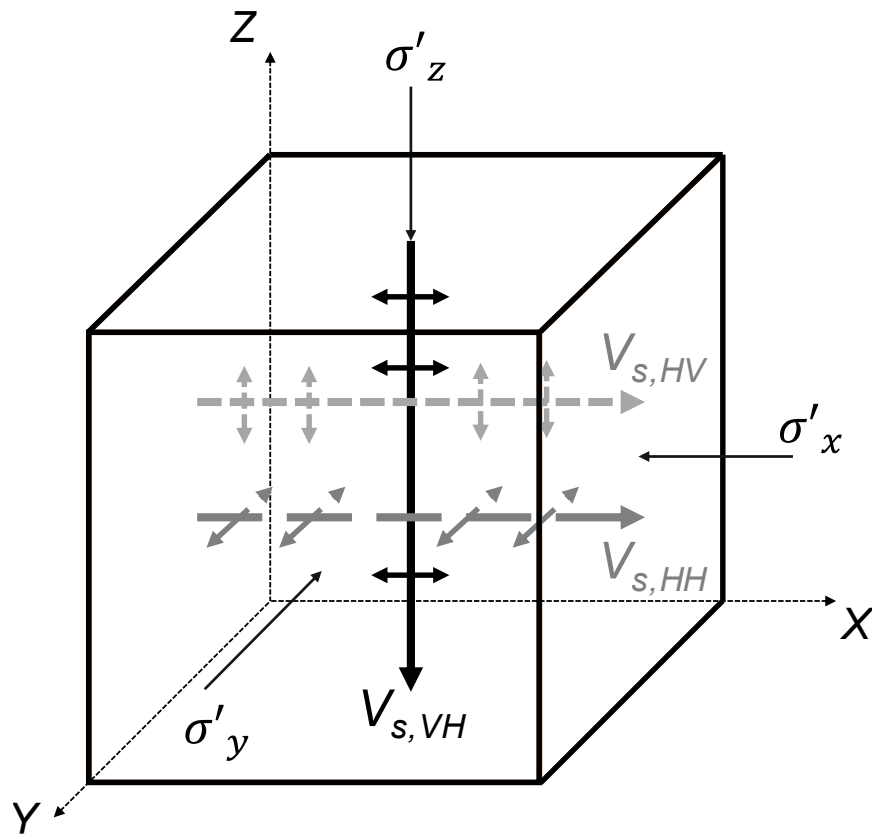


Figure 3.1: Notation for the various shear waves propagating through the soil specimen.

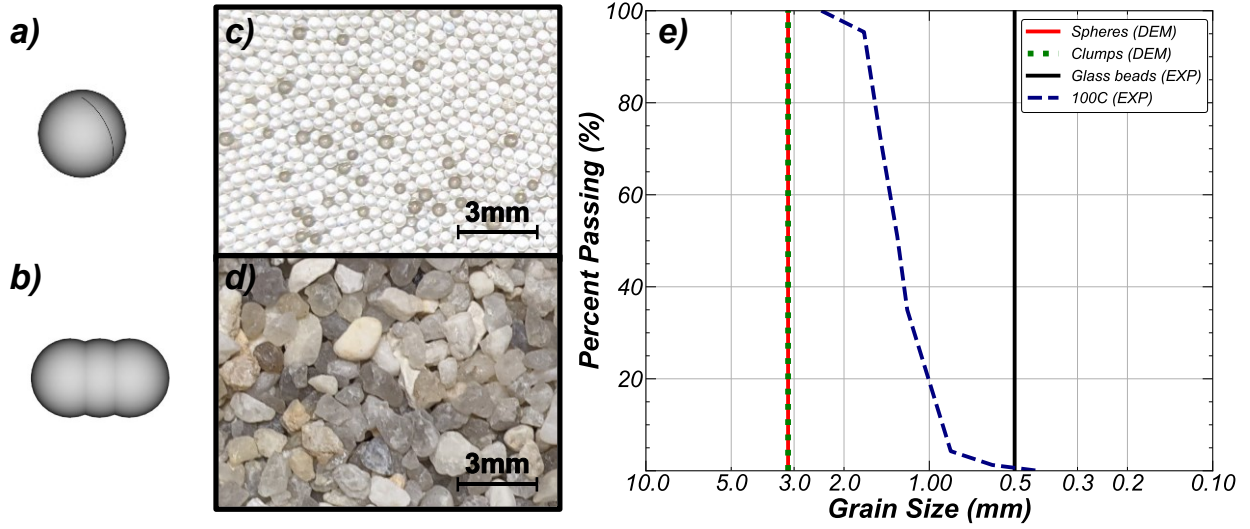


Figure 3.2: Images of (a) spheres, (b) elongated clump used in DEM simulations, (c) glass beads, (d) 100C sand used in experiments, and (e) grain size distributions for the materials.

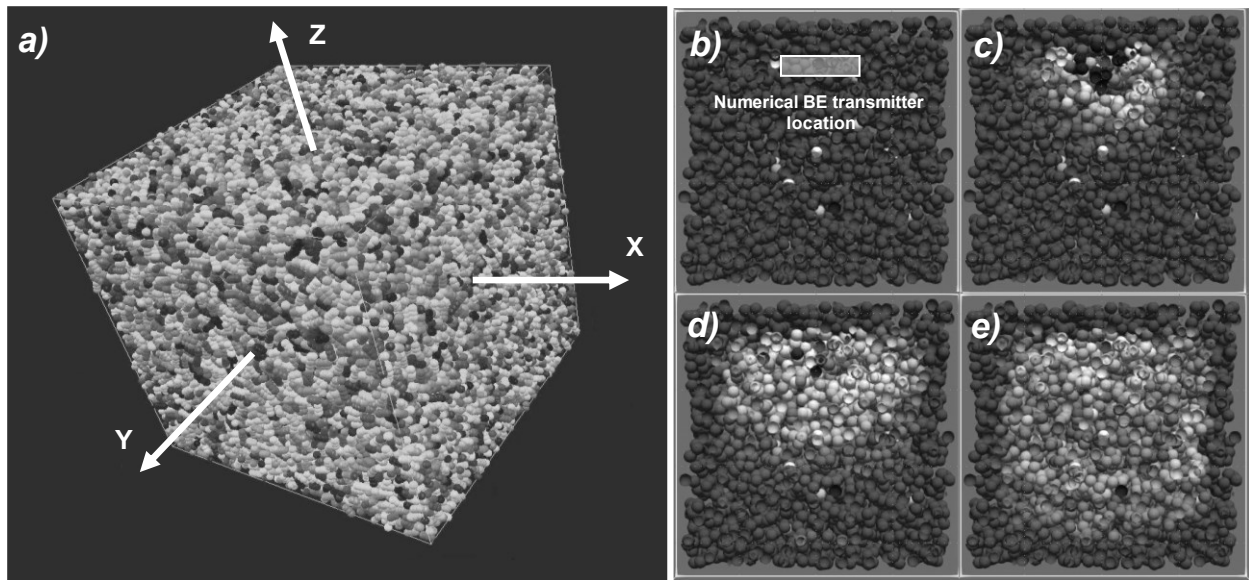


Figure 3.3: (a) Image of DEM specimen with clumps, and (b),(c),(d),(e) map of particle velocities at different times during the simulation showing the propagation of the shear wave.

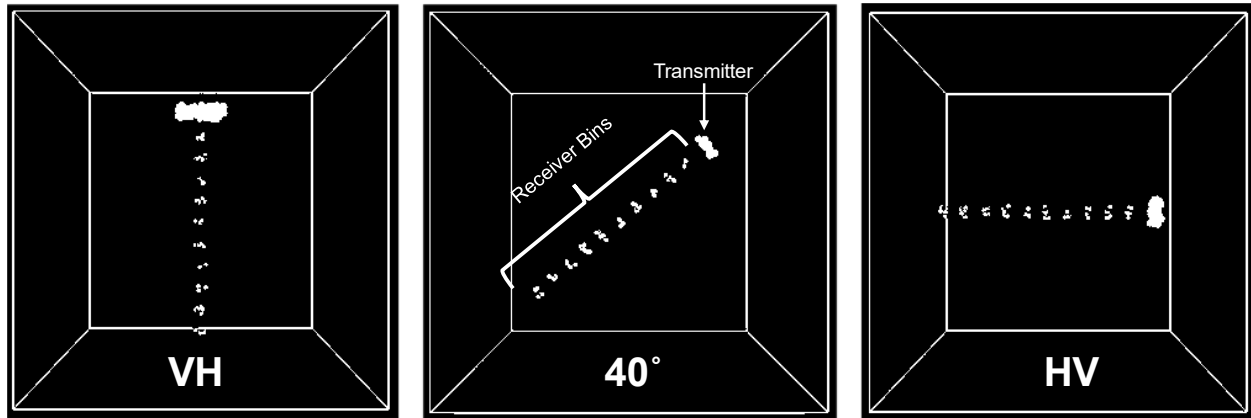


Figure 3.4: Numerical wave transmission setup for $V_{s,VH}$, $V_{s,40^\circ VHtoHV}$, and $V_{s,HV}$ waves showing the transmitter and receiver bins.

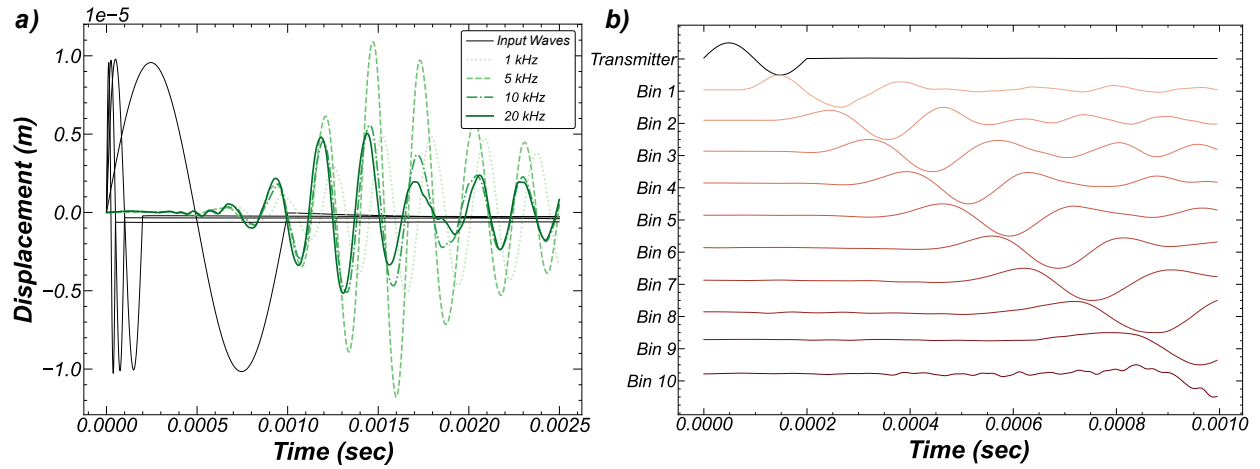


Figure 3.5: (a) Influence of input frequency on the received signals in the DEM simulations and (b) waterfall plot from the received signals from each of the receiver bins for a specimen made of spheres and isotropically compressed at a p' of 20 kPa.

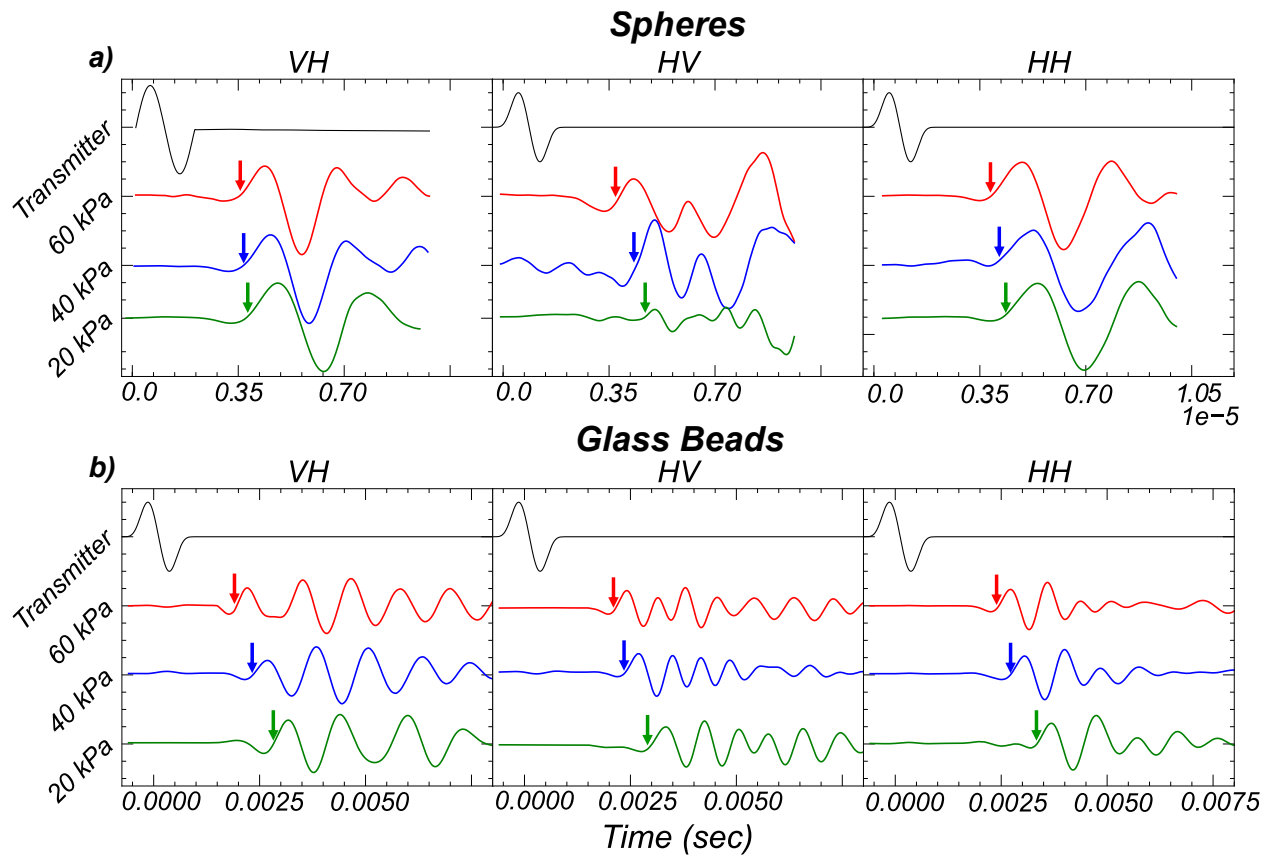


Figure 3.6: Transmitted and received BE signals during (a) a simulation of an isotropically-compressed spheres specimen and (b) an experiment an isotropically-compressed glass beads specimen. The arrows indicate the first arrival of the received signal.

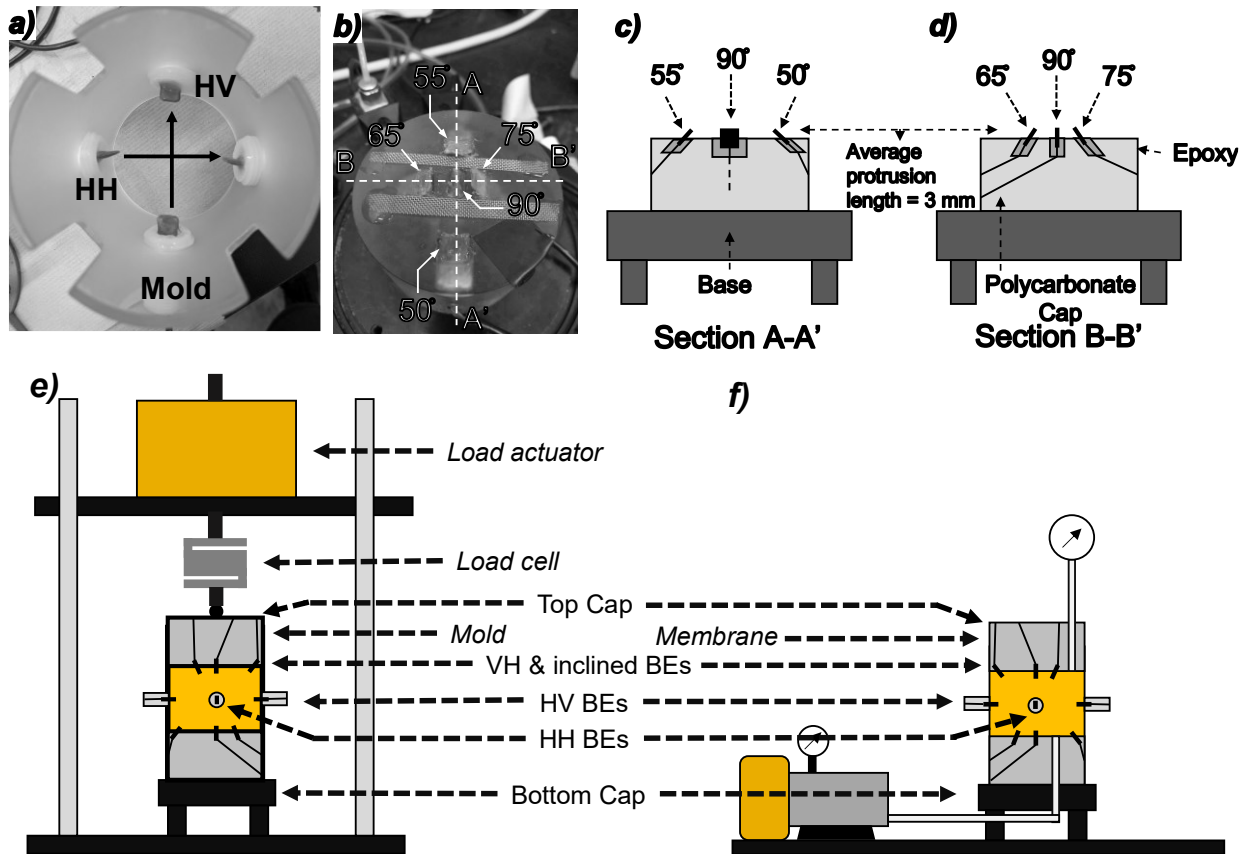


Figure 3.7: Photograph of (a) horizontal BEs, (b) top and bottom end caps, (c),(d) cross-sectional drawing of the bottom end cap with five BEs, and schematics of the equipment used for (e) 1D and (f) isotropic compression tests, where the major differences in the setups are highlighted in italic font. The top end cap has the same configuration as the bottom end cap.

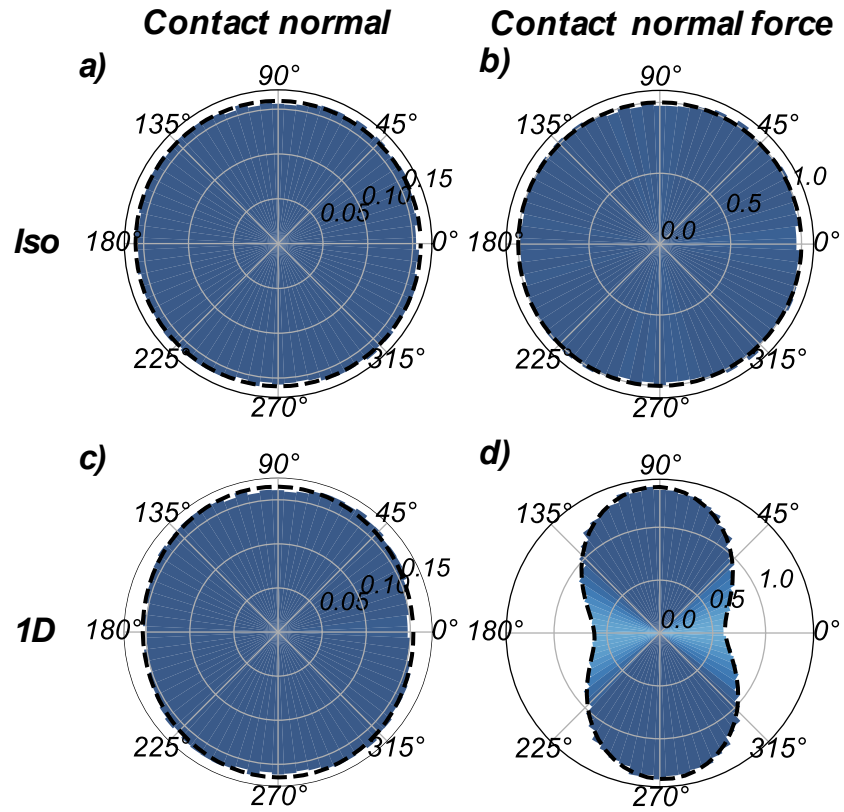


Figure 3.8: Angular distributions of (a),(c) contact normal, and (b),(d) contact normal forces for the spheres specimens subjected to isotropic and 1D compression of 40 kPa; dashed lines show the best fit lines using Eqs. 3.1 and 3.2.

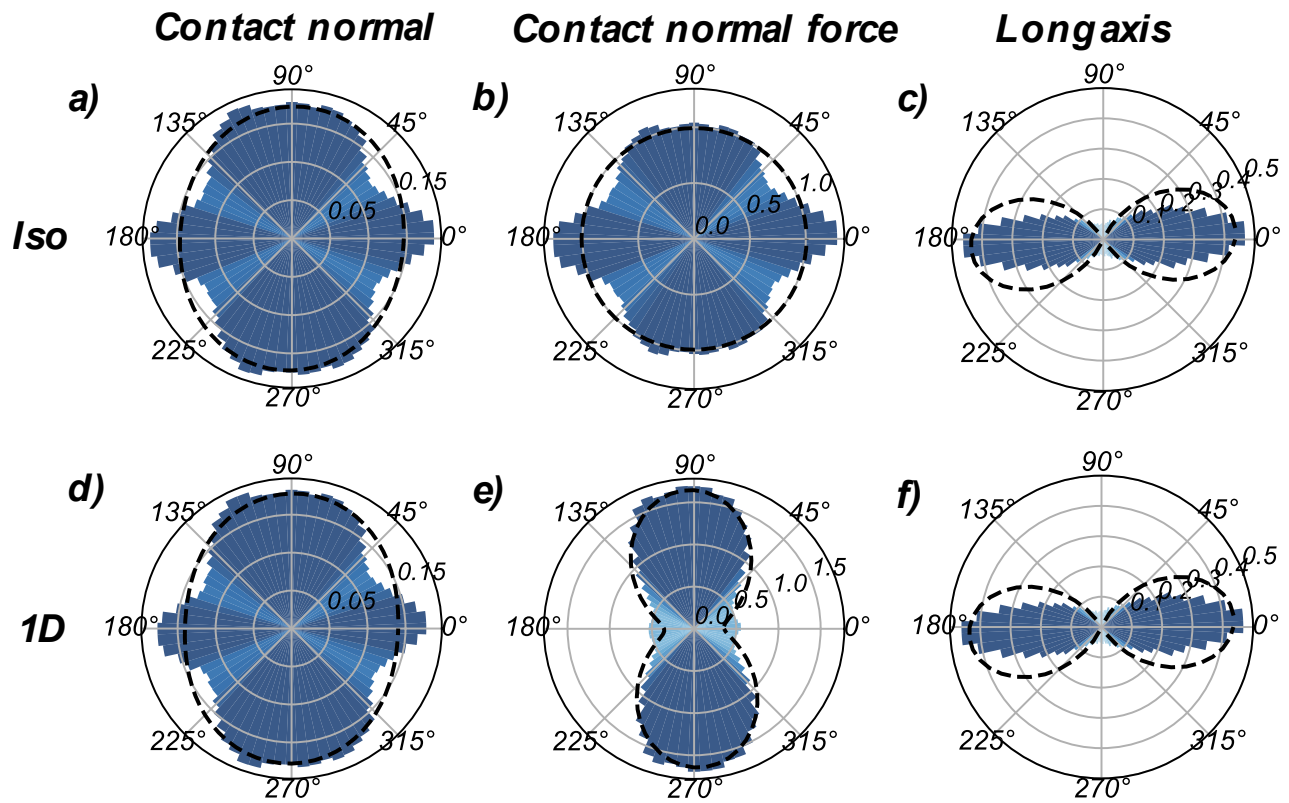


Figure 3.9: Angular distributions of (a),(d) contact normals, (b),(e) contact normal forces, and (c),(f) particle long axes for the clumps specimens subjected to isotropic and 1D compression of 40 kPa; dashed lines show the best fit lines using Eqs. 3.1, 3.2, and 3.3.

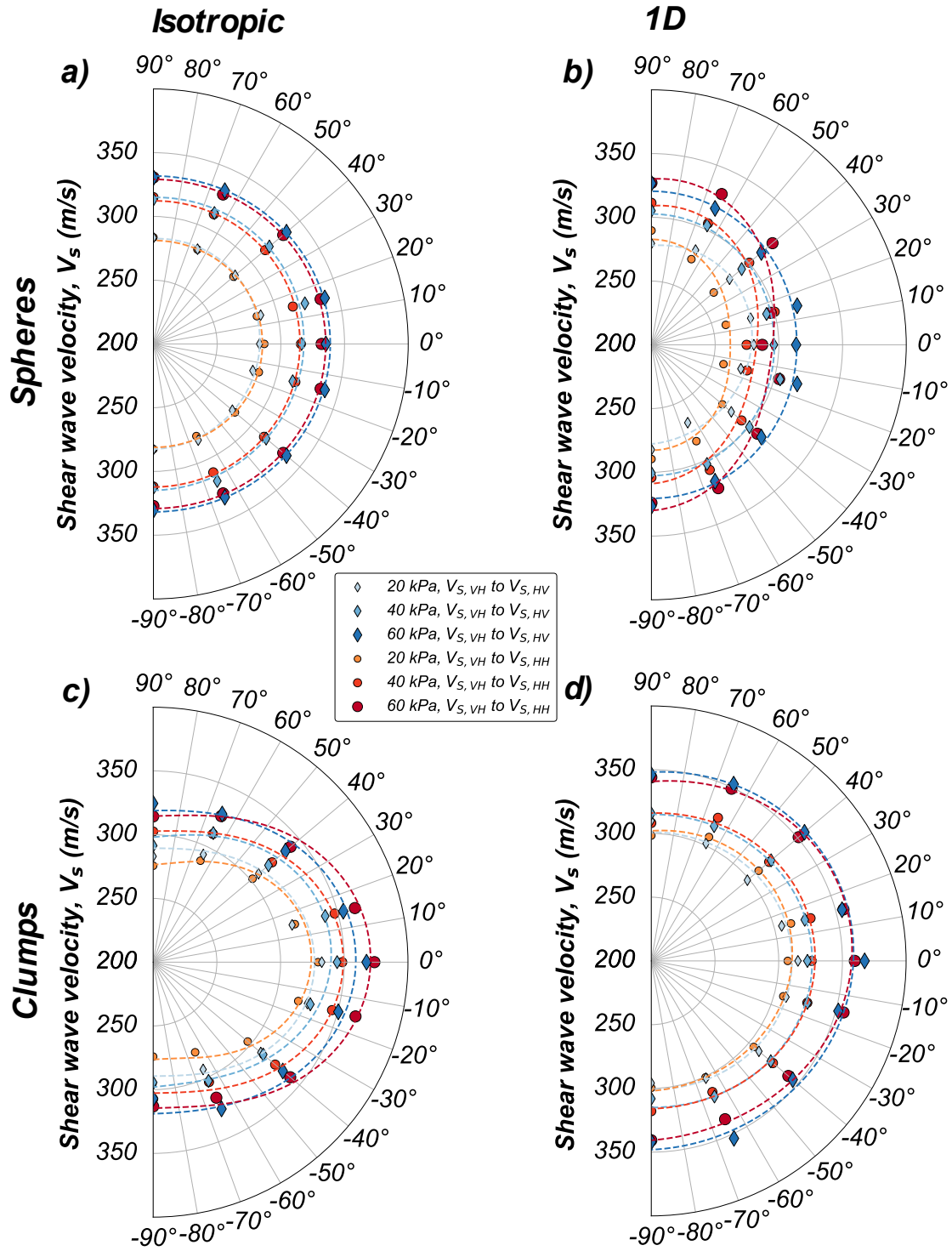


Figure 3.10: DEM angular distributions of V_s for (a),(b) sphere and (c),(d) clump specimens subjected to varying p' magnitudes; dashed lines show the best fit lines for the

VH to HV and VH to HV sweeps using Eq. 3.4.

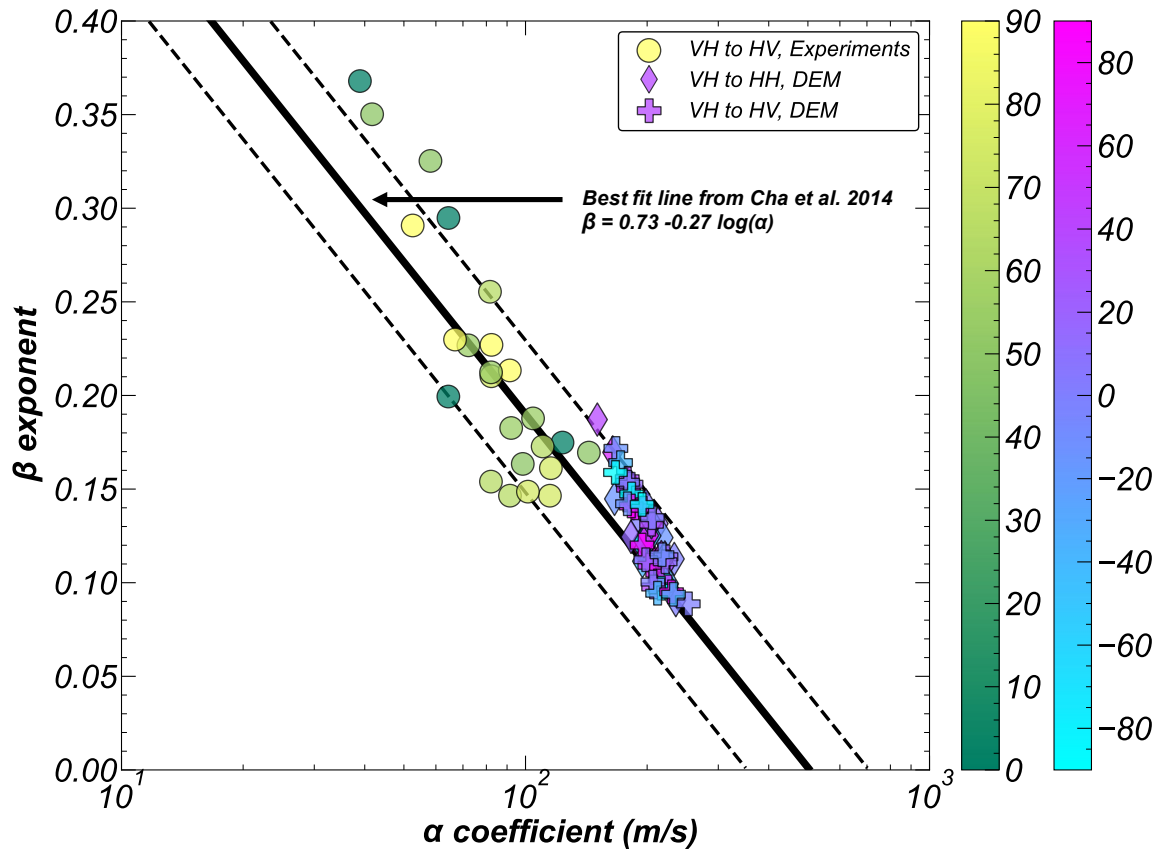
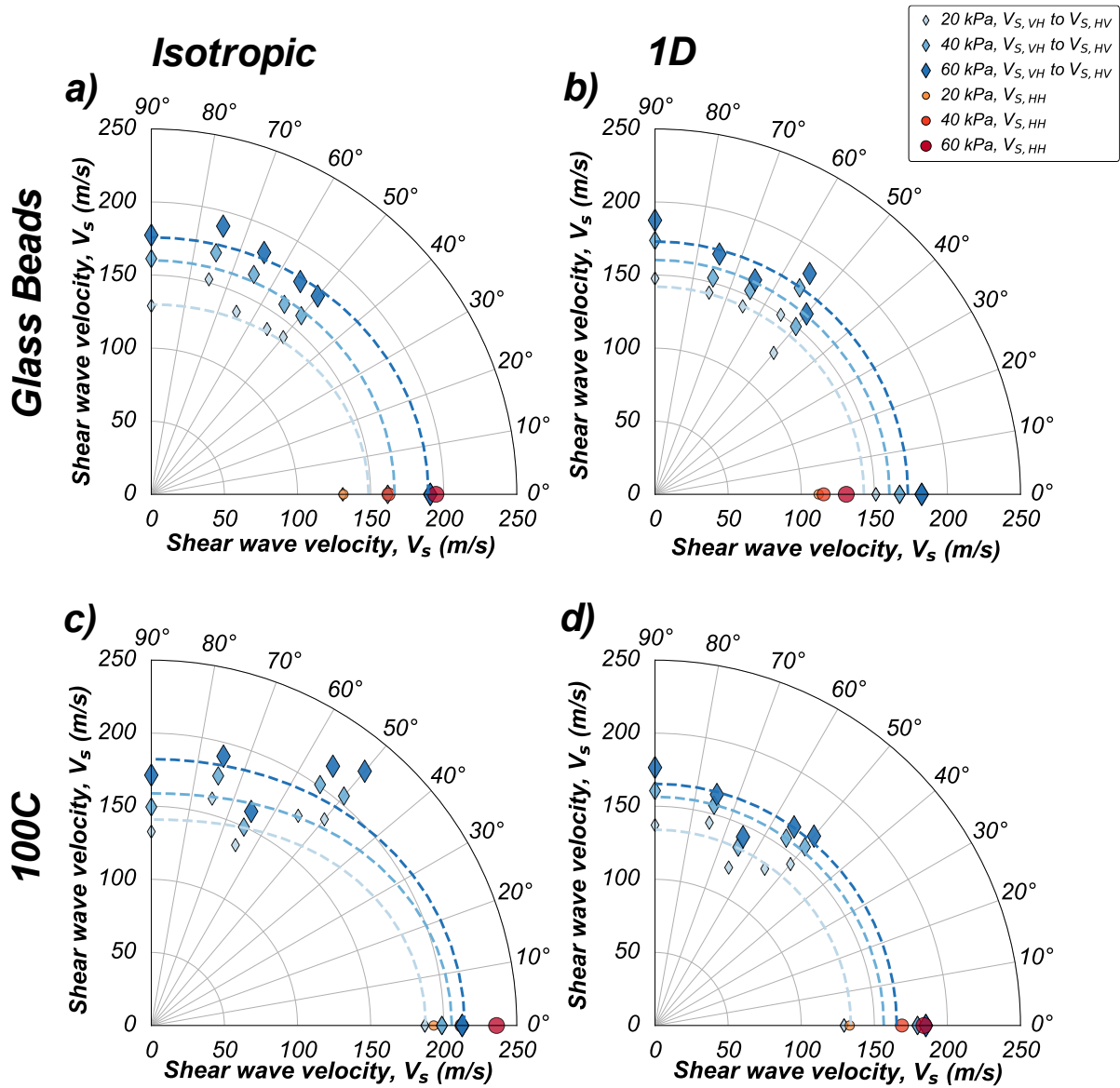


Figure 3.11: Comparison of α coefficients and β exponents for the VH to HV from experiments and DEM and VH to HH sweep from DEM. The solid line shows the best fit and the dashed lines shows the one standard deviation bounds of data presented in Cha et al. (2014). Different colors denote the angular orientation of BEs with shades of green for experimental results and shades of blue for DEM results.



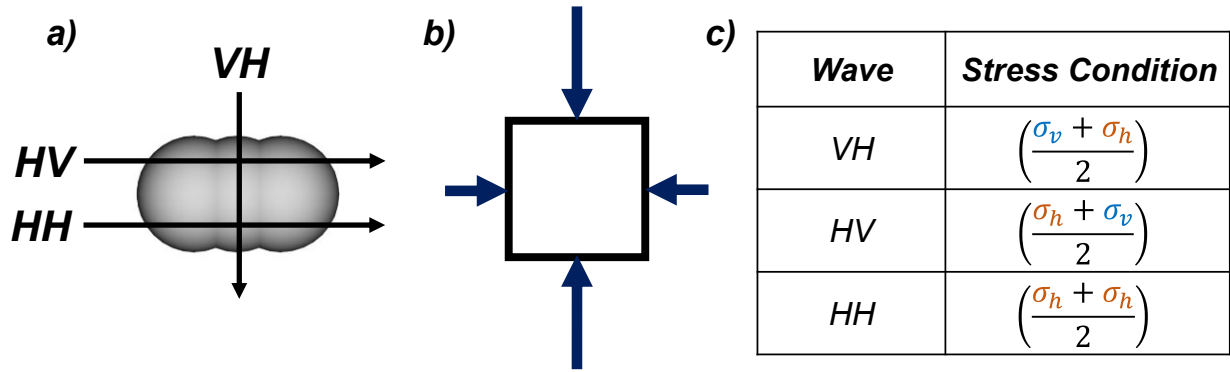


Figure 3.13: Illustration of (a) fabric and (b) stress state for normally consolidated soil under 1D compression, and (c) stress conditions for *VH*, *HV*, and *HH* waves.

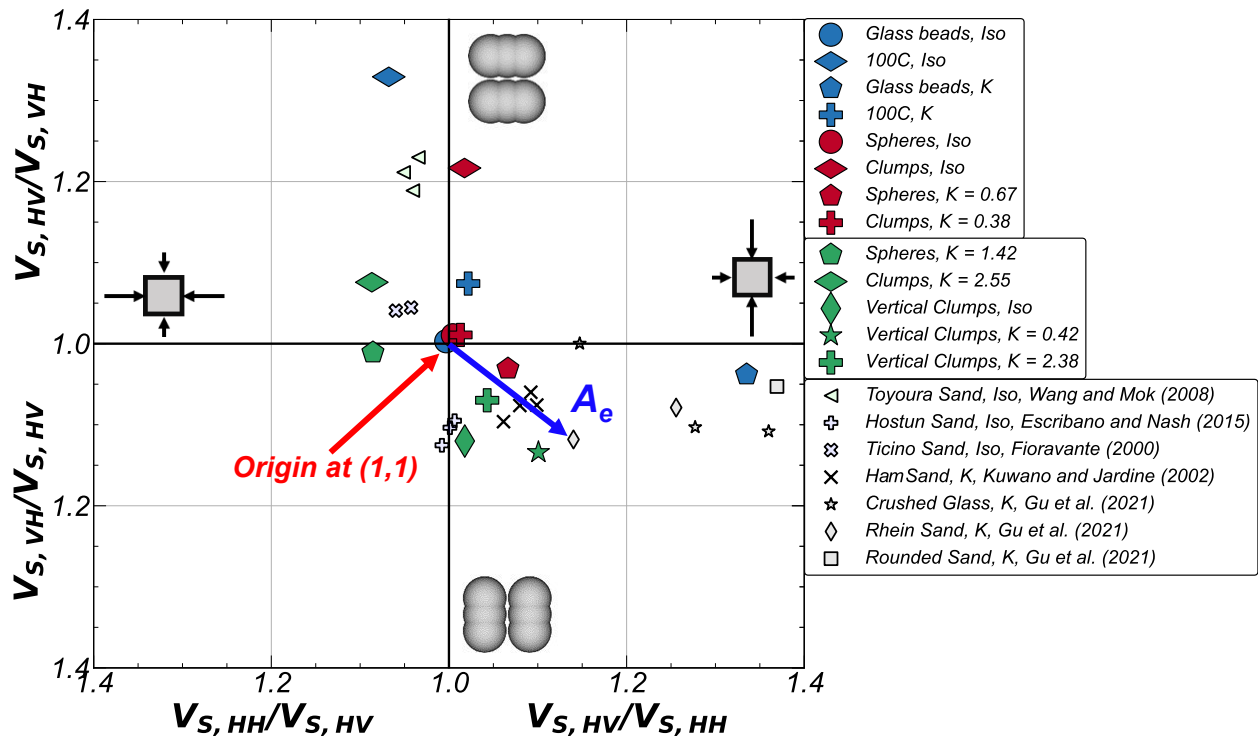


Figure 3.14: Shear wave velocity ratios for the different fabric and stress states at an effective stress of 40 kPa along with data from the literature.

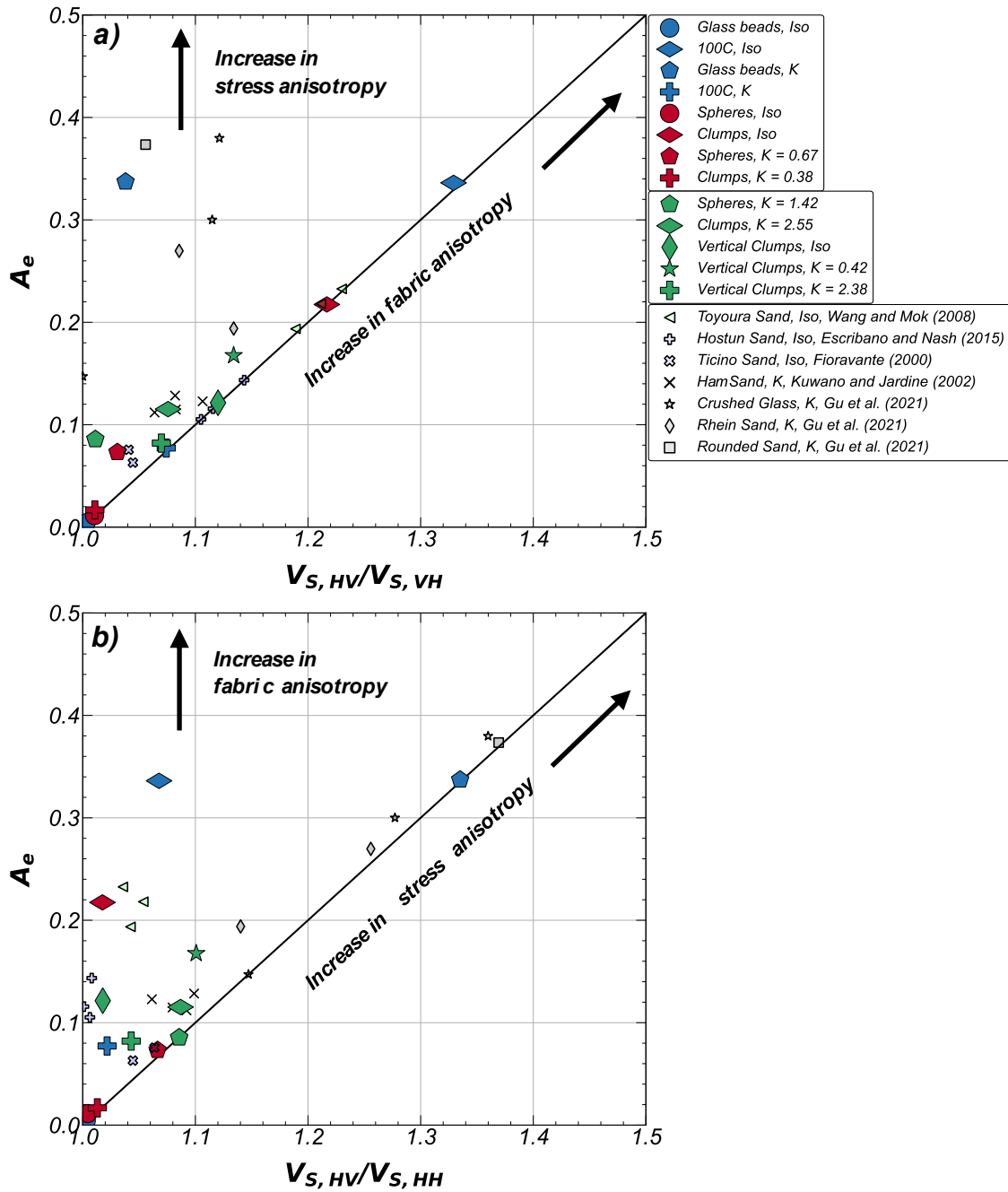


Figure 3.15: Comparison between the net anisotropy, A_e , and (a) $V_{s,HV}/V_{s,VH}$ and (b) $V_{s,HV}/V_{s,HH}$ ratio for numerical and experimental specimens and literature data.

Supplementary figures

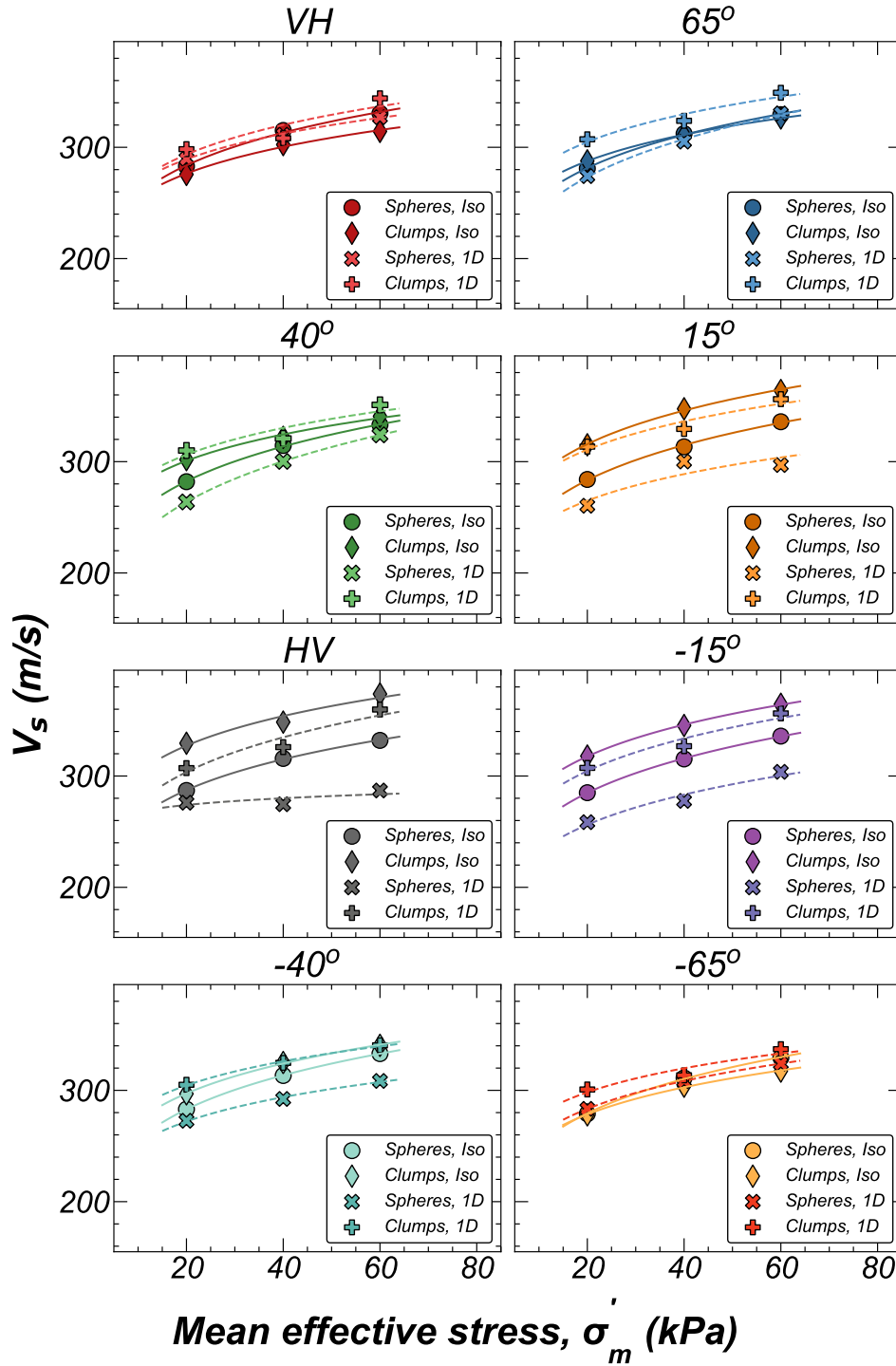


Figure 3.16: Increase in V_s with increase in σ'_m for spheres and clumps under isotropic (Iso) and 1D compression for VH to HV sweep.

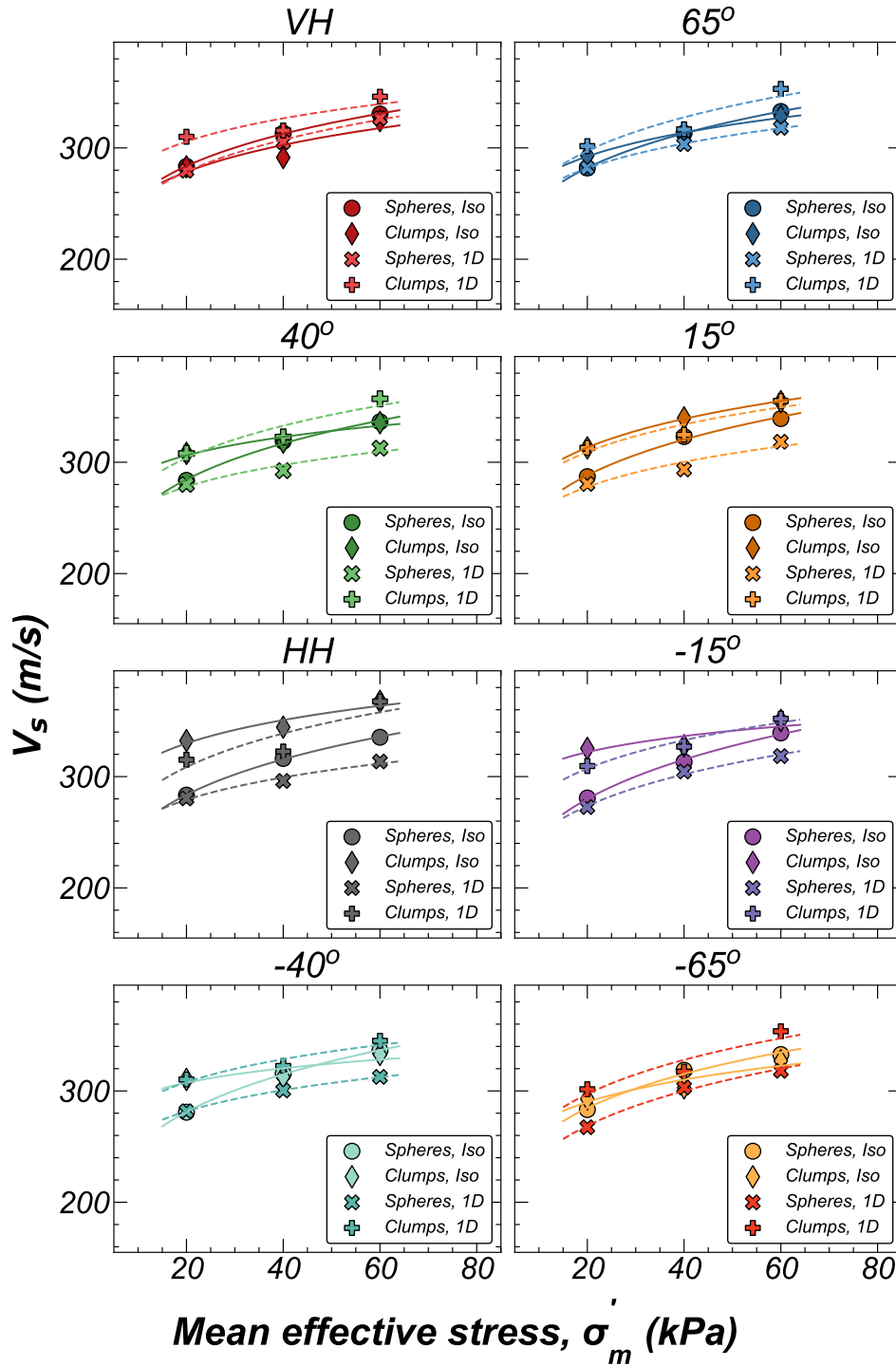


Figure 3.17: Increase in V_s with increase in σ'_m for spheres and clumps under isotropic (Iso) and 1D compression for VH to HH sweep.

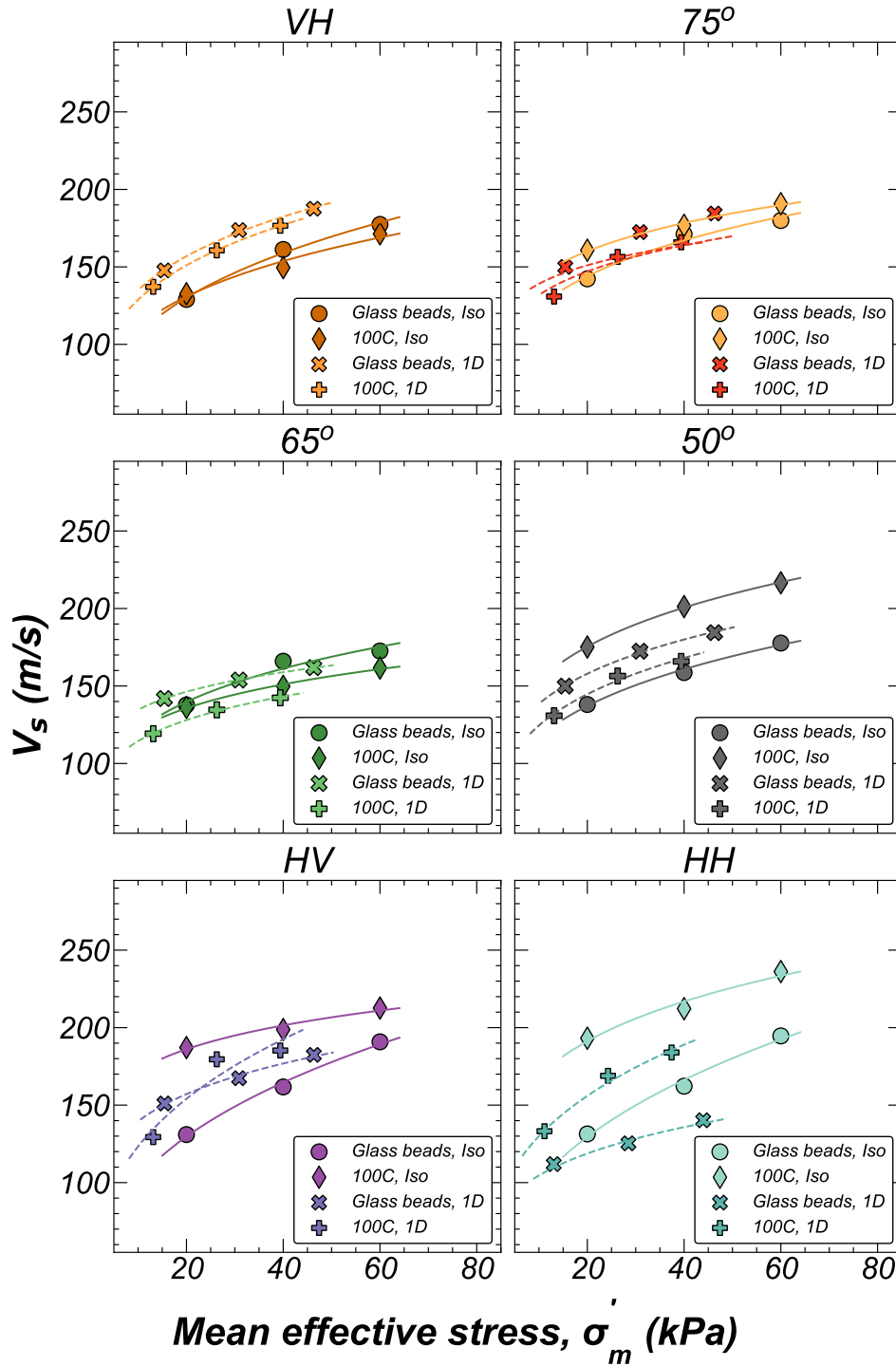


Figure 3.18: Increase in V_s with increase in σ'_m for glass beads and 100C sand under isotropic (Iso) and 1D compression.

Chapter 4

Effect of particle size distribution and contact parameters on the particle connectivity and contact force transmission of granular assemblies

Author's note: This paper will be submitted as a technical note to the Springer Granular Matter authored by Mandeep Singh Basson, Alejandro Martinez, and Jason T. DeJong. The paper is presented herein with minor edits for consistency with the other chapters of this Dissertation.

4.1 Abstract

The particle size distribution of a granular assembly influences the number of contacts between particles and how the contact forces are transmitted within the assembly, which affect the mechanical behavior of granular soils, including their stiffness, shear strength, dilatancy, and ultimately, the response during monotonic and cyclic loading. This study uses discrete element modeling (DEM) simulations to explore the effect of particle size distribution on the proportion of inactive particles, distributions of particle connectivity, and contact force transmission between particles of varying sizes. These simulations are performed on isotropically compressed assemblies with particle size distributions of low

and high polydispersity, along with bimodal distributions, considering variations in the coefficient of uniformity (C_u) between 1.95 and 5.76. Additionally, the study explores the influence of contact parameters such as particle stiffness, interparticle friction coefficient, and damping coefficient on the proportion of inactive particles. The results indicate that as polydispersity increases, the percentage of inactive particles increases while the connectivity of the larger particles also increases. Highly polydisperse specimens with well-graded and bimodal gradations (higher C_u of 5.76 and 8.69, respectively) exhibit a larger percentage of inactive particles, predominantly comprising of finer particles. Additionally, these gradations show an increase in particle connectivity with larger particle sizes, as coarser particles are connected to a higher number of finer particles, leading to coarser particles carrying significantly higher contact forces. The inactive particles primarily consist of the smaller ten percentile of particle sizes. Moreover, the changes in contact parameters affect the particle packing, where an increase in friction coefficient and stiffness ratio and a decrease in damping coefficient led to a higher proportion of inactive particles and a decrease in the PCs for the coarser particles. These findings highlight the complex nature of stress transmission in granular materials, which is deeply affected by the polydispersity of the particle size distribution and contact properties of the particles.

4.2 Introduction

The mechanical behavior of granular materials, such as sandy and gravelly soils, depends on fundamental properties such as particle size distribution (PSD), particle shape, surface roughness, mineralogy, porosity, and inherent fabric. The PSD, which describes the cumulative distribution of mass as a function of particle size, is a material property that

reflects the geologic history and has been extensively used to characterize soils from engineering and geologic perspectives (e.g., Been and Jefferies 1985; Cubrinovski and Ishihara 2002; Blott and Pye 2012; Wiącek and Molenda 2014; Ciantia et al. 2019; Catt 2020). Overall, the PSD quantifies the proportion of particles of any size and polydispersity indicates the width of PSD within a granular assembly. For example, an assembly with uniform PSD (poorly graded soils) indicates low polydispersity, whereas a soil with wider PSD (well graded soils) indicates a high polydispersity in terms of particle sizes. Extensive research shows that PSD plays a crucial role in determining the packing characteristics, transmission of contact forces, and rearrangement of particles during compression and shearing (e.g., Yamamuro and Lade 1997; Chaney et al. 1998; Wiącek and Molenda 2018).

Past research has shown a significant effect of the PSD on the stress-dilatancy, jamming, and compression behaviors of soils (e.g., Chang and Meidani 2013; Wiącek and Molenda 2014; Amirpour Harehdasht et al. 2017; Doygun et al. 2019; Ghadr and Assadi-Langroudi 2019; Basson et al. 2023a; Ahmed et al. 2023), as well as their permeability, friction angle, and erosion properties (e.g., Farahnak Langroudi et al. 2013; Cha and Santamarina 2019). Typically, the coarser particles in granular assemblies carry larger contact forces, forming the so-called strong force networks. In contrast, the finer particles tend to occupy the void spaces between the coarser particles and provide buckling resistance to the specimen, forming weak force networks (e.g., Liu et al. 2021a; b; Basson et al. 2023b; Yilmaz et al. 2023). The interplay of the strong and weak force networks has been explored for shearing, compression (e.g., Radjai et al. 1999; Basson and Martinez 2020; Zhao and Krut 2020), wave transmission (Mital et al. 2020), and granular flow problems (Xiu et al. 2018).

The transmission of contact forces by a given particle is affected by the number of contacts it has with its neighboring particles, denoted as particle connectivity (*PC*). Coarser particles have been shown to have higher *PC* than finer particles and are most active for contact force transmission (Basson et al. 2023b). The finer particles can be inactive, meaning they do not significantly contribute to contact force transmission. These particles can either have a *PC* of 0 (i.e., floaters) or 1 (i.e., rattlers). Recent studies have highlighted the effect of inactive particles (floaters and rattlers) on the transmission of contact forces in polydisperse soils (e.g., Farahnak Langroudi et al. 2013; Shire et al. 2014; Duverger et al. 2021; Liu et al. 2021a; b).

Discrete element modeling (DEM) has been widely used to investigate the macro-scale response of granular materials and to establish connections between the macro-scale behaviors and the interactions at the particle and contact scales (e.g., Bathurst and Rothenburg 1990; Santamarina 2003; O’Sullivan 2011; Huang et al. 2014; Bernhardt et al. 2016; Basson et al. 2020; Basson and Martinez 2020). Building upon previous research, this study aims to investigate the effects of the polydispersity of the PSD on the distribution of inactive particles, particle connectivity, and contact force transmission considering the influence of contact parameters, including the interparticle friction coefficient, stiffness ratio, and global viscous damping. To achieve this, isotropically compressed specimens with different PSDs, including mono-sized, low and high polydispersity, bimodal, and curved distributions, are simulated to examine how the particle size affects the proportion of inactive particles, distribution of particle connectivity and contact normal forces.

4.3 DEM simulation details

Isotropic compression simulations were performed using the three-dimensional DEM code YADE (Šmilauer et al. 2010). Cubical specimens composed of spherical particles were compressed isotropically to a mean confining stress (p') of 100 kPa. The PSDs of two assemblies were adapted from naturally occurring coarse-grained soils sourced from a marine deposit in Mauricetown, New Jersey (Sturm 2019; Ahmed 2021; Reardon et al. 2022). These gradations represent a poorly graded soil with low polydispersity, referred to as 100A, and a well-graded soil with high polydispersity, referred to as 25ABCD. Important differences include the maximum particle size (D_{max}), which is significantly larger for the 25ABCD gradation with a value 25.89 mm in comparison to that of 5.82 mm for the 100A gradation, and the coefficient of uniformity (C_u), defined as the ratio of the 60th percentile particle diameter (D_{60}) to the 10th percentile particle diameter (D_{10}), with values of 5.76 and 1.95 for the 25ABCD and 100A gradations, respectively. Table 4.1 presents a summary of the gradation parameters, while Fig. 4.1(a) provides the particle size distributions. The 30th percentile particle diameter (D_{30}) is relatively similar between 100A and 25ABCD, with values of 2.11 and 2.32 mm, respectively.

Three additional gradations, consisting of mono-sized particles, a bimodal distribution, and a curved distribution, were simulated to model additional variations in particle connectivity and contact force transmission (Table 4.1, Fig. 4.1(a)). The bimodal gradation is representative of a gap-graded soil with high polydispersity that has a range of missing particle sizes and is routinely encountered in natural alluvial deposits, gravelly soil, or in filters material used in the construction of geosystems such as dams and levees (e.g., Farahnak Langroudi et al. 2013; Shire et al. 2014). The gap in bimodal gradations results in

non-uniform arrangement of particles which could produce lower particle connectivities (Liu et al. 2021a). The curved gradation represents a continuous and gradual transition between different particle sizes within the same maximum and minimum particle sizes as the bimodal gradation. The gradual transition, with a tail towards the finer particles, was created using the method presented by Liu et al. (2021a) and is commonly observed in naturally occurring coarse-grained soils. The curved gradation has a similar D_{10} as the 100A distribution, while the 25ABCD and bimodal gradations have similar D_{50} . Images of the five assemblies are shown in Fig. 4.1.

The contact model and parameters control the response of the simulated specimen to the applied loading. A linear elastic contact model incorporating Mohr-Coulomb plasticity and global viscous damping was used to simulate the interaction between the particles. Table 4.2 presents the contact parameters used in this study, with the bold font indicating the reference values. The low reference μ of 0.01 was adopted to produce *dense* specimens (Liu et al. 2021a) and a reference ξ of 0.05 was adopted to ensure equilibrium was maintained without altering the results significantly (Ng 2006). The normal contact stiffness was determined based on a constant normal stiffness to particle diameter ratio (k/D), which normalizes the effect of particle size (Scholtès et al. 2009; Šmilauer et al. 2010). Parametric studies were conducted to examine the effect of the stiffness-to-particle diameter ratio (k/D), global viscous damping (ξ), particle friction coefficient (μ), and number of particles (N) on the particle connectivity and proportion of inactive particles in a specimen with 25ABCD gradation (Table 4.2).

To prepare the specimens, a cloud of initially non-contacting particles was isotropically compressed to a mean effective stress (p) of 100 kPa. The final void ratios of the specimens at 100 kPa are summarized in Table 4.3. Periodic boundaries were used to ensure uniform deformational fields (Zhang and Evans 2018). The specimen size ($D_{specimen}$) was calculated based on the maximum of two quantities: 20 times D_{50} and 5 times the specimen's largest particle diameter (D_{max}). The $D_{specimen}/D_{50}$ ratio varied between 26.11 for 100A to 20.52 for 25ABCD, while the $D_{specimen}/D_{max}$ ratio varied between 10.6 for 100A and 4.2 for 25ABCD, which is generally consistent with the recommendations in the literature (O'Sullivan 2011; Huang et al. 2014). The stresses and particle packing were tracked using a measurement cube with a side D_{50} times smaller than the specimen dimension. To ensure that specimen size and number of particles in the specimen were sufficient to provide representative results, especially for specimen with high polydispersity, three specimens were created for 25ABCD gradation using 50,000, 100,000, and 150,000 particles. The results indicate that the number of particles did not significantly affect the void ratio, mechanical coordination number and % of inactive particles in the specimen, potentially due to the use of periodic boundary conditions (Table 4.3). More details regarding the DEM simulations of materials with varying gradation are presented by Basson et al. (2023b).

4.4 Results and discussion

This section presents the simulation results describing the effect of the PSD on the distribution of particle connectivity values and the proportion of inactive particles in the granular assemblies, along with the effect of the contact stiffness, inter-particle friction coefficient, damping coefficient, and the number of particles.

4.4.1 Effect of particle size distribution

The particle size distribution of a specimen influences the packing characteristics and transmission of contact forces between particles. In specimens with broader PSDs, the wider range of particle sizes enables finer particles to effectively fill the void spaces leading to tighter packing (e.g., Wiącek and Molenda 2018; Yilmaz et al. 2023). The packing characteristics of a specimen are typically evaluated by the analysis of contact distribution between the particles. The Mechanical Coordination Number (MCN) has been widely adopted as a measure of particle connectivity and is computed based on the equation presented in (Thornton 2000) as:

$$MCN = \frac{2C - N_1}{N - N_0 - N_1} \quad (4.1)$$

where C is the number of contacts in the assembly, N is the total number of particles, N_0 is the number of particles with zero contacts, and N_1 is the number of particles with one contact. Table 4.3 summarizes the MCN of the tested specimens compressed to 100 kPa. The MCN for all the specimens with mono-sized, 100A, 25ABCD, bimodal, and curved gradations are relatively similar, suggesting that the MCN may fail to capture the contact distribution in specimens with broader gradations due to averaging of the number of contacts for both coarser and finer particles. As an alternative, the Particle Connectivity (PC) parameter has been adopted as an effective measure of the connectedness that can consider individual particle sizes (Liu et al. 2021a; Basson et al. 2023b). PC represents the number of contacts of a particle with its neighboring particles, providing a more detailed representation of the distribution of contacts through the specimen. The particles with a PC of either zero (i.e., floaters) or one (i.e., rattlers) are considered inactive as they do not contribute to the overall

contact force transmission in the specimen. Cumulative distributions of PC with the number of particles and cumulative particle volume provide insights into the connectivity characteristics of different specimens. Fig. 4.2 illustrates these distributions for the different specimens. To generate these distributions, PC values were grouped into bins, and the corresponding number of particles (Fig 4.2(a)) and total particle volume (Fig. 4.2(b)) within each bin were determined. All the assemblies were composed of approximately 50000 particles compressed to a p' of 100kPa using the reference contact parameters (Table 4.2).

Significant variations are observed in the PC distribution between the different specimens. For the cumulative distribution in terms of the number of particles, the specimen with curved gradation exhibits the highest number of inactive particles (i.e., PC of 0 or 1), accounting for approximately 53% of the particles, with predominantly finer particles filling up the void spaces. In contrast, the specimen with mono-sized particles has the lowest number of inactive particles, with less than 1% of particles exhibiting PC values of 0 or 1 (Fig. 4.2(a)). The specimen made of 25ABCD gradation has 18%, followed by the 100A and bimodal gradations with 12% and less than 3% inactive particles by number, respectively.

The dominance of finer particles as inactive is validated by the cumulative distribution of PC with particle volume. For example, while the curved gradation specimen has 53% inactive particles by number, their total volume is around 2.3%. Similarly, the volume of inactive particles in all the other specimens remains below 1% (Fig. 4.2(b)). The cumulative distribution of PC with particle volume exhibits a similar shape as the input PSD. Among the tested specimens, the 25ABCD gradation shows the widest PC distribution, the bimodal gradation exhibits a bimodal distribution, the curved gradation shows a curved distribution,

the 100A specimen produces a narrow distribution, and a mono sized specimen produces the narrowest distribution with a maximum PC of 9, with most PC values between 3 and 9. The PC distributions for the mono-sized particle specimen align with those typically observed in randomly deposited spheres, falling between the maximum PC values of 6 for loose face-centered cubic and 12 for dense hexagonal packings (Bernal and Mason 1960). Additionally, the results reveal that specimens with specific similarities in PSDs could have different packing characteristics. For instance, at similar D_{50} , the curved gradation specimen has the highest number of inactive particles by number and the lowest PC compared to the bimodal and 25ABCD gradations. At similar D_{30} , the mono-sized particle specimen has the lowest number of inactive particles and PC followed by specimens with 100A and 25ABCD gradations. However, at similar D_{10} the specimens with 100A and curved gradation show similar cumulative distribution of PC with volume, despite the fact that the curved gradation specimen having more inactive particles when compared by number.

An increase in C_U produces broader distributions of PC with particle sizes. In specimens with higher polydispersity, finer particles encircle the coarser particles, significantly increasing the PC for coarse particles as shown in Fig. 4.1(b,c,d,e,f) and Fig. 4.2(c). The distributions presented in Fig. 4.2(c) were obtained by computing the average particle size for each PC bin. For example, the average particle size in the PC bin of 298-299 for 25ABCD is 23 mm. Similarly, a PC of 42 in the 100A assembly corresponds to an average particle size of 6.2 mm, and a PC of 272 in the bimodal assembly corresponds to an average particle size of 9.7 mm. The specimen with 25ABCD gradation shows a wider distribution of PC with average particle size, reaching the highest magnitude of PC of 802 due to the coarse particle in the specimen being connected to a large number of finer particles. The specimen with

bimodal gradation shows the second highest PC (272) followed by the 100A (45), curved (50) and mono-sized (10) specimens. Interestingly, Fig. 4.2(c) reveals that most inactive particles with PC values smaller than one have sizes close to the D_{10} of each gradation, indicated by the vertical lines. These findings suggest that the D_{10} particle size could be used as the threshold size between the active and inactive particles in granular assemblies. These findings suggest that the specimens with high polydispersity exhibit a coarse dominant fabric with the finer particles floating in the void space, which is corroborated by the force chain maps for each specimen presented in Fig 4.3. The specimens with high polydispersity show a concentration of force chains around the coarser particles, as shown in Fig. 4.3(d) for 25ABCD gradation and Fig. 4.3(f) for bimodal gradation. In contrast, the force chain maps for the mono-sized, 100A, and curved gradation specimens show a relatively uniform distribution of force chains (Figs. 4.3(b,c,e)). The results are in the range presented in the literature for various PSD (Farahnak Langroudi et al. 2013; Duverger et al. 2021; Liu et al. 2021a; b).

The coarser particles in the specimen carry disproportionately larger contact forces magnitudes. The distribution of normalized contact normal force (F_n/\bar{F}_n) for each contact, where \bar{F}_n is the average contact force in the assembly, highlights the effect of gradation on contact force transmission in a specimen. Fig 4.4. Presents two-dimensional colormaps of F_n/\bar{F}_n as a function of the sizes of the two particles involved in each contact. To create this colormap, the PSD for the gradations was divided into 10 equal bins and the F_n/\bar{F}_n was calculated for each bin. Additionally, contours are plotted for different values of F_n/\bar{F}_n , showing the particle sizes that carry different proportions of \bar{F}_n . The strong forces network is formed by contacts carrying $F_n/\bar{F}_n > 1.0$, and the contacts carrying $F_n/\bar{F}_n < 1.0$ form the

weak force network. Specimens with a low polydispersity (100A and curved) exhibit relatively uniform distributions with lower maximum F_n/\bar{F}_n values. In particular, the curved gradation specimen shows relatively similar distances between the F_n/\bar{F}_n contours ranging from 1 to 4, which indicates that the gradation with gradual curve results in a relatively uniform increase in contact force with increasing particle size. The specimens with high polydispersity show the greater magnitudes of F_n carried by the coarser particles, with the coarser particles carrying 30 times the average F_n in the 25ABCD and bimodal gradation specimens. The contours for $F_n/\bar{F}_n = 2$ and 3 for the specimen with 25ABCD gradation are concentrated towards the smaller particle sizes, while the F_n/\bar{F}_n contours in the specimen with bimodal gradation are concentrated closer to the D_{50} which corresponds to the gap in the bimodal gradation specimen. The concentration of the contour of F_n/\bar{F}_n of 1.0 towards the smaller particle sizes for the curved, 25ABCD, and bimodal gradations indicates that the particles coarser than about D_{20} , D_{20} , and D_{30} carry the strong contact forces, respectively, as compared to D_{40} for specimen with 100A gradation. These findings have been used to explain the enhanced dilatancy experienced during triaxial shearing for specimens with higher polydispersity (Basson et al. 2023b).

4.4.2 Effect of simulation parameters

4.4.2.1 Effect of particle friction coefficient (μ)

Mohr-Coulomb plasticity uses μ to determine the mobilized shear resistances and the slip conditions between particles. The μ parameter models the effect of particle surface roughness and angularity. Typically, in DEM simulations, μ can be used to control the amount of volume reduction that takes place during compression, typically employed for preparation of specimens with different densities. Ultimately, the packing of particles in a specimen is

controlled by its density, with denser specimens exhibiting higher PC values as compared to a looser one. Specimens with 25ABCD gradation were created with different μ to evaluate the effect of changes in μ on PC in a specimen with high polydispersity. For comparison, a μ value of 0.01 produces a relatively denser specimen (void ratio of 0.26) as compared to a μ value of 0.4 (void ratio of 0.34) (Basson et al. 2023a) (Table 4.3). Fig. 4.5 shows the variation of particle connectivity for different μ values. As expected, the relatively looser specimen with a μ of 0.4 has a higher percentage of inactive particles (73%) as compared to the relatively denser specimen with a μ of 0.01 (18%) (Fig. 4.5(a)). The overall PC increases with a decrease in μ , where a specimen with μ of 0.4 has the maximum PC of 198 compared to 802 for specimens with μ of 0.01 (Fig. 4.5(b)). The impact of changes in μ on PC is more noticeable in the coarser particles, while finer particles show relatively similar PC values, suggesting limited influence of finer particles on PC (Fig. 4.5(c)). The number of inactive particles increases in a linear fashion with increasing void ratio (increasing μ), while it decreases with increasing MCN (decreasing μ), as shown by the circle data points in Fig. 4.6.

4.4.2.2 Effect of particle stiffness (k/D)

The stiffness parameter controls the magnitude of the interpenetration of particles under a given force. For a soft particle DEM approach, the stiffness parameter controls the overlap between the particles, where larger stiffness produces smaller overlaps (Šmilauer et al. 2010). These reduced overlaps lead to a decrease in the number of contacts between the particles, consequently reducing the overall PC in the specimen. Realistically, the stiffness of the particles is controlled by the mineralogy and the surface roughness, where harder minerals produce stiffer responses and particles with lower surface roughness also produce stiffer responses. Specimens with 25ABCD gradations were created with k/D varied between

1e7 N/m³ and 1e9 N/m³ to investigate the impact of the contact stiffness on the distribution of PC values for specimen with wider gradation while keeping the other reference contact parameters unchanged. The proportion of inactive particles by number increases with particle stiffness, with an increase from 33% to 72% as the stiffness ratio is increased from 1e7 N/m³ to 1e9 N/m³ (Fig. 4.7(a)). The largest PC value decreased from 652 to 188 with an increase in stiffness ratio (Fig. 4.7(b)). The mechanism leading to this reduction in PC values with increasing particle stiffness is shown in Fig. 4.8. The decrease in the overlaps for higher stiffness affects the PC for coarser particles more than finer particles, which is corroborated by the PC distribution with average particle sizes shown in Fig. 4.7(c). Additionally, the decrease in particle overlaps leads to larger void space between coarser particles as indicated by an increase in the void ratio (Fig. 4.6), and the trends of % inactive particle are in line with changes in μ .

4.4.2.3 Effect of global viscous damping (ξ)

The ξ controls the dissipation of energy in the simulation. A higher damping coefficient dissipates a greater amount energy and reduces the micromechanical vibrations in the system. The particles return to rest faster and tend to stay at rest for a more extended time. An increase in ξ can effectively dampen the particle movements and reduce the overall mobility of the particles, leading to the particles staying in contact with the neighboring particles for longer durations which increases the overall PC of the specimen (Ng 2006). The global viscous damping was increased from 0.05 to 0.25 and 0.5 to highlight its effect on the PC in a specimen of 25ABCD gradation while keeping the other reference values unchanged. The proportion of inactive particles decreases, and the overall PC values increase slightly with an increase in the damping ratio (Figs. 4.9(a,b)). Similar to a change in μ and k/D , a

change in ξ affects the coarser particles more than the finer particles, further indicating limited influence of finer particles on the PC in a specimen (Fig. 4.9(c)).

4.5 Conclusions

A series of isotropic compression 3D DEM simulations were performed to investigate the effect of differences in gradations on the percentage of inactive particles, distribution of particle connectivity, and contact force transmission in granular assemblies. Additionally, a parametric study was conducted to identify the effect of contact law parameters. The results were presented as the cumulative distributions of particle connectivity computed based on the cumulative number and volume of particles as well as based on particle sizes. The results indicate that the highly polydisperse specimens with 25ABCD and bimodal gradations (i.e., with a higher C_v) have a larger percentage of inactive particles by number, which are predominantly the finer particles. However, the coarser particles in these gradations are surrounded by a higher number of finer particles, as shown by the increase in PC with an increase in particle size, and they carry the largest magnitude of contact normal forces. An increase in stiffness ratio, a decrease in particle friction coefficient, and a decrease in global viscous damping decrease the overall proportion of inactive particles in the specimen. Overall, this study provided enhanced understanding of the effect of PSD and contact law parameters on packing and force transmission in granular material specimen using DEM. Future studies could potentially explore the effect of particle shapes, gravity, and shear loading on the packing, force transmission, and fraction of inactive particles.

4.6 Acknowledgements

The National Science Foundation (NSF) provided the funding for this work under grant No. CMMI-1916152. The authors would also like to thank Katerina Ziotopoulou, Rachel Reardon, Francisco Humire, Sharif Ahmed, Nathan Love, Trevor Carey, and Anna Chiaradonna for their insights and recommendations.

4.7 References

- Ahmed, S. S. 2021. "Study on particle shape, size and gradation effects on the mechanical behavior of coarse-grained soils." PhD Thesis. University of California Davis.
- Ahmed, S. S., A. Martinez, and J. T. DeJong. 2023. "Effect of gradation on the strength and stress-dilation behavior of coarse-grained soils in drained and undrained triaxial compression." *J. Geotech. Geoenviron. Eng.*, 149 (5): 04023019.
- Amirpour Harehdasht, S., M. Karray, M. N. Hussien, and M. Chekired. 2017. "Influence of particle size and gradation on the stress-dilatancy behavior of granular materials during drained triaxial compression." *Int. J. Geomech.*, 17 (9): 04017077.
- Basson, M. S., R. Cudmani, and G. V. Ramana. 2020. "Evaluation of macroscopic soil model parameters using the discrete element method." *Advances in Computer Methods and Geomechanics*, Lecture Notes in Civil Engineering, A. Prashant, A. Sachan, and C. S. Desai, eds., 713–725. Singapore: Springer Singapore.
- Basson, M. S., and A. Martinez. 2020. "A DEM study of the evolution of fabric of coarse-grained materials during oedometric and isotropic compression." *Geo-Congress 2020*, 473–481. Minneapolis, Minnesota: American Society of Civil Engineers.

- Basson, M. S., A. Martinez, and J. T. DeJong. 2023a. "Effect of particle size distribution on monotonic shear strength and stress-dilatancy of coarse-grained soils." *GeoCongress 2023*, 10. Los Angeles.
- Basson, M. S., A. Martinez, and J. T. DeJong. 2023b. "DEM investigation of the effect of gradation on the strength, dilatancy, and fabric evolution of coarse-grained soils." *Submitted for possible publication in Journal for Geotechnical and Geoenvironmental Engineering*.
- Bathurst, R. J., and L. Rothenburg. 1990. "Observations on stress-force-fabric relationships in idealized granular materials." *Mechanics of Materials*, 9 (1): 65–80.
- Been, K., and M. G. Jefferies. 1985. "A state parameter for sands." *Géotechnique*, 35 (2): 99–112.
- Bernal, J. D., and J. Mason. 1960. "Packing of spheres: co-ordination of randomly packed spheres." *Nature*, 188 (4754): 910–911.
- Bernhardt, M. L., G. Biscontin, and C. O'Sullivan. 2016. "Experimental validation study of 3d direct simple shear dem simulations." *Soils and Foundations*, 56 (3): 336–347.
- Blott, S. J., and K. Pye. 2012. "Particle size scales and classification of sediment types based on particle size distributions: review and recommended procedures." *Sedimentology*, 59 (7): 2071–2096.
- Catt, J. 2020. "Soil particle size distribution and mineralogy as indicators of pedogenic and geomorphic history: examples from the Loessial soils of England and Wales." *Geomorphology and soils*, 202–218. Routledge.
- Cha, M., and J. C. Santamarina. 2019. "Pressure-dependent grain dissolution using discrete element simulations." *Granular Matter*, 21 (4): 101.

- Chaney, R., K. Demars, P. Lade, C. Liggiio, and J. Yamamuro. 1998. "Effects of non-plastic fines on minimum and maximum void ratios of sand." *Geotechnical Testing Journal*, 21 (4): 336.
- Chang, C. S., and M. Meidani. 2013. "Dominant grains network and behavior of sand-silt mixtures: stress-strain modeling." *International Journal for Numerical and Analytical Methods in Geomechanics*, 37 (15): 2563–2589.
- Ciantia, M. O., M. Arroyo, C. O'Sullivan, A. Gens, and T. Liu. 2019. "Grading evolution and critical state in a discrete numerical model of Fontainebleau sand." *Géotechnique*, 69 (1): 1–15.
- Cubrinovski, M., and K. Ishihara. 2002. "Maximum and minimum void ratio characteristics of sands." *Soils and Foundations*, 42 (6): 65–78.
- Doygun, O., H. G. Brandes, and T. T. Roy. 2019. "Effect of gradation and non-plastic fines on monotonic and cyclic simple shear strength of silica sand." *Geotech Geol Eng*, 37 (4): 3221–3240.
- Duverger, S., J. Duriez, P. Philippe, and S. Bonelli. 2021. "Rattlers' involvement for possibly looser critical states under higher mean stress." *EPJ Web Conf.*, (M. A. Aguirre, S. Luding, L. A. Pugnaloni, and R. Soto, eds.), 249: 11002.
- Farahnak Langroudi, M., A. Soroush, P. Tabatabaie Shourijeh, and R. Shafipour. 2013. "Stress transmission in internally unstable gap-graded soils using discrete element modeling." *Powder Technology*, 247: 161–171.
- Ghadr, S., and A. Assadi-Langroudi. 2019. "Effect of grain size and shape on undrained behaviour of sands." *Int. J. of Geosynth. and Ground Eng.*, 5 (3): 18.

- Huang, X., K. J. Hanley, C. O'Sullivan, and F. C. Y. Kwok. 2014. "Effect of sample size on the response of dem samples with a realistic grading." *Particuology*, 15: 107–115.
- Liu, D., C. O'Sullivan, and J. A. H. Carraro. 2021a. "Influence of particle size distribution on the proportion of stress-transmitting particles and implications for measures of soil state." *J. Geotech. Geoenviron. Eng.*, 147 (3): 04020182.
- Liu, D., C. O'Sullivan, and J. A. H. Carraro. 2021b. "The influence of particle size distribution on the stress distribution in granular materials." *Géotechnique*, 1–15.
- Mital, U., R. Kawamoto, and J. E. Andrade. 2020. "Effect of fabric on shear wave velocity in granular soils." *Acta Geotech.*, 15 (5): 1189–1203.
- Ng, T.-T. 2006. "Input parameters of discrete element methods." *J. Eng. Mech.*, 132 (7): 723–729.
- O'Sullivan, C. 2011. *Particulate discrete element modelling*.
- Radjai, F., S. Roux, and J. J. Moreau. 1999. "Contact forces in a granular packing." *Chaos*, 9 (3): 544–550.
- Reardon, R., F. Humire, S. S. Ahmed, K. Ziotopoulou, A. Martinez, and J. T. DeJong. 2022. "Effect of gradation on the strength and stress-dilatancy of coarse-grained soils: a comparison of monotonic direct simple shear and triaxial tests." *Geo-Congress 2022*, 226–236. Charlotte, North Carolina: American Society of Civil Engineers.
- Santamarina, J. C. 2003. "Soil behavior at the microscale: particle forces." *Soil Behavior and Soft Ground Construction*, 25–56. Cambridge, Massachusetts, United States: American Society of Civil Engineers.
- Scholtès, L., B. Chareyre, F. Nicot, and F. Darve. 2009. "Micromechanics of granular materials with capillary effects." *International Journal of Engineering Science*, 12.

- Shire, T., C. O'Sullivan, K. J. Hanley, and R. J. Fannin. 2014. "Fabric and effective stress distribution in internally unstable soils." *J. Geotech. Geoenviron. Eng.*, 140 (12): 04014072.
- Šmilauer, V., E. Catalano, B. Chareyre, S. Dorofeenko, J. Duriez, A. Gladky, J. Kozicki, C. Modenese, L. Scholtès, and L. Sibille. 2010. "Yade reference documentation." *Yade Documentation*, 474: 1–531.
- Sturm, A. 2019. "On the liquefaction potential of gravelly soils: characterization, triggering and performance." PhD Thesis. University of California Davis.
- Thornton, C. 2000. "Numerical simulations of deviatoric shear deformation of granular media." *Géotechnique*, 50 (1): 43–53.
- Wiącek, J., and M. Molenda. 2014. "Effect of particle size distribution on micro- and macromechanical response of granular packings under compression." *International Journal of Solids and Structures*, 51 (25–26): 4189–4195.
- Wiącek, J., and M. Molenda. 2018. "Numerical analysis of compression mechanics of highly polydisperse granular mixtures with different psd-s." *Granular Matter*, 20 (1): 17.
- Xiu, T.-X., W. Wang, K. Liu, Z.-Y. Wang, and D.-Z. Wei. 2018. "Characteristics of force chains in frictional interface during abrasive flow machining based on discrete element method." *Adv. Manuf.*, 6 (4): 355–375.
- Yamamuro, J. A., and P. V. Lade. 1997. "Static liquefaction of very loose sands." *Canadian Geotechnical Journal*, 34 (6): 905–917.
- Yilmaz, Y., Y. Deng, C. S. Chang, and A. Gokce. 2023. "Strength–dilatancy and critical state behaviours of binary mixtures of graded sands influenced by particle size ratio and fines content." *Géotechnique*, 73 (3): 202–217.

- Zhang, L., and T. M. Evans. 2018. "Boundary effects in discrete element method modeling of undrained cyclic triaxial and simple shear element tests." *Granular Matter*, 20 (4): 60.
- Zhao, C.-F., and N. P. Kruyt. 2020. "An evolution law for fabric anisotropy and its application in micromechanical modelling of granular materials." *International Journal of Solids and Structures*, 196–197: 53–66.

4.8 Tables and figures

Table 4.1: Average properties of the simulated gradations

<i>Soil</i>	D_{min} (mm)	D_{10} (mm)	D_{30} (mm)	D_{50} (mm)	D_{60} (mm)	D_{max} (mm)	C_u	C_c
Mono	2.21	2.21	2.21	2.21	2.21	2.21	1.0	1.0
100A	0.89	1.66	2.11	2.79	3.25	5.82	1.95	0.82
25ABCD	0.74	1.06	2.30	4.61	6.08	25.89	5.76	0.82
Bimodal	0.75	0.78	0.91	4.75	6.78	8.98	8.69	0.16
Curved	0.82	1.56	3.04	4.52	5.12	8.23	3.28	1.16

Table 4.2: DEM simulations parameters. Parameters in bold font indicate the control parameters for parametric study

<i>Parameter</i>	<i>Symbol</i>	<i>Value</i>
Stiffness ratio	k/D	1e7, 1e8 , 1e9 N/m ³
Normal to shear stiffness ratio	k_s/k_n	0.2
Particle density	ρ	2650 kg/m³
Friction coefficient during sample preparation	μ	0.01 , 0.1, 0.2, 0.4
Global viscous damping	ξ	0.05 , 0.25, 0.5
Number of particles	N	50000 , 100000, 150000

Table 4.3: Summary of tests conducted with the obtained void ratios, mechanical coordination numbers, and % of inactive particles at 100 kPa. Bold parameters indicate the parameters changed for parametric study.

<i>Specimen</i>	<i>Stiffness, k/D</i>	<i>Friction, μ</i>	<i>Damping, ξ</i>	<i>Number of Particles, N</i>	<i>Void Ratio, e</i>	<i>Mechanical Coordination Number, MCN</i>	<i>% of inactive particles by number</i>
Mono	1e8	0.01	0.05	50000	0.57	6.33	1
100A	1e8	0.01	0.05	50000	0.48	6.21	13
Bimodal	1e8	0.01	0.05	50000	0.31	6.32	3
Curved	1e8	0.01	0.05	50000	0.35	6.28	53
25ABCD	1e8	0.01	0.05	50000	0.26	6.25	20
Parametric study on 25ABCD	1e8	0.1	0.05	50000	0.29	5.61	33
	1e8	0.2	0.05	50000	0.31	5.12	42
	1e8	0.4	0.05	50000	0.34	4.43	61
	1e8	0.4	0.25	50000	0.37	4.37	54
	1e8	0.4	0.5	50000	0.39	4.32	47
	1e8	0.4	0.05	100000	0.35	4.38	59
	1e8	0.4	0.05	150000	0.36	4.46	62
	1e7	0.4	0.05	50000	0.31	5.36	34
	1e9	0.4	0.05	50000	0.37	4.18	73

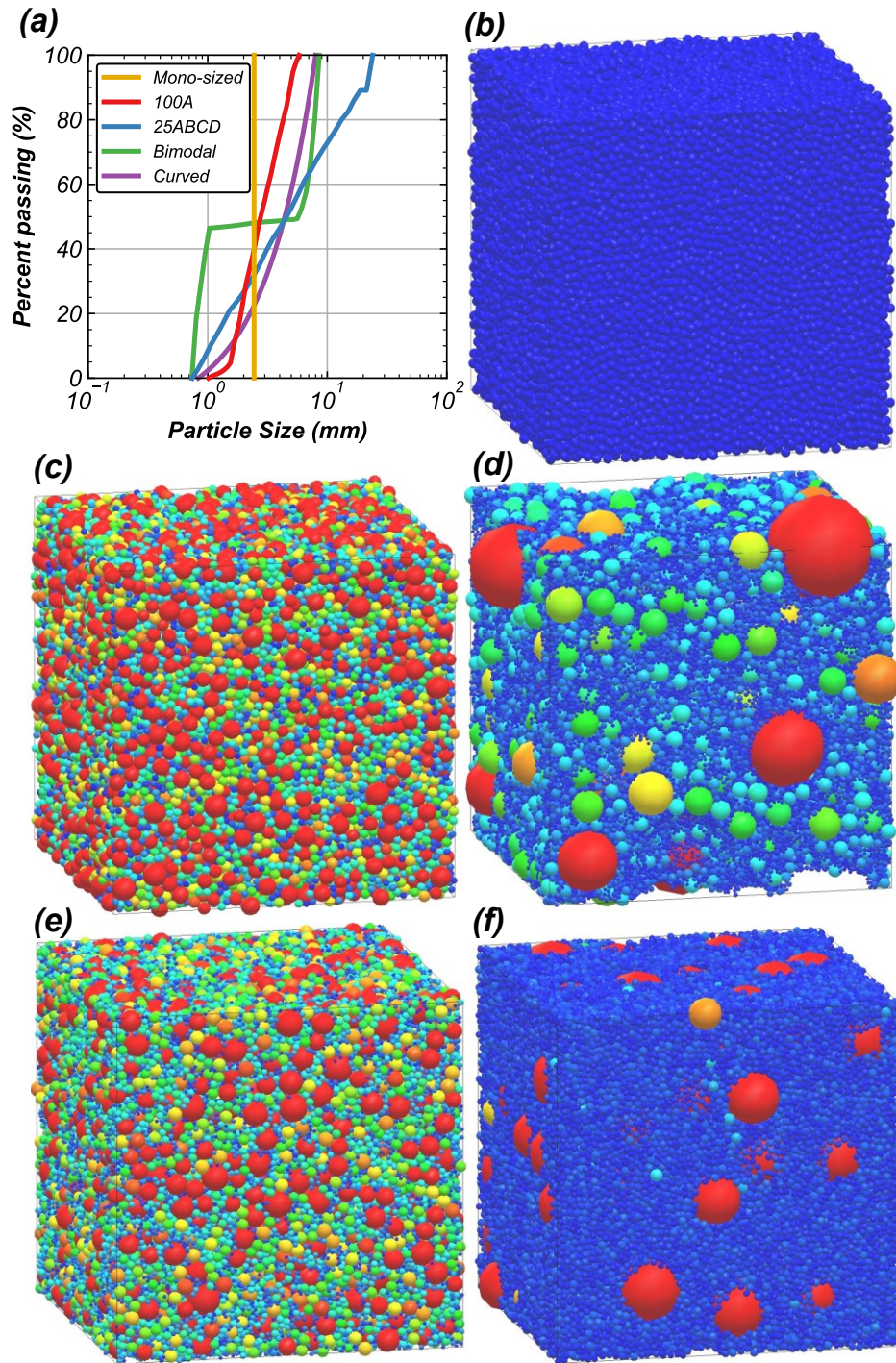


Figure 4.1: (a) Particle size distribution, and images of the specimen for (b) mono-sized, (c) 100A, (d) 25ABCD, (e) curved and (f) bimodal gradations.

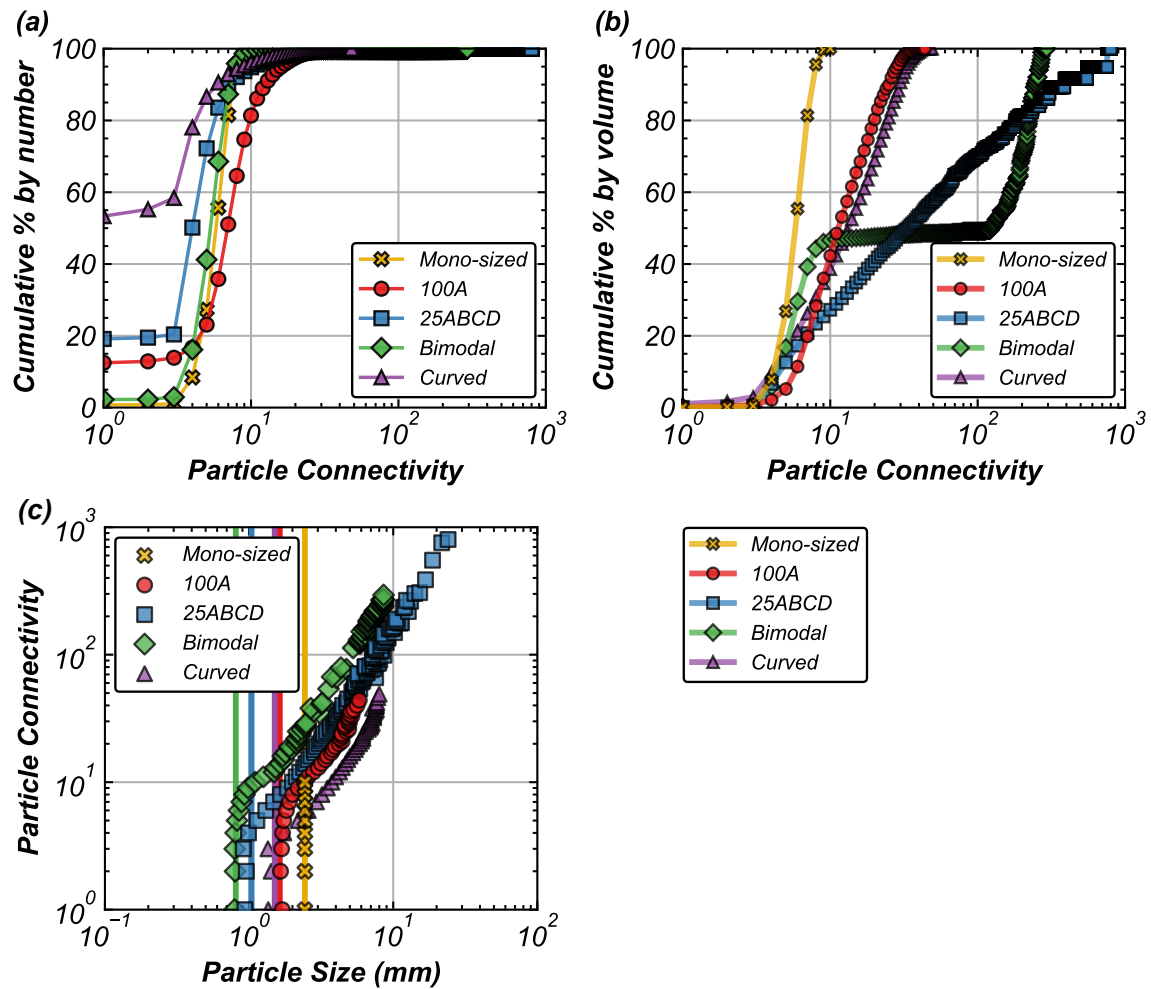


Figure 4.2: Cumulative distribution of particle connectivity for (a) number of particles and (b) volume of particles, and (c) variation of PC with particle sizes in specimens made of mono-sized, 100A, 25ABCD, bimodal, and curved gradations. The vertical lines denote the D_{10} of the gradation.

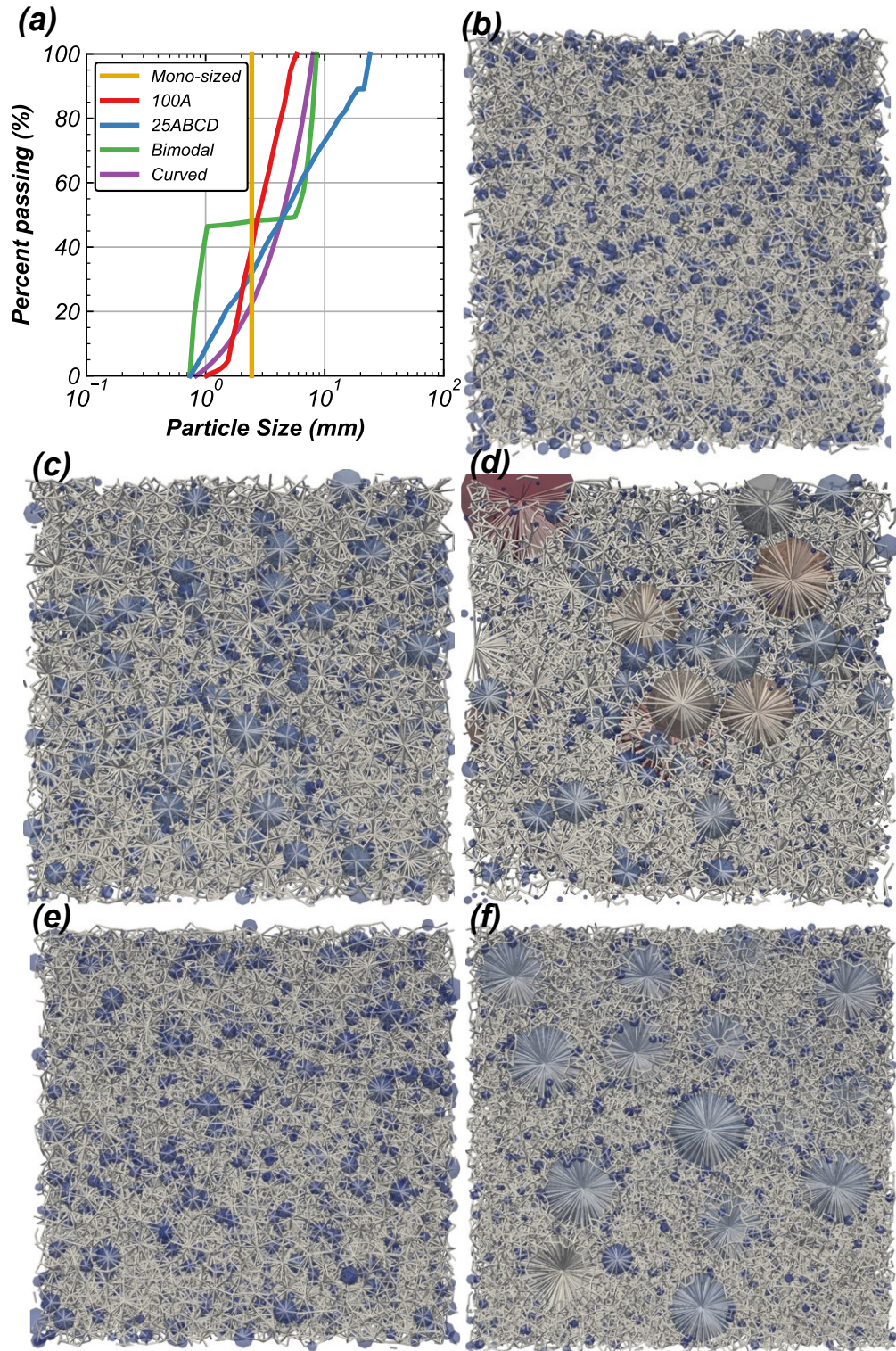


Figure 4.3: (a) Particle size distribution, and force chain maps of the specimen for (b) mono-sized, (c) 100A, (d) 25ABCD, (e) curved and (f) bimodal gradations.

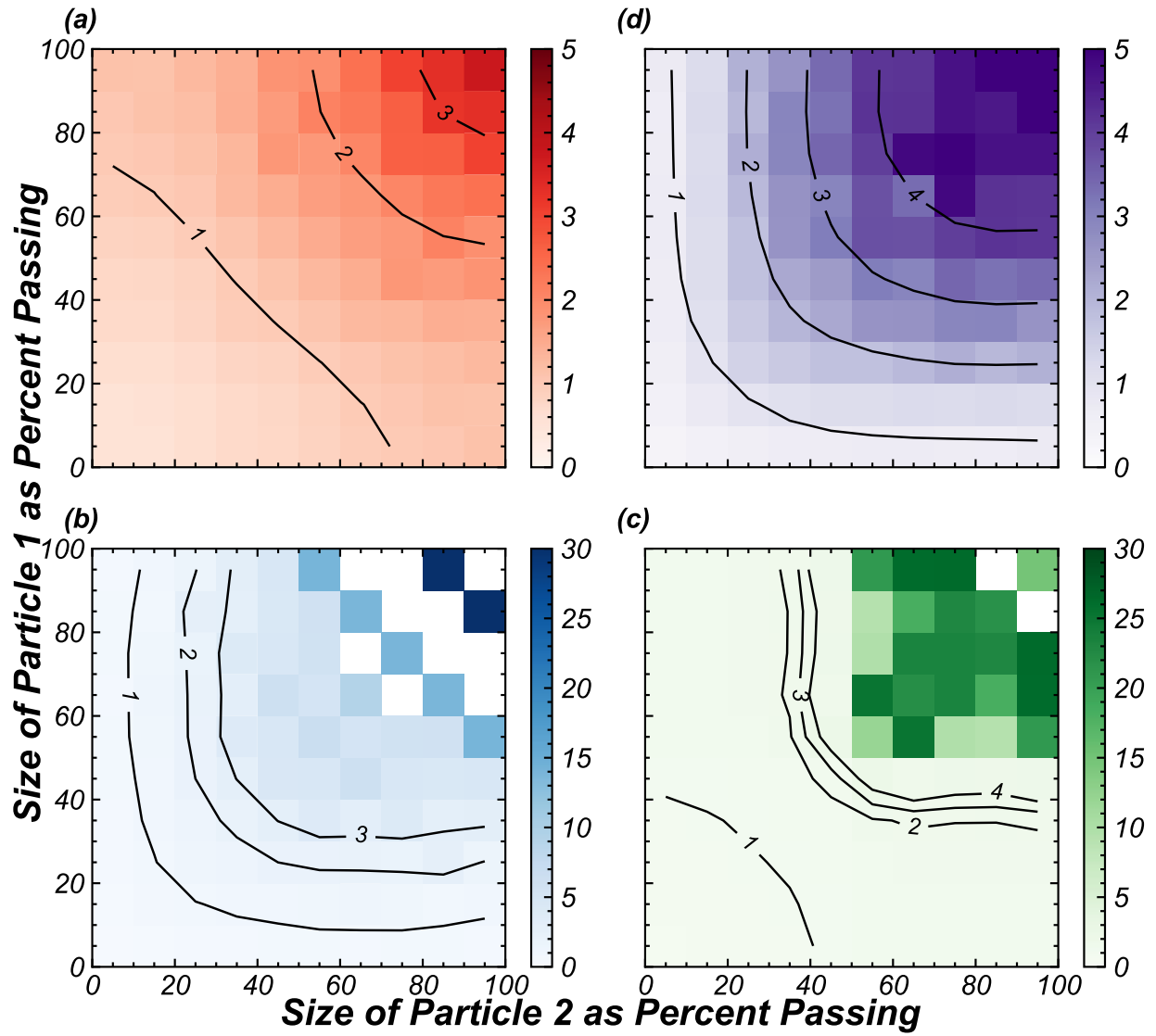


Figure 4.4: Distribution of F_n/\bar{F}_n with particle sizes (as percent passing) for specimens with (a) 100A, (b) curved, (c) 25ABCD, and (d) bimodal gradations.

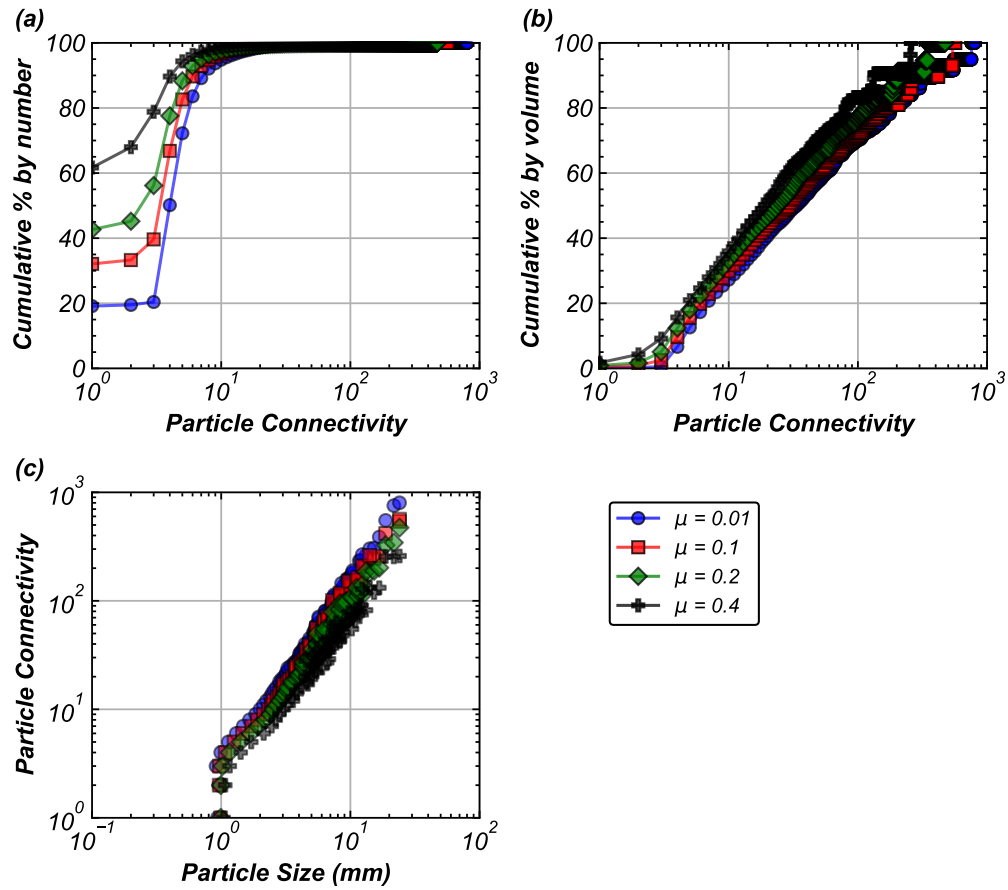


Figure 4.5: Variation of cumulative distribution of particle connectivity for (a) number of particles and (b) volume of particles, and (c) variation of PC with particle sizes in specimen of 25ABCD gradation with change in μ values of 0.01, 0.1, 0.2, and 0.4.

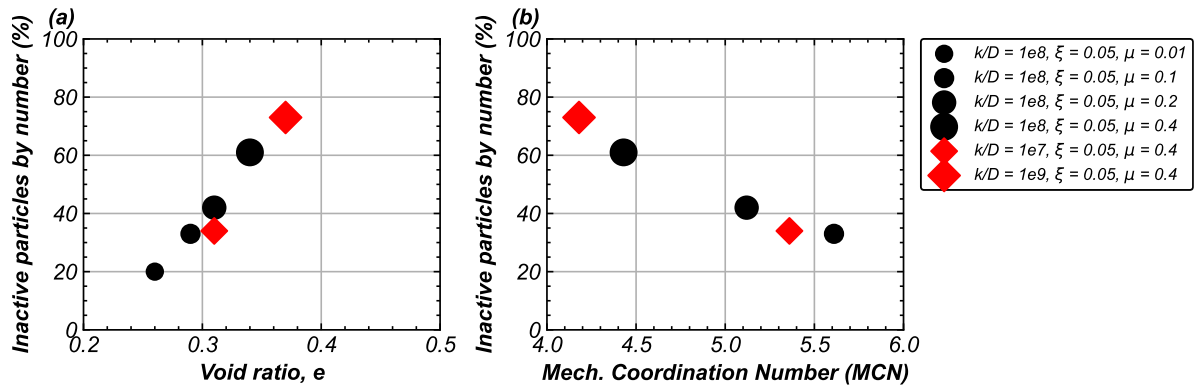


Figure 4.6: Comparison of percentage of inactive particles by number with (a) void ratio, and (b) mechanical coordination number for the various parametric cases.

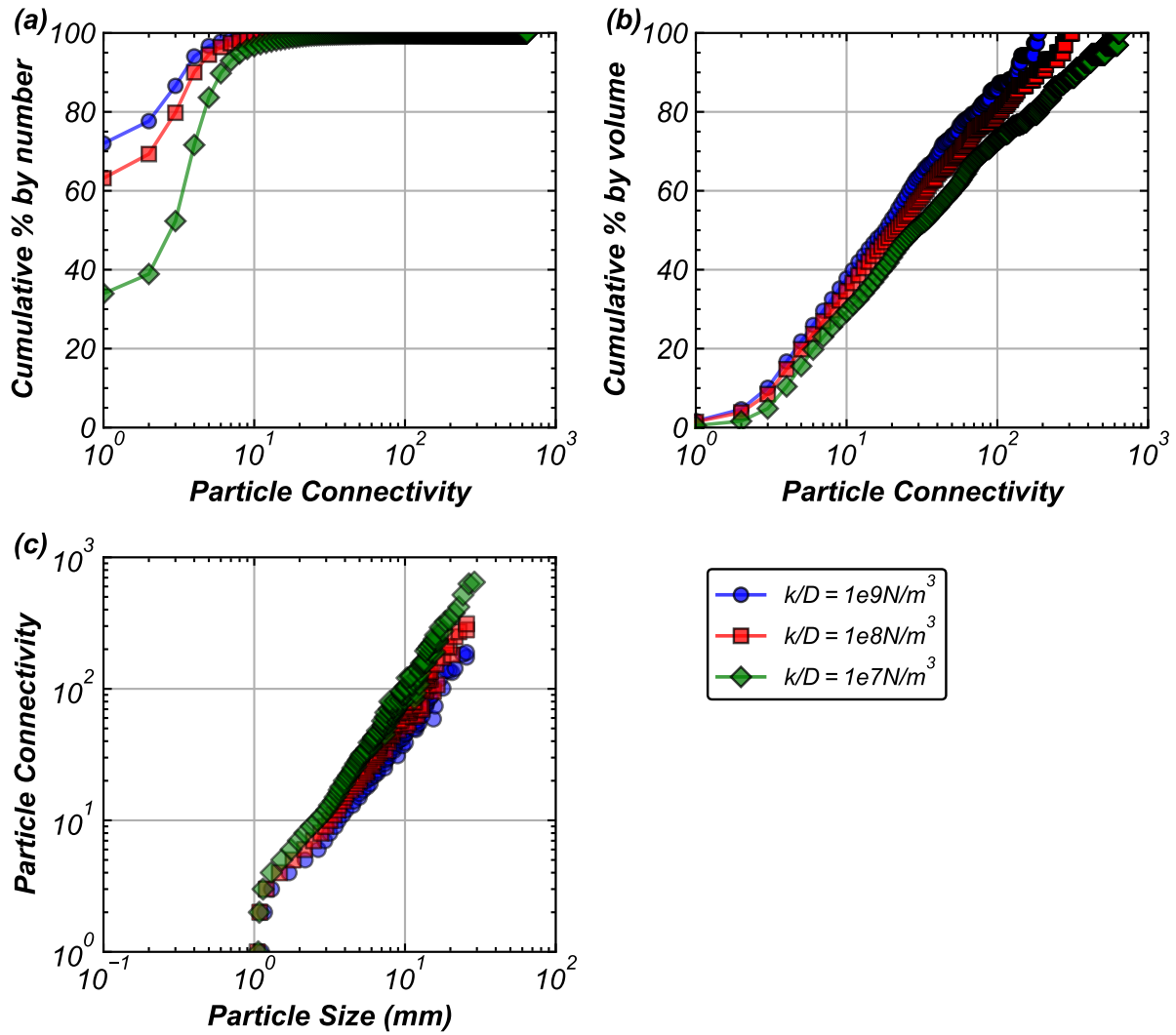


Figure 4.7: Variation of cumulative distribution of particle connectivity for (a) number of particles and (b) volume of particles, and (c) variation of PC with particle sizes in 25ABCD gradation specimen with change in the k/D values of $1e9 \text{ N/m}^3$, $1e8 \text{ N/m}^3$, and $1e7 \text{ N/m}^3$.

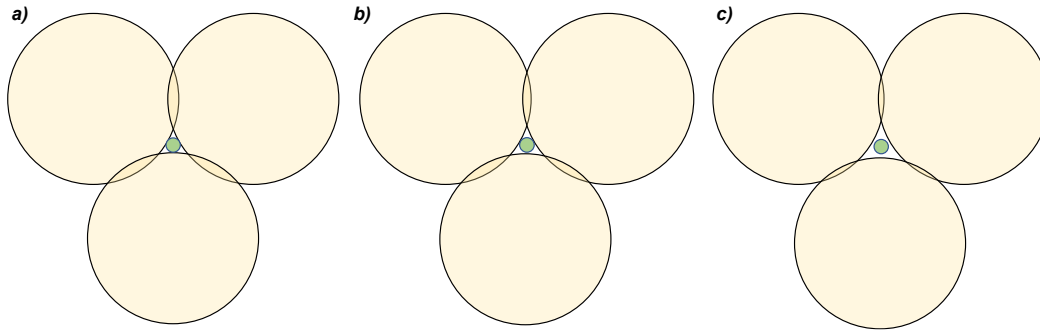


Figure 4.8: Schematic showing the contacts between coarser particles (yellow) and finer particle (green) for (a) lower k/D , (b) intermediate k/D , and (c) high k/D values without gravity.

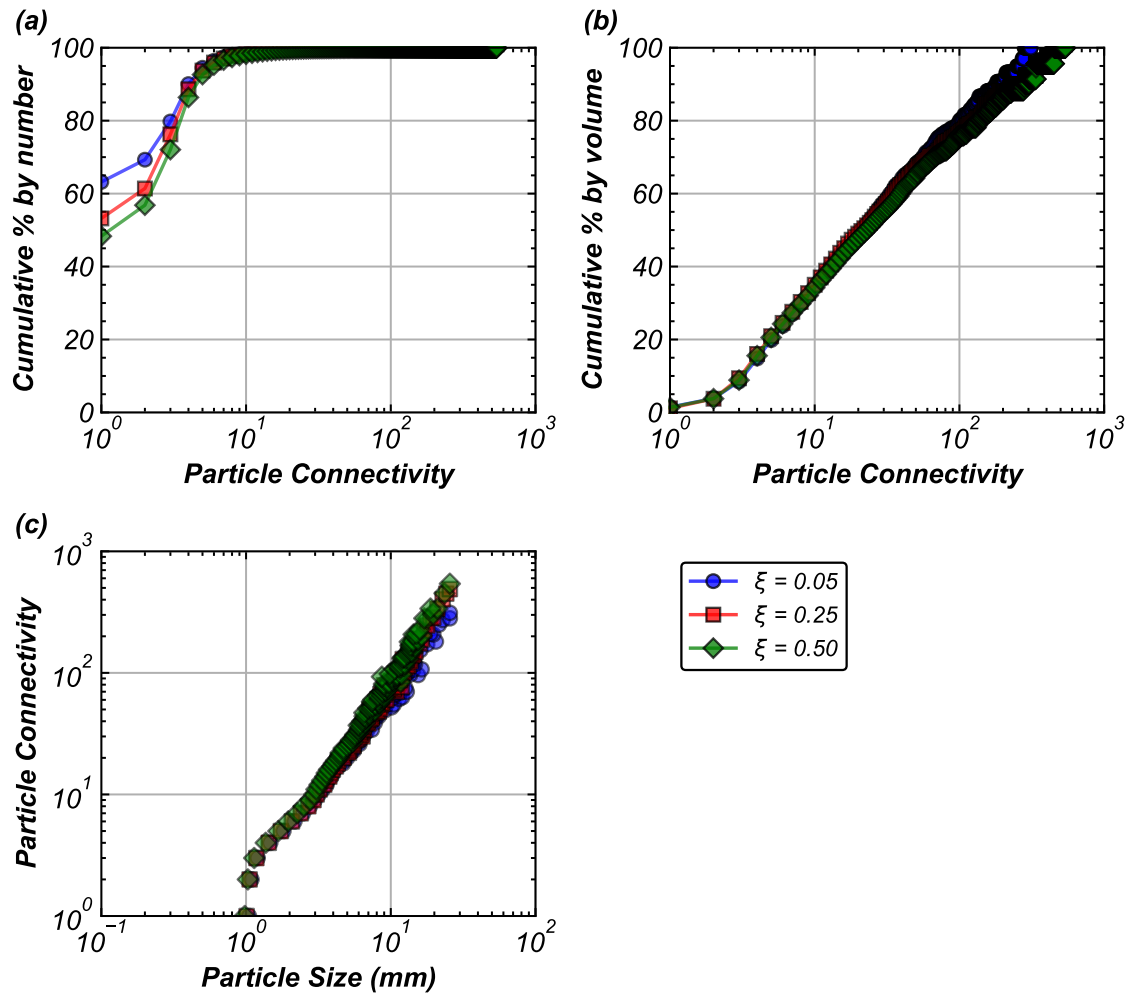


Figure 4.9: Variation of cumulative distribution of particle connectivity for (a) number of particles and (b) volume of particles, and (c) variation of PC with particle sizes in 25ABCD gradation specimen with change in the ξ of 0.05, 0.25, 0.50.

Chapter 5

DEM investigation of the effect of gradation on the strength, dilatancy, and fabric evolution of coarse-grained soils

Author's note: This paper will be submitted as a journal paper to the ASCE Journal of Geotechnical and Geoenvironmental Engineering authored by Mandeep Singh Basson, Alejandro Martinez, and Jason T. DeJong. The paper is presented herein with minor edits for consistency with the other chapters of this Dissertation.

5.1 Abstract

Design and analysis of geosystems built on coarse-grained soils with broader gradations are typically based on the methodologies developed for clean sands without explicit consideration of the effects of gradation, potentially leading to uncertainty in performance predictions. This study investigates the effect of changes in the gradation on the shear strength, stress-dilatancy behavior, critical state parameters, and fabric evolution of coarse grained-soils using 3D discrete element method (DEM) simulations. The DEM simulations of monotonic isotropically consolidated drained and undrained triaxial tests were conducted on specimens with coefficients of uniformity (C_u) between 1.9 and 6.4 composed of non-spherical particles following initial calibration of modeling parameters against a

complimentary set of experimental triaxial data. Results are used to evaluate the peak and critical state shear strengths, dilatancy responses, critical state lines, shear-induced pore pressures, and fabric evolution. Notably, an increase in C_u leads to increases in shear strength, dilative volume change, rate of dilation, negative pore pressure magnitude, and rate of pore pressure generation. The findings are compared with established frameworks to highlight the differences in response resulting from variations in C_u . The particle-level measurements indicate that gradation affects the packing characteristics and contact force transmission, where broader gradations result in the better interlocking of coarser particles and the formation of strong force networks aligned with the major principal stress direction. In contrast, finer particles provide resistance to buckling within these strong force networks. Additionally, particles smaller than D_{10} are inactive in stress transmission, while the percentage of particles active in stress transmission increases with an increasing C_u . The combination of macro and micro results contributes to understanding the mobilization of stress and its dependency on dilatancy in soils of varying gradation.

5.2 Introduction

Soils commonly found in natural deposits like alluvial gravelly soils contain a wide range of particle sizes. Naturally deposited by braided rivers, these deposits contain coarser particles significantly larger than clean sands, leading to coefficient of uniformity (C_u) values of 40 or higher (e.g, DeJong et al. 2016; Pires-Sturm et al. 2022). The particle size distribution (PSD) of these soils play a governing role in their behavior (Cubrinovski and Ishihara 2002). Understanding the strength, stress-dilatancy, critical state (CS), and liquefaction response of

these soils is crucial due to their frequent presence within or beneath critical geosystems such as dams, levees, tunnels, bridges, foundations, and pavements.

Several studies have investigated the influence of gradation on the stress-dilatancy and volume change response of well-graded soils. While the reported trends provide insights into the behavior of well-graded soils, some discrepancies and knowledge gaps still exist. For example, studies agree that an increase in C_u decreases the maximum and minimum void ratios, changing the position of the critical state line in the void ratio (e) and mean effective confining stress (p') space (e.g., Chaney et al. 1998; Cubrinovski and Ishihara 2002; Li et al. 2015; Youd 1973, Ahmed et al. 2023). Some studies report a decrease in shear strength with an increase in the gravel fraction (e.g., Knodel et al. 1990; Fragaszy et al. 1992; Evans and Zhou 1995), whereas most other studies indicate an increase in the shear strength and dilative volumetric response with an increase in the gravel fraction (e.g., Simoni and Houlsby 2006; Hamidi et al. 2012; Amirpour Harehdasht et al. 2017). Studies have reported increased stiffness measured through isotropic compression and shear wave velocity as the range of particle sizes becomes broader (e.g., Menq 2003; Sturm 2019; Ahmed et al. 2023). While studies have shown that at the same initial void ratio, more widely graded soils exhibit a more contractive behavior and lower undrained shear strengths (e.g., Yang and Luo 2017; Jiang et al. 2018; Harehdasht et al. 2017, 2018; Deng et al. 2021), recently Ahmed et al. (2023) reported that for the same initial state parameter (ξ_0 , as defined by Been and Jefferies 1985), more broadly graded soils exhibit a greater dilation angle, peak friction angle, and undrained shear strength. From a micromechanical perspective, the stress-dilatancy response is influenced by the packing characteristics and the transmission of contact forces. In soils with broader gradations, the coarser particles are in contact with a larger number of finer

particles, which promotes better interlocking. Additionally, a higher proportion of coarser particles actively participate in transmitting contact forces, forming a strong force network that aligns with the major principal stress direction. The finer particles within the specimen provide resistance to buckling within these strong force networks (e.g., Muir Wood and Maeda 2008; Li et al. 2015; Liu et al. 2021).

In practice, the stress-dilatancy response of well-graded gravelly soils is typically assessed using relationships such as those developed by Rowe (1962) and Bolton (1986). These widely adopted relationships are based on experimental data acquired from testing on poorly graded clean sands. Over the years, these relationships have been revisited, and additional ones have been proposed to capture the effects of particle shape, gradation, mineralogy, stress history, relative density and state, and fabric (e.g., Vaid and Sasitharan 1992, Simoni and Houlsby 2006, Muir Wood and Maeda 2008, Chakraborty and Salgado 2010). Despite recent advances, there are still gaps in the specific mechanisms responsible for the aforementioned effects of gradation on the mechanical behavior of soils, such as which state variable better captures the effects of density and effective stress, what is the role of the finer and coarser fractions of the soil in the mobilization of strength and dilatancy, and what corrections, if any, are needed to predict the stress-dilatancy of well-graded soils with established frameworks.

In this study, monotonic drained and undrained triaxial compression simulations are conducted using the discrete element method (DEM) to investigate the influence of gradation on the peak and critical state shear strengths, dilatancy responses, critical state lines, generation of shear-induced pore pressures, and evolution of the fabric of coarse-grained

soils. DEM is used to isolate the effect of gradation from those of particle shape and particle crushing. Three different granular assemblies with C_U values ranging from 1.9 to 6.4 are examined over a range of initial state parameters following initial calibration of modeling parameters against a complimentary set of experimental triaxial data. Both drained, and undrained monotonic responses are presented. The simulation results are compared with the seminal works of Bolton (1986) and Been and Jefferies (1985) to evaluate their ability to capture the effects of varying gradation. Moreover, a detailed analysis of soil fabric is presented, focusing on the influence of coarser particles and relative size difference between the coarser and finer particles on the particle connectivity and contact force transmission, along with the evolution of fabric anisotropy, to highlight the disparities in microscale response between different gradations at similar state parameters.

5.3 Simulation methodology

5.3.1 Simulated granular materials

The particle shape and gradations of the simulated materials were based on those of naturally occurring coarse-grained soil sourced from a marine deposit in Mauricetown, New Jersey. These soils have been extensively investigated at the University of California Davis using laboratory testing (Ahmed 2021; Reardon et al. 2022), physical modeling (Sturm 2019; Sawyer 2020; Carey et al. 2022), and numerical modeling (Chiaradonna et al. 2022; Basson et al. 2023). The simulated PSDs were upscaled compared to the experimental distributions by a factor of 20 to achieve reasonable computational simulation times, as typically done in DEM simulations (Ciantia et al. 2015; Roessler and Katterfeld 2018; Coetzee 2019). The

experimentally obtained (EXP) and DEM PSDs for the selected gradations are presented in Fig. 5.1(a), while the gradation characteristics are shown in Table 5.1.

The particle shape and size distribution influence the initial packing characteristics and evolution of fabric during shearing (e.g., Shinohara et al. 2000; Zhao et al. 2017; Ghadr and Assadi-Langroudi 2019). In DEM simulations, realistic particle shapes from natural sands are typically recreated using polyhedras (Seyedi Hosseininia 2012; Harkness et al. 2016), ellipses (Markauskas et al. 2010; Yan et al. 2010), mathematical modeling of particle shapes (Kawamoto et al. 2016; Wei et al. 2018), or particle clumps (Garcia et al. 2009). Prior research has demonstrated that approximating particle shapes using clumped spherical particles is a computationally efficient method that does not require additional contact law modifications (Ferrellec and McDowell 2008; Wu et al. 2021). Limitations of this method include underestimating angularity due to the use of spherical particles to form the clumps (Price et al. 2007) and the need to correct the mass and inertia of the clumped particles (Garcia et al. 2009; Suhr and Six 2020). Nonetheless, clumped particles have been widely adopted to simulate a variety of realistic particle shapes (Maeda and Hirabayashi 2006; Markauskas et al. 2010; Wu et al. 2021; Tolomeo and McDowell 2022).

The particle shapes were recreated using different clump templates in the DEM simulations. Seven different clump templates with two or three overlapping spheres were designed based on the recommendation from Suhr and Six (2020). The particle shape templates were created to approximate experimentally-measured distributions of particle roundness, perimeter, width/length, circle ratio, area, diameter sphericities, regularity (Cho et al. 2006), overall regularity (Liu and Yang 2018), and SAGI (Altuhafi et al. 2016) of 100A

particles, determined using the method developed by Zheng and Hryciw (2015). Three of the seven templates, presented in Fig. 5.1(b), were chosen based on the comparison between the average, upper quartile, and lower quartile values of particle shape parameters between the real and simulated particles (Fig. 5.2(a)). As shown, all the parameters are reasonably approximated by the three clump templates, with the exception of roundness. This is because the roundness parameter quantifies the radii of particle corners, which cannot be reproduced with only two or three spherical particles comprising a clump. To generate the specimens, the clump templates were applied uniformly to all three gradations to isolate the effect of gradation from that of particle shape.

The percentages by mass of the selected clump templates included in the granular assemblies were chosen based on a parametric study aimed at matching the experimentally measured minimum and maximum void ratios (e_{max} and e_{min} , respectively). Typically, in DEM simulations, the e_{max} and e_{min} are estimated by preparing specimens at a given confining stress with large and small friction coefficients (μ_{prep}) and damping (ζ_{prep}), which produce the loosest and densest packings that can be attained by the simulated assemblies (Muir Wood and Maeda 2008; Gu et al. 2020; Zuo et al. 2023). Here, a confining stress of 10 kPa was selected for determining e_{max} and e_{min} . Multiple specimens with the 100A gradation were generated using different percentages by mass of the clump templates to create the densest ($\mu_{prep} = 0.01$, $\zeta_{prep} = 0.05$) and loosest ($\mu_{prep} = 0.5$, $\zeta_{prep} = 0.5$) packings. Fig. 5.2(b) compares the experimental and numerical e_{max} and e_{min} values for the different distributions of clump templates. The assemblies with 70% clump #1, 20% clump #2, and 10% clump #3 were selected for all the simulations because they matched the experimental e_{max} and e_{min} values and provided reasonable calibration for the drained triaxial response, as described in more

detail below. Based on these proportions of clump templates, the e_{max} and e_{min} values were determined for the 33ABC and 25ABCD gradations, which also showed a reasonable match with the experimental values reported by Ahmed et al. (2023) as shown in Fig. 5.2(c).

5.3.2 Simulation methodology

Monotonic drained and undrained triaxial simulations were performed using the three-dimensional DEM code YADE (Šmilauer et al. 2010). The triaxial simulations were performed on three-dimensional cubical specimens with periodic boundary conditions, which ensured homogenous strain fields and prevented strain localization in the specimens (Huang et al. 2014a; Zhang and Evans 2018). The specimen size ($D_{specimen}$) was different for the specimens of different gradations, as shown in Fig. 5.3. $D_{specimen}$ was determined based on recommendations from previous studies (O’Sullivan 2011; Huang et al. 2014a) specifying $D_{specimen}$ as the maximum size between 20 times D_{50} or 4 times the largest particle diameter (D_{max}). The $D_{specimen}/D_{50}$ ratio ranged between 21.0 for 25ABCD and 22.1 for 100A, while the $D_{specimen}/D_{max}$ ratio varied between 4.2 for 25ABCD and 10.6 for 100A. To evaluate the effect of the specimen size on the response, an additional specimen with $D_{specimen}$ 2.1x the aforementioned value and with 1.5x the number of particles (75,000 as compared to 50,000) for the 25ABCD gradation. Fig. S5.1 presents a comparison between the drained triaxial results for 25ABCD and 25ABCD (2.1x) specimens prepared at a confining pressure (p') of 100 kPa. Increasing the specimen size and the number of particles in the 25ABCD (2.1x) specimen does not produce significant variations in the response, and any observed differences in the strain hardening and volumetric response can be attributed to variations in the initial void ratio (e_0). Specifically, the peak q value difference was approximately 1.2%, and the volumetric strain ε_v differences were 1.1%. Finally, the tested specimens consisted

of about 35,000 clumps for the 100A specimen and about 50,000 clumps for 33ABC and 25ABCD specimens.

The simulation procedure consisted of two steps: specimen preparation and shearing. The specimens were prepared by isotropically compressing a cloud of non-contacting clumps to an isotropic p' of 100, 400, or 800 kPa. This sample preparation technique produces specimens with negligible initial fabric anisotropy, as described in Basson and Martinez (2023) and shown later. The gravitational field was not simulated during sample preparation and shearing. The prepared specimens were then sheared to an axial strain of 25% with a constant strain rate. A uniform compressive strain field was applied for the drained simulations while the confining stress was maintained at a constant value using servo control algorithms. The undrained conditions were performed using the constant volume approximation, as typically done in DEM simulations and laboratory experiments (e.g., Dyvik et al. 1987; Bonilla 2004; Hanley et al. 2013; Zhang and Rothenburg 2020). During the tests, a uniform compressive strain field was applied in the vertical direction, and a uniform extension field was applied in the two horizontal directions, ensuring a constant specimen volume. The shearing strain rates for all simulations were calculated by keeping the inertial number below 10^{-4} and the unbalanced force ratio below 10^{-2} to achieve a quasi-static response (da Cruz et al. 2005; Martin et al. 2020). The stresses and strains reported were computed in a measurement cube slightly smaller than the specimen size.

The linear elastic contact model with Mohr-Coulomb plasticity was used to model the contact interactions between the clumped particles. The normal contact stiffness was determined based on a constant normal stiffness to particle diameter ratio (k/d), which

normalizes the effect of particle size (Scholtès et al. 2009). Table 5.2 summarizes the contact parameters used in all the simulations. These values were obtained by iteratively changing the contact parameters and comparing the DEM results of drained triaxial simulations on the 100A specimen to the corresponding experimental results reported by Ahmed et al. (2023). Fig. 5.4 compares the experimental and DEM results for specimens prepared at a confining pressure (p') of 100 kPa and with initial void ratios, as reported in Ahmed et al. (2023). The comparison shows a satisfactory agreement in the initial stiffness, peak deviator stress (q) ($q = \sigma'_1 - \sigma'_3$) (Fig. 5.4(a)), and void ratio (e) evolution with the p' (Fig. 5.4(d)). Specifically, the initial stiffness of the q - e_a curves, measured from the origin to a q of 50% of the peak value, is 22.6 MPa, 34.2 MPa, and 45.6 MPa in the simulation, and 25.5 MPa, 37.8 MPa, and 52.4 MPa in the experiment for the tests with e of 0.80-0.82, 0.75-0.75, and 0.68-0.69, respectively. The peak q values differ approximately -8.2%, 1.0%, and -0.3% between the simulations and experiments. The calibrated parameters overestimate the dilation rate (Fig. 5.4(b)) and underestimate the deviatoric stress at a critical state (Fig. 5.4(a)). These differences are likely due to differences in the particle shape (i.e., larger roundness of the clumps as shown in Fig. 5.2(a)) and boundary effects (i.e., periodic in DEM versus a flexible membrane in the experiment). Nonetheless, the obtained contact parameters are considered appropriate for the simulations and are applied consistently across the specimens of all gradations subjected to drained and undrained triaxial compression.

5.4 Triaxial compression simulations

This section presents the results of 27 drained and 24 undrained triaxial simulations performed on 100A, 33ABC, and 25ABCD specimens. First, the critical state lines (CSLs) are

presented to highlight the effect of gradation and determine the state parameters of the tested specimens. Representative drained responses of specimens at different ξ_0 and mean confining stresses are then presented. Then, differences in specimen fabric at initial, peak, and critical state are presented to quantify the differences in fabric evolution. Next, the undrained response of specimens at different ξ_0 is presented. Finally, a discussion and comparison of the results with the corresponding ξ_0 are provided and compared to Been and Jefferies (1985) trends. The details of the drained and undrained simulations can be found in Tables 5.3 and 5.4.

5.4.1 Critical state lines

The response of a specimen under triaxial compression, and the associated strength and stress-dilatancy parameters, are influenced by the specimen density and confining stress conditions, collectively represented by the specimen state. Previous studies have proposed various definitions for the specimen state, typically represented by the position of the current specimen state relative to a reference state (Been and Jefferies 1985; Bolton 1986; Wang et al. 2002). The relative density (D_R) and ξ_0 are widely state parameters, where D_R of the specimen is obtained by comparing the initial void ratio (e_0) to the e_{max} and e_{min} , while the ξ_0 quantifies the difference in between e_0 and the void ratio at critical state (e_{cs}) under the same p' . Since the e_{max} and e_{min} obtained from DEM simulations depend on the applied confining stress and the inter-particle friction coefficient (Abbireddy and Clayton 2010), subjectivity is associated with the definition of the D_R . In addition, Ahmed et al. (2023) showed that ξ_0 is a more robust parameter for discerning the effects of gradation on the mechanical response of soils. Therefore, in this study, a comparison of drained and undrained triaxial compression responses is performed based on ξ_0 .

The CS represents a specimen state with no further changes in volume and stress despite continuous shearing (Schofield and Wroth 1968). For the DEM simulations, the drained and undrained responses were considered to have attained a critical state value during shearing at the axial strain of 25% because the responses show no changes in q , p' , ε_v , and e . The average e , q , and p' obtained for the last 2.5% axial strain of each simulation were used to estimate the CSLs in e - $\log(p')$ and q - p' spaces (Fig. 5.5). In the figure, the solid lines show the drained stress paths, and the dashed line shows the undrained stress paths. The specimens with dilative tendencies showed an increase in e (drained) or p' (undrained), while the contractive specimens showed corresponding decreases in e and p' . The CSLs in e - $\log(p')$ space show a clear curvature in response as p' is increased; therefore, the CSLs were obtained by least square fitting of data points to a power function (Li et al. 1999; Wang et al. 2002):

$$e_{cs} = e_r - \lambda \left(\frac{p'}{p_{atm}} \right)^\alpha \quad (5.1)$$

where e_r is the reference e at a p' of 1 kPa, p_{atm} is the atmospheric pressure (101.3 kPa), and λ and α are the fitting parameters that control the slope and curvature of the CSL. In the study, the value for the α parameter is kept constant at 0.7 based on the recommendation of Li et al. (1999) and Huang et al. (2014b). Using a constant α value enables comparison of the CSLs in terms of their position (e_r) and slope (λ) in e - $\log(p')$ space. The stress paths in the q - p' space converge to linear CSLs with a slope of M . This slope was used to obtain the critical state friction angle (ϕ'_{cs}) as:

$$\phi'_{cs} = \sin^{-1} \left(\frac{3M}{6+M} \right) \quad (5.2)$$

The change in gradation affects the CSL parameters, e_r , λ , and M . In the e - $\log(p')$ space, the reference void ratio e_r decreases significantly with an increase in C_U , decreasing from 0.94 for 100A to 0.66 for 33ABC, and to 0.59 for 25ABCD, which is in agreement with the decrease of e_{max} and e_{min} with increasing C_U (Fig. 5.2b, Sturm and DeJong 2022). Similarly, the slope of the CSL shows a significant decrease from a value of -0.019 for the 100A material to -0.008 for 33ABC, however further broadening of the gradation did not result in appreciable changes in λ . A similar decrease in e_r and λ with C_U is reported from experimental (Ahmed et al. 2023; Amirpour Harehdasht et al. 2017; Yang and Luo 2018) and DEM studies (Yan and Dong 2011; Huang et al. 2014b; Li et al. 2015). In the q - p' space, an increase in C_U results in modest decreases in M , from 1.26 ($\phi'_{cs} = 31.3$) for 100A, 1.22 ($\phi'_{cs} = 30.45$) for 33ABCD, and 1.14 ($\phi'_{cs} = 28.6$) for 25ABCD. This small change in ϕ'_{cs} as a result of changes in gradation is consistent with the results presented in past studies (Shinohara et al. 2000; Muir Wood and Maeda 2008; Voivret et al. 2009). However, other experimental results have shown either no effect or a slight increase in M with increasing C_U (Ahmed et al. 2023; Polanía et al. 2023). This difference in trends may be caused by effects of particle size, which are absent in the DEM simulations presented here, or by the different boundary conditions between experiments and simulations (i.e., flexible membrane versus periodic boundaries).

5.4.2 Drained triaxial response

Representative results from drained triaxial simulations conducted on 100A, 33ABC, and 25ABCD specimens prepared at different ξ_0 are presented for a p' of 100 kPa (Fig. 5.6) and 800 kPa (Fig. 5.7). For brevity, the response of the specimens subjected to a confining stress

of 400 kPa is not presented here but is elaborated on in Basson et al. (2023). Throughout this study, the response of 100A is presented in red, 33ABC in green, and 25ABCD in blue. Table 5.3 provides the e_0 , D_R , and ξ_0 for the drained simulations.

The simulation results show the behaviors characteristic of coarse-grained soil specimens subjected to triaxial shearing (Figs. 5.6 and 5.7). Namely, at the same p' of 100 kPa, the denser specimens (smaller ξ_0) exhibit a higher initial stiffness, greater peak q , and a more dilative volume change than the looser specimens (larger ξ_0) for all three materials. The denser specimens show a distinct peak q value followed by strain softening until the specimen reaches the critical state. The dilative volume change of the denser specimens increases rapidly at small axial strains, and they reach stable values at axial strains between 10 and 15%. In contrast, the q of the looser specimens continues to increase until reaching its maximum value at a critical state. For these specimens, the volume change is predominantly contractile, with the exception of the 100A specimen, which shows modest dilation. At a p' of 800 kPa, all materials mobilize a greater q which is reached at a greater ε_a than for the specimens subjected to a p' of 100 kPa (Fig. 5.7). The dilative volume changes are smaller for the specimens subjected to the greater p' , and the specimens exhibit a higher magnitude of contraction at a p' of 800 kPa.

A comparison of the drained triaxial response for the 100A, 33ABC, and 25ABCD specimens at a similar ξ_0 of about -0.10 and subjected to a p' of 100 kPa exemplify the effect of C_u , where specimens with broader gradations mobilize greater peak q values and exhibit more dilative responses (Fig. 5.8). At the peak state, the 25ABCD and 33ABC specimens mobilize the highest q ; however, at the critical state, the 100A specimen mobilizes the

highest q followed by 33ABC and 25ABCD specimens, respectively. The 25ABCD specimens show the highest dilation rate and the largest dilative volume change, followed by the 33ABC and 100A specimens. These observations are consistent with results presented in past studies (Ahmed et al. 2023; Amirpour Harehdasht et al. 2017; Simoni and Houlsby 2006).

5.4.3 Stress-dilatancy behavior

Bolton (1986) modified Rowe's (1962) stress-dilatancy relationship based on the data obtained from experimental tests conducted on poorly graded sands with C_u values smaller than 2.5. Bolton (1986) presents a relationship between the difference in peak and critical state friction angles and maximum dilation angle (ψ_{max}):

$$\phi'_p - \phi'_{cs} = b \cdot \psi_{max} \quad (5.3)$$

The peak friction angle was computed based on the peak stress ratio ($\eta_{peak} = q/p'$ at peak state) using the equation:

$$\phi'_p = \sin^{-1} \left(\frac{3\eta_{peak}}{6 + \eta_{peak}} \right) \quad (5.4)$$

ψ_{max} was computed based on the equation presented in Vaid and Sasitharan (1992) as:

$$\psi_{max} = \sin^{-1} \left(\frac{2}{\frac{3}{(d\varepsilon_v/d\varepsilon_a)_{max}} + 1} \right) \quad (5.5)$$

where $(d\varepsilon_v/d\varepsilon_a)_{max}$ is the maximum rate of dilative volume change with respect to axial strain. Bolton (1986) proposed a b value of 0.8 for plane strain shearing, while other studies have reported a range of b values between 0.2 and 0.6 for triaxial compression conditions (Chakraborty and Salgado 2010).

The drained DEM results indicate an increase in the b parameter with an increase in C_U . Namely, the b parameter was 0.30 for 100A, 0.38 for 33ABC, and 0.42 for 25ABCD. The b parameter was determined by fitting a straight line passing through the origin to the $\phi'_p - \phi'_{cs}$ versus ψ_{\max} relationships, as shown in Fig. 5.9(a). Previous studies suggest a smaller influence of C_U on the b parameter (Amirpour Harehdasht et al. 2017; Reardon et al. 2022; Ahmed et al. 2023). However, the DEM results show a non-linear increase of b with C_U . The difference between the experimental and simulation results could be attributed to the effect of particle size, which is present in the experiment but absent in the simulations.

A comparison of the $\phi'_p - \phi'_{cs}$ versus p' at failure results from the drained triaxial simulations and the empirical trends from Bolton (1986) reveals differences in the trends for the broader gradations (Fig. 5.9(b)). Specifically, the data points for the 33ABC and 25ABCD specimens with $D_R \sim 45\%$ are closer to the $D_R = 75\%$ trendline from Bolton. The data points for both the $D_R \sim 65\%$ and $D_R \sim 80\%$ specimens for the 33ABC and 25ABCD specimens are located above the $D_R = 100\%$ trendline. Comparison of the 100A results shows smaller differences, with the specimen with $D_R \sim 45\%$ plotting close to the empirical trendline of $D_R = 50\%$, the specimens at $D_R \sim 65\%$ plotting slightly below the 75% empirical trendline, and the specimen at $D_R \sim 80\%$ plotting slightly below the 100% trendline. The systematic underprediction of $\phi'_p - \phi'_{cs}$ for a given p' for broader gradations can be attributed to increased dilative response, which may not be captured by the Bolton (1986) results on poorly graded soils. Similar observations regarding this systematic underprediction have been reported in experimental triaxial and direct simple shear tests by Ahmed et al. (2023) and Reardon et al. (2021).

5.5 Fabric evolution during drained triaxial simulations

This section presents the influence of widening gradation on the soil fabric, aiming to explain the differences in the shear strength and stress-dilatancy behavior observed in drained triaxial simulations. In particular, the particle packing and contact force transmission characteristics at the initial, peak, and critical states, along with the evolution of fabric anisotropy with increasing axial strain, are evaluated for 100A, 33ABC, and 25ABCD specimens at a similar ξ_0 of -0.1 (i.e., Fig. 5.8).

5.5.1 Particle connectivity

Soil gradation governs the packing characteristics and the transmission of global stresses to individual particles. The presence of a wide range of particle sizes allows the finer particles to fill the voids between coarser particles, leading to increased interlocking and improved contact force transmission (Chang and Meidani 2013; Doygun et al. 2019; Wiącek and Molenda 2014; Yilmaz et al. 2023). The packing characteristics can be evaluated using the coordination or mechanical coordination numbers, where the latter does not consider the influence of particles with zero or one contact (Thornton 2000). However, these quantities are defined based on the average contact number per particle for an assembly; thus, they obscure the differences in contact numbers between the coarser and finer particles of an assembly. Instead, the Particle Connectivity (PC) is calculated for each particle as the number of contacts with its neighbors, allowing for the evaluation of distributions as a function of particle size. PC has recently been adopted as a more effective measure of packing characteristics for broader gradations (Liu et al. 2021a; b).

Broader gradations produce a wider distribution of PC. The PC distributions for 100A, 33ABCD, and 25ABCD soils with ξ_0 of -0.1 at the initial, peak, and critical state are presented in Figs. S5.2(a), 5.10(a) and 5.11(a), respectively. The cumulative distributions are generated by calculating the cumulative volume of individual particles with a given PC value. At the initial, peak, and critical states, the 25ABCD specimen has the greatest PC number for any given cumulative % by volume, and the 100A specimen has the lowest PC number. For example, at the peak state, the 25ABCD specimen has a maximum PC of 434, while the 100A specimen has a maximum PC of 34 (Fig. 5.10(a)). The trends reported here are in agreement with those presented by (Liu et al. 2021a; b).

Greater PC values in the more broadly graded specimens mean that the particles are in a more statically indeterminate state, producing an enhanced interlocking which would produce a greater dilation during shearing (Santamarina 2003). This is observed in the triaxial response reported in Fig. 5.8, where the 25ABCD specimen exhibits a more dilative response. The PC decreases as the axial strain increases for all the specimens (e.g., from 1019 at initial to 434 at peak and 275 at critical state for 25ABCD, Figs. 5.10(a) and 5.11(a)) due to particle rearrangement from dilation. The particle fraction not active in contact force transmission (PC less than 1) is a very small percentage (less than 1%) of the overall specimen for all specimens, indicating stable packings.

The broader gradations produce wider ranges of PC values. The distribution of average particle size corresponding to individual PC value at the initial, peak, and critical states of specimens with ξ_0 of -0.1 is presented in Figs. S5.2(b), 5.10(b) and 5.11(b), respectively. The results demonstrate that particle size increases with PC for all three specimens, and that the

more broadly graded specimens have greater PC values. For instance, the largest particle in the 25ABCD specimen has a diameter of 71.7 mm and is connected to 434 and 275 particles at the peak and critical states, respectively. In comparison, the largest particle in the 100A specimen is 6.2 mm and is connected to 34 and 31 particles at the peak and critical states, respectively. These results also suggest that the greater PC in the more broadly graded specimens promote greater interlocking, leading to higher peak strengths and increased dilation for broader gradations (i.e., Fig. 5.8). Interestingly, the average particle size for PC values of zero and one is close to the 10th percentile value (D_{10}), as indicated by vertical lines in Figs. S5.2(b), 5.10(b), and 5.11(b). Additionally, the distributions become nearly vertical at lower PC values between 1 and 5. Overall, these findings indicate that on average the smaller particles in an assembly are less participative in the force transmission, with D_{10} providing a reasonable estimation of the size demarcating active and inactive particles.

5.5.2 Contact force transmission

The presence of coarser particles significantly influences the contact force transmission within the specimen. The effect of gradation on the distribution of contact normal forces (F_n) is highlighted by plotting the normalized contact normal force (F_n/\bar{F}_n) for each contact, normalized to the average contact normal force in the specimen as a function of particle size. A two-dimensional colormap is generated to visualize the distribution of F_n/\bar{F}_n for all the contacts in the assembly, as a function of the sizes of the two particles involved in each contact. To create the colormap, the PSD for the soils was divided into 10 equal-sized bins, with the first one being from D_0 to D_{10} , and the last one being from D_{90} to D_{100} , and the average F_n/\bar{F}_n is indicated by the shade of the respective cell. Additionally, contours are drawn for F_n/\bar{F}_n values of 1.0, 1.5, and 2.0, showing the particle sizes that carry different proportions

of \bar{F}_n . The contacts transmitting a force greater than the average force ($F_n/\bar{F}_n > 1.0$) form the strong force chain network, and the contacts transmitting a force smaller than the average force form the weak force chain network (defined by Radjai et al. 1997). The distribution of F_n/\bar{F}_n for 100A, 33ABC and 25ABCD specimens at the initial, peak, and critical states of specimens with ξ_0 of -0.1 is presented in Figs. S5.2(c,d,e), 5.10(c,d,e) and 5.11(c,d,e), respectively.

The distributions for the more broadly graded specimens show a disproportionate increase in F_n/\bar{F}_n with particle size. In the 100A specimen at the peak state, the magnitude of F_n/\bar{F}_n gradually increases with particle size, with the coarsest particles transmitting about 3.5 times the average force. The boundary between the strong and weak force chain networks can be approximated by D_{40} in the initial state but shifts towards coarser particle sizes at the peak and critical states. The coarsest particles in the 33ABC and 25ABCD specimens transmit greater than 30 and 50 times the average contact force at the peak state, respectively. The D_{25} and D_{20} function as the average particle size boundary demarcating the strong and weak force networks for 33ABC and 25ABCD specimens at initial state, respectively, indicating that the majority of the particles by size (D_{25} to D_{100} for 33ABC and D_{20} to D_{100} for 25ABCD) carries contact forces higher than the average. These findings align with the observation that the finer particles in granular assemblies tend to occupy the void space and provide buckling resistance to the strong force chain (Basson and Martinez 2020; Liu et al. 2021). The particle size that carries any given F_n/\bar{F}_n value slightly increases from the initial to the peak and critical states. Similar findings have been past reported connecting the collective buckling of the strong and weak force chains to the particle motions in shear

banding (Oda and Kazama 1998; Yilmaz et al. 2023) and to explain the classic stress-dilatancy theories (Tordesillas et al. 2011).

5.5.3 Anisotropy in contact force distribution

Vector analysis of contact normal forces reveals the preferential orientation of the force chain network, which can be separated into the strong and weak networks. In this study, the orientations of normal forces are presented in terms of angular distributions obtained from fitting analytical functions to the contact normal forces (F_n) (Basson et al. 2021; Rothenburg and Bathurst 1992). The fitted analytical function has the following form:

$$F(\theta) = \bar{F}_n (1 + a_{CNF} \cos 2(\theta - \theta_{CNF})) \quad (5.6)$$

where a_{CNF} is the parameter that controls the anisotropy of the distribution, θ_{CNF} is the preferred orientation from the horizontal direction and the \bar{F}_n is the average contact force for the F_n distribution. The fitted angular distributions for the 100A, 33ABC, and 25ABCD specimens with a ξ_0 of -0.1 at the initial, peak, and critical states are presented in Figs. S5.2(f,g,h), 5.12(f,g,h) and 5.13(f,g,h), respectively. A comparison of the closeness of fit using equation 7 to the obtained data is presented in Fig. S5.3. The angular distributions were obtained along xz planes and are presented for three ranges of particle sizes. The small particles were defined as those smaller than D_{10} to capture the inactive particles (i.e., Figs. S5.2(b), 5.10(b) and 5.11(b)), the medium particles were considered as those larger than D_{10} but with F_n/\bar{F}_n smaller than 1.0 in the initial state (i.e., D_{40} for 100A, D_{25} for 33ABC and D_{20} for 25ABCD per Figs. S5.2(c), S5.2(d) and S5.2(e)), and the large particles were defined as those with F_n/\bar{F}_n greater or equal to 1.0 (i.e., strong force network) in the initial state. Table 5.5 tabulates the magnitude of a_{CNF} for the fitted distributions for the three particle size ranges.

The angular distributions and the associated a_{CNF} , for the small, medium, and large particles, are influenced by the gradation, with a stronger tendency for the strong force networks to be transmitted through the larger particles in the broader gradations. Initially, all specimens exhibit negligible force anisotropy, indicated by nearly circular distributions, due to the isotropic stress state after compression (Figs. S5.1(f,g,h)). This is shown by the a_{CNF} magnitude for the small, medium, and large particles at the initial state in all specimens which is below 0.04. At the peak and critical states, the distributions become peanut-shaped with a larger contact force in the vertical direction (i.e., aligned with the major principal stress) with a a_{CNF} magnitudes between 0.34 to 0.58 (Figs. 5.10(f,g,h) and Figs. 5.11(f,g,h), Table 5). At the critical state, the distribution of the larger particles (i.e., strong force network) exhibit greater anisotropy than those for the medium and fine particles (i.e., weak force network), and this difference increases as the C_U is increased. For example, in the 33ABC and 25ABCD specimens, the a_{CNF} magnitude for large particles is 0.40 and 0.41, respectively, whereas the a_{CNF} magnitude for small particles is 0.12 and 0.04, respectively, with near circular angular distributions. The disparity between the a_{CNF} magnitude for larger and smaller particle confirms that the strong force network aligns itself to the direction of the major principal stress state, while the weak force network provides the buckling resistance to the strong force columns. These observations are consistent with past studies on strong and weak force columns (Minh et al. 2014; Kruyt 2016; Sufian et al. 2021).

5.6 Undrained triaxial response and fabric evolution

The undrained triaxial response of 100A, 33ABC, and 25ABCD is presented in terms of the evolution of q and excess pore pressure (Δu) with axial strain for specimens prepared at

different ξ_0 at a p' of 100 kPa (Fig. 5.12) and 800 kPa (Fig. 5.13). The denser specimen (smallest ξ_0) mobilizes greatest q for any given p' due to the generation of negative Δu with greater magnitudes. At small axial strains, the denser specimens generate slightly positive Δu followed by a reduction in Δu reaching the minimum negative value at critical state. The looser specimens generate slightly positive or slightly negative Δu throughout the entire simulations. The specimens subjected to a p' of 800 kPa show a less dilative response, in agreement with the drained results.

A comparison of the undrained triaxial response for the 100A, 33ABC and 25ABCD specimens at a ξ_0 between -0.05 and -0.09 subjected to a p' of 100 kPa highlight the effect of gradations, where specimens with broader gradations generate larger negative Δu (Fig. 5.14). At the peak and critical states, the 33ABC specimen mobilizes the highest q followed by 25ABCD and 100A specimens, respectively. The 33ABC specimen shows the highest magnitude of Δu and rate of pore pressure generation, followed by the 25ABCD and 100A specimens, likely due to the former's more negative state ($\xi_0 = -0.09$). These observations are consistent with the drained simulation response (i.e., Fig. 5.8) showing a more dilative response for the more broadly graded specimens as well as with past experimental studies (Ahmed et al. 2023, Amirpour Harehdasht et al. 2017, and Simoni and Houlsby 2006). The packing characteristics, transmission of contact forces and evolution of fabric for these specimens (Figs. S5.4, S5.5, S5.6) show similar trends to those described for the drained triaxial simulation. Namely, the particles with larger sizes have greater PC, carry larger contact forces, and have contact force angular distributions that are more anisotropic and aligned with the major principal stress direction. With increasing axial strain, the packing density (PC) continuously increases (Figs. S5.4(a,b), S5.5(a,b), S5.6(a,b)), and the

distribution of contact forces with particle size remains relatively consistent (Figs. S5.5(c,d,e), S5.6(c,d,e), S5.7(c,d,e)).

5.7 Gradation effects on stress-dilatancy and pore pressure generation

Recent studies indicate that the ξ_0 is more robust in capturing the effects of gradation on the strength and stress-dilatancy behavior of coarse-grained soil (Ahmed et al. 2023; Li et al. 2015). Unlike D_R , ξ_0 captures the difference between e_0 and e_{cs} , which considers the dependency on p' . In addition, due to the influence of gradation on the slope and position of the CSL (i.e., Fig. 5.5), a given D_R value for different soils does not ensure the same difference between the initial and critical states. The variation of ϕ'_p , $\phi'_p - \phi'_{cs}$, and ψ_{max} with ξ_0 for drained simulations is presented in Figs. 5.15(a), (b), (c), respectively, along with the dashed lines representing the bounds proposed by Been and Jefferies (1985). For all the gradations, ϕ'_p , $\phi'_p - \phi'_{cs}$, and ψ_{max} increase as ξ_0 becomes more negative. Moreover, at the same ξ_0 , ϕ'_p , $\phi'_p - \phi'_{cs}$, and ψ_{max} increase as the soils become more broadly graded. The values of ϕ'_p and $\phi'_p - \phi'_{cs}$ converge for the specimens with greater ξ_0 , while the difference between the values for the 100A and 25ABCD specimens grows as the ξ_0 decreases. This increase in the spread is due to an increase in the dilative tendencies with an increase in gradation and is corroborated by a relatively rapid increase in the ψ_{max} with decreases in ξ_0 for the 25ABCD and 33ABC specimens compared to 100A (Fig. 5.15(c)). These trends can be explained by the larger PC values and the greater anisotropy of the contact force angular distributions in the more broadly graded specimens (i.e., Figs. S5.1(a,f,g,h), Figs. 5.10(a,f,g,h), and Figs. 5.11(a,f,g,h)).

The results for the 100A specimen align closely with the lower bound proposed by Been and Jefferies (1985), while the results for 33ABC and 25ABCD specimens plot above the bounds. These results suggest that the bounds presented by Been and Jefferies (1985) fail to explicitly capture the systematic variation in behavior as soil gradation becomes broader, also observed in experimental results by Ahmed et al. (2023). Additionally, comparison of $\phi'_p - \phi'_{cs}$ and ϕ'_p with D_R in Fig. 5.16 reveals that while there is a general increase in $\phi'_p - \phi'_{cs}$ and ϕ'_p with D_R , D_R fails to effectively capture the systematic increase in the parameters resulting from an increase in gradation.

The maximum pore pressure generated at the critical state (u_{min}) and the minimum rate of pore pressure generation $(\delta u / \delta \varepsilon_a)_{min}$ during undrained shearing are intimately related to the volume change tendencies of the specimens. The variations of u_{min} and $(\delta u / \delta \varepsilon_a)_{min}$ as a function of ξ_0 are presented in Figs. 5.15(d,e). Both u_{min} and $(\delta u / \delta \varepsilon_a)_{min}$ becomes more negative as ξ_0 is decreased for all the gradations. For the same ξ_0 , the 25ABCD and 33ABC specimens produce more negative u_{min} and $(\delta u / \delta \varepsilon_a)_{min}$ values than the 100A specimen, in agreement with the greater dilative tendencies for the more broadly graded soils shown in the drained simulations. The trends in the undrained responses are also related to the greater PC values and anisotropy of the contact force angular distributions in the more broadly graded specimens (i.e., Figs. S5.5(a,f,g,h), Figs. S5.6(a,f,g,h), and Figs. S5.7(a,f,g,h)). These observations further advance the trends regarding pore pressure generation for specimens with similar ξ_0 observed in past research (Kokusho et al. 2004; Gong et al. 2012; Ghadr and Assadi-Langroudi 2019; Ahmed et al. 2023).

5.8 Conclusions

This paper investigates the effect of changes in gradation on the shear strength, volume change, and stress-dilatancy of coarse-grained soils using DEM simulations on specimens with C_U between 1.9 and 6.4. Monotonic simulations were performed to highlight the gradation effects on the drained and undrained triaxial response, critical state lines, and parameters such as ϕ'_p , $\phi'_p - \phi'_{cs}$, ψ_{max} , u_{min} , and $(\delta u / \delta \epsilon_a)_{min}$.

Specimens with broader gradation mobilized greater peak shear strengths, dilative volume changes, rates of dilation, negative excess pore pressures, and rates of pore pressure generation when compared at the same ξ_0 . In specimens with broader gradations, the coarsest particles form a significant number of contacts with their neighboring particles, carrying a majority of the contact forces. The coarsest particle for the 25ABCD (i.e., $C_U = 6.37$) specimen is connected to 12 times more particles than the coarsest particle in the 100A (i.e., $C_U = 1.98$) specimen at similar ξ_0 . This greater interlocking of the coarser particles leads to a greater dilation during shearing, resulting in greater peak shear strengths for the more broadly-graded specimens. The largest particles in the 25ABCD specimen carry up to 50 times the average contact force, while the coarsest particles in the 100A specimen carry about 3.5 times the average contact force. The fraction of particles in the strong force network increases as the gradation becomes broader, from D_{40} to D_{100} for poorly graded 100A specimen to D_{20} to D_{100} for the broadly-graded 25ABCD specimen. The D_{10} size is close to the threshold average size of the inactive particles in force transmission. The contact force distributions indicate that the strong force network (carried by coarser particles) aligns itself with the major principal stress direction, while the weak force network and inactive

particles provide buckling resistance, and this effect becomes pronounced with an increase in gradation.

The results indicate the position and slope of the critical state line in the $e-\log(p')$ plane decrease as the gradation becomes wider, and at similar ξ_0 the ϕ'_p , $\phi'_p - \phi'_{cs}$ and ψ_{max} increase with an increase gradation. In contrast, when plotted in terms of D_R the effects of gradation are obscured. Comparison of the simulation results with the trends presented in Bolton (1986) and Been and Jefferies (1985) suggests that these frameworks do not explicitly capture the effect of gradation. Specifically, the simulation results for the more broadly-graded specimens indicate that they plot higher in $\phi'_p - \phi'_{cs}$ vs. p' space than those predicted by Bolton's framework. Also, while the 100A specimen results align with the lower bound presented by Been and Jefferies (1985) in ϕ'_p vs. ξ_0 and of $\phi'_p - \phi'_{cs}$ vs. ξ_0 spaces, the 25ABCD specimen results have greater of ϕ'_p and $\phi'_p - \phi'_{cs}$ values than the reported upper bound for any given ξ_0 . Overall, these results indicate that gradation has a significant effect on the peak strength and dilatancy of coarse-grained soils, driven by the disproportionately high role of the coarsest particles in the assembly in transmitting contact forces. These effects are readily captured when ξ_0 is used as the state parameter for comparison between different soils.

5.9 Data availability statement

Raw data from the DEM simulations and the codes used in this study are available from the corresponding author, upon reasonable request. The experimental data used from Ahmed et al. (2023) are available at DesignSafe-CI under PRJ-3732 at 10.17603/ ds2-crtg-j217.

5.10 Acknowledgements

Financial support for this project comes from the National Science Foundation (NSF) under Grant CMMI-1916152. Any opinions, findings, conclusions, or recommendations expressed in this paper are those of the authors and do not necessarily reflect the views of NSF. The authors would also like to acknowledge contribution and discussions of Rachel Reardon, Francisco Humire, Sharif Ahmed, Trevor Carey, Nathan Love, Anna Chiaradonna, and Katerina Ziotopoulou.

5.11 References

- Abbireddy, C. O. R., and C. R. I. Clayton. 2010. "Varying initial void ratios for dem simulations." *Géotechnique*, 60 (6): 497–502.
- Ahmed, S. S. 2021. "Study on particle shape, size and gradation effects on the mechanical behavior of coarse-grained soils." PhD Thesis. University of California Davis.
- Ahmed, S. S., A. Martinez, and J. T. DeJong. 2023. "Effect of gradation on the strength and stress-dilation behavior of coarse-grained soils in drained and undrained triaxial compression." *Journal of Geotechnical and Geoenvironmental Engineering*, 149 (5): 04023019.
- Altuhafi, F. N., M. R. Coop, and V. N. Georgiannou. 2016. "Effect of particle shape on the mechanical behavior of natural sands." *Journal of Geotechnical and Geoenvironmental Engineering*, 142 (12): 04016071.
- Amirpour Harehdasht, S., M. Karray, M. N. Hussien, and M. Chekired. 2017. "Influence of particle size and gradation on the stress-dilatancy behavior of granular materials

- during drained triaxial compression.” *International Journal of Geomechanics*, 17 (9): 04017077.
- Basson, M. S., and A. Martinez. 2020. “A DEM study of the evolution of fabric of coarse-grained materials during oedometric and isotropic compression.” *Geo-Congress 2020*, 473–481. Minneapolis, Minnesota: American Society of Civil Engineers.
- Basson, M. S., and A. Martinez. 2023. “A multi-orientation system for determining angular distributions of shear wave velocity in soil specimens.” *Geotechnical Testing Journal*, 46 (2): 20210277.
- Basson, M. S., A. Martinez, and J. T. DeJong. 2023. “Effect of particle size distribution on monotonic shear strength and stress-dilatancy of coarse-grained soils.” *GeoCongress 2023*, 10. Los Angeles.
- Basson, M. S., J. Miller, and A. Martinez. 2021. “Experimental estimation of fabric in granular materials using shear wave velocity measurements.” *Soil Dynamics*, Lecture Notes in Civil Engineering, T. G. Sitharam, S. V. Dinesh, and R. Jakka, eds., 311–323. Singapore: Springer Singapore.
- Been, K., and M. G. Jefferies. 1985. “A state parameter for sands.” *Géotechnique*, 35 (2): 99–112.
- Bolton, M. D. 1986. “The strength and dilatancy of sands.” *Géotechnique*, 36 (1): 65–78.
- Bonilla, R. R. O. 2004. “Numerical simulations of undrained granular media.” University of Waterloo.
- Carey, T. J., A. Chiaradonna, N. C. Love, D. W. Wilson, K. Ziotopoulou, A. Martinez, and J. T. DeJong. 2022. “Effect of soil gradation on embankment response during liquefaction:

- a centrifuge testing program." *Soil Dynamics and Earthquake Engineering*, 157: 107221.
- Chakraborty, T., and R. Salgado. 2010. "Dilatancy and shear strength of sand at low confining pressures." *Journal of Geotechnical and Geoenvironmental Engineering*, 136 (3): 527–532.
- Chaney, R., K. Demars, P. Lade, C. Liggio, and J. Yamamuro. 1998. "Effects of non-plastic fines on minimum and maximum void ratios of sand." *Geotechnical Testing Journal*, 21 (4): 336.
- Chiaradonna, A., K. Ziotopoulou, T. J. Carey, J. T. DeJong, and R. W. Boulanger. 2022. "Dynamic behavior of uniform clean sands: evaluation of predictive capabilities in the element- and the system-level scale." *Geo-Congress 2022*, 444–454. Charlotte, North Carolina: American Society of Civil Engineers.
- Cho, G.-C., J. Dodds, and J. C. Santamarina. 2006. "Particle shape effects on packing density, stiffness, and strength: natural and crushed sands." *Journal of Geotechnical and Geoenvironmental Engineering*, 132 (5): 591–602.
- Ciantia, M. O., M. Arroyo, F. Calvetti, and A. Gens. 2015. "An approach to enhance efficiency of dem modelling of soils with crushable grains." *Géotechnique*, 65 (2): 91–110.
- Coetzee, C. J. 2019. "Particle upscaling: calibration and validation of the discrete element method." *Powder Technology*, 344: 487–503.
- da Cruz, F., S. Emam, M. Prochnow, J.-N. Roux, and F. Chevoir. 2005. "Rheophysics of dense granular materials: discrete simulation of plane shear flows." *Physical Review E*, 72 (2): 021309.

- Cubrinovski, M., and K. Ishihara. 2002. "Maximum and minimum void ratio characteristics of sands." *Soils and Foundations*, 42 (6): 65–78.
- DeJong, J. T., A. P. Sturm, and M. Ghafghazi. 2016. "Characterization of gravelly alluvium." *Soil Dynamics and Earthquake Engineering*, 91: 104–115.
- Dyvik, R., T. Berre, S. Lacasse, and B. Raadim. 1987. "Comparison of truly undrained and constant volume direct simple shear tests." *Géotechnique*, 37 (1): 3–10.
- Evans, M. D., and S. Zhou. 1995. "Liquefaction behavior of sand-gravel composites." *Journal of Geotechnical Engineering*, 121 (3): 287–298.
- Ferrellec, J.-F., and G. R. McDowell. 2008. "A simple method to create complex particle shapes for dem." *Geomechanics and Geoengineering*, 3 (3): 211–216.
- Fragaszy, R. J., J. Su, F. H. Siddiqi, and C. L. Ho. 1992. "Modeling strength of sandy gravel." *Journal of Geotechnical Engineering*, 118 (6): 920–935.
- Garcia, X., J.-P. Latham, J. Xiang, and J. P. Harrison. 2009. "A clustered overlapping sphere algorithm to represent real particles in discrete element modelling." *Géotechnique*, 59 (9): 779–784.
- Ghadr, S., and A. Assadi-Langroudi. 2019. "Effect of grain size and shape on undrained behaviour of sands." *International Journal of Geosynthetics and Ground Engineering*, 5 (3): 18.
- Gong, G., X. Zha, and J. Wei. 2012. "Comparison of granular material behaviour under drained triaxial and plane strain conditions using 3d dem simulations." *Acta Mechanica Sinica*, 25 (2): 186–196.

- Gu, X., J. Zhang, and X. Huang. 2020. "DEM analysis of monotonic and cyclic behaviors of sand based on critical state soil mechanics framework." *Computers and Geotechnics*, 128: 103787.
- Hamidi, A., E. Azini, and B. Masoudi. 2012. "Impact of gradation on the shear strength-dilation behavior of well graded sand-gravel mixtures." *Scientia Iranica*, 19 (3): 393–402.
- Hanley, K. J., X. Huang, C. O'Sullivan, and F. Kwok. 2013. "Challenges of simulating undrained tests using the constant volume method in dem." 277–280. Sydney, Australia.
- Harkness, J., A. Zervos, L. Le Pen, S. Aingaran, and W. Powrie. 2016. "Discrete element simulation of railway ballast: modelling cell pressure effects in triaxial tests." *Granular Matter*, 18 (3): 65.
- Huang, X., K. J. Hanley, C. O'Sullivan, and F. C. Y. Kwok. 2014a. "Effect of sample size on the response of dem samples with a realistic grading." *Particuology*, 15: 107–115.
- Huang, X., C. O'Sullivan, K. J. Hanley, and C. Y. Kwok. 2014b. "Discrete-element method analysis of the state parameter." *Géotechnique*, 64 (12): 954–965.
- Kawamoto, R., E. Andò, G. Viggiani, and J. E. Andrade. 2016. "Level set discrete element method for three-dimensional computations with triaxial case study." *Journal of the Mechanics and Physics of Solids*, 91: 1–13.
- Knodel, P., R. Fragaszy, W. Su, and F. Siddiqi. 1990. "Effects of oversize particles on the density of clean granular soils." *Geotechnical Testing Journal*, 13 (2): 106.
- Kokusho, T., T. Hara, and R. Hiraoka. 2004. "Undrained shear strength of granular soils with different particle gradations." *Journal of Geotechnical and Geoenvironmental Engineering*, 130 (6): 621–629.

- Kruyt, N. P. 2016. "On weak and strong contact force networks in granular materials." *International Journal of Solids and Structures*, 92–93: 135–140.
- Li, G., Y.-J. Liu, C. Dano, and P.-Y. Hicher. 2015. "Grading-dependent behavior of granular materials: from discrete to continuous modeling." *Journal of Engineering Mechanics*, 141 (6): 04014172.
- Li, X.-S., Y. F. Dafalias, and Z.-L. Wang. 1999. "State-dependant dilatancy in critical-state constitutive modelling of sand." *Canadian Geotechnical Journal*, 36 (4): 599–611.
- Liu, D., C. O'Sullivan, and J. A. H. Carraro. 2021. "The influence of particle size distribution on the stress distribution in granular materials." *Géotechnique*, 1–15.
- Liu, X., and J. Yang. 2018. "Shear wave velocity in sand: effect of grain shape." *Géotechnique*, 68 (8): 742–748.
- Maeda, K., and H. Hirabayashi. 2006. "Influence of grain properties on macro mechanical behaviors of granular media by dem." *Journal of applied mechanics*, 9: 623–630.
- Markauskas, D., R. Kačianauskas, A. Džiugys, and R. Navakas. 2010. "Investigation of adequacy of multi-sphere approximation of elliptical particles for dem simulations." *Granular Matter*, 12 (1): 107–123.
- Martin, E. L., C. Thornton, and S. Utili. 2020. "Micromechanical investigation of liquefaction of granular media by cyclic 3d dem tests." *Géotechnique*, 70 (10): 906–915.
- Minh, N. H., Y. P. Cheng, and C. Thornton. 2014. "Strong force networks in granular mixtures." *Granular Matter*, 16 (1): 69–78.
- Muir Wood, D., and K. Maeda. 2008. "Changing grading of soil: effect on critical states." *Acta Geotechnica*, 3 (1): 3–14.

- Oda, M., and H. Kazama. 1998. "Microstructure of shear bands and its relation to the mechanisms of dilatancy and failure of dense granular soils." *Géotechnique*, 48 (4): 465–481.
- O'Sullivan, C. 2011. *Particulate discrete element modelling*.
- Pires-Sturm, A., R. Jaeger, and J. DeJong. 2022. "Estimating maximum and minimum void ratio from index parameters." *In Proceeding of*. Baltimore, MD.
- Polanía, O., M. Cabrera, M. Renouf, E. Azéma, and N. Estrada. 2023. "Grain size distribution does not affect the residual shear strength of granular materials: an experimental proof." *Physical Review E*, 107 (5): L052901.
- Price, M., V. Murariu, and G. Morrison. 2007. "Sphere clump generation and trajectory comparison for real particles." *Proc. 4th Int. Conf. Discrete Element Methods, Brisbane*, 1–8.
- Radjai, F., D. E. Wolf, S. Roux, M. Jean, and J. J. Moreau. 1997. "Force networks in dense granular media." *Powders & grains*, 97: 211–214.
- Reardon, R. A. 2021. "Monotonic and cyclic direct simple shear testing of coarse-grained soils." Master's Thesis. UC Davis.
- Reardon, R., F. Humire, S. S. Ahmed, K. Ziotopoulou, A. Martinez, and J. T. DeJong. 2022. "Effect of gradation on the strength and stress-dilatancy of coarse-grained soils: a comparison of monotonic direct simple shear and triaxial tests." *Geo-Congress 2022*, 226–236. Charlotte, North Carolina: American Society of Civil Engineers.
- Roessler, T., and A. Katterfeld. 2018. "Scaling of the angle of repose test and its influence on the calibration of dem parameters using upscaled particles." *Powder Technology*, 330: 58–66.

- Rothenburg, L., and R. J. Bathurst. 1992. "Micromechanical features of granular assemblies with planar elliptical particles." *Géotechnique*, 42 (1): 79–95.
- Rowe, P. W. 1962. "The stress-dilatancy relation for static equilibrium of an assembly of particles in contact." *Proceedings of the Royal Society of London. Series A, Mathematical and Physical Sciences*, 269 (1339): 500–527.
- Sawyer, B. D. 2020. "Cone penetration testing of coarse-grained soils in the centrifuge to examine the effects of soil gradation and centrifuge scaling." Master's Thesis. University of California Davis.
- Schofield, A., and P. Wroth. 1968. *Critical state soil mechanics*. McGraw-Hill, New York, NY.
- Scholtès, L., B. Chareyre, F. Nicot, and F. Darve. 2009. "Micromechanics of granular materials with capillary effects." *International Journal of Engineering Science*, 12.
- Seyedi Hosseininia, E. 2012. "Investigating the micromechanical evolutions within inherently anisotropic granular materials using discrete element method." *Granular Matter*, 14 (4): 483–503.
- Shinohara, K., M. Oida, and B. Golman. 2000. "Effect of particle shape on angle of internal friction by triaxial compression test."
- Simoni, A., and G. T. Houlsby. 2006. "The direct shear strength and dilatancy of sand–gravel mixtures." *Geotechnical and Geological Engineering*, 24 (3): 523–549.
- Šmilauer, V., E. Catalano, B. Chareyre, S. Dorofeenko, J. Duriez, A. Gladky, J. Kozicki, C. Modenese, L. Scholtès, and L. Sibille. 2010. "Yade reference documentation." *Yade Documentation*, 474: 1–531.
- Sturm, A. 2019. "On the liquefaction potential of gravelly soils: characterization, triggering and performance." PhD Thesis. University of California Davis.

- Sufian, A., M. Artigaut, T. Shire, and C. O'Sullivan. 2021. "Influence of fabric on stress distribution in gap-graded soil." *Journal of Geotechnical and Geoenvironmental Engineering*, 147 (5): 04021016.
- Suhr, B., and K. Six. 2020. "Simple particle shapes for dem simulations of railway ballast: influence of shape descriptors on packing behaviour." *Granular Matter*, 22 (2): 43.
- Tolomeo, M., and G. R. McDowell. 2022. "Modelling real particle shape in dem: a comparison of two methods with application to railway ballast." *International Journal of Rock Mechanics and Mining Sciences*, 159: 105221.
- Tordesillas, A., J. Shi, and T. Tshaikiwsky. 2011. "Stress-dilatancy and force chain evolution." *International Journal for Numerical and Analytical Methods in Geomechanics*, 35 (2): 264–292.
- Vaid, Y. P., and S. Sasitharan. 1992. "The strength and dilatancy of sand." *Canadian Geotechnical Journal*, 29 (3): 522–526.
- Voivret, C., F. Radjaï, J.-Y. Delenne, and M. S. El Youssoufi. 2009. "Multiscale force networks in highly polydisperse granular media." *Physical Review Letters*, 102 (17): 178001.
- Wang, Z.-L., Y. F. Dafalias, X.-S. Li, and F. I. Makdisi. 2002. "State pressure index for modeling sand behavior." *Journal of Geotechnical and Geoenvironmental Engineering*, 128 (6): 511–519.
- Wei, D., J. Wang, and B. Zhao. 2018. "A simple method for particle shape generation with spherical harmonics." *Powder Technology*, 330: 284–291.
- Wu, M., J. Wang, A. Russell, and Z. Cheng. 2021. "DEM modelling of mini-triaxial test based on one-to-one mapping of sand particles." *Géotechnique*, 71 (8): 714–727.

- Yan, B., R. A. Regueiro, and S. Sture. 2010. "Three-dimensional ellipsoidal discrete element modeling of granular materials and its coupling with finite element facets." *Engineering Computations*, 27 (4): 519–550.
- Yan, W. M., and J. Dong. 2011. "Effect of particle grading on the response of an idealized granular assemblage." *International Journal of Geomechanics*, 11 (4): 276–285.
- Yang, J., and X. D. Luo. 2018. "The critical state friction angle of granular materials: does it depend on grading?" *Acta Geotechnica*, 13 (3): 535–547.
- Yilmaz, Y., Y. Deng, C. S. Chang, and A. Gokce. 2023. "Strength–dilatancy and critical state behaviours of binary mixtures of graded sands influenced by particle size ratio and fines content." *Géotechnique*, 73 (3): 202–217.
- Youd, T. 1973. "Factors controlling maximum and minimum densities of sands." *Evaluation of Relative Density and its Role in Geotechnical Projects Involving Cohesionless Soils*, E. Selig and R. Ladd, eds., 98-98–15. 100 Barr Harbor Drive, PO Box C700, West Conshohocken, PA 19428-2959: ASTM International.
- Zhang, L., and T. M. Evans. 2018. "Boundary effects in discrete element method modeling of undrained cyclic triaxial and simple shear element tests." *Granular Matter*, 20 (4): 60.
- Zhang, W., and L. Rothenburg. 2020. "Comparison of undrained behaviors of granular media using fluid-coupled discrete element method and constant volume method." *Journal of Rock Mechanics and Geotechnical Engineering*, 12 (6): 1272–1289.
- Zhao, S., N. Zhang, X. Zhou, and L. Zhang. 2017. "Particle shape effects on fabric of granular random packing." *Powder Technology*, 310: 175–186.

Zuo, K., X. Gu, J. Zhang, and R. Wang. 2023. "Exploring packing density, critical state, and liquefaction resistance of sand-fines mixture using dem." *Computers and Geotechnics*, 156: 105278.

5.12 Tables and figures

Table 5.1: Gradation characteristics of the simulated materials

<i>Soil</i>	<i>D₁₀ (mm)</i>	<i>D₃₀ (mm)</i>	<i>D₅₀ (mm)</i>	<i>D₆₀ (mm)</i>	<i>C_u</i>	<i>C_c</i>	<i>e_{max}</i>	<i>e_{min}</i>
100A	1.67	2.14	2.83	3.31	1.98	0.83	1.01	0.62
33ABC	2.50	4.82	8.76	11.20	4.48	0.83	0.74	0.45
25ABCD	2.84	6.54	12.72	18.10	6.37	0.83	0.68	0.41

Table 5.2: DEM simulations parameters

<i>Parameter</i>	<i>Symbol</i>	<i>Value</i>
Normalized normal stiffness	k_n/d	2.5e8 Pa
Shear to normal stiffness ratio	k_s/k_n	0.2
Particle density	ρ	2650 kg/m ³
Friction coefficient during sample preparation	μ_{prep}	0.1 to 0.4
Friction coefficient during shearing	μ_{shear}	0.5
Global damping during preparation	ζ_{prep}	0.05 to 0.5
Global damping during shearing	ζ_{shear}	0.05

Table 5.3: Parameters of drained triaxial simulations

<i>Soil</i>	<i>Mean effective confining stress, p' (kPa)</i>	<i>Initial void ratio, e_0</i>	<i>Initial state parameter, ξ_0</i>	<i>Relative Density, D_R</i>
<i>100A</i>	100	0.853	-0.04	40
	100	0.802	-0.10	53
	100	0.692	-0.21	82
	400	0.866	0.00	37
	400	0.801	-0.08	54
	400	0.693	-0.18	81
	800	0.836	0.02	45
	800	0.805	-0.03	53
	800	0.686	-0.14	83
<i>33ABC</i>	100	0.655	0.03	31
	100	0.632	0.01	39
	100	0.518	-0.11	78
	400	0.676	0.06	24
	400	0.635	0.01	38
	400	0.511	-0.11	80
	800	0.666	0.06	28
	800	0.619	0.02	44
	800	0.518	-0.09	78
<i>25ABCD</i>	100	0.603	0.02	28
	100	0.586	0.01	35
	100	0.471	-0.10	79
	400	0.595	0.02	31
	400	0.585	0.02	35
	400	0.481	-0.08	75
	800	0.585	0.04	35
	800	0.574	0.02	39
	800	0.479	-0.07	76

Table 5.4: Parameters of undrained triaxial simulations

<i>Soil</i>	<i>Mean effective confining stress, p' (kPa)</i>	<i>Initial void ratio, e_0</i>	<i>Initial state parameter, ξ_0</i>	<i>Relative Density, D_R</i>
<i>100A</i>	100	0.854	-0.048	40
	100	0.802	-0.1	53
	100	0.753	-0.149	66
	800	0.837	-0.007	44
	800	0.805	-0.039	53
	800	0.716	-0.128	76
<i>33ABC</i>	100	0.645	0.011	35
	100	0.632	-0.002	39
	100	0.574	-0.06	59
	800	0.625	-0.01	42
	800	0.619	0.004	44
	800	0.583	-0.032	56
<i>25ABCD</i>	100	0.573	-0.009	40
	100	0.562	-0.02	44
	100	0.521	-0.062	60
	800	0.572	0.016	40
	800	0.544	-0.016	51
	800	0.511	-0.054	64

Table 5.5: Anisotropy of contact normal force angular for drained simulations

<i>Specimen</i>	<i>State</i>	<i>Particle Size</i>	a_{CNF}
100A	Initial	D < 10%	0.04
		10% < D < 40%	0.01
		D > 40%	0.03
100A	Peak	D < 10%	0.42
		10% < D < 40%	0.44
		D > 40%	0.54
100A	Critical	D < 10%	0.28
		10% < D < 40%	0.33
		D > 40%	0.42
33ABC	Initial	D < 10%	0.01
		10% < D < 25%	0.01
		D > 25%	0.01
33ABC	Peak	D < 10%	0.34
		10% < D < 25%	0.41
		D > 25%	0.60
33ABC	Critical	D < 10%	0.12
		10% < D < 25%	0.33
		D > 25%	0.40
25ABCD	Initial	D < 10%	0.00
		10% < D < 20%	0.01
		D > 20%	0.02
25ABCD	Peak	D < 10%	0.29
		10% < D < 20%	0.35
		D > 20%	0.58
25ABCD	Critical	D < 10%	0.04
		10% < D < 20%	0.36
		D > 20%	0.41

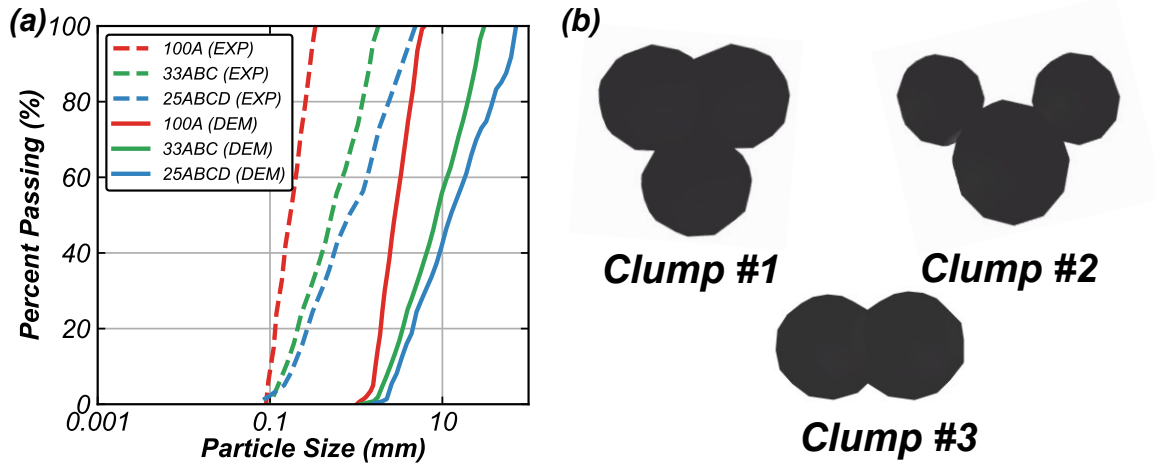


Figure 5.1: (a) Particle size distribution of the simulated materials and (b) templates for clumped particles.

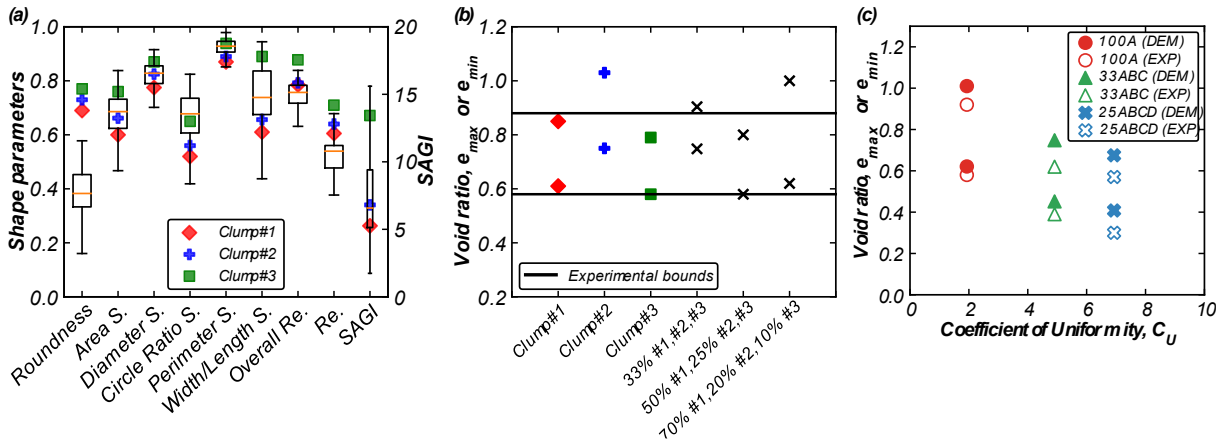
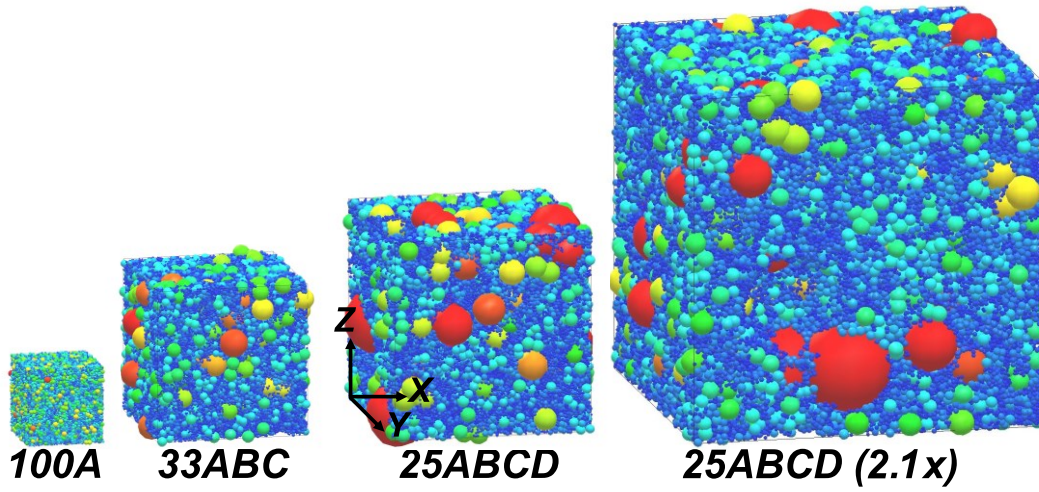
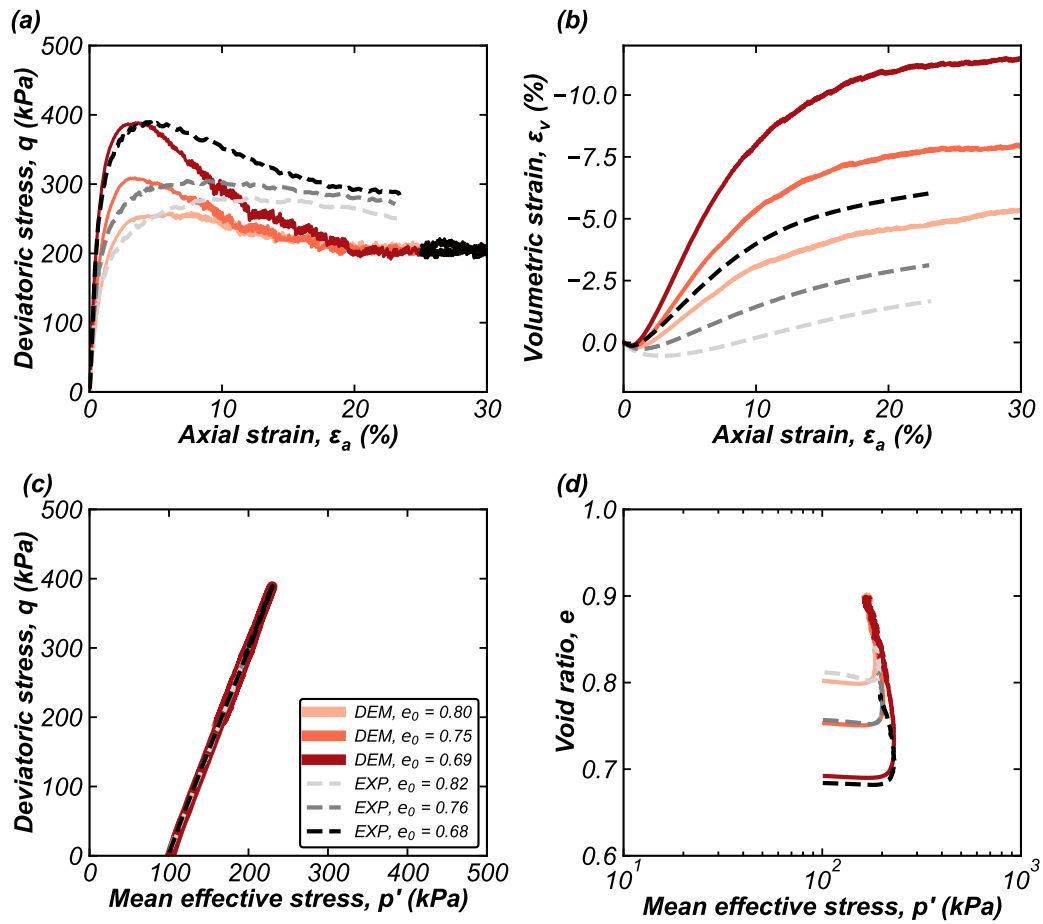


Figure 5.2: Comparison of (a) particle shape parameters between real (box and whiskers) and simulated particles, (b) e_{max} and e_{min} for different clump mixes, and (c) bounds for e_{max} and e_{min} from experiments and DEM simulations for different gradations. Note: $Re.$ = regularity and S = sphericity.



Figures 5.3: Images of 100A, 33ABC, 25ABCD, and 25ABCD (2.1x) specimens. The particle color is normalized between the maximum (red) and minimum (blue) diameter in the specimen.



Figures 5.4: Comparison of the (a) q , (b) ε_v , (c) stress path in q - p' space, and (d) stress path in e - $\log(p')$ space between drained triaxial simulations and experiments.

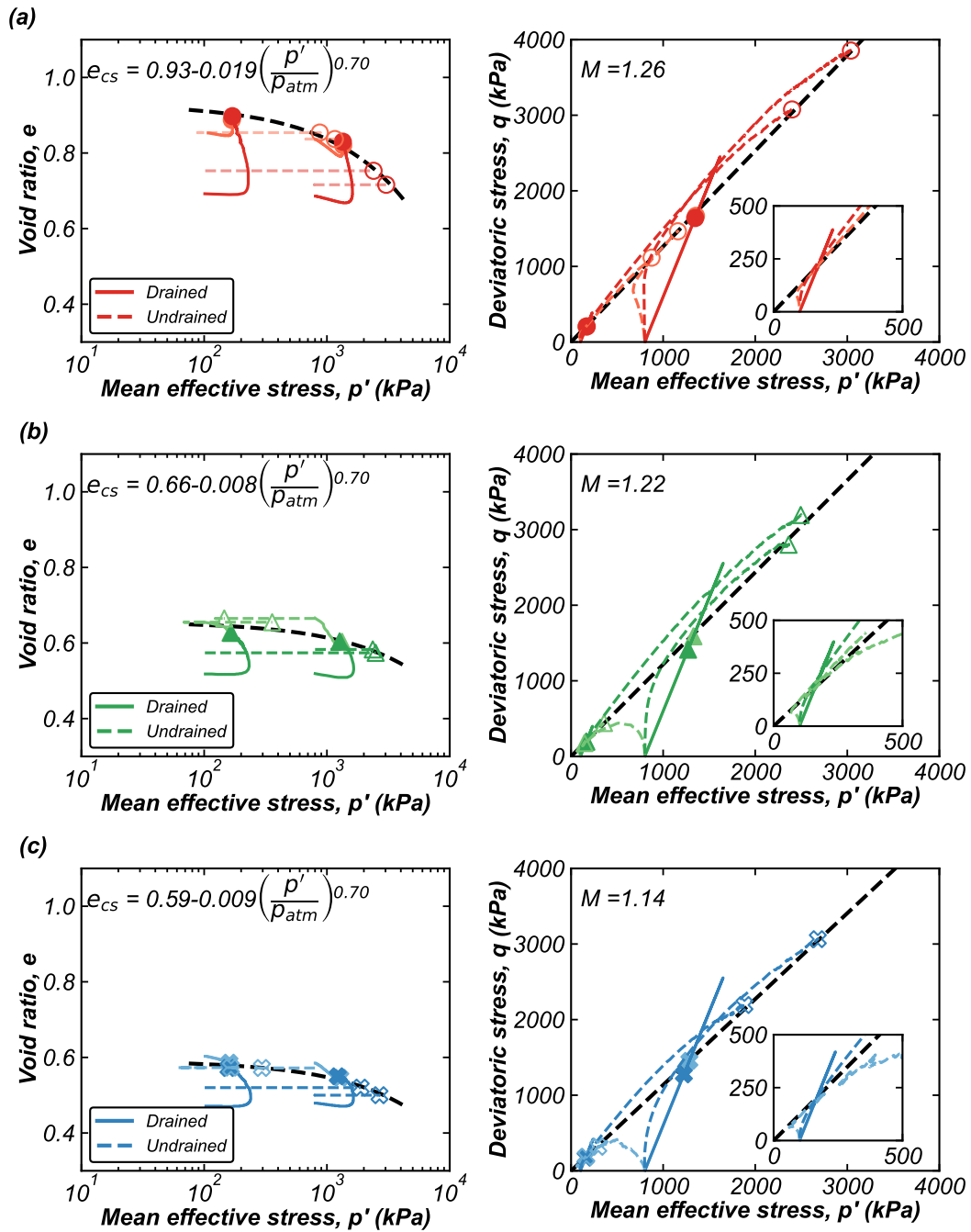


Figure 5.5: Stress paths and critical state lines with respective fittings in the $e\text{-}\log(p')$ and $q\text{-}p'$ spaces for (a) 100A, (b) 33ABC, and (c) 25ABCD.

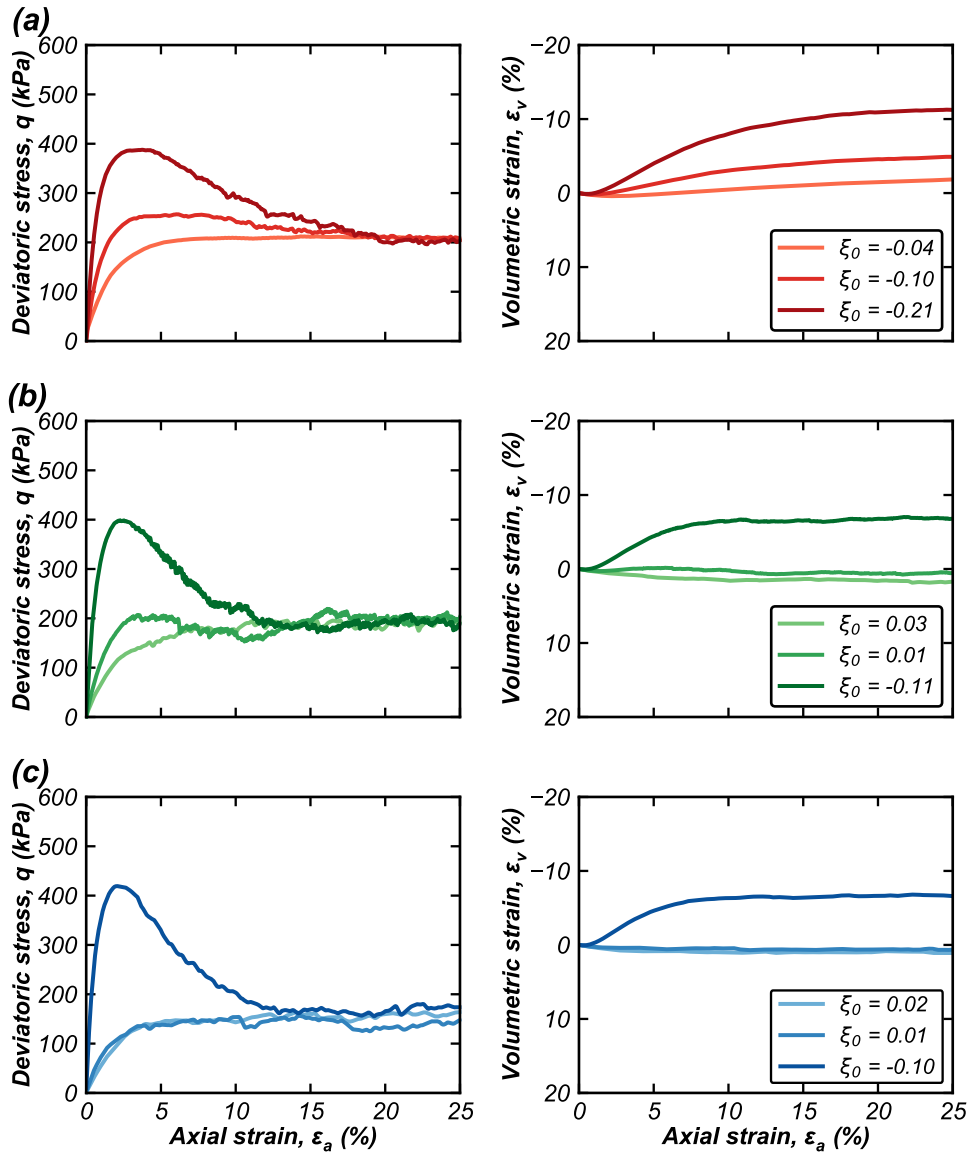


Figure 5.6: Drained triaxial results at $p' = 100 \text{ kPa}$ for (a) 100A, (b) 33ABC, and (c) 25ABCD.

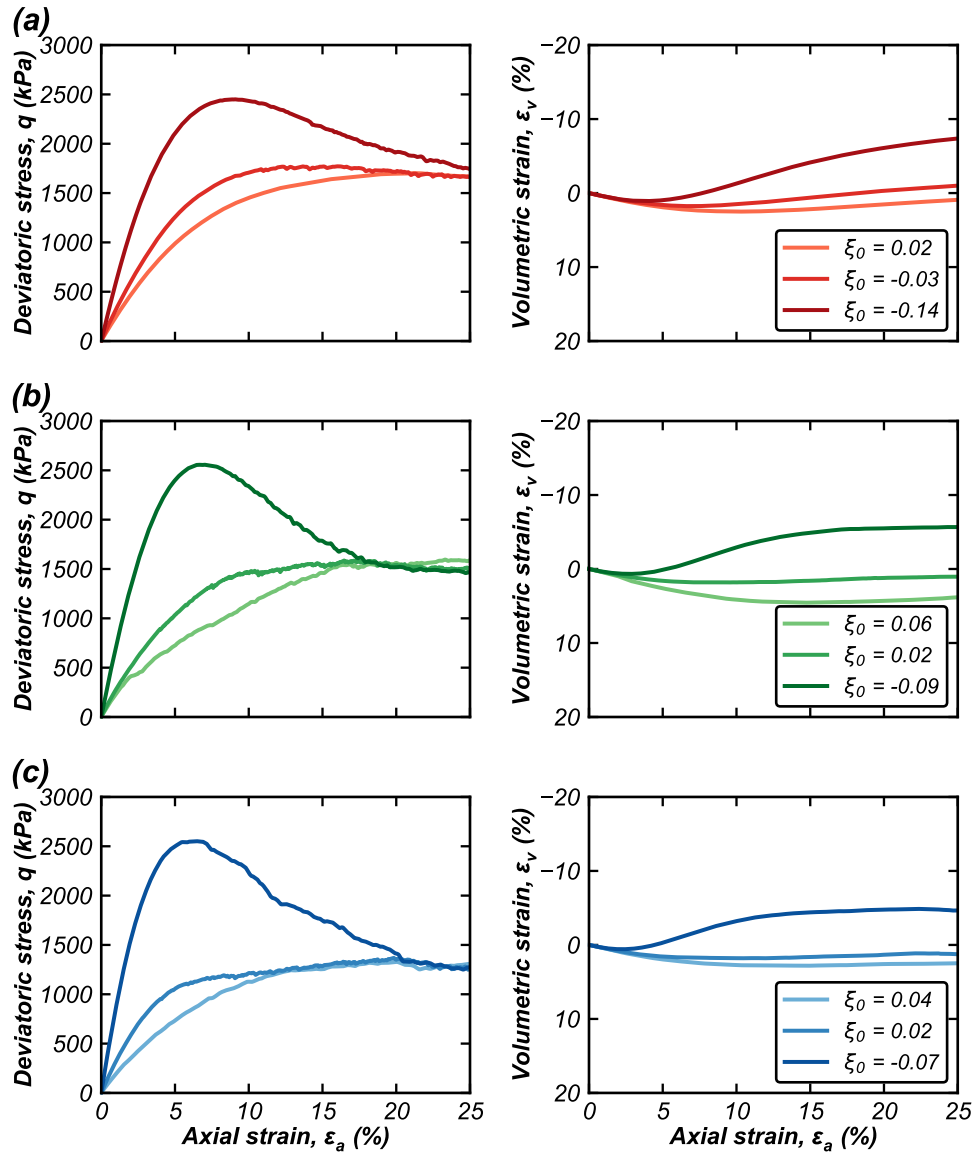


Figure 5.7: Drained triaxial results at $p' = 800 \text{ kPa}$ for (a) 100A, (b) 33ABC, and (c) 25ABCD.

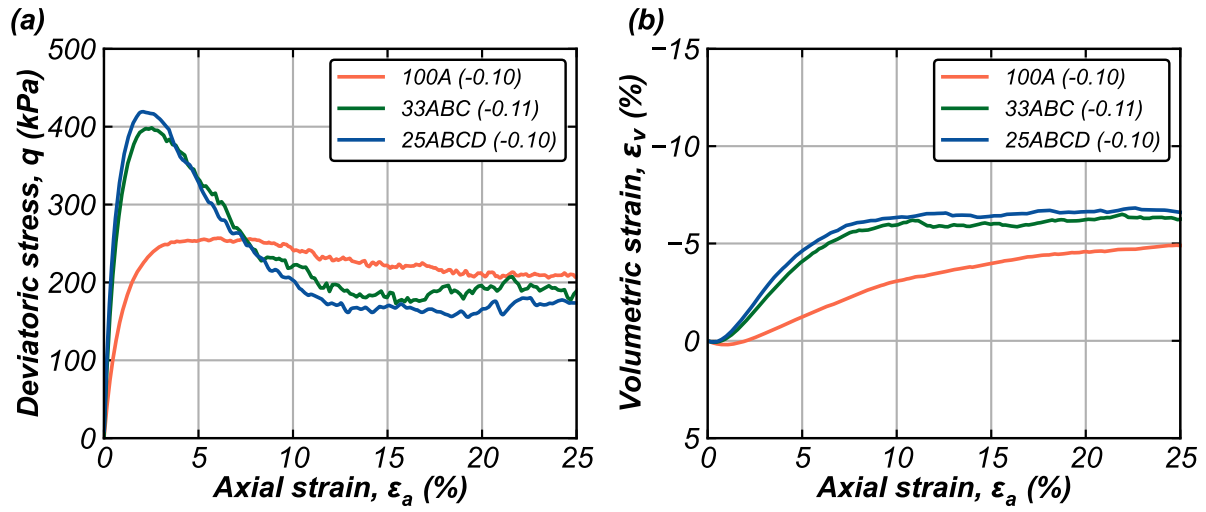


Figure 5.8: Comparison of (a) q/p' and (b) ϵ_v for 100A, 33ABC, and 25ABCD specimens with $\xi_0 = -0.1$ and $p' = 100$ kPa subjected to drained shearing.

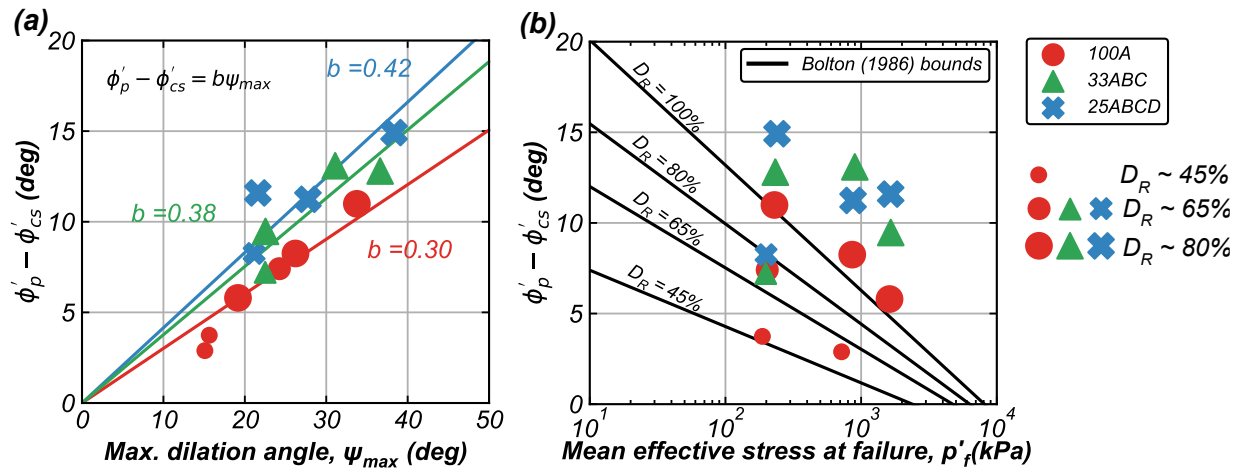


Figure 5.9: (a) $\phi'_p - \phi'_{cs}$ versus ψ_{max} , and (b) $\phi'_p - \phi'_{cs}$ versus p'_f for monotonic drained triaxial tests. The black lines in (b) represent the bounds from Bolton (1986).

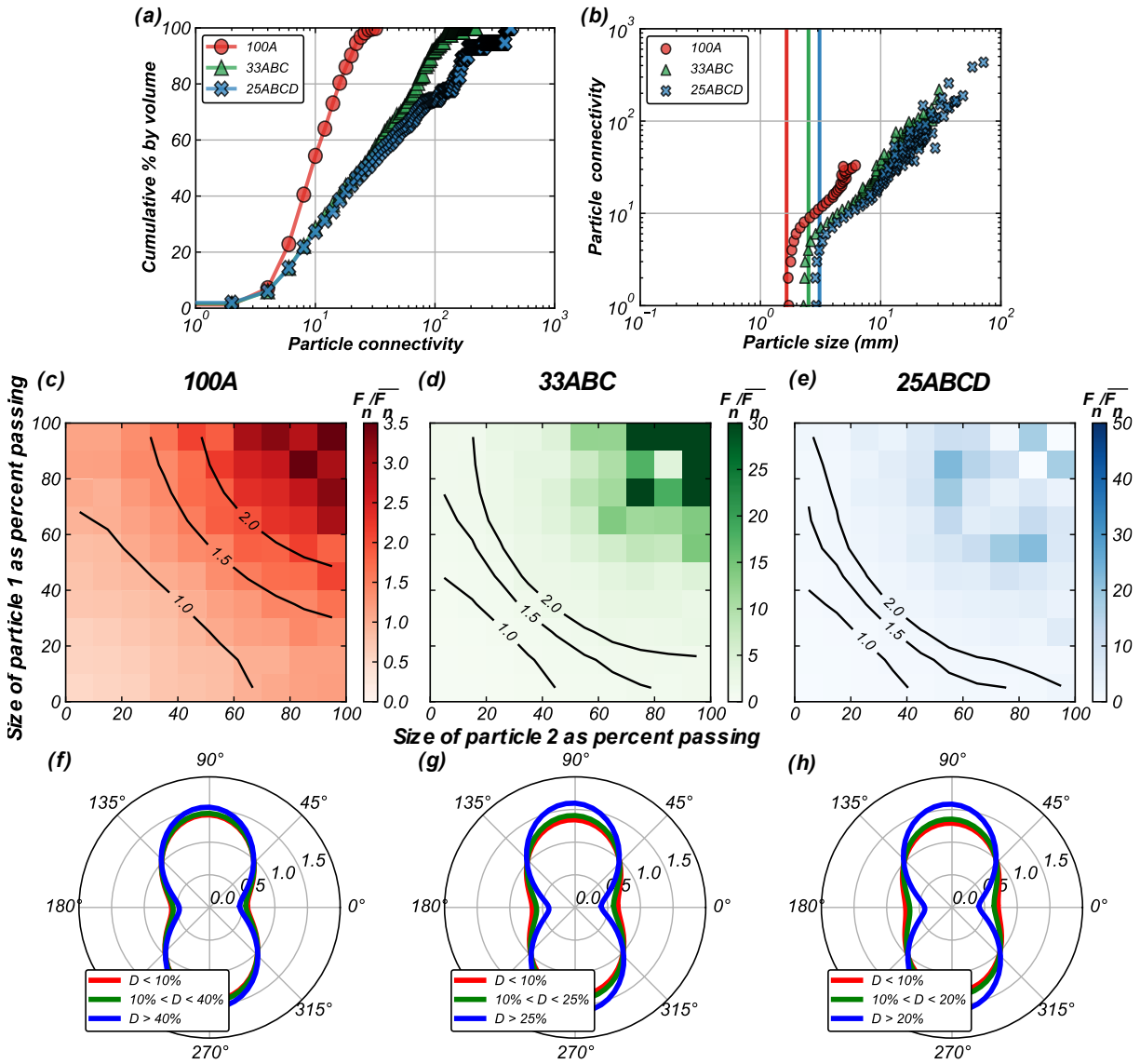


Figure 5.10: (a) Cumulative distribution of PC, (b) variation of PC with the particle size, (c),(d),(e) distribution of contact normal forces with particle sizes (as percent passing), and (f),(g),(h) angular distributions of contact forces for the peak strength states for 100A, 33ABC and 25ABCD specimens subjected drained triaxial compression at $p' = 100$ kPa and

$$\xi_0 = -0.1.$$

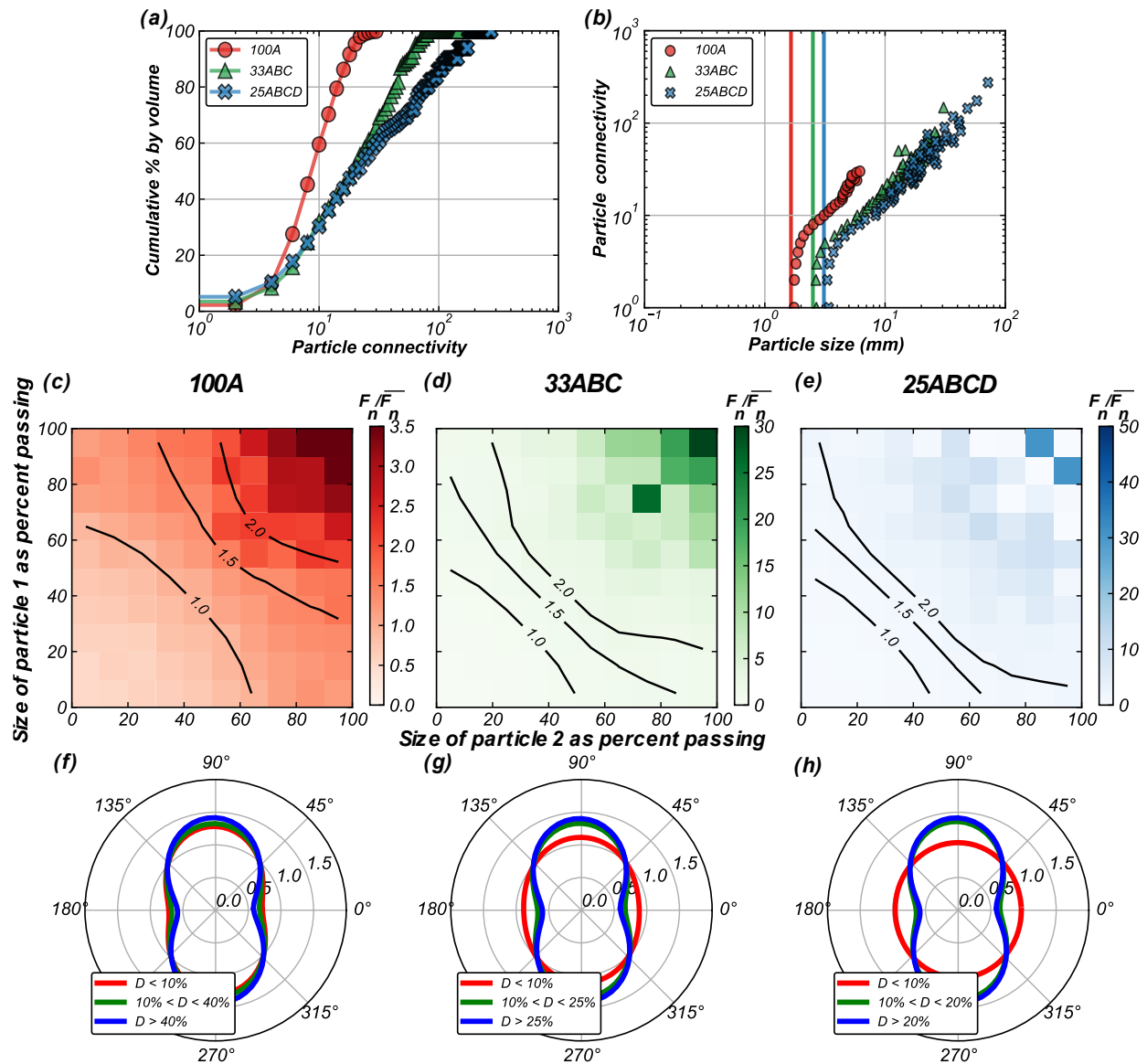


Figure 5.11: (a) Cumulative distribution of PC, (b) variation of PC with the particle size, (c),(d),(e) distribution of contact normal forces with particle sizes (as percent passing), and (f),(g),(h) angular distributions of contact forces for the critical states for 100A, 33ABC and 25ABCD specimens subjected drained triaxial compression at $p' = 100$ kPa and $\xi_0 = -0.1$.

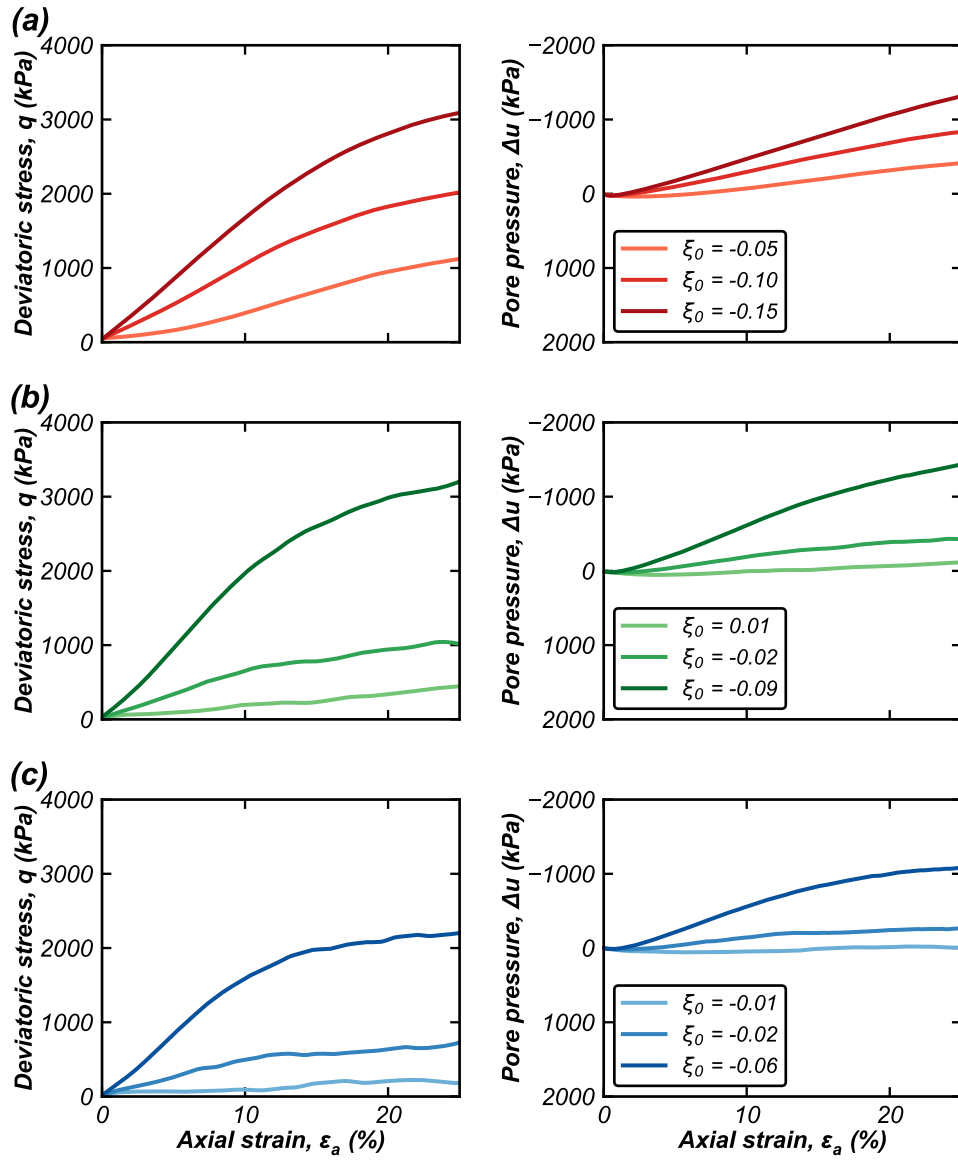


Figure 5.12: Undrained triaxial results at $p' = 100 \text{ kPa}$ for (a) 100A, (b) 33ABC, and (c) 25ABCD.

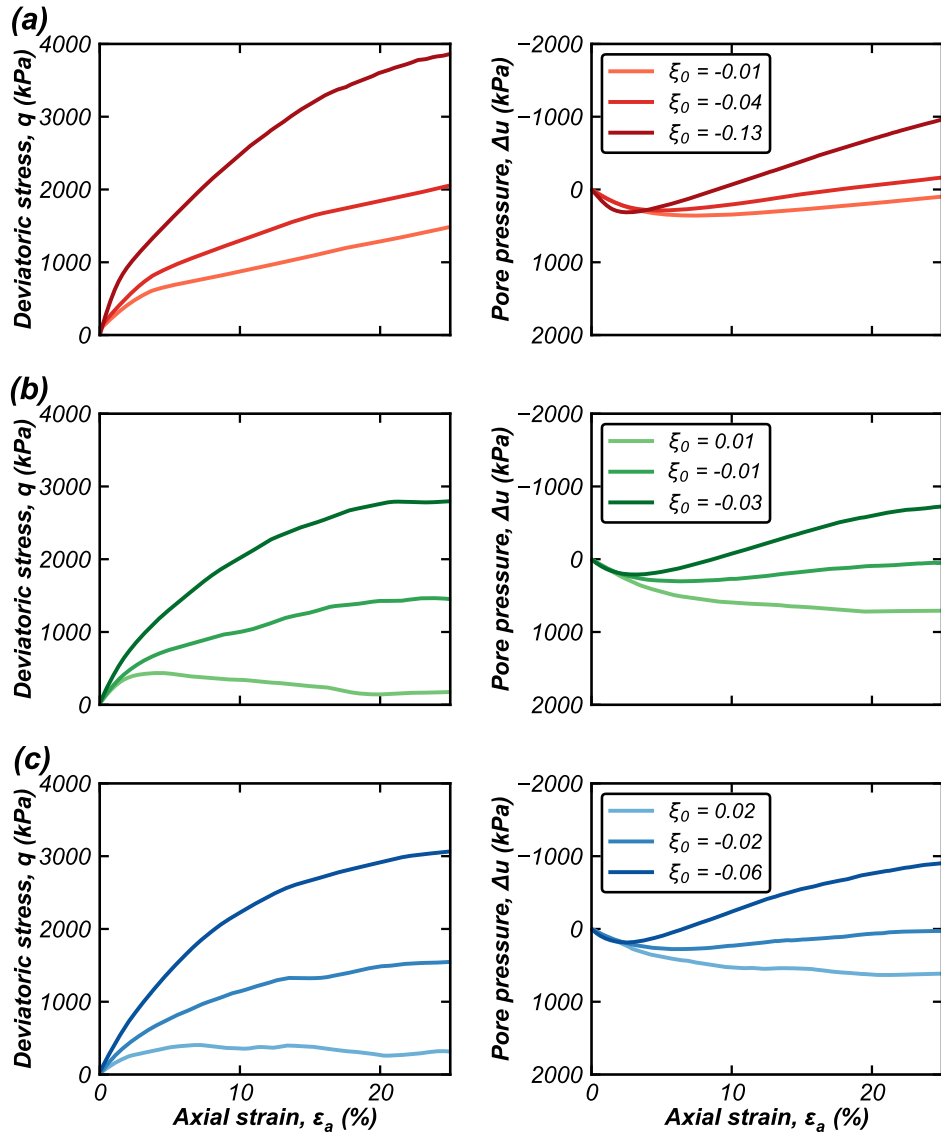


Figure 5.13: Undrained triaxial results at $p' = 800 \text{ kPa}$ for (a) 100A, (b) 33ABC, and (c) 25ABCD.

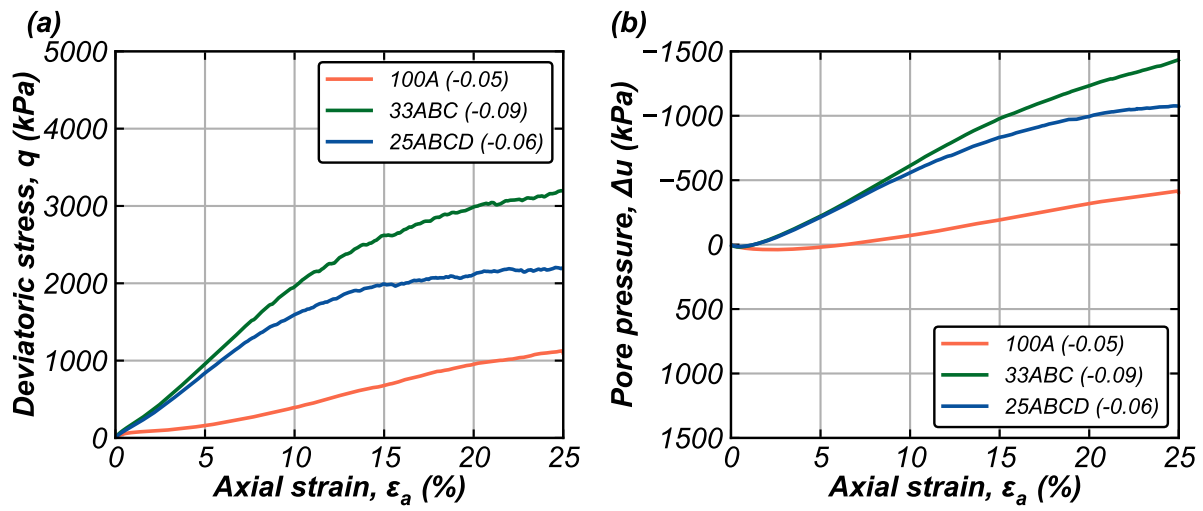


Figure 5.14: Comparison of (a) q and (b) ϵ_v for 100A, 33ABC, and 25ABCD specimens with $\xi_0 = -0.1$ and $p' = 100$ kPa subjected to undrained shearing.

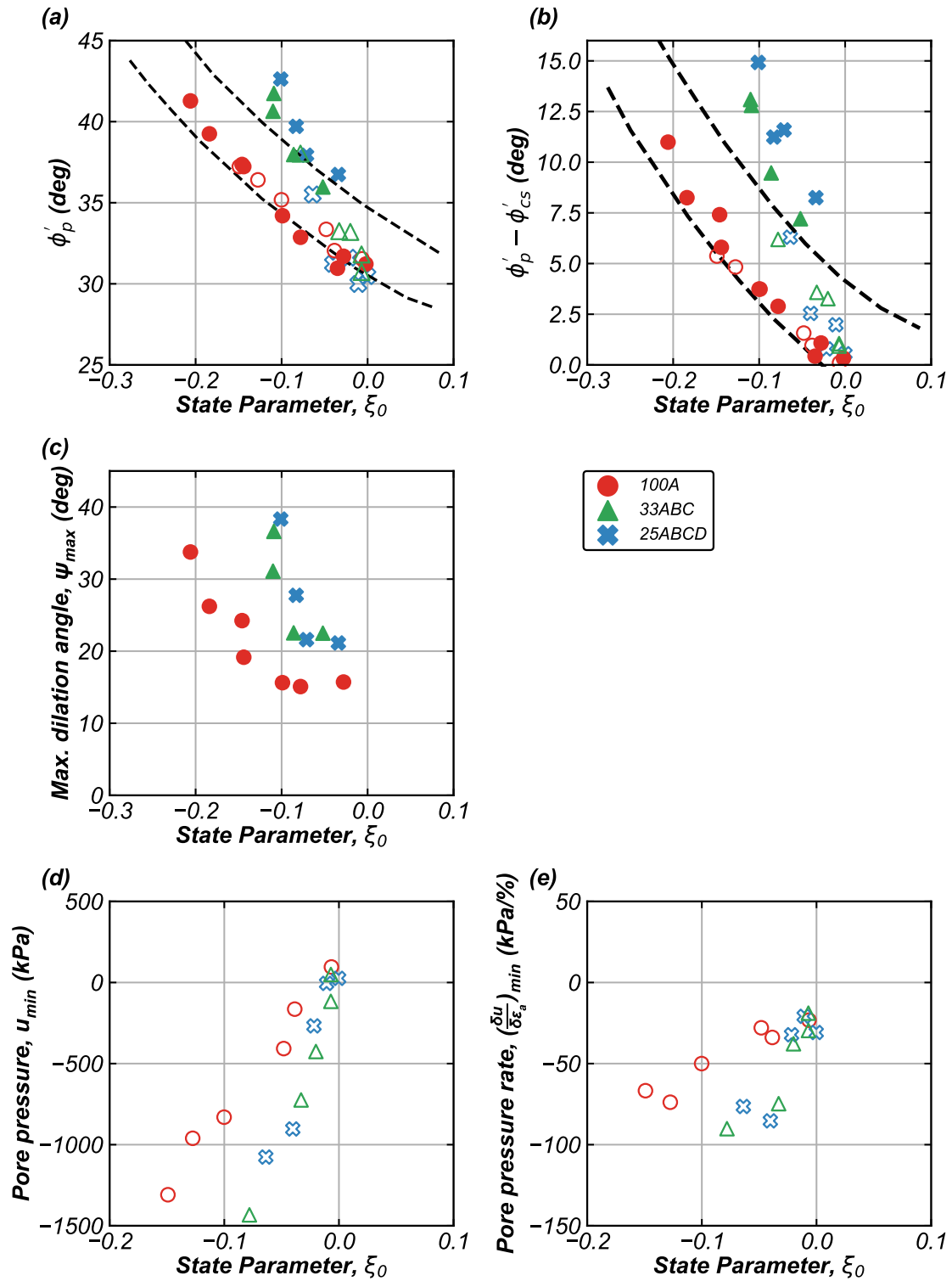


Figure 5.15: Variation of (a) ϕ'_p , (b) $\phi'_p - \phi'_{cs}$, (c) ψ_{max} , (d) u_{min} , and (e) $(\delta u / \delta \epsilon_a)_{min}$ with ξ_0 for drained and undrained tests.

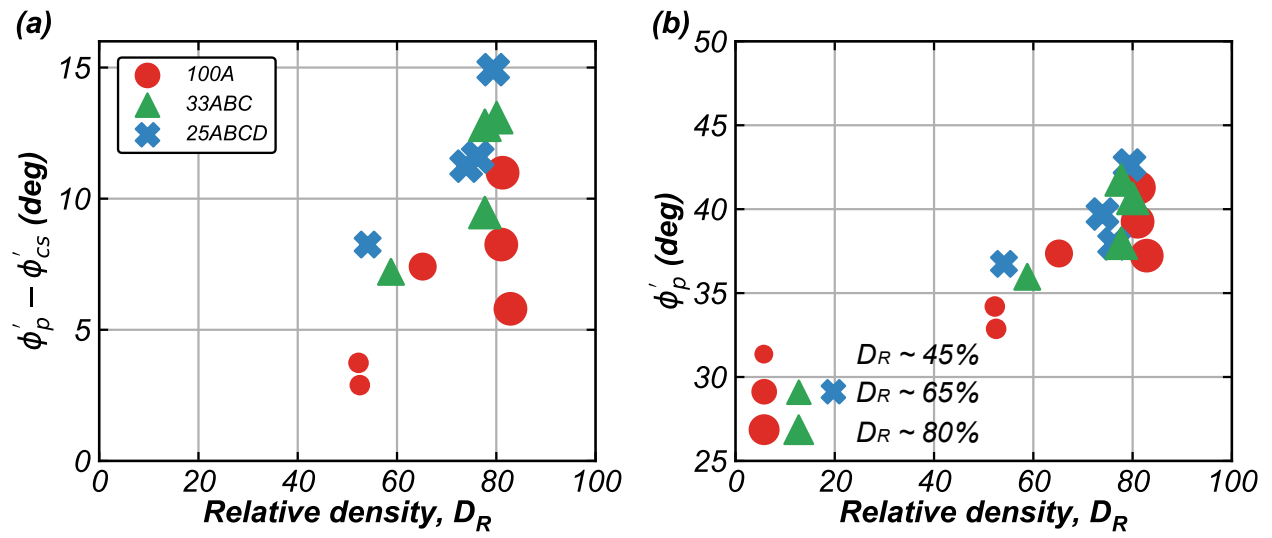


Figure 5.16: Variation of (a) $\phi'_p - \phi'_{cs}$ and (b) ϕ'_p with D_R for drained tests.

Supplementary figures

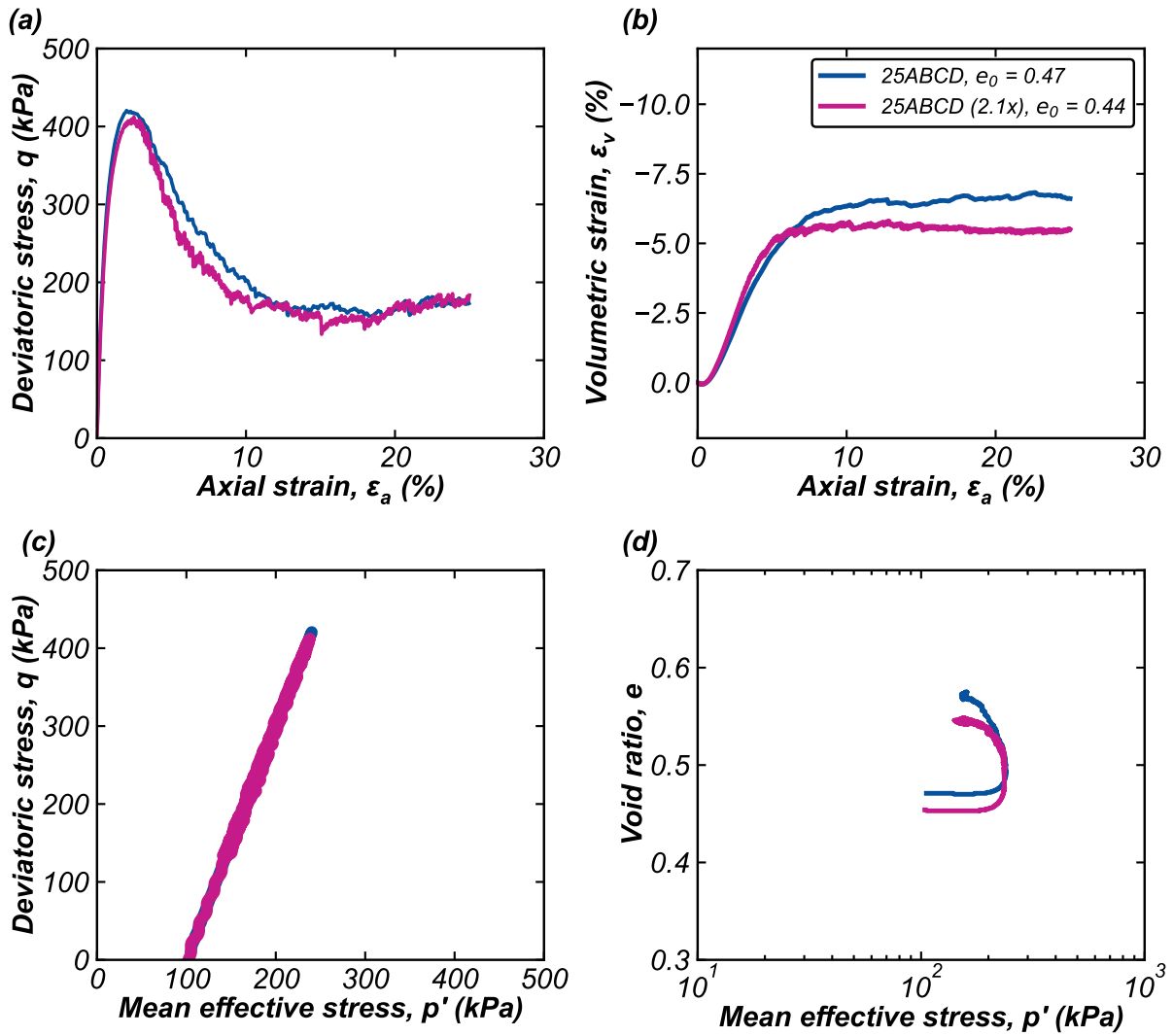


Figure S5.1: Comparison of the (a) q , (b) ε_v , (c) stress path in q - p' space, and (d) stress path in e - $\log(p')$, space between 25ABCD and 25ABCD (2.1x) specimen for drained triaxial simulations at $p' = 100$ kPa.

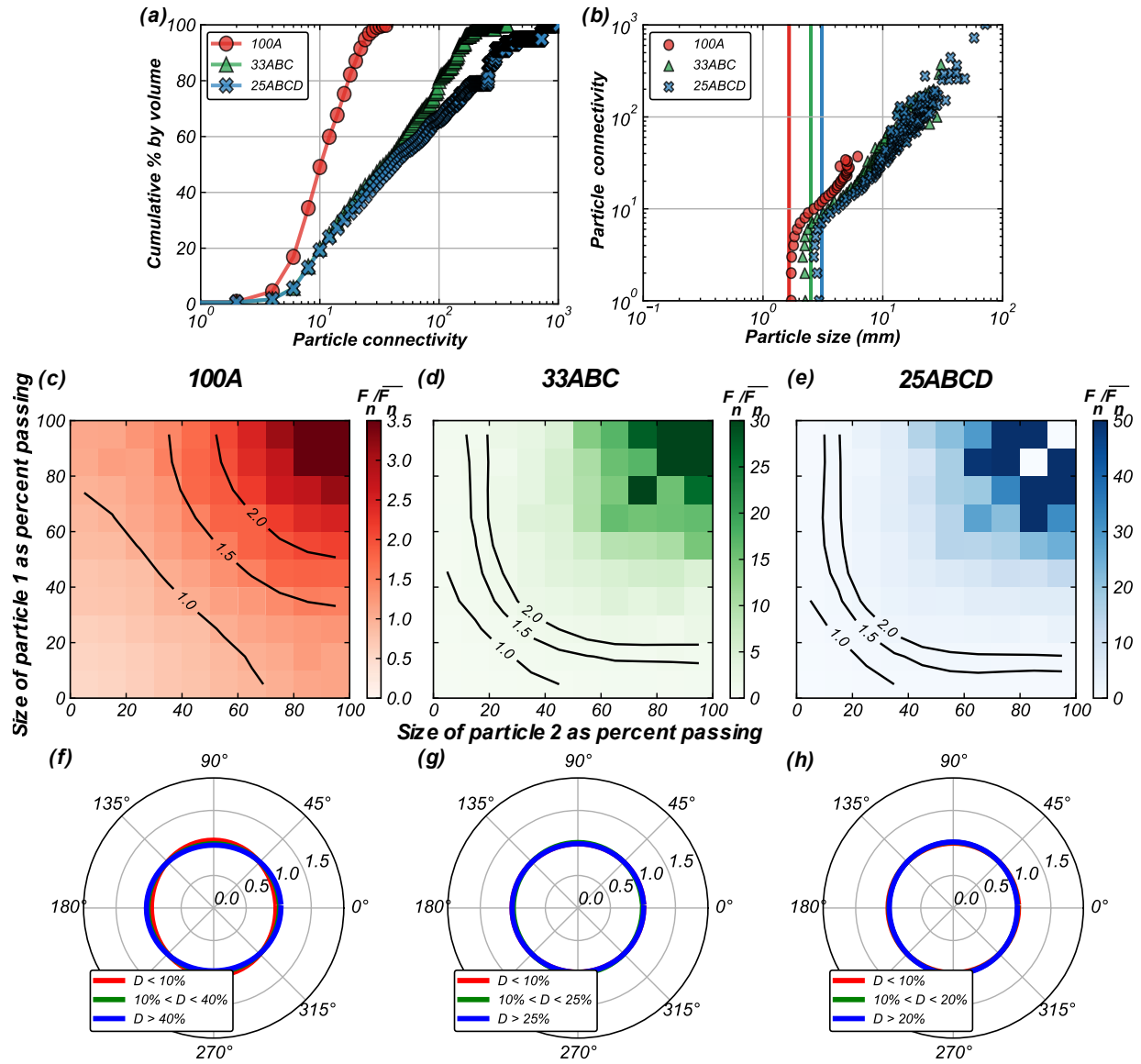


Figure S5.2: (a) Cumulative distribution of PC, (b) variation of PC with the particle size, (c,d,e) distribution of contact normal forces with particle sizes (as percent passing), and (f,g,h) angular distributions of contact forces for the initial states for 100A, 33ABC and 25ABCD specimens subjected to drained triaxial compression at $p' = 100$ kPa and $\xi_0 = -0.1$.

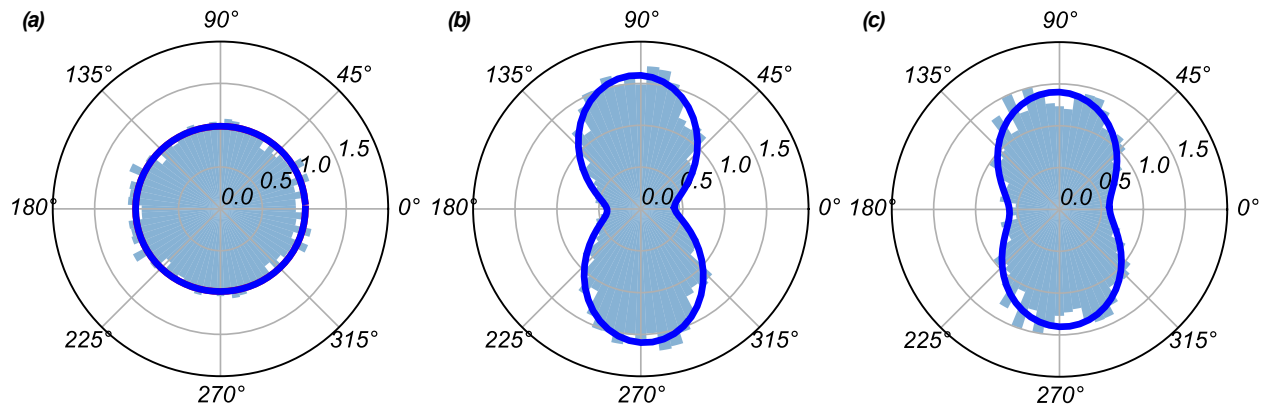


Figure S5.3: Comparison of obtained data and fitted lines using Eq. 7 at (a) initial (Fig. S3h), (b) peak (Fig. 10(h)) and (c) critical (Fig. 11(h)) state for strong forces for 25ABCD specimen subjected to drained triaxial compression at $p' = 100$ kPa and $\xi_0 = -0.1$.

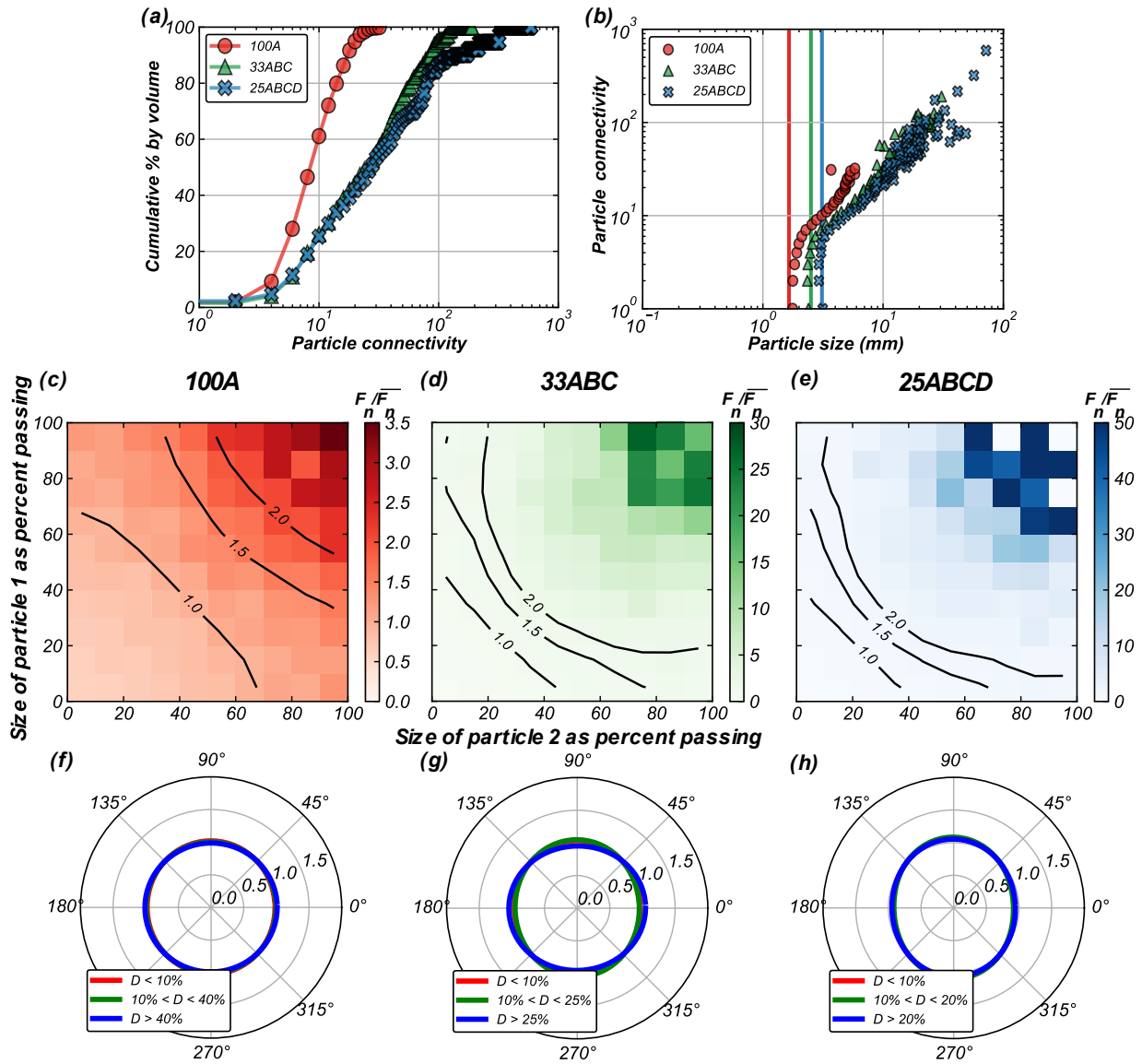


Figure S5.4: (a) Cumulative distribution of PC, (b) variation of PC with the particle size, (c,d,e) distribution of contact normal forces with particle sizes (as percent passing), and (f,g,h) angular distributions of contact forces for the initial states for 100A, 33ABC and 25ABCD specimens subjected to undrained triaxial compression at $p' = 100$ kPa and $\xi_0 = 0.06$.

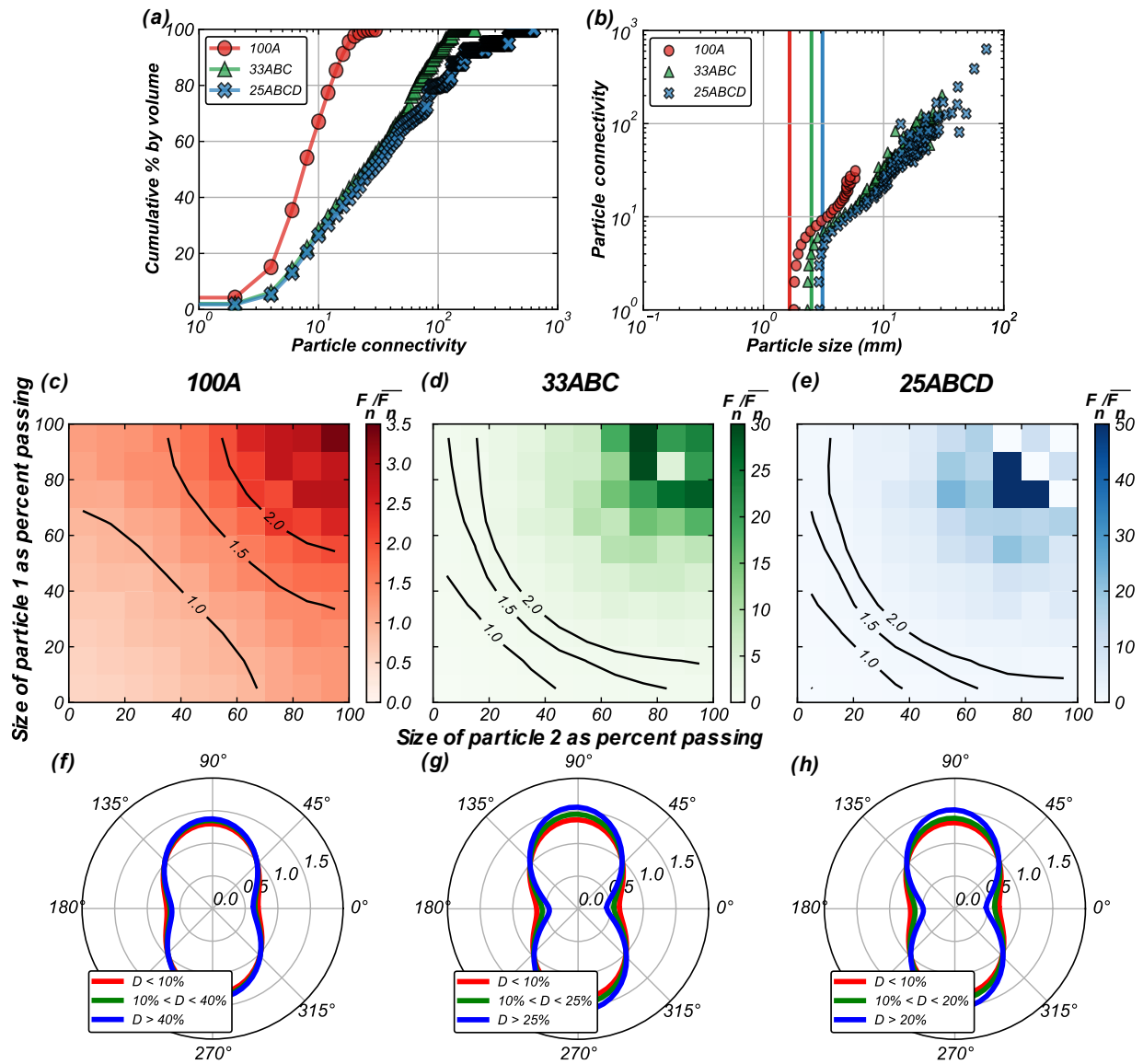


Figure S5.5: (a) Cumulative distribution of PC, (b) variation of PC with the particle size, (c,d,e) distribution of contact normal forces with particle sizes (as percent passing), and (f,g,h) angular distributions of contact forces for the peak states for 100A, 33ABC and 25ABCD specimens subjected to undrained triaxial compression at $p' = 100$ kPa and $\xi_0 = 0.06$.

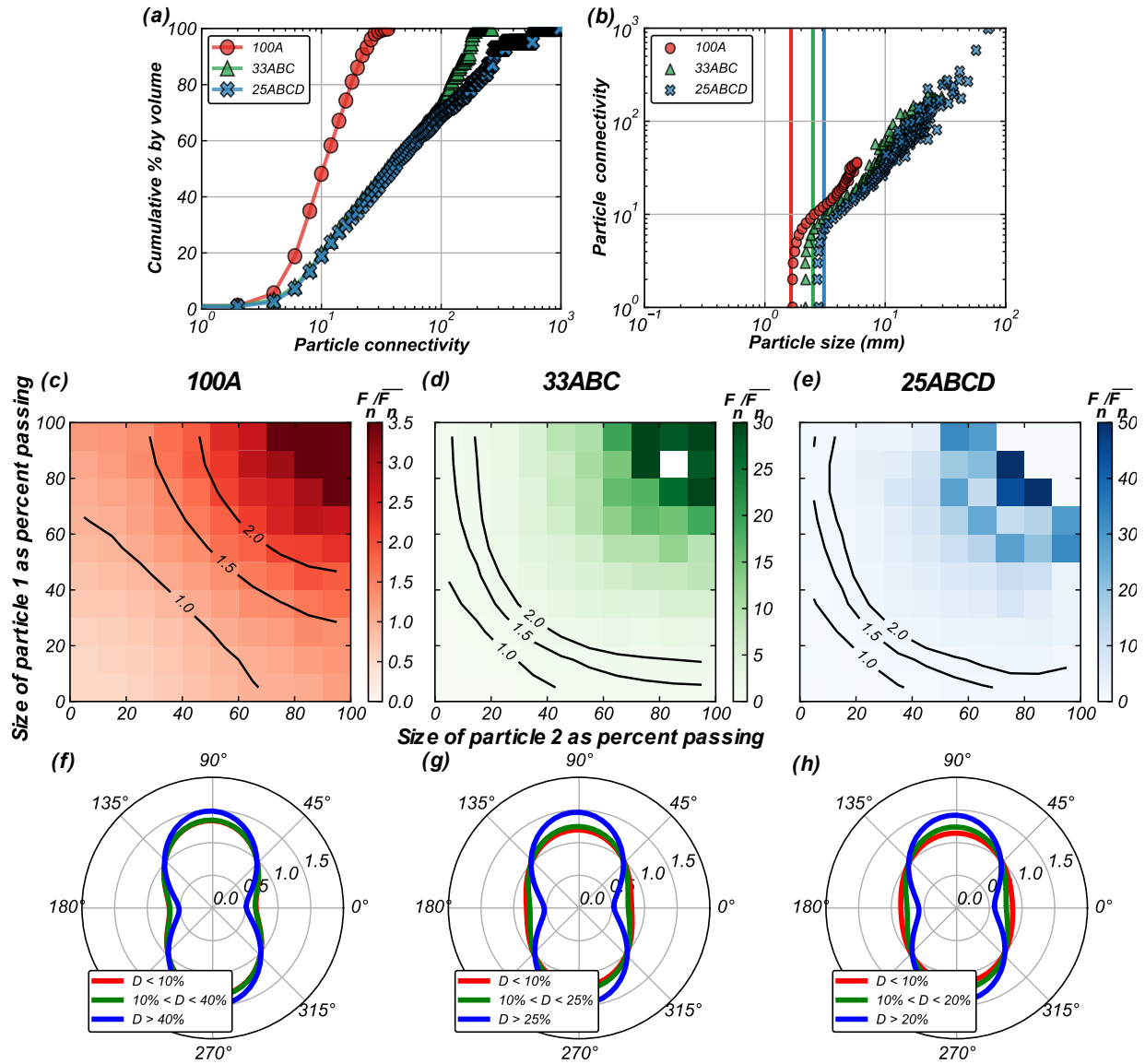


Figure S5.6: (a) Cumulative distribution of PC, (b) variation of PC with the particle size, (c,d,e) distribution of contact normal forces with particle sizes (as percent passing), and (f,g,h) angular distributions of contact forces for the critical states for 100A, 33ABC and 25ABCD specimens subjected to undrained triaxial compression at $p' = 100$ kPa and $\xi_0 = 0.06$.

Chapter 6

DEM simulations of the liquefaction triggering resistance and post-triggering strain accumulation of coarse-grained soils with varying gradations

Author's note: This paper will be submitted as a journal paper to the ASCE Journal of Geotechnical and Geoenvironmental Engineering authored by Mandeep Singh Basson, Alejandro Martinez, and Jason T. DeJong. The paper is presented herein with minor edits for consistency with the other chapters of this Dissertation.

6.1 Abstract

The evaluation of liquefaction triggering potential and induced strains is crucial for liquefaction assessment of geosystems constructed on, or comprised of, coarse-grained soils. A series of cyclic constant volume direct simple shear (DSS) tests were simulated using the discrete element method (DEM) to investigate the influence of gradation on the pre- and post-liquefaction behavior of coarse-grained soils, including the liquefaction triggering resistance, shear strain accumulation, and fabric evolution. The DEM simulations were conducted on isotropically consolidated cubical specimens composed of non-spherical particles with a range of coefficient of uniformity (C_u) between 1.9 and 6.4. Macro-scale

analysis reveals that specimens with broader gradations yield lower liquefaction triggering resistance than poorly graded specimens at similar relative densities. However, the more broadly-graded specimens have higher liquefaction triggering resistance when compared at the same initial state parameter. After liquefaction is triggered, the specimens with broader gradation accumulate shear strains at smaller rates than the poorly-graded specimens. Particle-level measurements, such as the particle connectivity, percentage of sliding contacts, and anisotropy in the strong and weak force networks indicate the impact of gradation on particle packing within the specimen. Specifically, the presence of coarser particles in the broadly graded specimens promotes stable packing and enhanced interlocking by forming a substantially large number of contacts, which limits the particle movement and produces lower post-liquefaction strain accumulation. In contrast, the finer particles minimally contribute to overall specimen stability. Additionally, wider gradations increase the anisotropy in contact forces, with strong forces aligning along the major principal stress direction and weak forces providing resistance against buckling. These insights contribute to a better understanding of pre- and post-liquefaction triggering behavior in granular soils and the implication for the design of resilient infrastructure built on, or comprised of, coarse-grained broadly graded soils.

6.2 Introduction

Earthquake-induced soil liquefaction is a natural phenomenon due to the weakening of load-bearing contact force networks caused by the accumulation of excess pore water pressures (e.g., Ishihara et al. 1975; Seed et al. 1976; Idriss and Boulanger 2008). Liquefaction leads to a substantial loss of soil shear strength and accumulation of shear strains, posing a

significant threat to the stability of critical infrastructure, including dams, levees, tunnels, building foundations, pipelines, bridges, and causing floating of critical buried structures (e.g., Rollins and Seed 1990; Bray et al. 2014; Cubrinovski et al. 2017). Gravelly alluvial soils deposited by rivers and streams are among the most common natural deposits that underlie or comprise the aforementioned critical infrastructures. These soils consist of a wide range of particle sizes, including coarser particles that are notably larger than clean sands, leading to a coefficient of uniformity (C_U) value greater than 40 (e.g., Kokusho et al. 2004; DeJong et al. 2016). Given the numerous case studies documenting liquefaction in coarse-grained broadly-graded soils in the field (e.g., Kokusho et al. 1995; Towhata et al. 2014; Zhou et al. 2020), it is vital to understand the effect of differences in the particle size distribution (PSD) on the liquefaction behavior of soils.

Numerous laboratory experimental and physical modeling investigations have been conducted to examine the effect of PSD on the liquefaction triggering resistance. Although these studies have made significant contributions to understanding liquefaction in broadly graded soils, there are still inconsistencies and knowledge gaps, particularly in isolating the specific effects of increasing C_U compared to an increase in particle sizes. For instance, studies indicate that increases in C_U while maintaining the median particle size (D_{50}) can produce either an increase (Yilmaz et al. 2008) or a decrease in the liquefaction resistance (Chang et al. 2014; Doygun et al. 2019; Reardon 2021; Humire 2022), or show no clear correlation (Wichtmann et al. 2019). Vaid et al. (1990) reported that specimens with higher C_U but similar D_{50} have increased liquefaction resistance at low relative densities (D_R). In contrast, at higher D_R , there is a decrease in liquefaction resistance with increasing C_U . Kokusho et al. (2004) observed only a small difference in liquefaction resistance for soils

with different C_U while keeping the minimum particle diameter constant. Most studies report that soils with broader gradations exhibit a more dilative post-liquefaction response, which ultimately leads to lower liquefaction-induced deformations (e.g., Evans and Zhou 1995; Hubler et al. 2018; Humire 2022; Carey et al. 2022; Pires-Sturm and DeJong 2022), and only a few studies have systematically studied the post-liquefaction strain accumulation in coarse-grained soils that undergo cyclic mobility (rather than flow liquefaction) (Tasiopoulou et al. 2020; Humire and Ziotopoulou 2022). These observations are consistent with observations from monotonic testing where soils with higher C_U demonstrate higher peak strengths and greater rates of dilation (Hamidi et al. 2012; Amirpour Harehdasht et al. 2017; Basson et al. 2023a; Ahmed et al. 2023).

The discrepancies observed in laboratory testing and physical modeling investigations may be attributed to either the coupling of changes in gradation with other particle properties, such as particle shape and D_{50} , differences in the definition of state used for comparison (i.e., relative density (D_R) versus void ratio versus state parameter), or limitations and boundary effects inherent to the testing device. For instance, the size of the specimen and the compliance of the particle-membrane interface may artificially increase the liquefaction resistance for soils with a relatively large size difference between the coarser and finer particles (Evans et al. 1992; Humire 2022). Recent studies indicate that changes in monotonic soil behavior, particularly the trends in peak friction angle, dilation angle, and excess pore pressure generation, resulting from a widening of gradation, can be effectively captured by comparing the response with the initial state parameter (i.e., the difference between the current void ratio and critical state void ratio at a given mean effective stress, ξ_0 , per Been and Jefferies (1985)) (e.g., Huang et al. 2014b; Basson et al. 2023b; Ahmed et al.

2023). The ξ_0 is able to capture the changes in the void ratio and the shift in the critical state lines with a widening of gradation, in comparison to using either the initial void ratio or D_R .

Discrete element modeling (DEM) has been recently adopted as a numerical tool to understand the effect of changes in gradation on particle packing, shear strength, stress-dilatancy, and liquefaction resistance independent of other particle characteristics (e.g., Huang et al. 2019; Kuei et al. 2020; Yang et al. 2022b; Basson et al. 2023b; Banerjee et al. 2023; Zuo et al. 2023). From a micro-scale perspective, the liquefaction resistance and post-liquefaction strain accumulation are influenced by particle contact interactions and the distribution of contacts between the particles of different sizes within the specimen. In soils with broader gradations, the coarser particles form a larger number of contacts and carry a higher magnitude of contact forces as compared to finer particles. Additionally, the presence of finer particles promotes pore space filling, leading to improved particle packing and enhanced particle interlocking. The enhanced interlocking limits particle movement and can reduce deformations during repeated cyclic loading.

This study investigates the effect of gradation on the pre- and post-liquefaction triggering response and evolution of the fabric of coarse-grained soils using cyclic constant volume direct simple shear DEM simulations. The tested specimens are created based on three PSDs with C_U ranging between 1.9 to 6.4 and tested over a range of D_R and ξ_0 . The macroscale results are presented as shear stress – shear strain curves, shear-induced pore pressures – cycle number relationships, liquefaction triggering curves, and post-triggering strain accumulation. Analysis of soil fabric is presented, examining the percentage of sliding contacts, particle packing characterized by mechanical coordination number and particle

connectivity, and the evolution of fabric anisotropy at different points during cyclic shearing to reinforce the obtained macroscale differences as a result of changes in gradation.

6.3 Simulation methodology

6.3.1 Simulated granular materials

The simulated particle size distributions and particle shapes were based on a range of naturally available well-graded soils sourced from a marine deposit from Cape May formation near Mauricetown, New Jersey. The sourced soils were segregated into four poorly graded soils named as 100A, 100B, 100C, and 100D, where the former is the finer and the latter is the coarser. The poorly graded soils were mixed into different proportions to create soils with different gradations. The 33ABC soil comprises equal parts (33%) of 100A, 100B, and 100C, while the 25ABCD soil comprises equal parts (25%) each of 100A, 100B, 100C, and 100D. These soils have been extensively tested at the University of California Davis using centrifuge physical modeling (Sturm 2019; Sawyer 2020; Carey et al. 2022), laboratory testing (Humire 2022; Reardon et al. 2022; Ahmed et al. 2023), and numerical modeling (Chiaradonna et al. 2022; Basson et al. 2023a; b). To achieve realistic computation times, the simulated PSDs were upscaled by 20 times compared to the experimental PSDs, based on recommendations of past studies (Ciantia et al. 2015; Coetzee 2019). Table 6.1 summarizes the gradation and packing characteristics of the simulated soils, while Fig. 6.1(a) presents the PSD of both the experimentally tested (EXP) and simulated (DEM) soils.

The particle shape influences the packing characteristics and the overall behavior of soils subjected to cyclic loading (e.g., Ashmawy et al. 2003; Santamarina and Cho 2004; Athanassiadis et al. 2014). An attempt was made to recreate the natural particle shapes using

clumped particles. Clumping multiple spherical particles into particles of specific shapes has been widely adopted in past DEM studies as a computationally-efficient way to recreate particle shapes (Garcia et al. 2009; Zheng and Hryciw 2017). Based on the recommendations presented in the literature (Ferrellec and McDowell 2008; Suhr and Six 2020), seven clump templates were generated to match the particle shape parameters. Three clump templates (Fig. 6.1(b)) out of the seven were selected as they best matched the particle perimeter, width/length, circle ratio, area, diameter sphericities, and regularity values obtained from real soils (Fig. 6.1(c)). All the specimens were created with 70% clump #1, 20% clump #2, and 10% clump #3 because specimens with those mixes better matched the experimental maximum and minimum void ratios (e_{max} and e_{min} , respectively). In the DEM simulations, the e_{max} and e_{min} were obtained through manipulation of the inter-particle friction coefficient μ_{prep} and the damping coefficient ζ_{prep} for specimens prepared at a confining stress of 10 kPa, as typically done (Muir Wood and Maeda 2008; Gu et al. 2020a; Zuo et al. 2023). To achieve the e_{max} , μ_{prep} , and ζ_{prep} of 0.5 were used, whereas, for e_{min} , lower values of μ_{prep} of 0.01 and ζ_{prep} of 0.05 were chosen. Subjectivity is involved in selecting these parameters, as noted in O'Sullivan(2011) and Kuhn et al. (2014). However, these specific parameters values were selected as they provided a close match to the experimentally obtained e_{max} and e_{min} values (Fig. 6.1(d)). Other aspects considered in the decision of particle shape and proportion of clump templates were the ability to obtain reasonable calibrations for the drained triaxial response and liquefaction triggering curve for direct simple shear, as described in more detail below. More information on the selection of clump templates is presented in Basson et al. (2023b).

6.3.2 Simulation procedure

Constant volume cyclic direct simple shear (DSS) simulations were conducted using the three-dimensional DEM code YADE (Šmilauer et al. 2010). Cubical specimens, as shown in Fig. 6.2, were generated with clumped particles based on the gradations presented in Fig. 6.1(a). Periodic boundaries were employed around the specimens to ensure homogenous strain fields throughout the simulation procedure. The simulation procedure consisted of a sample preparation stage followed by a cyclic shearing stage. During sample preparation, a cloud of initially non-overlapping particles was randomly created inside a larger cubical box and isotropically compressed to an initial mean effective stress (p'_0) of 100 kPa using a servo-control algorithm. This sample preparation technique produces specimens with negligible initial fabric and stress anisotropy (Basson and Martinez 2023a). The void ratio and density of the specimen were controlled by changes in the friction coefficient during the sample preparation stage (μ_{prep}) within the range of 0.01 and 0.5 while keeping the damping ζ_{prep} constant at 0.05. Specimens were created for target D_R ranges between 39% to 43% and 58% to 60%, and additional specimens were prepared to compare responses at similar initial state parameters (ξ_0) of -0.01 and -0.06. Basson et al. (2023b) performed drained and undrained triaxial compression simulations to define the critical state lines for the 100A, 33ABC, and 25ABCD soils. These critical state lines, presented in Fig. 6.3, illustrate that the position and slope of the critical state line in the $e-\log(p')$ plane decrease as the gradation becomes wider. Additionally, a relative decrease in the difference between e_{max} and e_{min} values (Table 6.1) is observed with a broadening of gradation (also shown in Fig. 6.1(c)). The implications of these observations on the comparison of cyclic behavior with respect to ξ_0 and D_R are presented in the subsequent section.

During the cyclic shearing stage, constant specimen volume was maintained by fixing its height constant. This constant volume approximation is widely used in DEM simulations due to its computational efficiency and reasonable agreement with laboratory testing (e.g., Bonilla 2004; Hanley et al. 2013; Keishing and Hanley 2020). It is noted that the presence of fines in the specimens with wider gradations could potentially alter the permeability and affect the excess pore pressure generation rate, as noted by Carey et al. (2022) and Zhang and Rothenburg (2020). Nonetheless, the constant volume method was adopted to achieve reasonable calibration to the trends obtained from constant volume laboratory testing of the dry specimen with similar gradations (Humire et al. forthcoming). Cyclic shear strains were induced by applying a strain gradient from the bottom to the top of the specimen, with the bottom remaining fixed to mimic the loading strain gradient applied in the experiments. The strain gradient was reversed when the horizontal shear stresses (τ_{xz}) reached a specified target shear stress (τ_{target}). The strain rate for the strain gradient was chosen to ensure that the specimen was sheared in the quasi-static regime by keeping the inertial number below 10^{-3} . The value of τ_{target} was computed based on the cyclic shearing ratio (CSR) as:

$$CSR = \frac{\tau_{target}}{p'_0} \quad (6.1)$$

where p'_0 is the initial mean effective stress. This cyclic shearing method produced a strain-controlled 'zig-zag' loading time history as shown in Fig. 6.4, which has been widely adopted in the DSS simulations using DEM (Kuhn et al. 2014; Banerjee et al. 2023). The stresses and strains were computed in a measurement cube slightly smaller than the specimen size. The gravity was set to zero during both sample preparation and cyclic shearing. In total,

specimens with different ξ_0 and D_R values were tested at a p'_0 of 100 kPa at CSRs of 0.05, 0.10, 0.15, and 0.20. Table 6.2 summarizes the details of the tested specimens.

The contact interactions between the particles were simulated based on a linear elastic model incorporating Mohr-Coulomb plasticity. Table 6.3 summarizes the contact parameters used in this study. To eliminate the effect of differences in D_{50} on the overall response, the normal contact stiffness was computed based on the normalized particle stiffness, represented by the ratio of particle normal stiffness to particle diameter (k/d), as suggested by Scholtès et al. (2009) and implemented by Šmilauer et al. (2010). The contact parameter values were obtained by performing a parametric comparison between the experimental and simulation results obtained from drained triaxial results (Basson et al. 2023b). To assess the suitability of these parameters to simulate the pre- and post-liquefaction triggering response of specimens, constant-volume cyclic DSS simulations were performed on 100A specimens and compared to the responses obtained from experimental DSS testing on specimen made of 100A gradation presented in Humire et al. (forthcoming). Figs. 6.5(a,b,c) compares the experimental and simulation results for a 100A specimen at a similar $D_R \sim 42\%$, and Figs. 6.5(d,e,f) compares the results for specimen at a similar $\xi_0 \sim -0.11$. The results show a strong similarity between the experimental and the simulation results and offer valuable insights into the challenges of calibrating simulation parameters to reproduce experimental results based on the chosen definition of specimen state. Specifically, for specimens prepared at similar D_R , the liquefaction triggering curves, presented as CSR-N curves based on the number of cycles (N_L) to triggering of liquefaction when the pore pressure ratio (ru) reaches a value of 0.99 (Fig. 6.5(c)), are relatively similar between the experiments and the simulations, despite the steeper slope of the DEM results. In contrast,

the post-triggering response exhibits notable differences (Fig. 6.5(b)). However, in comparison for specimens at similar ξ_0 , the post-liquefaction response is similar (Fig. 6.5(e)) while the liquefaction triggering response differs significantly between the two specimens (Fig. 6.5(f)). Although the simulation of pore water is not incorporated in this study, the excess pore pressure was computed based on the standard practice of assuming constant volume and incompressible fluid. Consequently, the equivalent excess pore pressure ratio (r_u) was computed as the reduction in p' normalized by its initial value, as:

$$r_u = \frac{p'_0 - p'}{p'_0} \quad (6.2)$$

where p' is the current mean effective stress. The point at which the r_u exceeds 0.99 was considered the liquefaction triggering threshold, during which the number of cycles required to reach liquefaction (N_L) was recorded. The test stage before triggering is referred to as pre-triggering, while the stage after triggering is referred to as post-triggering. Additionally, the experiments and DEM simulations exhibit a similar failure slope (M_f) approximating the dilation phase of the butterfly shaped response. Specifically, the experiments yield M_f of 35.8° compared to 34.1° for DEM simulations for specimen at similar D_R 43% and of 35.8° compared to 34.4° for DEM simulations for specimen at similar $\xi_0 \sim 0.11$. The differences described here in the cyclic response between the experiments could be possible due to the variation in the particle shape (DEM specimen consists of clumped particles as shown in Fig. 6.1(b)) and boundary effects (periodic boundaries in DEM as compared to stacked rings and membrane in the experiments). Despite the differences in the response, the comparison of numerical and experimental results indicates that the contact

parameters used in this investigation produce realistic responses of cyclic behavior in sandy soils.

The relative difference between the specimen size ($D_{specimen}$) and the particle size controls the number of particles in the specimen and can influence the specimen behavior. $D_{specimen}$ was computed based on the maximum of either 20 times the D_{50} or 4 times the largest particle diameter (D_{max}) for a given PSD, based on the recommendations presented in past research (e.g., O'Sullivan 2011; Huang et al. 2014a; Mutabaruka et al. 2019). The $D_{specimen}/D_{50}$ ratio ranged from 22.1 for 100A to 21.0 for 25ABCD, while the $D_{specimen}/D_{max}$ ratio varied between 10.6 for 100A to 4.2 for 25ABCD. Based on these values, the tested specimens consisted of 35,000 clumps for 100A specimens and 50,000 clumps for 33ABC and 25ABCD specimens. An additional specimen was created with 2.1 times the $D_{specimen}$ and 1.5 times the number of clumps for the 25ABCD specimen to evaluate the appropriateness of the chosen specimen size. Figure 6.6 compares the response between the 25ABCD and 25ABCD (2.1x) specimens prepared at similar initial states and tested at a CSR of 0.1. Increasing the specimen size and the number of particles does not significantly affect the overall response. Specifically, the number of cycles to triggering of liquefaction, post-triggering strain accumulation, and rate of pore pressure generation are relatively similar between the two specimens. Therefore, the smaller specimen was used for the simulations to reduce the computational cost.

6.4 Cyclic direct simple shear simulations

This section presents the results of cyclic DSS simulations performed on 100A, 33ABC, and 25ABCD specimens. First, representative results are compared in terms of shear stress, shear

strains, and generation of excess pore pressures. Subsequently, the liquefaction triggering curves and accumulation of shear strain results are presented and compared for specimens at similar D_R and ξ_0 .

6.4.1 Cyclic direct simple shear response

The cyclic shearing response of all the specimens exhibits the typical macroscopic behavior of coarse-grained soils. Figure 6.7 presents representative results in terms of τ_{xz} versus p' , τ_{xz} versus shear strains (γ_{xz}), and r_U versus the number of cycles (N) obtained from DSS simulations on the 100A, 33ABC, and 25ABCD specimens. The specimens were prepared at a ξ_0 range of -0.01 to -0.07 and D_R range of 39% to 43%, , subjected to CSRs of 0.05, 0.10, and 0.15. Figure 6.8 presents similar results for specimens prepared within a ξ_0 range of -0.06 to -0.14 and D_R range of 58% to 61% , subjected to CSRs of 0.10, 0.15, and 0.20. It is important to note that due to the difference in definitions, a similar D_R between specimens does not correspond to a similar ξ_0 . For example, a 100A specimen prepared at a D_R of 61% has a ξ_0 of -0.14, while a 25ABCD specimen prepared at a D_R of 60% has a ξ_0 of -0.06, indicating that the latter will exhibit a less dilative behavior. Conversely, a 100A specimen prepared at ξ_0 of -0.06 has a lower D_R of 40% compared to 25ABCD at 60%; despite the D_R differences, both specimens can be expected to be similarly dilative. These variations are attributed to the downward shift and flatter slope of critical state lines, along with the relative decrease in the difference of e_{max} and e_{min} values, with an increase in C_U , as shown in Fig. 6.3 and reported in experimental testing of similar gradations by Ahmed et al. (2023).

During cyclic shearing, the τ_{xz} for all the specimens undergoes alternating increasing and decreasing cycles to meet the τ_{target} magnitude, resulting in an overall contractile tendency

observed by a concomitant decrease in p' , accumulation of γ_{xz} , and increase in r_U (Figs. 6.7 and 6.8). With continuing cyclic loading p' eventually decreases to a value close to zero, and r_U reaches a value close to 1.0, indicating that the sample has liquified. Post-triggering, all specimens undergo alternating cycles of contraction and dilation, forming butterfly-shaped loops in $\tau_{xz} - p'$ space. Each loading cycle produces a noticeable increase in shear strains, and post-triggering shear strains accumulate progressively with each cycle. For specimens with the same D_R , a higher CSR accelerates the generation of excess pore pressure and leads to a faster decrease in p' , which decreases the N_L to triggering of liquefaction. Post-triggering, the accumulation of γ_{xz} is relatively similar for different CSR values, whereas the r_U oscillates over a broader average range for higher CSR values (0.72 to 1.0 for CSR of 0.2 versus 0.83 to 1.0 for CSR of 0.1 for 25ABCD specimen at D_R of 60%, Fig. 6.8). Looser specimens tend to undergo liquefaction with a sudden loss of strength (flow liquefaction) in a smaller number of cycles, as shown by a sudden increase in r_U (Fig. 6.7). In contrast, denser specimens tend to exhibit cyclic mobility, with higher liquefaction resistance and a gradual increase in r_U (Fig. 6.8).

Changes in gradation influence the overall cyclic shearing response, from the stress paths followed to the N_L and the accumulation of post-triggering shear strains. Additionally, the comparison of results concerning the influence of gradation depends on the chosen state (ξ_0 versus D_R). A broader gradation results in higher N_L and lower post-triggering γ_{xz} when comparing based on a similar ξ_0 value. However, when comparing based on a common D_R value, the more broadly graded specimens result in lower N_L and higher post-liquefaction γ_{xz} for specimens with D_R of 39-43% and 58-61% (Fig. 6.9). The looser specimens exhibit similar post-triggering behavior irrespective of gradation, while the denser specimens show

reduced post-triggering γ_{xz} as the gradation is broadened. This difference arises from the relative position of the initial state of the specimens with similar ξ_0 with respect to their critical state lines and the e_{max} and e_{min} values (Fig. 6.3), where a 100A specimen is closer to the critical state line and e_{max} for a similar ξ_0 . These observations indicate that comparing responses based on ξ_0 better captures fundamental differences from widening gradation. Similar efficacy of ξ_0 in capturing the effect of change in gradation on the monotonic and cyclic response has been presented in recent studies (Huang et al. 2014b; Basson et al. 2023b; Zuo et al. 2023; Ahmed et al. 2023).

6.4.2 Liquefaction triggering resistance

The CSR, density, and confining stress affect the N_L to triggering of liquefaction. Typically, these relationships are presented as liquefaction-triggering curves, representing a locus of specific combinations of CSR and N_L that result in triggering for a specimen at a given density and confining stress. The liquefaction triggering curves for 100A, 33ABC, and 25ABCD specimens with different initial D_R and ξ_0 are presented on a semi-log plot in Fig. 6.10. The obtained $CSR-N_L$ data points for the different specimens were fitted with a power function given as:

$$CSR = a N_L^{-b} \quad (6.3)$$

where coefficient a and exponent b were fitted using least squares. The fitted curves are plotted as dashed lines in Fig. 6.10, and the fitted parameters are summarized in Table 6.4.

An increase in the density of a specimen promotes tighter packing and better interlocking between the particles, leading to enhanced resistance to triggering and shifting of the triggering curves towards the top and right in $CSR - N$ space. The trends of liquefaction

triggering are presented as comparisons between the specimens prepared at similar D_R (Fig. 6.10(a)) and ξ_0 (Fig. 6.10(b)). The b values obtained for the specimens at a $D_R \sim 60\%$ are close to 0.5, higher than those reported in the literature for experimental DSS testing (e.g., Boulanger and Idriss 2014; Ulmer et al. 2022). This difference may be attributed to the challenges in accurately capturing the particle shape of natural sand particles in DEM, the lack of a standard method for determining e_{max} and e_{min} for DEM specimens, differences in boundary conditions, and possible localization during shearing in experiments. These factors may contribute to a relatively higher contact density than equivalent experimentally tested specimens at similar D_R values, as discussed by Bernhardt et al. (2016) and Banerjee et al. (2023), leading to a greater sensitivity to CSR due to improved interlocking and higher capacity to resist cyclic shear stresses. Similar increases in b values for denser specimens are presented in the past DEM studies (Xu et al. 2015; Gu et al. 2020b; Rahman et al. 2021; Zhang et al. 2023).

Gradation influences the number of cycles required to trigger liquefaction. Specimen with broader gradation requires more cycles to trigger liquefaction than poorly-graded specimens at similar ξ_0 (Fig. 6.10(a)). For example, at a CSR ~ 0.10 , the 25ABCD specimen requires 1.97 times more cycles at a ξ_0 of -0.01 and 6.03 times more cycles at a ξ_0 of -0.06 compared to the corresponding 100A specimens. However, the trends change when D_R is used as the basis of comparison. Specifically, the 25ABCD specimen with a D_R of 43% requires 0.56 times the cycles for the corresponding 100A specimen, and at a D_R of 60%, the 25ABCD specimen requires 0.59 times the cycles required for the 100A specimen at a CSR ~ 0.10 .

The influence of C_U on liquefaction triggering resistance can also be illustrated by comparing the cyclic liquefaction resistance of a specimen considering the CSR required to achieve a fixed N_L of 10 using the fitted parameters a and b (Table 6.4) and Equation 6.3. Figures 6.11(a,b) provides comparisons as functions of ξ_0 and D_R , respectively. At similar ξ_0 , the broadly graded 33ABC and 25ABCD specimens exhibit higher liquefaction resistance than the poorly graded 100A specimens. For example, at a similar ξ_0 of -0.6, 25ABCD requires 2.5 times the CSR (Fig. 6.11(a)) of a 100A specimen to trigger liquefaction. An opposite trend emerges when the results are compared in the term of D_R . At a similar D_R of 43%, 25ABCD requires 65% of the CSR (Fig. 6.11(b)) compared to the 100A specimen to trigger liquefaction. At a higher D_R of 60%, 25ABCD requires 67% of the CSR compared to a 100A specimen to trigger liquefaction. These findings align with the observations presented in past studies involving experimental and DEM DSS testing on various gradations (Doygun et al. 2019; Mutabaruka et al. 2019; Humire 2022; Banerjee et al. 2023). The findings highlight the importance of the specific parameter of state being used to capture the effects of gradation on the liquefaction triggering response, which may explain some of the inconsistencies reported in the literature, as previously described.

6.4.3 Post-liquefaction shear strain accumulation

Each post-triggering cycle produces an incremental increase in shear strains, which can be monitored by tracking the evolution of single (γ_{sa}) and double amplitude (γ_{da}) maximum shear strains (Shamoto et al. 1997; Humire et al. 2019; Tasiopoulou et al. 2020). γ_{sa} represents the maximum shear strain occurring during each half of the loading cycle, and the γ_{da} represents the cumulative shear strains experiences during both halves of the loading

cycle. More information about the γ_{sa} and γ_{da} maximum shear strains is presented in Humire and Ziotopoulou (2022).

The accumulation of shear strains after triggering is influenced by the state and gradation of the specimens, as shown in Figs. 6.12(a,b), which present γ_{sa} and γ_{da} as a function of N . Looser specimen, which suddenly loses shear strength once they liquefy, exhibit an instantaneous increase in the post-triggering liquefaction shear strains (100A specimen at $\xi_0 = -0.07$). In contrast, denser specimens show a more gradual accumulation of shear strains, with the accumulation rate decreasing as the number of cycles increases (specimen at $\xi_0 = -0.14$). The progressive reduction in the rate of shear strain accumulation is particularly pronounced for specimens with broader gradations, as shown in Figs. 6.12(c,d), which show γ_{sa} and γ_{da} as a function of cycles after triggering. Consequently, specimens with broader gradations result in smaller overall post-triggering shear deformations at similar ξ_0 and D_R . For instance, the 25ABCD specimen at $\xi_0 = -0.06$ and $D_R = 60\%$ accumulates a total of 5.3% γ_{sa} and 10.7% γ_{da} , compared to 7.3% γ_{sa} and 17.1% γ_{da} for 100A after five cycles post triggering (Fig 12(c,d)). These results are consistent with experimental test results on 100A, 33ABC, and 25ABCD gradations presented in Humire 2022. The decrease in the rate of shear strain accumulation may be attributed to the enhanced dilative tendencies exhibited by soils with broader gradations. Such soils experience greater interlocking between particles and a larger number of particles participating in contact force transmission, resulting in higher rates of dilation and lower overall shear deformations during liquefaction (e.g., Simoni and Houlsby 2006; Amirpour Harehdasht et al. 2017; Basson et al. 2023b; Ahmed et al. 2023). Further details about the

interparticle interactions and fabric evolution of the tested specimens are discussed in the next section.

6.5 Fabric evolution during cyclic shearing

This section examines the influence of gradation on the evolution of interparticle interactions and fabric to explain the differences in the liquefaction triggering resistance and post-triggering strain accumulation. In particular, the particle connectivity, percentage of sliding particle contacts, and fabric anisotropy is evaluated at different points during the simulations of 100A, 33ABC, and 25ABCD specimens at similar D_R and ξ_0 .

6.5.1 Particle connectivity

The gradation of a granular material controls the arrangement of particles in a specimen. The Mechanical Coordination Number (MCN), as described in Thornton (2000), has been widely adopted to provide insights into the evolution of particle contacts during loading. In such cases, MCN provides a scalar quantity that quantifies the number of force transmitting contacts in an assembly. In the absence of a gravitational field, the particles without any contact (floaters) or with one contact (rattlers) do not contribute to force transmission. Fig. 6.13 presents the evolution of MCN with the number of cycles, and Table 6.5 reports the MCN at triggering for specimens with different gradations and initial states. As r_u gradually increases (i.e., Figs. 6.4, 6.5, and 6.6), the MCN starts to decrease, eventually reaching the point of liquefaction triggering. Post-triggering, the MCN oscillates between its minimum and maximum value for each cycle. For comparison, at a similar ξ_0 (i.e., Fig. 13,a,c,d), the initial MCN for 100A (7.02) is smaller than for the 33ABC and 25ABCD specimens, whereas, at similar D_R values (i.e., Figs. 6.13(b,c,d)), the initial MCN for the 100A specimen (8.13) is

greater than for the 33ABC (7.59) and 25ABCD (7.62) specimen. At the point of triggering, the 25ABCD specimen shows a slightly smaller MCN at triggering (4.22) as compared to the 100A specimen (4.53) at a similar ξ_0 . Post-liquefaction, the minimum MCN during the contraction phase was observed to be 1.9 for 100A, 2.1 for 33ABC, and 2.3 for 25ABCD. These values suggest that specimens with broader gradations exhibit greater interlocking even at very low confinements. A greater interlocking likely increases resistance to particle rearrangement, resisting soil dilation, and decreasing post-liquefaction strain accumulation.

Recent studies indicate that the MCN fails to provide a complete description of the distribution of contacts for broader gradations due to the averaging across the coarse and finer particles (Liu et al. 2021a; b; Basson et al. 2023c). Instead, the Particle Connectivity (PC) parameter has been proposed as a more effective measure to capture the packing characteristics, quantifying the distribution of the total number of contacts for each particle. Further details about the computation of PC for the tested gradations are presented in Basson et al. (2023b; c). For the cyclic DSS simulations, the PC distributions were evaluated at the following four stages: (1) the start of the shearing (i.e., end of consolidation), (2) midway to triggering of liquefaction (r_U of 0.5, p' of 50 kPa), (3) contraction phase immediately after triggering, and (4) end of the first dilation phase after triggering. Fig. 6.14 shows a schematic of the stages chosen for PC analysis on data from a 25ABCD specimen subjected to a CSR of 0.10.

Specimens with broader gradations yield wider PC distributions. Fig. 6.15 presents the cumulative PC distribution for 100A, 33ABC, and 25ABCD specimens calculated as the sum of all the particle volumes for each PC value. The 25ABCD specimen consistently shows the

highest PC values for any given cumulative volume percentage throughout the shearing process. At the start of shearing (Fig. 6.15(a)), the 25ABCD specimen exhibits the highest PC value of 223, followed by 88 for the 33ABC specimen and 19 for the 100A specimen at a similar ξ_0 . As the shearing progresses, the contacts between the particles start to break down due to particle rearrangement, leading to lower PC values midway to triggering of liquefaction (Fig. 6.15(b)) across all the specimens. During the contraction phase shortly after triggering, a substantial percentage of particles experience contact loss due to the small confining stresses, resulting in a sudden increase in particles with PC smaller than one (i.e., floaters and rattlers) (Fig. 6.15(c)). This increase is more pronounced in the 100A specimen than in the 33ABC and 25ABCD specimens at a similar ξ_0 . For instance, the inactive particles increase from 7.1% to 43.6% for the 100A specimen, from 4.7% to 26.1% for the 33ABC specimen, and from 4.3% to 19.9% for the 25ABCD specimen between the start of shearing to immediately after triggering. These observations suggest that a greater proportion of particles are active in transmitting forces in specimens with broader gradation, which improves the overall stability and resistance to deformation at very low confinements. During the post-triggering dilation phase (Fig. 6.15(d)), the PC distributions are similar to those in the pre-triggering state, and this trend continues with each subsequent cycle of shearing.

The PC increases with particle size for all specimens, indicating that the coarser particles contribute more to the load-bearing process. Fig. 6.16 presents the distribution of average particle sizes for each PC value at the same four test stages. To calculate the average particle size, all the particles for a given PC were grouped into bins, and the average particle size within each bin was computed. For specimens with similar ξ_0 at the start of shearing, the

coarsest particle in the 25ABCD specimen with an average particle size of 71.7 mm is connected to 223 particles, while the coarsest particles in the 100A specimen with an average particle size of 6.2 mm are connected to 19 particles (Fig. 6.16(a)). As shearing progresses, the PC is reduced for each average particle size during the contraction phase immediately after triggering of liquefaction. During this phase, the PC for the coarsest particle decreases by 74% for 25ABCD, 75% for 33ABC, and 53% for 100A specimens (Fig. 6.16(c)). At smaller average particle sizes, the distributions have a steeper slope, indicating that the finer particles form the majority of the inactive particles in all the specimens. This indicates that the finer particles are less participative in the overall stability of the specimen, while the coarser particles promote more stable packing, similar to the observations presented in recent studies (Wiącek and Molenda 2018; Liu et al. 2021a; Basson et al. 2023b; Yilmaz et al. 2023).

6.5.2 Contact sliding

Cyclic deformations in a soil specimen produce instability by changing the direction of major principal stresses, resulting in particle rearrangement and the destruction of interparticle contacts carrying large forces. This instability reaches its peak at the point of triggering when a significant number of load-bearing particle contacts are destroyed (e.g., Wei and Wang 2017; Wei et al. 2018; Sassel et al. 2023). The creation and destruction of contacts between the particles depend on the amount and rate of particle movement during shearing, which is influenced by the interparticle friction and overall particle interlocking in the specimen (Gu et al. 2020b; Yang et al. 2022a). The contacts begin to slide when the tangential force at a contact exceeds the limiting force, defined as the product of the normal contact force and the friction coefficient by the Mohr-Coulomb frictional law. As the specimen approaches

triggering of liquefaction, most load-bearing contacts start sliding, and the specimen transitions from a solid to a liquid-like state (Yang et al. 2022b). After triggering of liquefaction, the specimen gradually regains stability as it dilates. Its resistance is mobilized as prior interparticle contacts are restored, or new contacts are formed during the alternating cycles of contraction and dilation.

Broader gradations show a lower proportion of sliding contacts pre- and post-liquefaction. Fig. 6.17 compares the percentage of sliding contacts for 100A, 33ABC, and 25ABCD specimens. The contacts are categorized into strong or weak force contacts based on the magnitude of the contact normal forces (F_n). Typically, the load-bearing contacts carry forces greater than the average force in the specimen ($F_n/\bar{F}_n > 1.0$, where \bar{F}_n is the average force, Fig. 6.17(a)) and form the strong force chain network while the contacts transmitting a force smaller than the average force ($F_n/\bar{F}_n < 1.0$, Fig. 6.17(b)) form the weak force chain network (Radjai et al. 1997). At the point of triggering, 100A specimens have a larger percentage of sliding strong and weak force contacts, followed by 33ABC and 25ABCD specimens (black dots in Fig. 6.17). At similar ξ_0 , the 100A specimen has 20.2% and 44.1% of sliding contacts for the strong and force contact networks, respectively, while the corresponding values for the 25ABCD specimen are 14.1% and 29.4% (Table 6.5). This difference is also evident, but less clear, when comparing the percent of sliding contacts based on the same D_R . Past studies suggest that the coarser particles in specimens with broader gradations carry the majority of the strong forces (Santamarina 2003; Liu et al. 2021a; Basson et al. 2023b), implying that a smaller number of sliding contacts between these coarser particles is involved in the liquefaction of specimens. Interestingly, during the dilation phase post-liquefaction, the greatest values of the sliding contacts increase more

rapidly for the 100A specimens than for the 25ABCD specimen. In the case of strong forces, the percent of sliding particles increases by 0.45% per cycle for the 25ABCD specimen (dashed line in Fig. 6.17(a)) and 0.92% per cycle for the 100A specimen (solid line in Fig. 6.17(a)). Similarly, for weak forces, the percent of sliding particles increased by 0.73% per cycle for 25ABCD specimen (dashed line in Fig. 6.17(b)) and 1.83% per cycle for 100A specimen (dashed line in Fig. 6.17(b)). The smaller rate of increase of percent of sliding contacts suggests a greater interlocking between particles (Figs. 13,15,16) limits the particle movement in more broadly graded specimens and could explain the lower post-liquefaction strain accumulation.

6.5.3 Contact force fabric anisotropy

Analysis of the angular distributions of normal forces provides an insight into the anisotropy and orientation of load bearing (i.e., strong forces) and supporting (i.e., weak forces) contact networks in a specimen. In this study, the contact normal force anisotropy is evaluated using the vector analysis approach presented in past studies (Rothenburg and Bathurst 1989). The magnitude and orientation of the contact normal forces across the specimens are characterized using an analytical function of the form:

$$F(\theta) = \bar{F}_n (1 + a_F \cos 2 (\theta - \theta_F)) \quad (4)$$

where a_F is the parameter that defines the anisotropy of the distribution and θ_F is the preferred orientation with respect to the horizontal direction (x-axis). Fig. 6.18 and Fig. 6.19 present the fitted angular distributions for the strong force and weak force networks, respectively, along the XZ planes, for the four stages during the cyclic tests (i.e., Fig. 14) for 100A, 33ABC, and 25ABCD specimens. Table 6.6 summarizes the fitted parameters $(a_F)_{strong}$

and $(\theta_F)_{strong}$ for the strong and $(a_F)_{weak}$ and $(\theta_F)_{weak}$ for the weak forces, obtained by least squares fitting on the data points obtained for the tested specimens, as shown in Fig. 6.18 and Fig. 6.19.

Broader gradations produce more anisotropic normalized F_n distributions. At the start of shearing, all the specimens show negligible anisotropy due to the initial isotropic compression, indicated by near-circular distributions (Figs. 6.17(a) and 6.18(a)) and a_F values smaller than 0.07 (Table 6.6). However, with an increase in shear strains midway to triggering of liquefaction, slight anisotropy emerges in the strong force network (Fig. 6.17(b)), as indicated by the elliptical distributions and a slight increase in a_F (0.06 for 100A and 0.12 for 33ABC and 25ABCD) and θ_F (21° for 100A to 59° for 33ABC) values. In contrast, the weak force networks maintain near isotropic distributions (Fig. 6.18(b)). During the contraction phase, the strong forces show significantly more anisotropic distributions and are oriented toward the major principal stress. Finally, during the dilation phase, the anisotropy in the strong forces reaches its maximum, and the distribution is also aligned in the direction of the major principal stress. Among the specimens at a similar ξ_0 , the 25ABCD specimen exhibits the highest anisotropy. Specifically, during the dilation phase, its distribution has an a_F value of 0.52, followed by the 33ABC specimen with an a_F of 0.48 and the 100A specimen with an a_F of 0.32. In contrast, the angular distributions for the weak forces show very small anisotropies, indicated by the near-circular distributions and a_F values smaller than 0.07, confirming that weak forces take limited participation in load bearing but provide buckling resistance to the strong force network. Overall, the findings suggest that the inclusion of coarser particles in broadly graded specimens increases the contact force anisotropy during cyclic loading, while finer particles have a comparatively

smaller impact on the overall stability, liquefaction triggering, and strain accumulation in the specimen.

6.6 Conclusions

This study examined the effect of gradation on the liquefaction triggering and post-triggering behavior of coarse-grained soils. The macroscale and microscale behavior were analyzed using cyclic constant volume direct simple shear DEM simulations of specimens comprised of particle shapes similar to natural sands and with C_U between 1.9 and 6.4. The simulations provide insights regarding various aspects of cyclic soil behavior, including liquefaction triggering resistance, post-triggering strain accumulation, sliding at particle contacts, particle packing, and anisotropy in strong and weak force networks.

The macro-scale results reveal interesting patterns in the behavior of specimens with broader gradations (i.e., 25ABCD specimen with $C_U = 6.37$) compared to poorly graded soil specimens (i.e., 100A specimen with $C_U = 1.98$) at similar relative density or state parameter values. Additionally, the results emphasize the significance of selecting the appropriate state parameter to capture the effects of gradation. The more broadly graded specimen exhibits higher liquefaction triggering resistance than the poorly graded specimen at similar state parameters. A contradictory trend emerges, with broadly graded specimen showing lower resistance at similar relative densities. Additionally, when plotted in terms of D_R the effects of gradation are obscured. Post-triggering, the well-graded specimens accumulate shear strains at a smaller rate than the poorly graded specimens at either similar state parameter or relative density.

The micro-scale results reveal that variation in macro-scale results is attributed to the tighter particle packing and increased interlocking of coarser particles for broadly graded specimens. The specimens with broader gradations show higher particle connectivity at all stages during cyclic shearing. At the start of shearing, the coarsest particles for broadly graded specimens have 11x more contact with neighboring particles than the poorly graded specimen. Similarly, at the point of triggering of liquefaction, the coarsest particles for the broadly graded specimen are connected to 6x more particles than the poorly graded specimen. Moreover, the percentage of inactive particles by volume at initial liquefaction is 2.3x lower for the specimen with broader gradation compared to the poorly graded specimen. The improved interlocking in more broadly graded specimens results in a lower percentage of sliding contacts for both strong and weak force-carrying contacts at the triggering of liquefaction and in subsequent cycles, which is linked to the slower rate of post-triggering strain accumulation in well-graded specimens. The analysis of the anisotropy of the contact force networks indicates that the strong forces align with the major principal direction, and the anisotropy in the strong forces increases as the gradation becomes broader. The weak forces are relatively isotropic and resist the buckling of strong force networks.

Overall, the findings presented in this paper provide insights into the influence of gradation on the pre- and post-triggering behavior of coarse-grained soils. Specifically, the range of particle sizes and the disproportionately higher contribution of coarser particles to the load bearing limits the overall deformation during cyclic loading, similar to those previously reported for monotonic loading. These effects are readily captured when ξ_0 is used as the state parameter for comparison between different soils.

6.7 Acknowledgements

Financial support for this project comes from the National Science Foundation (NSF) under Grant CMMI-1916152. Any opinions, findings, conclusions, or recommendations expressed in this paper are those of the authors and do not necessarily reflect the views of NSF. The authors would also like to acknowledge the contribution and discussions of Katerina Ziotopoulou, Rachel Reardon, Francisco Humire, Sharif Ahmed, Trevor Carey, Nathan Love, Anna Chiaradonna.

6.8 References

- Ahmed, S. S., A. Martinez, and J. T. DeJong. 2023. "Effect of Gradation on the Strength and Stress-Dilation Behavior of Coarse-Grained Soils in Drained and Undrained Triaxial Compression." *J. Geotech. Geoenviron. Eng.*, 149 (5): 04023019. <https://doi.org/10.1061/JGGEFK.GTENG-10972>.
- Amirpour Harehdasht, S., M. Karray, M. N. Hussien, and M. Chekired. 2017. "Influence of Particle Size and Gradation on the Stress-Dilatancy Behavior of Granular Materials during Drained Triaxial Compression." *Int. J. Geomech.*, 17 (9): 04017077. [https://doi.org/10.1061/\(ASCE\)GM.1943-5622.0000951](https://doi.org/10.1061/(ASCE)GM.1943-5622.0000951).
- Ashmawy, A. K., B. Sukumaran, and V. V. Hoang. 2003. "Evaluating the Influence of Particle Shape on Liquefaction Behavior Using Discrete Element Modeling." *Proceedings of The Thirteenth*, 8.
- Athanassiadis, A. G., M. Z. Miskin, P. Kaplan, N. Rodenberg, S. H. Lee, J. Merritt, E. Brown, J. Amend, H. Lipson, and H. M. Jaeger. 2014. "Particle shape effects on the stress

- response of granular packings.” *Soft Matter*, 10 (1): 48–59.
<https://doi.org/10.1039/C3SM52047A>.
- Banerjee, S. K., M. Yang, and M. Taiebat. 2023. “Effect of coefficient of uniformity on cyclic liquefaction resistance of granular materials.” *Computers and Geotechnics*, 155: 105232. <https://doi.org/10.1016/j.compgeo.2022.105232>.
- Basson, M. S., and A. Martinez. 2023a. “Numerical and experimental estimation of anisotropy in granular soils using multi-orientation shear wave velocity measurements.” *Granular Matter*.
- Basson, M. S., and A. Martinez. 2023b. “A Multi-orientation System for Determining Angular Distributions of Shear Wave Velocity in Soil Specimens.” *Geotech. Test. J.*, 46 (2): 20210277. <https://doi.org/10.1520/GTJ20210277>.
- Basson, M. S., A. Martinez, and J. T. DeJong. 2023a. “Effect of Particle Size Distribution on Monotonic Shear Strength And Stress-Dilatancy of Coarse-Grained Soils.” *GeoCongress 2023*, 10. Los Angeles.
- Basson, M. S., A. Martinez, and J. T. DeJong. 2023b. “DEM investigation of the effect of gradation on the strength, dilatancy, and fabric evolution of coarse-grained soils.” *Submitted for possible publication in Journal for Geotechnical and Geoenvironmental Engineering*.
- Basson, M. S., A. Martinez, and J. T. DeJong. 2023c. “Effect of particle size distribution and contact parameters on the particle connectivity and contact force transmission of granular assemblies.” *Submitted for possible publication in Granular Matter*.
- Been, K., and M. G. Jefferies. 1985. “A state parameter for sands.” *Géotechnique*, 35 (2): 99–112. <https://doi.org/10.1680/geot.1985.35.2.99>.

- Bonilla, R. R. O. 2004. "Numerical Simulations of Undrained Granular Media." University of Waterloo.
- Boulanger, R. W., and I. M. Idriss. 2014. "CPT-Based Liquefaction Triggering Procedure." *J. Geotech. Geoenviron. Eng.*, 142 (2): 04015065. [https://doi.org/10.1061/\(ASCE\)GT.1943-5606.0001388](https://doi.org/10.1061/(ASCE)GT.1943-5606.0001388).
- Bray, J., M. Cubrinovski, J. Zupan, and M. Taylor. 2014. "Liquefaction Effects on Buildings in the Central Business District of Christchurch." *Earthquake Spectra*, 30 (1): 85–109. <https://doi.org/10.1193/022113EQS043M>.
- Carey, T. J., A. Chiaradonna, N. C. Love, D. W. Wilson, K. Ziotopoulou, A. Martinez, and J. T. DeJong. 2022. "Effect of soil gradation on embankment response during liquefaction: A centrifuge testing program." *Soil Dynamics and Earthquake Engineering*, 157: 107221. <https://doi.org/10.1016/j.soildyn.2022.107221>.
- Chang, W.-J., C.-W. Chang, and J.-K. Zeng. 2014. "Liquefaction characteristics of gap-graded gravelly soils in K0 condition." *Soil Dynamics and Earthquake Engineering*, 56: 74–85. <https://doi.org/10.1016/j.soildyn.2013.10.005>.
- Chiaradonna, A., K. Ziotopoulou, T. J. Carey, J. T. DeJong, and R. W. Boulanger. 2022. "Dynamic Behavior of Uniform Clean Sands: Evaluation of Predictive Capabilities in the Element- and the System-Level Scale." *Geo-Congress 2022*, 444–454. Charlotte, North Carolina: American Society of Civil Engineers.
- Ciantia, M. O., M. Arroyo, F. Calvetti, and A. Gens. 2015. "An approach to enhance efficiency of DEM modelling of soils with crushable grains." *Géotechnique*, 65 (2): 91–110. <https://doi.org/10.1680/geot.13.P.218>.

- Coetzee, C. J. 2019. "Particle upscaling: Calibration and validation of the discrete element method." *Powder Technology*, 344: 487–503.
<https://doi.org/10.1016/j.powtec.2018.12.022>.
- Cubrinovski, M., J. D. Bray, C. De La Torre, M. J. Olsen, B. A. Bradley, G. Chiaro, E. Stocks, and L. Wotherspoon. 2017. "Liquefaction effects and associated damages observed at the Wellington CentrePort from the 2016 Kaikoura earthquake." *BNZSEE*, 50 (2): 152–173. <https://doi.org/10.5459/bnzsee.50.2.152-173>.
- DeJong, J. T., A. P. Sturm, and M. Ghafghazi. 2016. "Characterization of gravelly alluvium." *Soil Dynamics and Earthquake Engineering*, 91: 104–115.
<https://doi.org/10.1016/j.soildyn.2016.09.032>.
- Doygun, O., H. G. Brandes, and T. T. Roy. 2019. "Effect of Gradation and Non-plastic Fines on Monotonic and Cyclic Simple Shear Strength of Silica Sand." *Geotech Geol Eng*, 37 (4): 3221–3240. <https://doi.org/10.1007/s10706-019-00838-9>.
- Evans, M. D., H. Bolton Seed, and R. B. Seed. 1992. "Membrane Compliance and Liquefaction of Sluiced Gravel Specimens." *J. Geotech. Engrg.*, 118 (6): 856–872.
[https://doi.org/10.1061/\(ASCE\)0733-9410\(1992\)118:6\(856\)](https://doi.org/10.1061/(ASCE)0733-9410(1992)118:6(856)).
- Evans, M. D., and S. Zhou. 1995. "Liquefaction Behavior of Sand-Gravel Composites." *J. Geotech. Engrg.*, 121 (3): 287–298. [https://doi.org/10.1061/\(ASCE\)0733-9410\(1995\)121:3\(287\)](https://doi.org/10.1061/(ASCE)0733-9410(1995)121:3(287)).
- Ferrellec, J.-F., and G. R. McDowell. 2008. "A simple method to create complex particle shapes for DEM." *Geomechanics and Geoengineering*, 3 (3): 211–216.
<https://doi.org/10.1080/17486020802253992>.

- Garcia, X., J.-P. Latham, J. Xiang, and J. P. Harrison. 2009. "A clustered overlapping sphere algorithm to represent real particles in discrete element modelling." *Géotechnique*, 59 (9): 779–784. <https://doi.org/10.1680/geot.8.T.037>.
- Gu, X., X. Liang, Y. Shan, X. Huang, and A. Tessari. 2020a. "Discrete element modeling of shear wave propagation using bender elements in confined granular materials of different grain sizes." *Computers and Geotechnics*, 125: 103672. <https://doi.org/10.1016/j.compgeo.2020.103672>.
- Gu, X., J. Zhang, and X. Huang. 2020b. "DEM analysis of monotonic and cyclic behaviors of sand based on critical state soil mechanics framework." *Computers and Geotechnics*, 128: 103787. <https://doi.org/10.1016/j.compgeo.2020.103787>.
- Hamidi, A., E. Azini, and B. Masoudi. 2012. "Impact of gradation on the shear strength-dilation behavior of well graded sand-gravel mixtures." *Scientia Iranica*, 19 (3): 393–402. <https://doi.org/10.1016/j.scient.2012.04.002>.
- Hanley, K. J., X. Huang, C. O'Sullivan, and F. Kwok. 2013. "Challenges of simulating undrained tests using the constant volume method in DEM." 277–280. Sydney, Australia.
- Huang, X., K. J. Hanley, C. O'Sullivan, and F. C. Y. Kwok. 2014a. "Effect of sample size on the response of DEM samples with a realistic grading." *Particuology*, 15: 107–115. <https://doi.org/10.1016/j.partic.2013.07.006>.
- Huang, X., K. J. Hanley, Z. Zhang, and C. Kwok. 2019. "Structural degradation of sands during cyclic liquefaction: Insight from DEM simulations." *Computers and Geotechnics*, 114: 103139. <https://doi.org/10.1016/j.compgeo.2019.103139>.

- Huang, X., C. O'Sullivan, K. J. Hanley, and C. Y. Kwok. 2014b. "Discrete-element method analysis of the state parameter." *Géotechnique*, 64 (12): 954–965. <https://doi.org/10.1680/geot.14.P.013>.
- Hubler, J. F., A. Athanasopoulos-Zekkos, and D. Zekkos. 2018. "Monotonic and cyclic simple shear response of gravel-sand mixtures." *Soil Dynamics and Earthquake Engineering*, 115: 291–304. <https://doi.org/10.1016/j.soildyn.2018.07.016>.
- Humire, F. 2022. "Liquefaction and Post-Liquefaction Behavior of Coarse-Grained Soils." PhD Thesis. University of California, Davis,.
- Humire, F., R. Reardon, K. Ziotopoulou, and J. T. DeJong. forthcoming. "Effect of gradation and grain size on the liquefaction and post-liquefaction behavior of coarse-grained soils."
- Humire, F., and K. Ziotopoulou. 2022. "Mechanisms of shear strain accumulation in laboratory experiments on sands exhibiting cyclic mobility behavior." *Can. Geotech. J.*, 59 (8): 1401–1413. <https://doi.org/10.1139/cgj-2021-0373>.
- Humire, F., K. Ziotopoulou, M. S. Basson, and A. Martinez. 2019. "Framework for tracking the accumulation of shear strains during cyclic mobility." *Earthquake geotechnical engineering for protection and development of environment and constructions: proceedings of the 7th International Conference on Earthquake Geotechnical Engineering (ICEGE 2019), June 17-20 2019, Rome Italy*, 8.
- Idriss, I. M., and R. W. Boulanger. 2008. *Soil liquefaction during earthquakes*. Oakland, CA: Earthquake Engineering Research Institute (EERI).
- Ishihara, K., F. Tatsuoka, and S. Yasuda. 1975. "Undrained Deformation and Liquefaction of Sand Under Cyclic Stresses." *Soils and Foundations*, 15 (1): 29–44. <https://doi.org/10.3208/sandf1972.15.29>.

- Keishing, J., and K. J. Hanley. 2020. "Improving constant-volume simulations of undrained behaviour in DEM." *Acta Geotech.*, 15 (9): 2545–2558. <https://doi.org/10.1007/s11440-020-00949-1>.
- Kokusho, T., T. Hara, and R. Hiraoka. 2004. "Undrained Shear Strength of Granular Soils with Different Particle Gradations." *J. Geotech. Geoenviron. Eng.*, 130 (6): 621–629. [https://doi.org/10.1061/\(ASCE\)1090-0241\(2004\)130:6\(621\)](https://doi.org/10.1061/(ASCE)1090-0241(2004)130:6(621)).
- Kokusho, T., Y. Tanaka, T. Kawai, K. Kudo, K. Suzuki, S. Tohda, and S. Abe. 1995. "Case Study of Rock Debris Avalanche Gravel Liquefied During 1993 Hokkaido-Nansei-Oki Earthquake." *Soils and Foundations*, 35 (3): 83–95. <https://doi.org/10.3208/sandf.35.83>.
- Kuei, K. C., J. T. DeJong, and A. Martinez. 2020. "Particle Size Effects on the Strength and Fabric of Granular Media." *Geo-Congress 2020*, 349–358. Minneapolis, Minnesota: American Society of Civil Engineers.
- Kuhn, M. R., H. E. Renken, A. D. Mixsell, and S. L. Kramer. 2014. "Investigation of Cyclic Liquefaction with Discrete Element Simulations." *J. Geotech. Geoenviron. Eng.*, 140 (12): 04014075. [https://doi.org/10.1061/\(ASCE\)GT.1943-5606.0001181](https://doi.org/10.1061/(ASCE)GT.1943-5606.0001181).
- Liu, D., C. O'Sullivan, and J. A. H. Carraro. 2021a. "Influence of Particle Size Distribution on the Proportion of Stress-Transmitting Particles and Implications for Measures of Soil State." *J. Geotech. Geoenviron. Eng.*, 147 (3): 04020182. [https://doi.org/10.1061/\(ASCE\)GT.1943-5606.0002466](https://doi.org/10.1061/(ASCE)GT.1943-5606.0002466).
- Liu, D., C. O'Sullivan, and J. A. H. Carraro. 2021b. "The influence of particle size distribution on the stress distribution in granular materials." *Géotechnique*, 1–15. <https://doi.org/10.1680/jgeot.21.00127>.

- Muir Wood, D., and K. Maeda. 2008. "Changing grading of soil: effect on critical states." *Acta Geotech.*, 3 (1): 3–14. <https://doi.org/10.1007/s11440-007-0041-0>.
- Mutabaruka, P., M. Taiebat, R. J.-M. Pellenq, and F. Radjai. 2019. "Effects of size polydispersity on random close-packed configurations of spherical particles." *Phys. Rev. E*, 100 (4): 042906. <https://doi.org/10.1103/PhysRevE.100.042906>.
- O'Sullivan, C. 2011. *Particulate Discrete Element Modelling*.
- Pires-Sturm, A. P., and J. T. DeJong. 2022. "Influence of Particle Size and Gradation on Liquefaction Potential and Dynamic Response." *J. Geotech. Geoenviron. Eng.*, 148 (6): 04022045. [https://doi.org/10.1061/\(ASCE\)GT.1943-5606.0002799](https://doi.org/10.1061/(ASCE)GT.1943-5606.0002799).
- Radjai, F., D. E. Wolf, S. Roux, M. Jean, and J. J. Moreau. 1997. "Force networks in dense granular media." *Powders & grains*, 97: 211–214.
- Rahman, M. M., H. B. K. Nguyen, A. B. Fourie, and M. R. Kuhn. 2021. "Critical State Soil Mechanics for Cyclic Liquefaction and Postliquefaction Behavior: DEM study." *J. Geotech. Geoenviron. Eng.*, 147 (2): 04020166. [https://doi.org/10.1061/\(ASCE\)GT.1943-5606.0002453](https://doi.org/10.1061/(ASCE)GT.1943-5606.0002453).
- Reardon, R. A. 2021. "Monotonic and Cyclic Direct Simple Shear Testing of Coarse-Grained Soils." Master's Thesis. UC Davis.
- Reardon, R., F. Humire, S. S. Ahmed, K. Ziotopoulou, A. Martinez, and J. T. DeJong. 2022. "Effect of Gradation on the Strength and Stress-Dilatancy of Coarse-Grained Soils: A Comparison of Monotonic Direct Simple Shear and Triaxial Tests." *Geo-Congress 2022*, 226–236. Charlotte, North Carolina: American Society of Civil Engineers.

- Rollins, K. M., and H. B. Seed. 1990. "Influence of Buildings on Potential Liquefaction Damage." *J. Geotech. Engrg.*, 116 (2): 165–185. [https://doi.org/10.1061/\(ASCE\)0733-9410\(1990\)116:2\(165\)](https://doi.org/10.1061/(ASCE)0733-9410(1990)116:2(165)).
- Rothenburg, L., and R. J. Bathurst. 1989. "Analytical study of induced anisotropy in idealized granular materials." *Géotechnique*, 39 (4): 601–614. <https://doi.org/10.1680/geot.1989.39.4.601>.
- Santamarina, J. C. 2003. "Soil Behavior at the Microscale: Particle Forces." *Soil Behavior and Soft Ground Construction*, 25–56. Cambridge, Massachusetts, United States: American Society of Civil Engineers.
- Santamarina, J. C., and G. C. Cho. 2004. "Soil behaviour: the role of particle shape." *Advances in geotechnical engineering: The skempton conference*, 604–617. Thomas Telford, London.
- Sassel, T. S., F. Patino-Ramirez, K. J. Hanley, and C. O'Sullivan. 2023. "Linking the macro-scale response of granular materials during drained cyclic loading to the evolution of micro-structure, contact network and energy components." *Granular Matter*, 25 (2): 23. <https://doi.org/10.1007/s10035-023-01308-z>.
- Sawyer, B. D. 2020. "Cone Penetration Testing of Coarse-Grained Soils in the Centrifuge to Examine the Effects of Soil Gradation and Centrifuge Scaling." Master's Thesis. University of California Davis.
- Scholtès, L., B. Chareyre, F. Nicot, and F. Darve. 2009. "Micromechanics of granular materials with capillary effects." *International Journal of Engineering Science*, 12.

- Seed, H. B., P. P. Martin, and J. Lysmer. 1976. "Pore-Water Pressure Changes during Soil Liquefaction." *J. Geotech. Engrg. Div.*, 102 (4): 323–346. <https://doi.org/10.1061/AJGEB6.0000258>.
- Shamoto, Y., J.-M. Zhang, and S. Goto. 1997. "Mechanism of Large Post-Liquefaction Deformation in Saturated Sand." *Soils and Foundations*, 37 (2): 71–80. https://doi.org/10.3208/sandf.37.2_71.
- Simoni, A., and G. T. Houlsby. 2006. "The Direct Shear Strength and Dilatancy of Sand–gravel Mixtures." *Geotechnical and Geological Engineering*, 24 (3): 523–549. <https://doi.org/10.1007/s10706-004-5832-6>.
- Šmilauer, V., E. Catalano, B. Chareyre, S. Dorofeenko, J. Duriez, A. Gladky, J. Kozicki, C. Modenese, L. Scholtès, and L. Sibille. 2010. "Yade reference documentation." *Yade Documentation*, 474: 1–531.
- Sturm, A. 2019. "On the Liquefaction Potential of Gravelly Soils: Characterization, Triggering and Performance." PhD Thesis. University of California Davis.
- Suhr, B., and K. Six. 2020. "Simple particle shapes for DEM simulations of railway ballast: influence of shape descriptors on packing behaviour." *Granular Matter*, 22 (2): 43. <https://doi.org/10.1007/s10035-020-1009-0>.
- Tasiopoulou, P., K. Ziotopoulou, F. Humire, A. Giannakou, J. Chacko, and T. Travasarou. 2020. "Development and Implementation of Semiempirical Framework for Modeling Postliquefaction Shear Deformation Accumulation in Sands." *J. Geotech. Geoenviron. Eng.*, 146 (1): 04019120. [https://doi.org/10.1061/\(ASCE\)GT.1943-5606.0002179](https://doi.org/10.1061/(ASCE)GT.1943-5606.0002179).
- Thornton, C. 2000. "Numerical simulations of deviatoric shear deformation of granular media." *Géotechnique*, 50 (1): 43–53. <https://doi.org/10.1680/geot.2000.50.1.43>.

- Towhata, I., S. Maruyama, K. Kasuda, J. Koseki, K. Wakamatsu, H. Kiku, T. Kiyota, S. Yasuda, Y. Taguchi, S. Aoyama, and T. Hayashida. 2014. "Liquefaction in the Kanto region during the 2011 off the pacific coast of Tohoku earthquake." *Soils and Foundations*, 54 (4): 859–873. <https://doi.org/10.1016/j.sandf.2014.06.016>.
- Ulmer, K. J., R. A. Green, and A. Rodriguez-Marek. 2022. "Recommended b-Value for Computing Number of Equivalent Stress Cycles and Magnitude Scaling Factors for Simplified Liquefaction Triggering Evaluation Procedures." *J. Geotech. Geoenviron. Eng.*, 148 (12): 04022113. [https://doi.org/10.1061/\(ASCE\)GT.1943-5606.0002926](https://doi.org/10.1061/(ASCE)GT.1943-5606.0002926).
- Vaid, Y. P., J. M. Fisher, R. H. Kuerbis, and D. Negussey. 1990. "Particle Gradation and Liquefaction." *J. Geotech. Engrg.*, 116 (4): 698–703. [https://doi.org/10.1061/\(ASCE\)0733-9410\(1990\)116:4\(698\)](https://doi.org/10.1061/(ASCE)0733-9410(1990)116:4(698)).
- Wei, J., D. Huang, and G. Wang. 2018. "Microscale Descriptors for Particle-Void Distribution and Jamming Transition in Pre- and Post-Liquefaction of Granular Soils." *J. Eng. Mech.*, 144 (8): 04018067. [https://doi.org/10.1061/\(ASCE\)EM.1943-7889.0001482](https://doi.org/10.1061/(ASCE)EM.1943-7889.0001482).
- Wei, J., and G. Wang. 2017. "Discrete-element method analysis of initial fabric effects on pre- and post-liquefaction behavior of sands." *Géotechnique Letters*, 7 (2): 161–166. <https://doi.org/10.1680/jgele.16.00147>.
- Wiącek, J., and M. Molenda. 2018. "Numerical analysis of compression mechanics of highly polydisperse granular mixtures with different PSD-s." *Granular Matter*, 20 (1). <https://doi.org/10.1007/s10035-018-0788-z>.
- Wichtmann, T., K. Steller, T. Triantafyllidis, M. Back, and D. Dahmen. 2019. "An experimental parametric study on the liquefaction resistance of sands in spreader dumps of lignite

- opencast mines.” *Soil Dynamics and Earthquake Engineering*, 122: 290–309.
<https://doi.org/10.1016/j.soildyn.2018.11.010>.
- Xu, X. M., D. S. Ling, Y. P. Cheng, and Y. M. Chen. 2015. “Correlation between liquefaction resistance and shear wave velocity of granular soils: a micromechanical perspective.” *Géotechnique*, 65 (5): 337–348. <https://doi.org/10.1680/geot.SIP.15.P.022>.
- Yang, M., M. Taiebat, P. Mutabaruka, and F. Radjaï. 2022a. “Evolution of granular media under constant-volume multidirectional cyclic shearing.” *Acta Geotech.*, 17 (3): 779–802.
<https://doi.org/10.1007/s11440-021-01239-0>.
- Yang, M., M. Taiebat, and F. Radjaï. 2022b. “Liquefaction of granular materials in constant-volume cyclic shearing: Transition between solid-like and fluid-like states.” *Computers and Geotechnics*, 148: 104800.
<https://doi.org/10.1016/j.compgeo.2022.104800>.
- Yilmaz, Y., Y. Deng, C. S. Chang, and A. Gokce. 2023. “Strength–dilatancy and critical state behaviours of binary mixtures of graded sands influenced by particle size ratio and fines content.” *Géotechnique*, 73 (3): 202–217.
<https://doi.org/10.1680/jgeot.20.P.320>.
- Yilmaz, Y., M. Mollamahmutoglu, V. Ozaydin, and K. Kayabali. 2008. “Experimental investigation of the effect of grading characteristics on the liquefaction resistance of various graded sands.” *Engineering Geology*, 100 (3–4): 91–100.
<https://doi.org/10.1016/j.enggeo.2007.12.002>.
- Zhang, A., M. Jiang, and D. Wang. 2023. “Effect of fabric anisotropy on the cyclic liquefaction of sands: Insight from DEM simulations.” *Computers and Geotechnics*, 155: 105188.
<https://doi.org/10.1016/j.compgeo.2022.105188>.

- Zhang, W., and L. Rothenburg. 2020. "Comparison of undrained behaviors of granular media using fluid-coupled discrete element method and constant volume method." *Journal of Rock Mechanics and Geotechnical Engineering*, 12 (6): 1272–1289. <https://doi.org/10.1016/j.jrmge.2020.03.009>.
- Zheng, J., and R. D. Hryciw. 2017. "An image based clump library for DEM simulations." *Granular Matter*, 19 (2). <https://doi.org/10.1007/s10035-017-0713-x>.
- Zhou, Y.-G., P. Xia, D.-S. Ling, and Y.-M. Chen. 2020. "Liquefaction case studies of gravelly soils during the 2008 Wenchuan earthquake." *Engineering Geology*, 274: 105691. <https://doi.org/10.1016/j.enggeo.2020.105691>.
- Zuo, K., X. Gu, J. Zhang, and R. Wang. 2023. "Exploring packing density, critical state, and liquefaction resistance of sand-fines mixture using DEM." *Computers and Geotechnics*, 156: 105278. <https://doi.org/10.1016/j.compgeo.2023.105278>.

6.9 Tables and figures

Table 6.1: Gradation and packing characteristics of the simulated materials

<i>Soil</i>	D_{10} (mm)	D_{30} (mm)	D_{50} (mm)	D_{60} (mm)	C_u	C_c	e_{min}	e_{max}	$e_{max} - e_{min}$
100A	1.67	2.14	2.83	3.31	1.98	0.83	0.62	1.01	0.39
33ABC	2.50	4.82	8.76	11.20	4.48	0.83	0.45	0.74	0.29
25ABCD	2.84	6.54	12.72	18.10	6.37	0.83	0.41	0.68	0.27

Table 6.2: Parameters of specimens tested in constant volume cyclic DSS. Each specimen was tested at three CSRs at p' of 100 kPa

<i>Soil</i>	<i>Mean effective confining stress, p'_o (kPa)</i>	<i>Initial void ratio, e_o</i>	<i>Initial state parameter, ξ_o</i>	<i>Relative Density, D_R (%)</i>
<i>100A</i>	100	0.898	-0.01	28
	100	0.843	-0.07	42
	100	0.772	-0.14	61
<i>33ABC</i>	100	0.632	-0.02	39
	100	0.601	-0.06	50
	100	0.574	-0.08	58
<i>25ABCD</i>	100	0.562	-0.02	43
	100	0.521	-0.06	60

Table 6.3: DEM simulations parameters

<i>Parameter</i>	<i>Symbol</i>	<i>Value</i>
Normalized normal stiffness	k/d	2.5e8 Pa
Shear to normal stiffness ratio	k_s/k_n	0.2
Particle density	ρ	2650 kg/m ³
Friction coefficient during sample preparation	μ_{prep}	0.01 to 0.5
Friction coefficient during shearing	μ_{shear}	0.45
Global damping during preparation	ζ_{prep}	0.05 to 0.5
Global damping during shearing	ζ_{shear}	0.05

Table 6.4: *a* and *b* parameters from the liquefaction triggering curves at p' of 100 kPa

<i>Soil</i>	<i>Initial state parameter, ξ_0</i>	<i>Relative Density, D_R (%)</i>	<i>a</i>	<i>b</i>
100A	-0.01	28	0.09	0.27
	-0.07	42	0.17	0.38
	-0.14	61	0.79	0.51
33ABC	-0.02	39	0.18	0.53
	-0.06	50	0.47	0.57
	-0.08	58	0.63	0.52
25ABCD	-0.02	43	0.15	0.50
	-0.06	60	0.59	0.53

Table 6.5: Parameters at the triggering of liquefaction for 100A, 33ABC, and 25ABCD specimens at p' of 100 kPa

<i>Soil</i>	<i>Initial state parameter, ξ_0</i>	<i>Relative Density, D_R (%)</i>	<i>% sliding strong force</i>	<i>% sliding weak force</i>	<i>MCN</i>	<i>% inactive particles by volume</i>
<i>100A</i>	-0.01	28	20.2	44.1	4.56	44.3
	-0.07	42	18.2	41.2	4.53	43.1
<i>33ABC</i>	-0.06	50	16.8	39.5	4.25	26.5
	-0.08	58	15.3	36.8	4.47	26.1
<i>25ABCD</i>	-0.06	60	14.1	29.4	4.02	19.7

Table 6.6: Anisotropy of contact normal force angular distributions

<i>State</i>	<i>Specimen</i>	<i>Initial state parameter, ξ_0</i>	$(a_F)_{strong}$	$(\theta_F)_{strong}$	$(a_F)_{weak}$	$(\theta_F)_{weak}$
<i>Initial</i>	<i>100A</i>	-0.01	0.03	3.8	0.01	118.2
		-0.07	0.03	4.2	0.02	0.3
	<i>33ABC</i>	-0.06	0.03	1.4	0.01	119.2
		-0.08	0.04	2.7	0.00	33.1
	<i>25ABCD</i>	-0.06	0.02	1.5	0.01	10.1
<i>Mid way to liquefaction</i>	<i>100A</i>	-0.01	0.06	21.0	0.06	37.2
		-0.07	0.04	40.7	0.05	31.4
	<i>33ABC</i>	-0.06	0.13	59.4	0.05	56.5
		-0.08	0.12	32.6	0.04	51.2
	<i>25ABCD</i>	-0.06	0.12	35.7	0.01	25.5
<i>Contraction after liquefaction</i>	<i>100A</i>	-0.01	0.22	137.7	0.03	62.6
		-0.07	0.21	134.4	0.02	33.3
	<i>33ABC</i>	-0.06	0.35	126.2	0.04	21.2
		-0.08	0.38	135.1	0.03	34.3
	<i>25ABCD</i>	-0.06	0.41	133.5	0.07	88.6
<i>Dilation after liquefaction</i>	<i>100A</i>	-0.01	0.31	47.4	0.07	54.4
		-0.07	0.32	41.3	0.07	47.2
	<i>33ABC</i>	-0.06	0.43	42.2	0.02	42.1
		-0.08	0.48	43.4	0.04	56.0
	<i>25ABCD</i>	-0.06	0.52	46.2	0.05	55.3

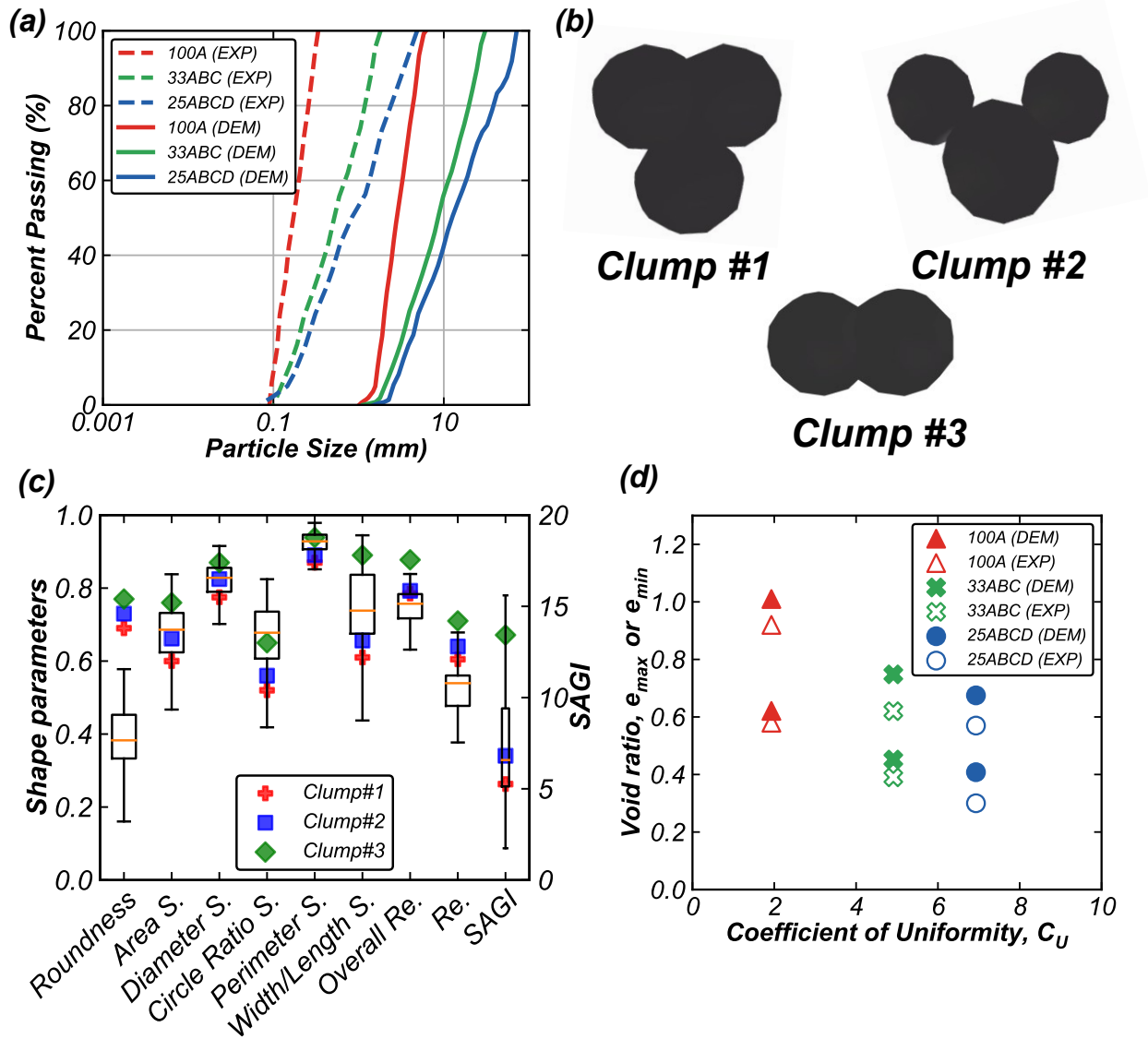


Figure 6.1: (a) Particle size distribution, (b) templates for clumped particles, (c) particle shape parameter distributions between real (box and whiskers) and clumped particles, and (d) e_{max} and e_{min} of the simulated materials. Note: *Re.* represents regularity and *S* represents sphericity.

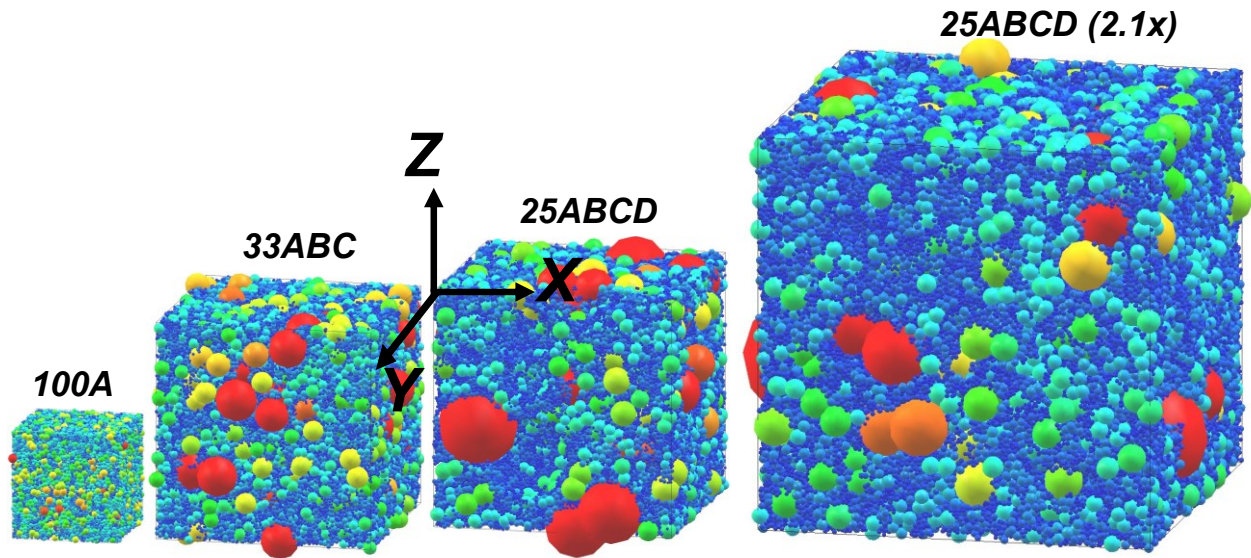


Figure 6.2: 100A, 33ABC, 25ABCD, and 25ABCD (2.1x) specimens. The colors represent the particle diameters and are normalized between the maximum (red) and minimum (blue) diameter across the specimen.

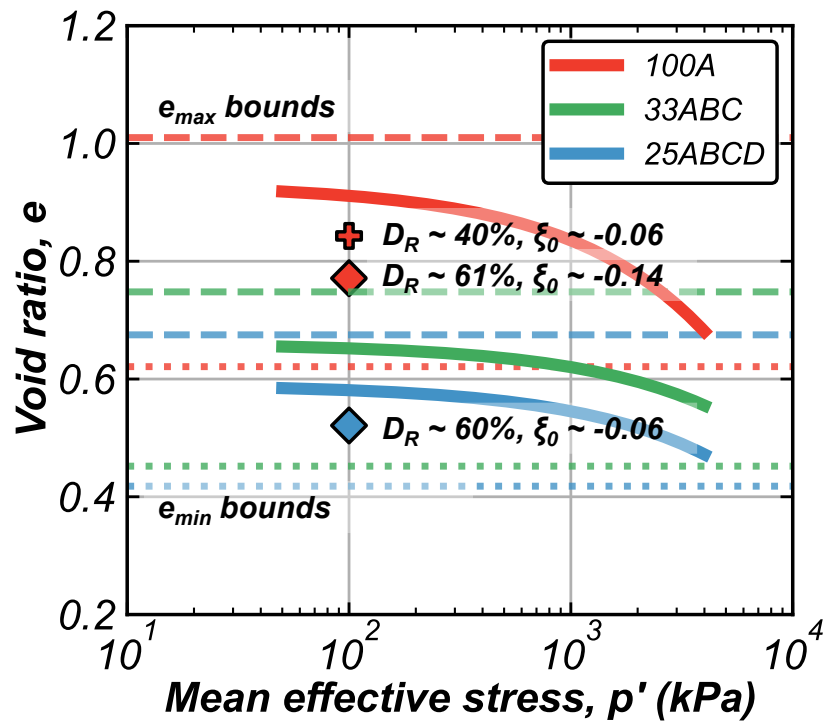


Figure 6.3: Critical state lines in the e - $\log(p')$ space based on the best fits presented in Basson et al. 2023(b). The dashed lines represent the respective e_{max} values, and dotted lines represent the respective e_{min} values.

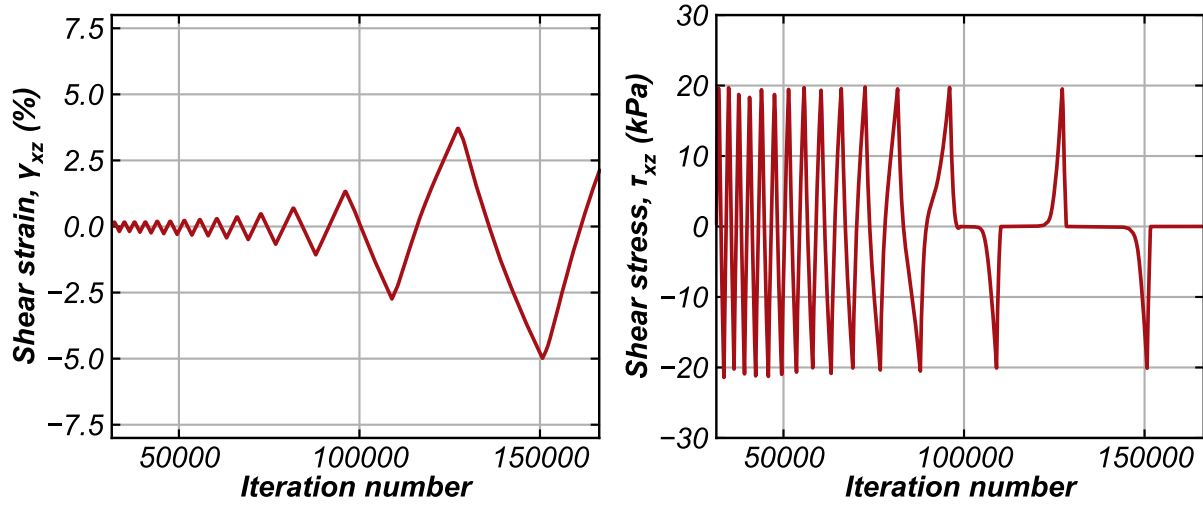


Figure 6.4: The variation of γ_{xz} and τ_{xz} with iteration number during the DSS simulation for a 100A specimen at a CSR of 0.2.

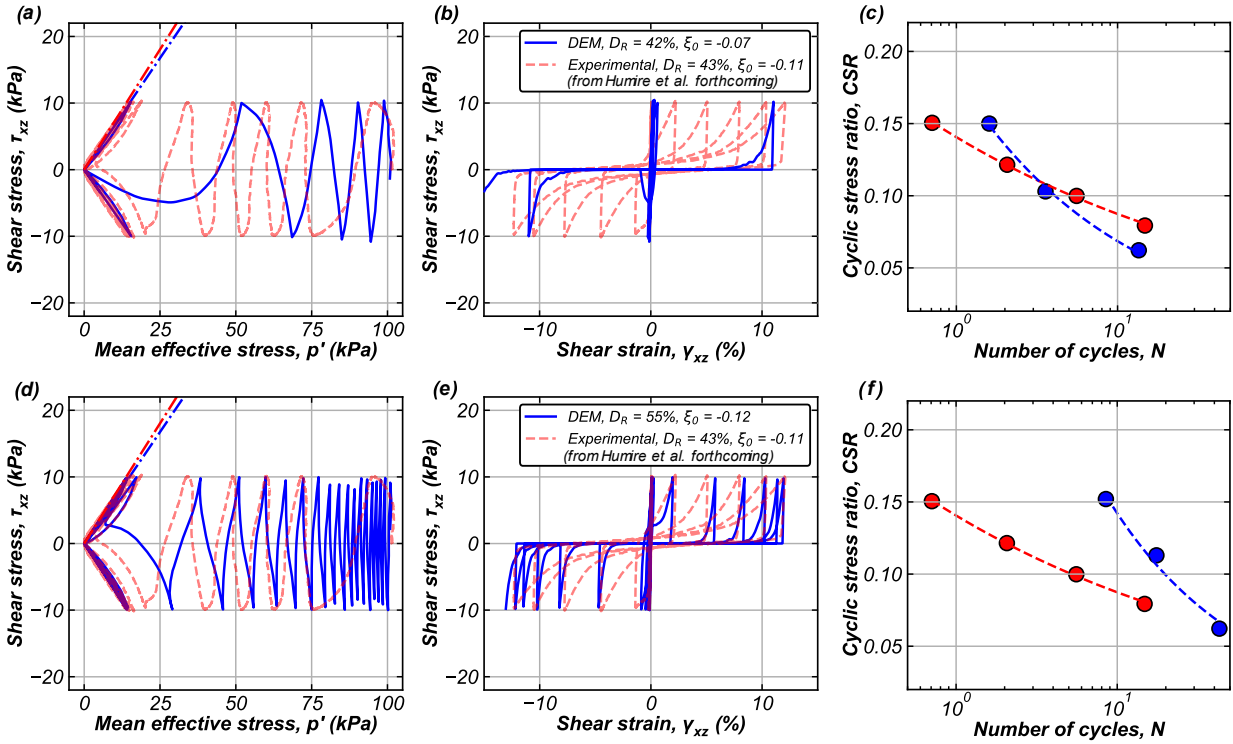


Figure 6.5: Comparison of the DSS results as (a,d) τ_{xz} versus p' , (b,e) τ_{xz} versus γ_{xz} , and (c,d) CSR versus N curve between DEM simulations and experiments for specimens prepared at a $D_R \sim 43\%$ and $\xi_0 \sim -0.11$, respectively. (a,b,d,e) present the response for specimen at CSR of 0.10. The dashed-dotted lines represent the failure slope (M_f) approximating the dilation phase of the butterfly-shaped response.

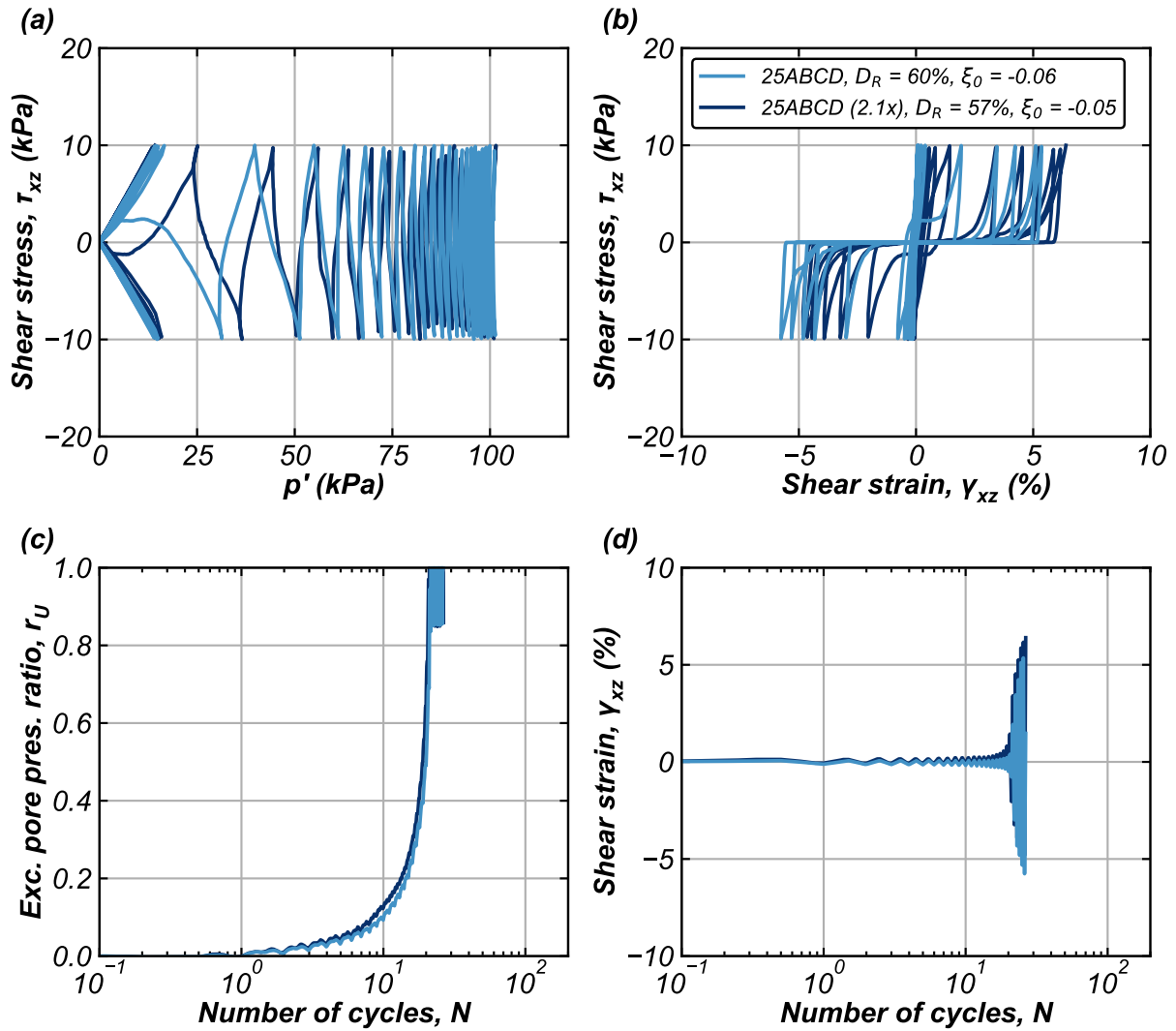


Figure 6.6: Comparison of DEM simulations results in terms of the (a) τ_{xz} versus p' , (b) τ_{xz} versus γ_{xz} , (c) r_U versus N , and (d) γ_{xz} versus N between 25ABCD and 25ABCD (2.1x) specimens.

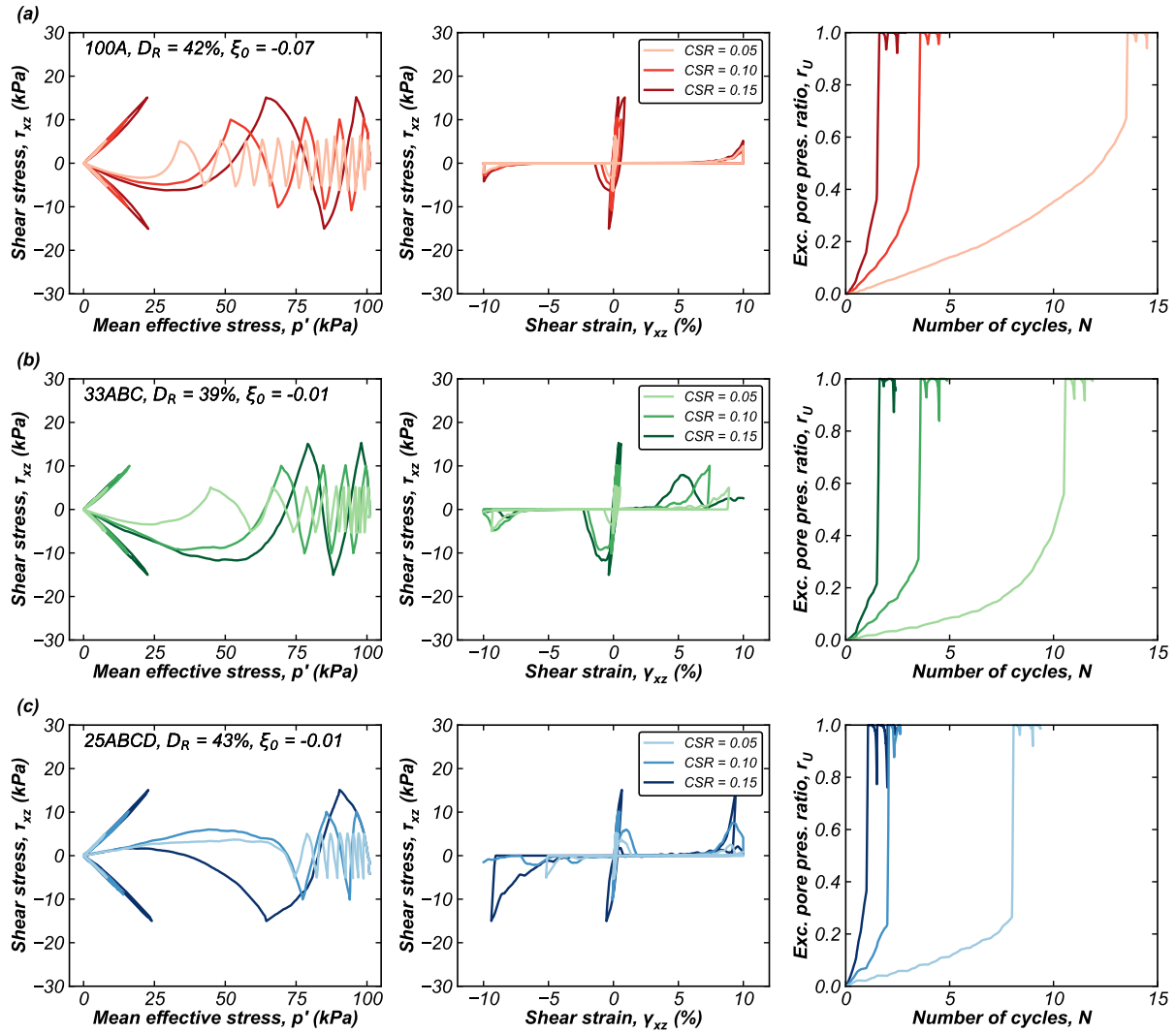


Figure 6.7: Comparison of DSS DEM simulation results for (a) 100A, (b) 33ABC, and (c)

25ABCD at p' of 100kPa and D_R between 39-43%.

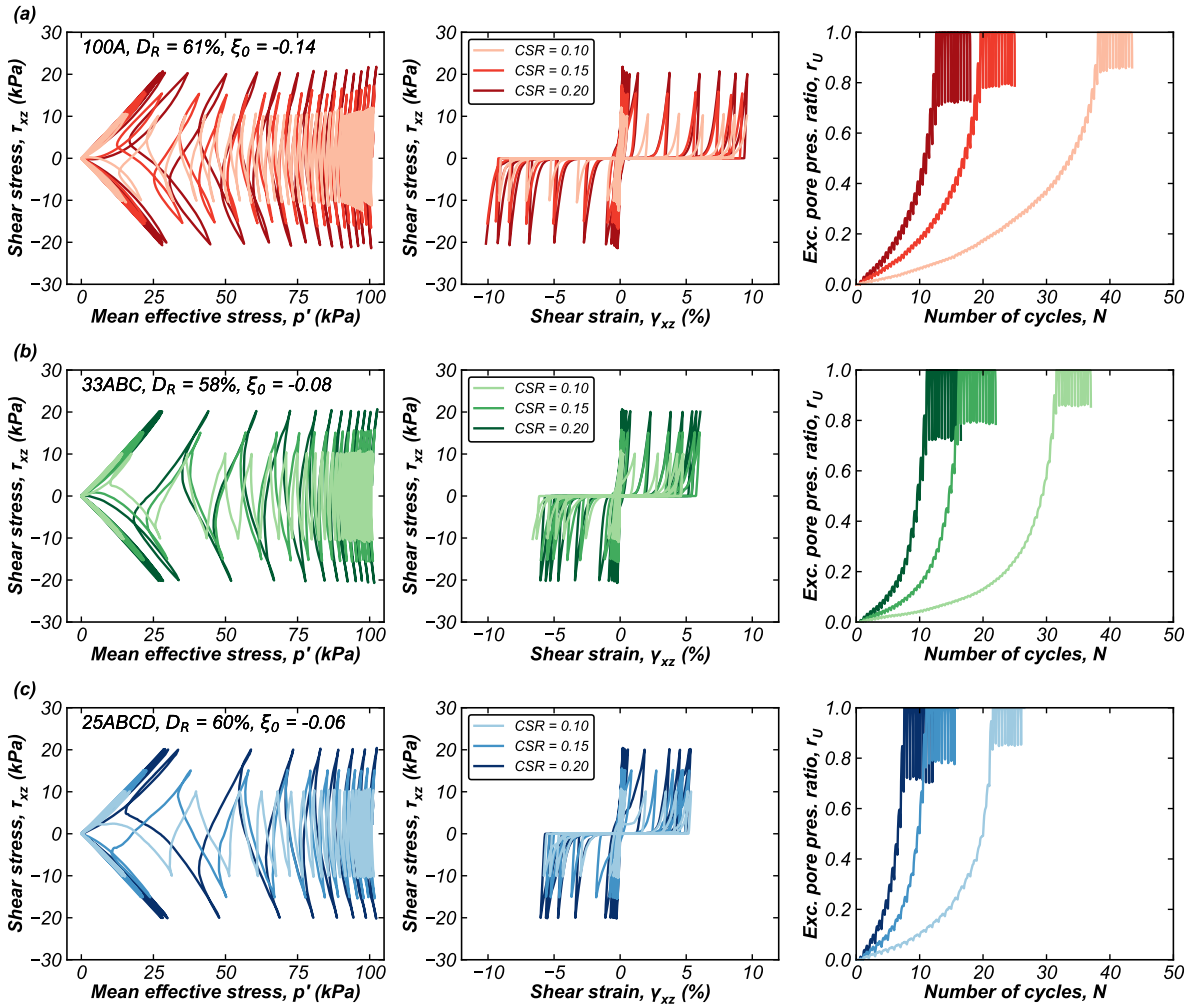


Figure 6.8: Comparison of DSS DEM simulation results for (a) 100A, (b) 33ABC, and (c)

25ABCD at p' of 100kPa and D_R between 58-61%.

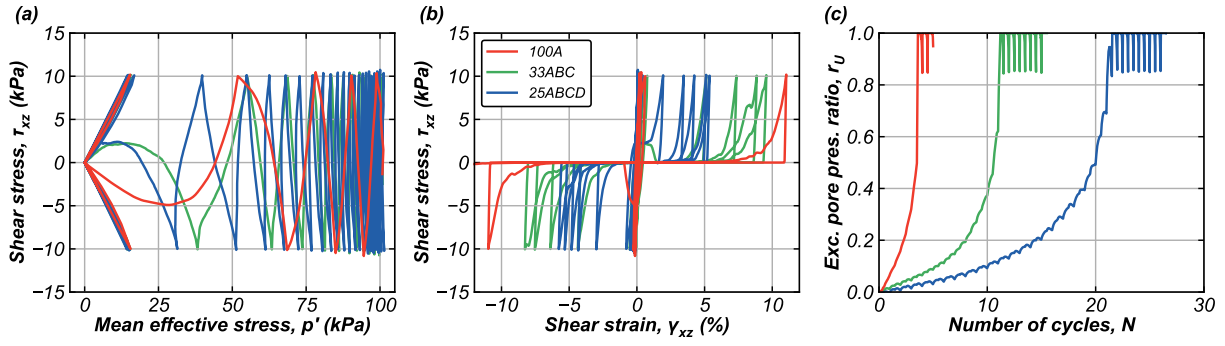


Figure 6.9: Comparison of DSS DEM simulation results as (a) τ_{xz} versus p' , (b) τ_{xz} versus γ_{xz} , and (c) r_u versus N for 100A, 33ABC, and 25ABCD at $\xi_0 \sim -0.06$.

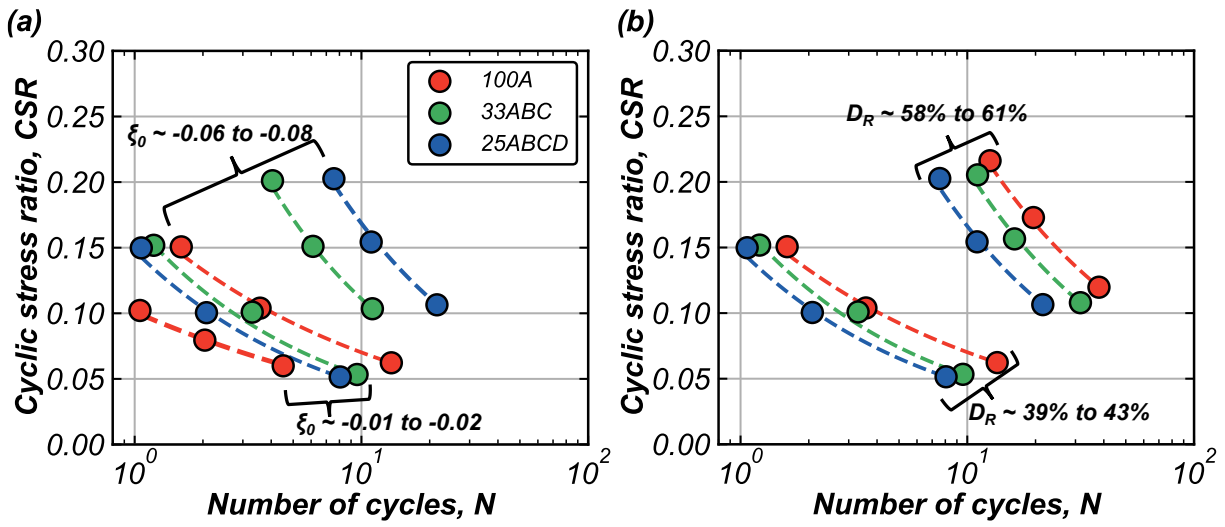


Figure 6.10: Liquefaction triggering curves in terms of CSR versus N for specimens with (a) similar D_R and (b) similar ξ_0 for 100A, 33ABC, and 25ABCD specimens at p' of 100kPa.

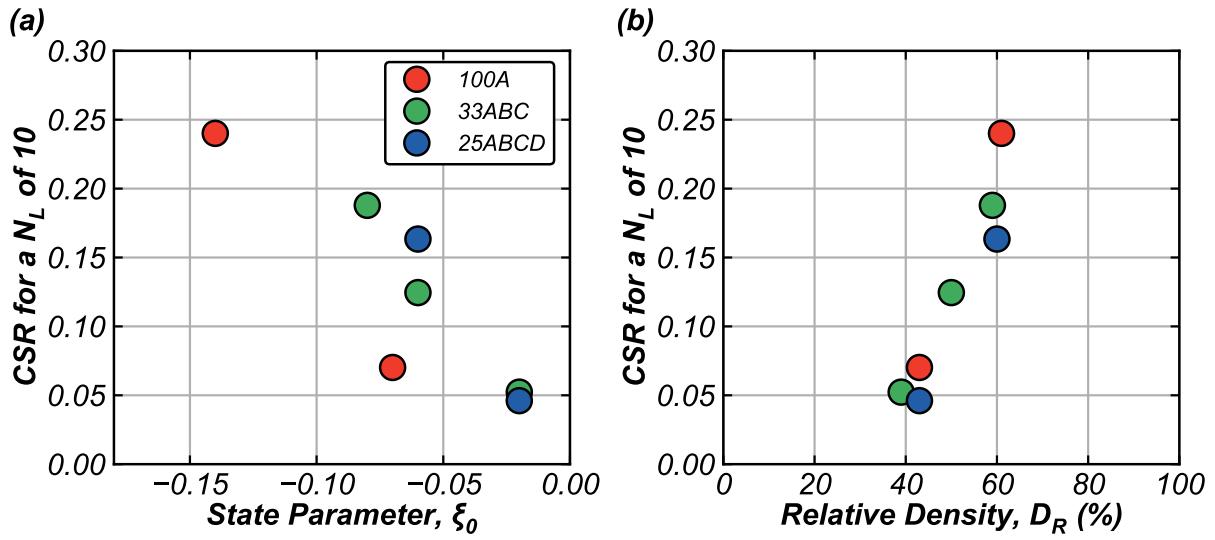


Figure 6.11: Comparison of cyclic strengths at N_L of 10 with (a) D_R and (b) ξ_0 for 100A, 33ABC, and 25ABCD specimens.

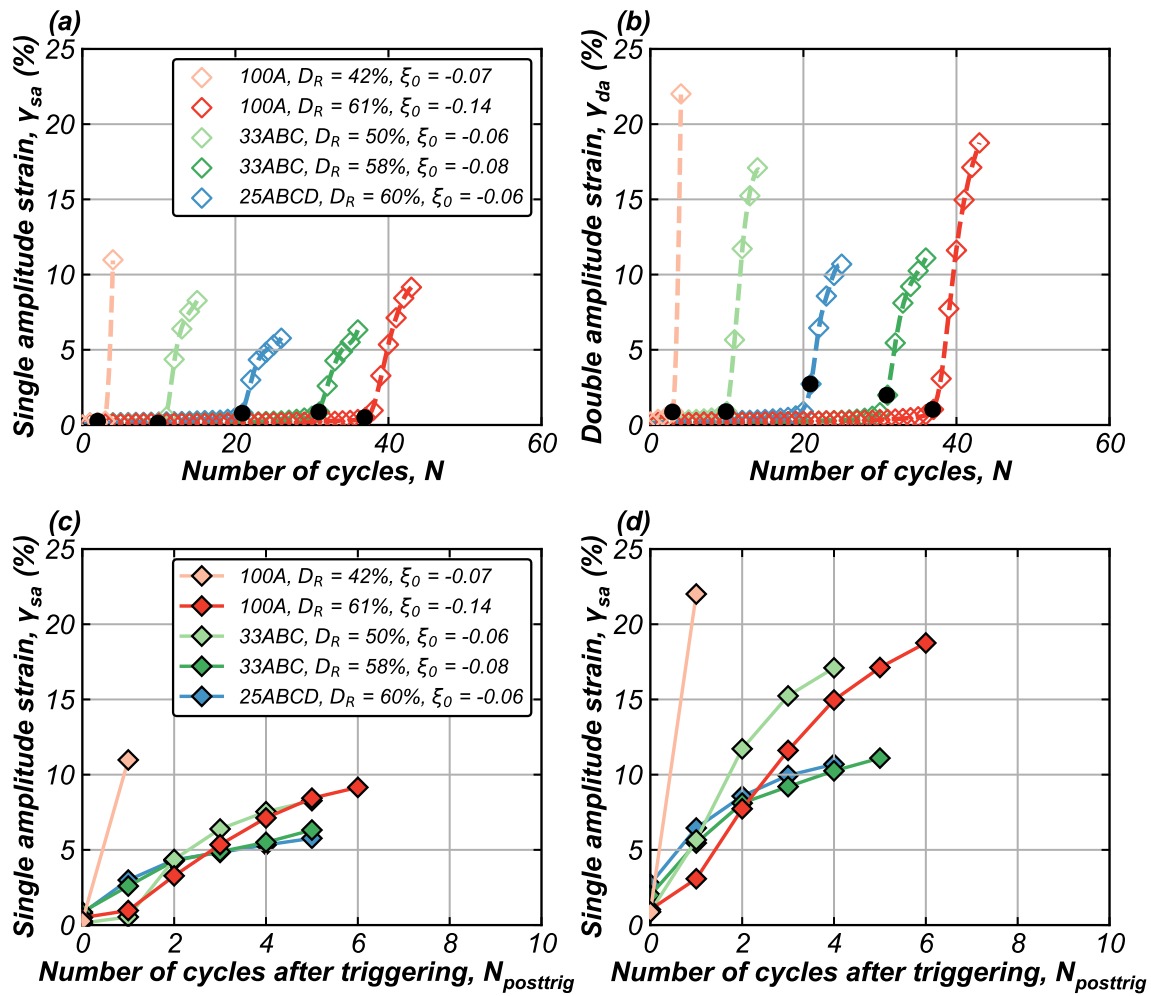


Figure 6.12: Comparison of (a) γ_{sa} and (b) γ_{da} with N , and (c) γ_{sa} and (d) γ_{da} with $N_{posttrig}$ for 100A, 33ABC, and 25ABCD specimens. Black dots represent the point of triggering.

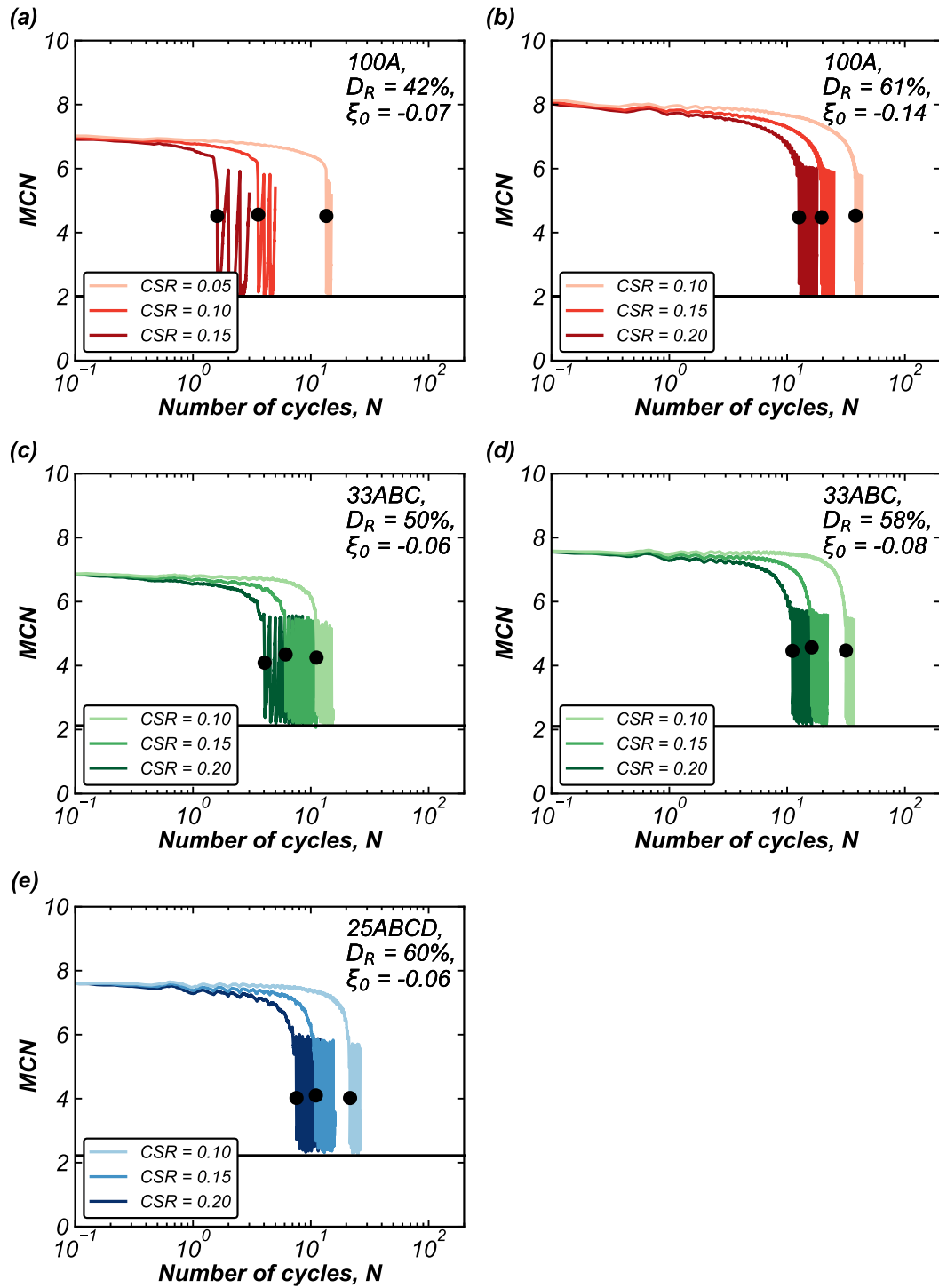


Figure 6.13: Comparison of MCN with N for (a,b) 100A, (c,d) 33ABC, and (e) 25ABCD specimens. Black dots represent the point of triggering liquefaction.

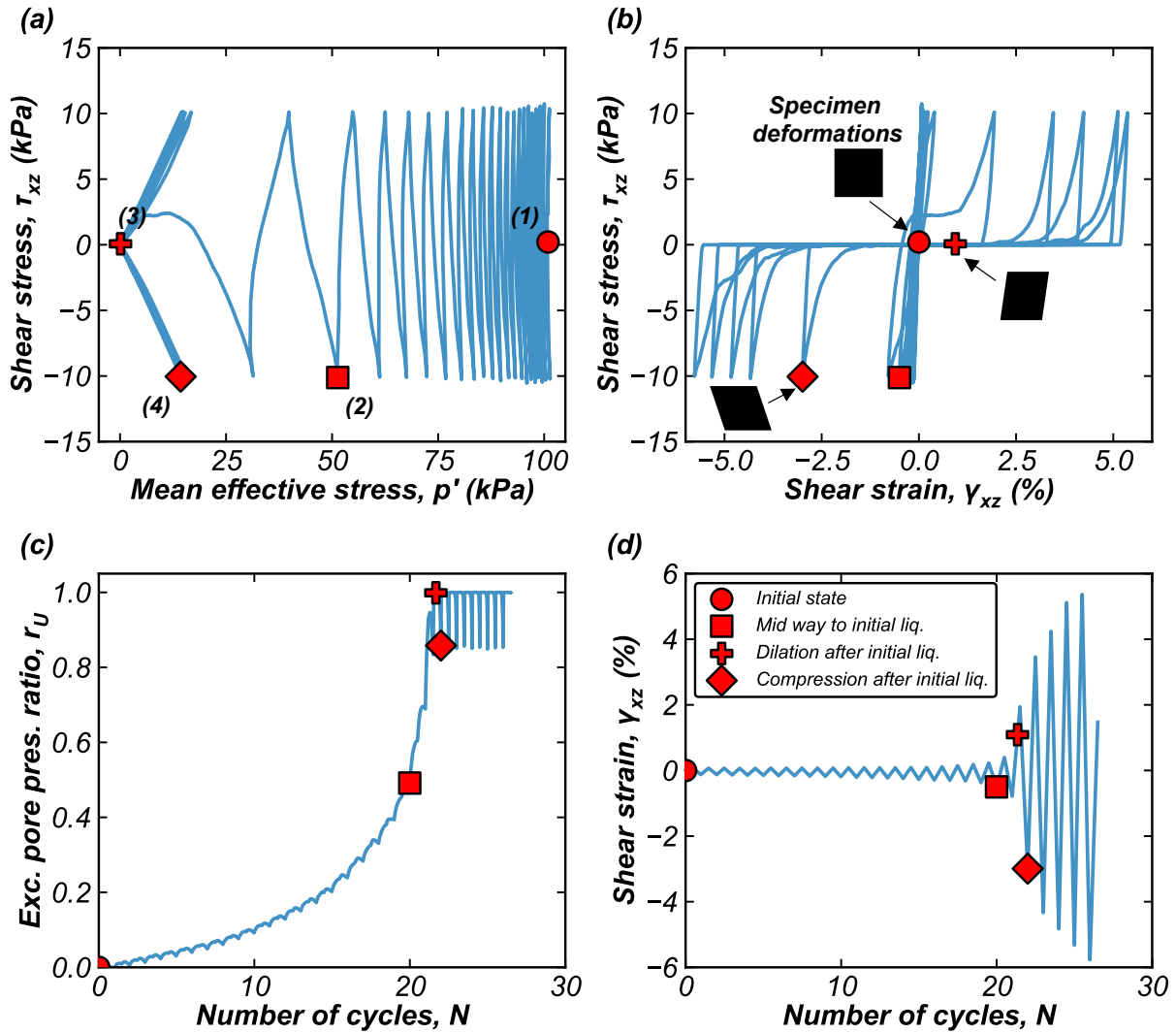


Figure 6.14: Schematic of point picked for fabric analysis at (1) start of shearing, (2) , (3) contraction phase immediately after triggering, and (4) end of first dilation phase post triggering on (a) τ_{xz} versus p' , (b) τ_{xz} versus γ_{xz} , (c) r_u versus N , and (d) γ_{xz} versus N for 25ABCD specimen at a ξ_0 of -0.06 tested for a CSR of 0.10.

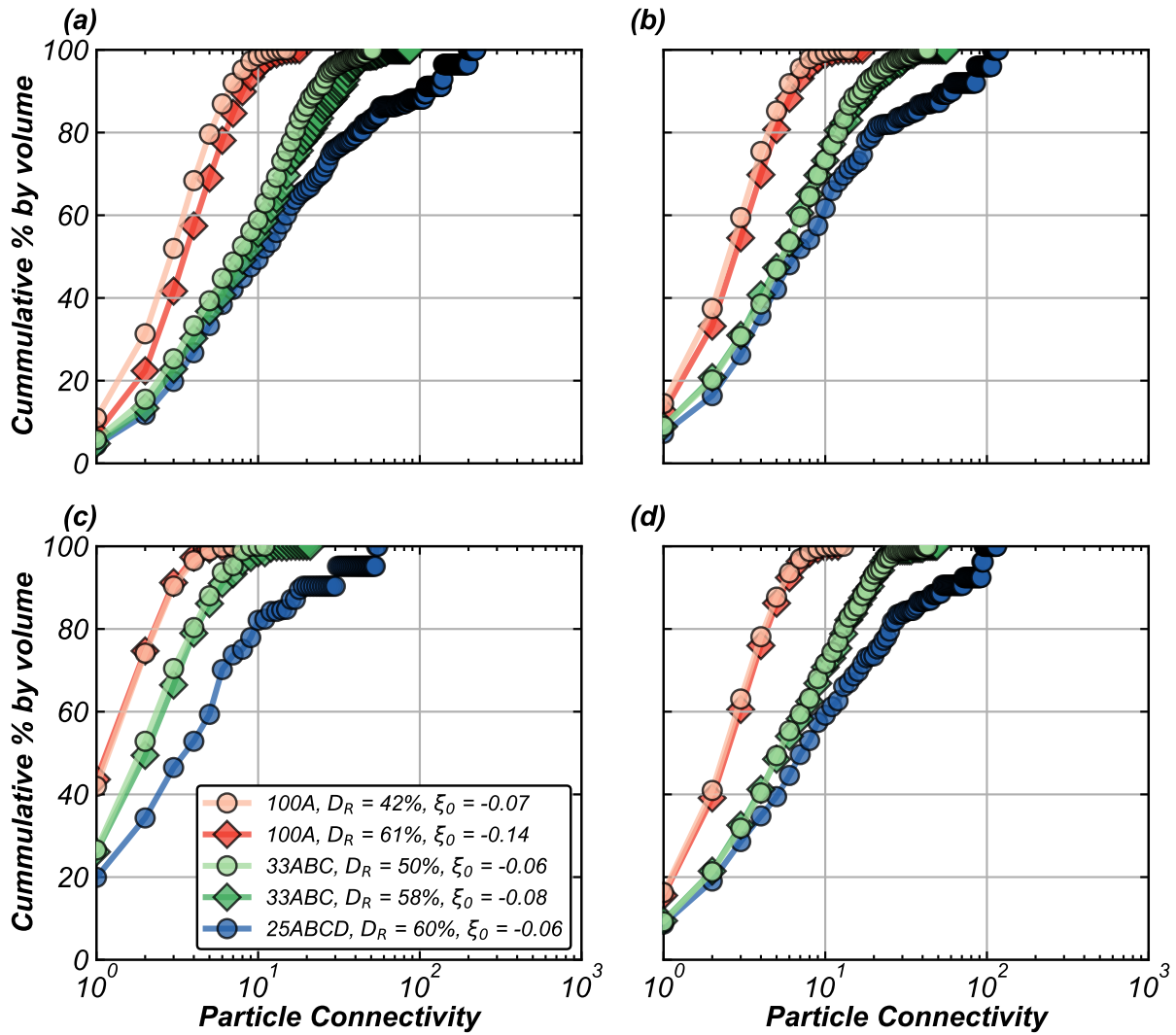


Figure 6.15: Cumulative distribution of PC for (a) initial state, (b) dilation before liquefaction, (c) contraction phase immediately after triggering, and (d) dilation phase post triggering for 100A, 33ABC, and 25ABCD specimens.

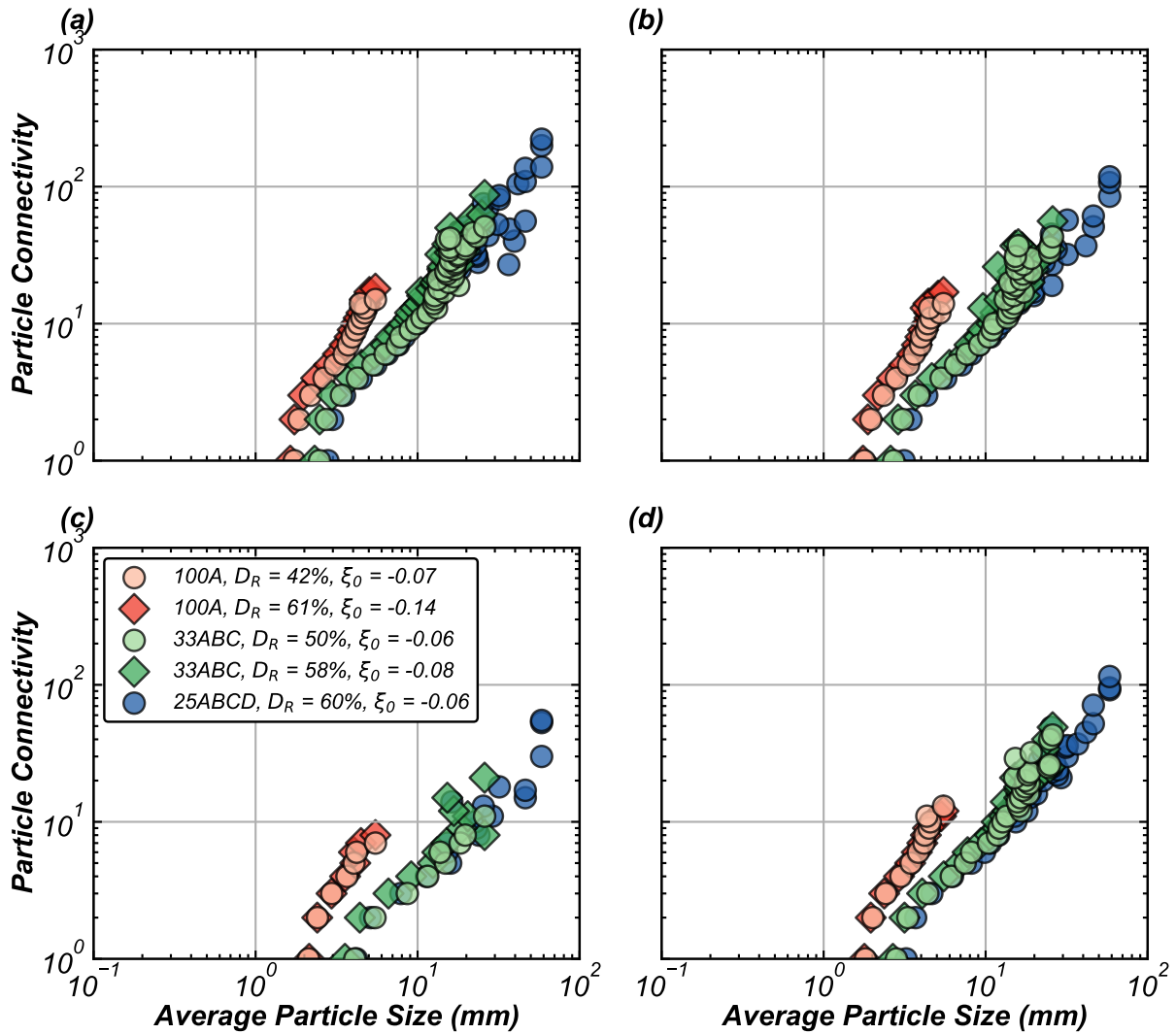


Figure 6.16: Variation of PC with the particle size for (a) initial state, (b) dilation before liquefaction, (c) contraction phase immediately after triggering, and (d) dilation phase post IL for 100A, 33ABC, and 25ABCD specimens.

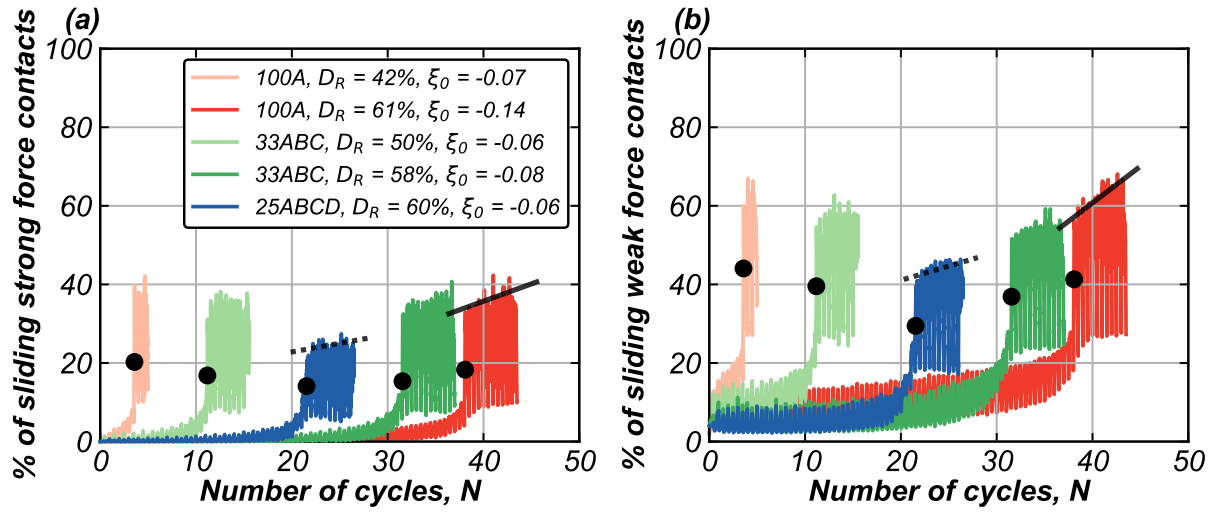


Figure 6.17: Percentage of sliding contacts carrying (a) strong forces and (b) weak forces with N for 100A, 33ABC, and 25ABCD specimens. Black dots represent the point of triggering.

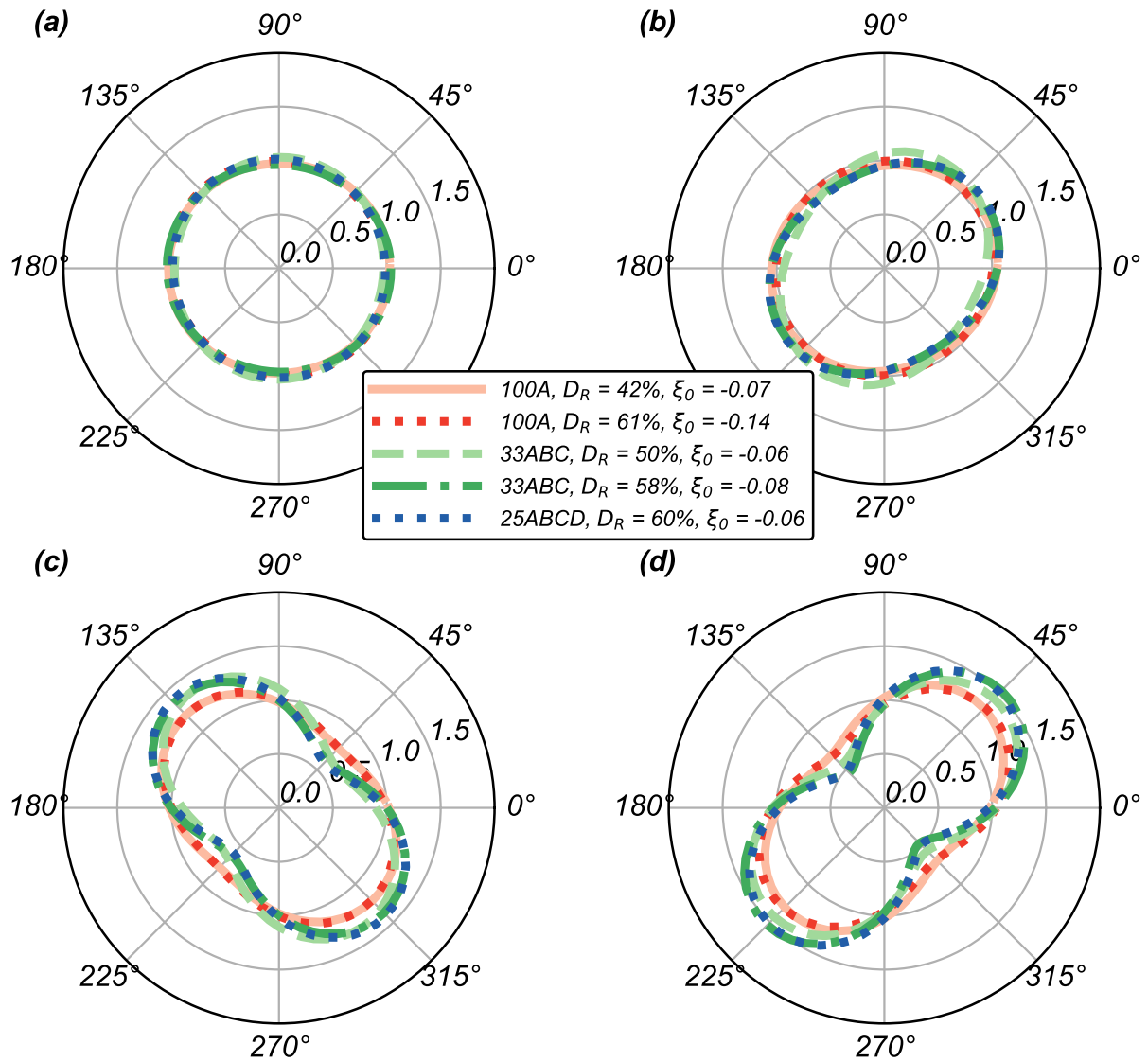
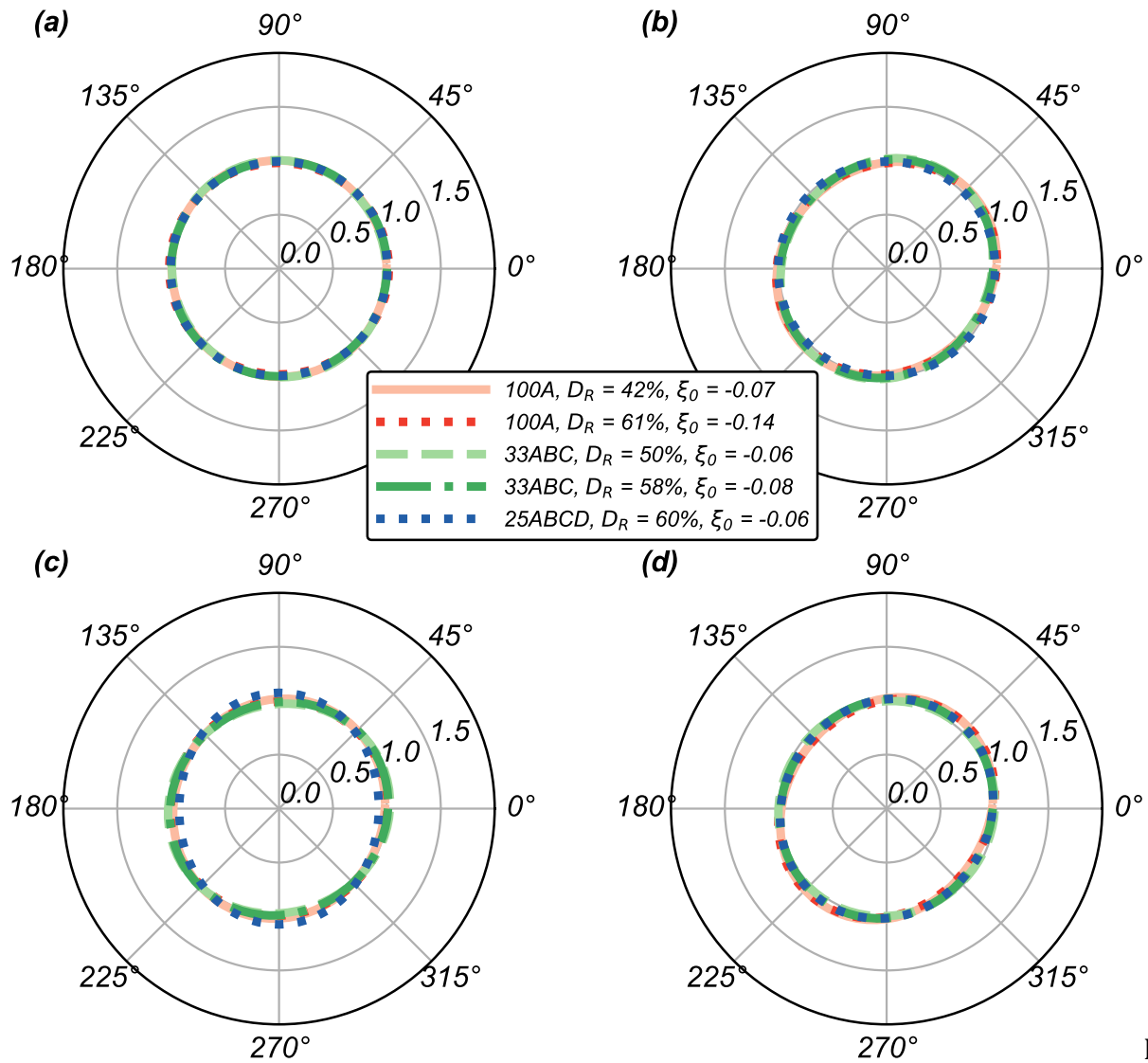


Figure 6.18: Angular distributions of normalized contact forces for (a) initial state, (b) dilation before liquefaction, (c) contraction phase immediately after triggering, and (d) dilation phase post triggering for strong forces for 100A, 33ABC, and 25ABCD specimens.



Fig

Figure 6.19: Angular distributions of normalized contact forces for (a) initial state, (b) dilation before liquefaction, (c) contraction phase immediately after triggering, and (d) dilation phase post triggering for weak forces for 100A, 33ABC, and 25ABCD specimens.

Chapter 7

Conclusions

This dissertation presented an investigation into the effect of inherent properties, such as the fabric- and stress-induced anisotropy and gradation, on the mechanical behavior of coarse-grained granular soils using Discrete Element Modeling (DEM) simulations and a newly developed experimental testing setup.

Chapter 2 described a newly developed testing setup that consists of seven bender element pairs that allow measuring shear wave velocity along different orientations and polarization planes. This system provides $V_{S,VH}$ (vertically propagating and horizontally polarized shear wave), $V_{S,HV}$ (horizontally propagating and vertically polarized shear wave), and $V_{S,HH}$ (horizontally propagating and horizontally polarized shear wave) measurements, as well as shear wave measurements (V_S) at 75°, 65°, 55°, and 50° (from the horizontal) to provide a sweep between $V_{S,VH}$ and $V_{S,HV}$. Experiments were conducted on glass beads and angular sand specimens under isotropic or 1D compression to assess the impact of the stress- and fabric-induced anisotropies on the V_S obtained across different orientations and polarization planes.

Chapter 3 presented the results of experiments and DEM simulations aimed at quantifying the anisotropy of V_S along different orientations and polarization planes in granular soil specimens. The influence of particle shape, depositional processes, and stress

state on the V_s anisotropy is investigated. Specimens with different stress anisotropy (isotropic versus 1D compression) and fabric anisotropy (spheres versus elongated clumps in DEM, glass beads versus natural elongated sand in experiments) were tested to highlight the effect on the polar distributions of V_s and to develop a framework for assessing the anisotropy of soil specimens.

Chapter 4 investigated the effect of the shape of the particle size distribution (PSD) on the proportion of inactive particles, distributions of particle connectivity, and contact force transmission between particles of varying sizes in granular assemblies by means of a series of isotropic compression 3D DEM simulations. The simulations were performed on the specimens made of five different PSDs. Additionally, a parametric study was conducted to identify the effect of particle contact law parameters on particle connectivity (PC) and the proportion of inactive particles in specimens with different magnitudes of polydispersity.

Chapter 5 explored the influence of gradation on the shear strength, volume change, and stress-dilatancy of coarse-grained soils using DEM simulations on specimens with C_u between 1.9 and 6.4. Monotonic drained and undrained simulations were performed to highlight the gradation effects on the drained and undrained triaxial response, critical state lines, and the associated slope and intercept parameters, and parameters such as the peak friction angle (ϕ'_p), difference of the peak and critical state friction angles ($\phi'_p - \phi'_{cs}$) and maximum dilation angle (ψ_{max}), excess pore pressure (u_{min}), and excess pore pressure generation rate ($(\delta u / \delta \epsilon_a)_{min}$). Additionally, a comparison of the simulation results with the trends presented in Bolton (1986) and Been and Jefferies (1985) is presented, along with a

comparison of results with relative density and initial state parameter, to identify a state parameter that captures systematic differences in the response of broadening of gradation.

Chapter 6 presented a 3D DEM investigation into the effect of gradation on the liquefaction resistance and post-liquefaction response of coarse-grained soils. Through cyclic constant volume direct simple shear simulations, both macroscale and microscale data were analyzed to provide insights into various aspects of cyclic soil behavior, including liquefaction triggering resistance, post-triggering strain accumulation, sliding at particle contacts, packing, and PC, and the anisotropy in strong and weak force networks. Additionally, the results are compared at similar relative densities and initial state parameters to emphasize the significance of selecting the appropriate state parameter to capture the effects of gradation.

7.1 Estimation of soil fabric

The testing setup described in Chapter 2, along with the presented results in Chapters 2 and 3, emphasizes the utility of using V_s measurements along different orientations and polarization planes to assess the anisotropy of soil specimens. The results suggest that the stress- and fabric-induced anisotropies can be identified by employing the parameters describing the angular distribution of V_s and by comparing $V_{s,HV}$ to $V_{s,HH}$, and $V_{s,VH}$ to $V_{s,HH}$. Additionally, a comparison of the obtained data to that of field studies suggests that the presence of stress- and fabric-induced anisotropy can be obtained indirectly through V_s measurements using existing methodologies such as SCPT, cross-hole, and down-hole testing. This information could be crucial for designing and analyzing geosystems affected by soil fabric, such as a dam with underlying seepage.

Specimens with negligible stress- (i.e., isotropic compression) and fabric-induced (spheres and glass beads) anisotropies have near-circular V_S polar distributions. Under 1D compression, these exhibit vertically elongated V_S polar distributions due to the greater vertical stresses and concomitant contact normal forces. Specimens of elongated clumps and natural angular sand show considerable fabric-induced anisotropy. Under isotropic compression, the V_S distribution for these specimens is horizontally elongated, controlled by the distribution of particle long-axis orientations.

The preferential direction of the stress- and fabric-induced anisotropies determines the existence of competing or supportive mechanisms. When the anisotropies are in opposite directions (e.g., horizontally-aligned elongated particles under 1D compression with $K < 1$), the V_S distribution is near-isotropic because their effect cancels out. When the anisotropies are in the same direction (e.g., horizontally aligned elongated particles under 1D compression with $K > 1$), the net anisotropy in the specimen increases.

Angular distributions of V_S illustrate the stiffness anisotropy visually, and fitting them with analytical equations provides quantitative anisotropy metrics. The V_S polar distributions were closely related to the contact normal force and particle long-axis orientation polar distributions. An equation to describe the experimentally determined angular distribution of V_S was proposed, which has the same form as established relationships used to describe the distribution of particle orientation and contact normal vectors. The coefficient a_n adequately quantifies the anisotropy of the angular V_S distribution, as presented in Chapters 2 and 3.

Systematic comparison of $V_{S,HV}/V_{S,VH}$ and $V_{S,HV}/V_{S,HH}$ and the proposed Anisotropy parameter (A_e) can help discern the effects of stress- and fabric-induced anisotropy on soil specimens. The specimen anisotropy can be visualized in $V_{S,HV}/V_{S,VH}$ versus $V_{S,HV}/V_{S,HH}$ space, or in A_e versus $V_{S,HV}/V_{S,VH}$ and $V_{S,HV}/V_{S,HH}$ spaces, which can help determine the type of anisotropy. However, challenges remain to decouple the effects of stress and fabric anisotropy when both simultaneously affect the response of a specimen. These results are presented in Chapter 3.

The magnitude of effective stress in specimens strongly influences the V_S magnitudes, irrespective of the material and loading conditions. This dependency was observed in measurements obtained in all orientations and polarization planes, and the α -coefficient and β -exponent values that describe the power function between both parameters agree with values published in the literature. The results show that the α -coefficient and β -exponent values are not constant for a given specimen, but they depend on the orientation and the polarization plane of the shear waves, as presented in Chapters 2 and 3.

7.2 Effect of gradation on the mechanical behavior of soils

Highly polydisperse and bimodal gradations, with a higher coefficient of uniformity (C_u), have a larger percentage of inactive particles by number during isotropic compression, predominantly consisting of finer particles. The coarser particles in these gradations are surrounded by a higher number of finer particles, as shown by the increase in PC with an increase in particle size, and they carry the largest magnitude of contact normal forces. The DEM simulations indicate that an increase in stiffness ratio, a decrease in particle friction

coefficient, and an increase in global viscous damping result in an overall decrease in the proportion of inactive particles in the specimen. These results are presented in Chapter 4.

The gradation had a significant effect on the mechanical response of soil specimens during triaxial shearing. Specimens with broader gradation mobilized greater peak shear strengths, dilative volume changes, rates of dilation, negative excess pore pressures, and rates of pore pressure generation when compared at the same initial state parameter, ξ_0 . The position and slope of the critical state line in the $e\text{-}\log(p')$ plane decrease as the gradation becomes wider, and at similar ξ_0 , ϕ'_p , $\phi'_p - \phi'_{cs}$, and ψ_{\max} , increase with an increase in gradation. In contrast, when plotted in terms of relative density, D_R , the gradation effects are obscured.

A comparison of the simulation results with the trends presented in Bolton (1986) and Been and Jefferies (1985) suggests that these frameworks do not explicitly capture the effect of gradation. Specifically, the simulation results for the more broadly-graded specimens indicate that they plot higher in $\phi'_p - \phi'_{cs}$ vs. p' space than those predicted by Bolton's framework. Also, while the 100A (i.e., $C_U = 1.98$) specimen results align with the lower bound presented by Been and Jefferies (1985) in ϕ'_p vs. ξ_0 and $\phi'_p - \phi'_{cs}$ vs. ξ_0 spaces, the 25ABCD (i.e., $C_U = 6.37$) specimen results have greater ϕ'_p and $\phi'_p - \phi'_{cs}$ values than those corresponding to the reported upper bound for any given ξ_0 .

In specimens with broader gradations, the coarsest particles form a significant number of contacts with their neighboring particles, carrying the greatest contact forces. The coarsest particle for the 25ABCD specimen (i.e., $C_U = 6.37$) is connected to 12x more particles than the coarsest particle in the 100A (i.e., $C_U = 1.98$) specimen at a similar ξ_0 . The greater

interlocking of the coarser particles leads to greater dilation during shearing, resulting in greater peak shear strengths for the more broadly graded specimens. The largest particles in the 25ABCD specimen carry up to 50x the average contact force, while the coarsest particles in the 100A specimen carry about 3.5x the average contact force. The fraction of particles in the strong force network increases as the gradation becomes broader, from D_{40} to D_{100} for the poorly graded 100A specimen to D_{20} to D_{100} for the broadly graded 25ABCD specimen. The D_{10} size is close to the average threshold size of the particles inactive in the transmission of contact forces for specimens of all considered gradations. The contact force distributions indicate that the strong force network (carried by the coarser particles) aligns with the major principal stress direction. In contrast, the weak force network and inactive particles provide buckling resistance, which becomes more pronounced with an increase in gradation. Overall, these results indicate that gradation significantly affects the peak strength and dilatancy of coarse-grained soils, driven by the disproportionately high role of the coarsest particles in the assembly in transmitting contact forces. These effects are readily captured when ξ_0 is used as the state parameter for comparing different soils. These findings are presented in detail in Chapter 5.

For the cyclic response, the specimen with broader gradation (25ABCD) exhibits lower liquefaction triggering resistance than the poorly-graded specimen (100A) at similar D_R , while showing higher resistance at similar ξ_0 . Post-liquefaction, the 25ABCD specimens accumulate less shear strains than 100A specimens at similar D_R and ξ_0 . At the point of liquefaction triggering, the 25ABCD specimen shows a lower percentage of sliding contacts for both strong and weak force-carrying contacts. Additionally, specimens with broader gradations show higher particle connectivity at all the points during shearing. At the start of

shearing, the largest particles for 25ABCD have 11x more contact with neighboring particles than the 100A specimen. Similarly, at the point of initial liquefaction, the largest particles for the 25ABCD specimen are connected to 6x more contact with neighboring particles than the 100A specimen. Moreover, the percentage of inactive particles at initial liquefaction is 2.3x lower for the 25ABCD specimen than the 100A specimen. These observations suggest that broader gradations promote tighter particle packing and greater interlocking of coarser particles, leading to enhanced dilative tendencies and lower post-liquefaction strain accumulation. The analysis of anisotropy in the contact force networks indicates that the strong forces align with the major principal direction, and the anisotropy in the strong forces increases with an increase in C_u . The weak forces are relatively isotropic and provide crucial to the buckling of the strong force networks. The breadth of the gradation, along with the disproportionately higher contribution of the coarser particles to interlocking and thus limiting of overall specimen deformation during cyclic loading, highlight the significance of gradation in understanding the cyclic shearing behavior of granular soils. These findings are presented in detail in Chapter 6.

7.3 Recommendations for future work

The future research directions that could address the limitations and knowledge gaps identified in this dissertation, and contribute to further advancements in understanding the fundamental behavior of granular soils, are as follows:

- Validation of the proposed V_s framework for identification of fabric- and stress-induced anisotropies: Comparing the indirect V_s assessment proposed in this dissertation with the direct measurements from X-ray computed tomography of the

same specimens would assist in verifying the trends reported in the proposed framework.

- Field testing validation of the proposed V_S framework: Conducting shear wave propagation tests in various directions and orientations using cross-hole and down-hole techniques, along with testing of undisturbed soil specimens in the laboratory using the proposed testing setup, would cross-validate the anisotropies obtained from both methods and assess the applicability of the V_S framework to field conditions.
- Modified BE testing setup for V_S measurements during triaxial testing: Modifying the proposed testing setup to accommodate standard triaxial specimens would enable continuous V_S measurements during isotropic and anisotropic triaxial compression tests. This would provide fundamental insights into the evolution of the stress- and fabric-induced anisotropies during shearing and facilitate the development of constitutive models incorporating soil fabric effects.
- Improved particle shape representation and capturing the deformation of surface asperities in DEM simulations: With better computational resources, the particle shape of sub-angular soils could be better represented using higher-order clump templates composed of a larger number of sub-particles. Exploring other particle shape recreation techniques, such as spherical harmonics or level-set discrete elements, could also mimic realistic particle shapes. Additionally, using different contact laws, such as the Greenwood-Williamson contact law, could help understand the effect of surface roughness and asperity deformation on the overall soil response during loading.

- Expansion of the V_s framework to different soil types: Considering the effect of soil type, including clays and organic soils, would require wave propagation simulations on specimens with platy particles. Using bonded contact models for DEM or material point method (MPM) could provide valuable insights for modifying the proposed V_s framework accordingly.
- Investigating the effect of particle crushing on V_s measurements: Further investigation into the influence of particle crushing on stiffness anisotropy is needed. This would guide modifications to the proposed framework to account for a variety of soils, including crushable carbonate soils.
- Investigation of sample preparation techniques on V_s measurements: Examining the effect of sample preparation methods, such as dry and moist tamping, funnel deposition, and air pluviation, on stiffness anisotropy would enhance understanding of the influence of specimen preparation on the presented V_s framework.
- Effect of boundary conditions and loading directions on monotonic and cyclic strength of coarse-grained soils: Simulating flexible membrane and stacked ring boundary conditions in DEM simulations would improve the calibration of overall responses between experiments and simulations. Additionally, drained and undrained triaxial extension and hollow cylinder simulations could help identify the effect of gradation on the strength anisotropy of coarse-grained soils.
- Investigations on the monotonic and cyclic strength of diverse gradations: Incorporating a wider range of gradations, such as bimodal mixtures of fines and coarse soils, would provide valuable insights into the engineering behavior of

granular soils and aid in understanding anisotropy from different particle size perspectives (fine-fine, fine-coarse, and coarse-coarse).

- Investigation of D_{50} changes on the critical states lines and monotonic and cyclic strength of coarse-grained soils: Conducting additional simulations to evaluate the effect of increasing D_{50} using a non-normalized contact law, where stiffness is not held constant with an increase in particle size, would help explain the changes in soil behavior as a result of variations in D_{50} , which could provide insights into the trends observed in experimental results showing the coupled effect of D_{50} and C_u .
- Incorporating coupled solid-pore fluid modeling in DEM simulations: The current undrained simulations rely on a constant volume approximation to enforce undrained conditions. However, centrifuge and experimental studies have shown that the permeability of broadly graded soils is significantly influenced by the presence of the finer particle, which affects the pore pressure dissipation characteristics during cyclic loading. Conducting additional simulations using Computational Fluid Dynamics (CFD) with DEM would allow for consideration of permeability changes and explore their impact on cyclic response, liquefaction triggering resistance, and post-liquefaction strain accumulation in broadly graded soils.
- Assessing the applicability of sand-based liquefaction triggering correlations for varying gradations: Simulating Cone Penetration Tests (CPT) using DEM, along with drained/undrained-monotonic/cyclic triaxial and direct simple shear (DSS) simulations, would assist in investigating the suitability of using strength response-

penetration resistance relationships developed for clean sands for soils with broader gradations.

- DSS DEM simulations that consider shear stress bias: Conducting DSS simulations to investigate the effect of gradation on the monotonic and cyclic response of coarse-grained soils under sloping ground conditions, with different initial static shear stress ratios, could provide insights into the variability of the K_α correction curves available in the literature and provide modifications for broadly graded soils.
- DSS DEM simulations at different overburden stresses: Conducting DSS simulations to investigate the effect of gradation on the monotonic and cyclic response of coarse-grained soils under different overburden pressures could provide insights into the variability of the K_σ correction curves available in the literature and provide modifications for broadly graded soils.
- Using DEM simulations as clean test data for training machine learning (ML) algorithms: The data obtained from DEM simulations of drained/undrained-monotonic/cyclic strengths and cone penetration tests can serve as valuable training data for machine learning algorithms. These algorithms can be trained to develop triggering correlations that incorporate the influence of gradations in predicting liquefaction potential and strength response.